# Study on a Hybrid Wind Turbine System with Intrinsic Compressed Air Energy Storage Provision

by

**Christopher Krupke**

A thesis submitted in partial fulfilment of the requirements for the degree of

Doctor of Philosophy in Engineering

The University of Warwick

School of Engineering

May 2016

# *Table of Contents*

# *List of Figures*

# *List of Tables*

# *Acknowledgement*

I would like to express my gratitude to my supervisor Professor Jihong Wang for her continued support, expert guidance and encouragement as well as the financial resources required to conduct this research. She provided me with opportunities that I endeavoured not to take for granted.

I would also like to thank all my colleagues and friends from the Power and Control Systems Research Lab, especially Dr Oleh Kiselychnyk and Dr Xing Luo, for their support throughout my time here. Further thanks go to all technicians from the workshop for their friendly help with every manufacturing matter.

I must also thank Dr Ken Mao, Professor JiDai Wang and Dr Zhiwei Wang for their advice on gearbox design and the extensive support in the manufacturing process of the device.

Further acknowledgement goes to the studentship support from EPSRC DTA and the School of Engineering, the University of Warwick.

Finally, I would like to thank all my friends who kept me sane and made sure that I develop some social skills in my time off.

Christopher Krupke

May 2016

# *Declarations*

I hereby declare that the material in this thesis has not been submitted for a higher degree at any other university. This thesis entirely contains research work carried out by Mr Christopher Krupke under the supervision of Professor Jihong Wang, unless references are given.

Some parts of this thesis were included in the following publications:

C. Krupke, J. Wang, J. Clarke, and X. Luo, "Dynamic modelling of a hybrid wind turbine in connection with compressed air energy storage through a power split transmission device," in *Advanced Intelligent Mechatronics (AIM), 2015 IEEE International Conference on*, 2015, pp. 79-84.

C. Krupke and J. Wang, "Modelling and robust control of an inverted pendulum driven by a pneumatic cylinder," in *Advanced Intelligent Mechatronics (AIM), 2015 IEEE International Conference on*, 2015, pp. 812-817.

X. Luo, J. Wang, M. Dooner, J. Clarke, and C. Krupke, "Overview of current development in compressed air energy storage technology," *Energy Procedia,* vol. 62, pp. 603-611, 2014.

X. Luo, J. Wang, C. Krupke, and H. Xu, "Feasibility study of a scroll expander for recycling low-pressure exhaust gas energy from a vehicle gasoline engine system," *Energies,* vol. 9, p. 231, 2016.

C. Krupke, J. Wang, J. Clarke, and X. Luo, " Modelling and Experimental Study of a Wind Turbine System in Hybrid Connection with Compressed Air Energy Storage," *Energy conversion, ieee transactions on*, issue 99, 2016.

J. Wang, X. Luo, C. Krupke, and M. Dooner, in *The World Scientific Handbook of Energy: Chapter 3 Compressed Air Energy Storage*. vol. 4, G. Crawley, 2016.

# *Abstract*

Recent years have witnessed the expansion of the wind power industry, spawned from international legislation that commits countries to increasing their share of renewable energy, compared to their gross energy consumption. However, increased exploitation of wind power poses challenges for power network operation. The variability and uncertainty of wind power may lead to network capacity constraints, system stability issues and potential wind power curtailment in the near future. Energy storage is considered to be one of the most viable options to support the integration of increased wind power to the power network. This project is concerned with developing a hybrid wind turbine with intrinsic compressed air energy storage provision, so that the power output of a wind turbine can be controlled, thus providing flexibility.

The proposed hybrid wind turbine makes use of compressed air energy storage on a turbine level. An efficient power split device in the form of a planetary gear box is designed to couple a horizontal axis wind turbine with a scroll air expander/compressor machine, i.e. a single device that can swap its operation, and a permanent magnet synchronous generator/motor. The hybrid wind turbine can operate in conventional standalone fashion. In addition, power can be added and taken away to/from the system through the expansion and compression mode. The hybrid wind turbine also offers standalone energy storage provision, so that power can be extracted from the grid and returned at later times.

The whole system mathematical model is derived and successfully validated by means of a small scale experimental test rig. Equipped with feedback control, the hybrid wind turbine can smooth the generated power output under varying wind speeds. Following this, efficiency analysis is carried out in this thesis and a feasibility study on a 1MW hybrid wind turbine is conducted. The results obtained from the project demonstrate that the proposed hybrid wind turbine system is feasible and that it can help improve the wind turbine efficiency in addition to smoothing the power output. Therefore, it can be a valuable asset for wind power integration into the power network.

# *List of Abbreviations*

| | |
|---|---|
| AA-CAES | Advanced Adiabatic Compressed Air Energy Storage |
| BGS | British Geological Survey |
| CAES | Compressed Air Energy Storage |
| CAPEX | Avoided Investment Costs |
| CCTG | Combined Cycle Gas Turbines |
| CFD | Computational Fluid Design |
| CHP | Combined Heat and Power |
| DFIG | Doubly Fed Induction Generator |
| DSO | Distribution Network Operator |
| DSR | Demand-Side Response |
| EDLC | Electric Double-Layer Capacitor |
| EESG | Electrically Excited Synchronous Generator |
| EMF | Electromotive Force |
| HAWT | Horizontal Axis Wind Turbine |
| HVDC | High Voltage Direct Current |
| I/O | Input/output |
| IMAGES | Integrated Market-fit and Affordable Grid Scale Energy Storage |
| LAN | Local Area Network |
| LCOE | Levelised Cost of Energy |
| li-ion | Lithium-ion |
| MPPT | Maximum Power Point Tracking |
| NaS | Sodium-Sulphur |
| NiCd | Nickel-Cadmium |
| OPEX | Avoided Operational Costs |
| PCM | Phase Change Material |
| PHS | Pumped Hydro Storage |
| PMSG | Permanent Magnet Synchronous Generator |

| | |
|---|---|
| PMSM | Permanent Magnet Synchronous Motor |
| PSB | Polysulfide Bromide Battery |
| PSD | Power Split Device |
| RCP | Rapid Control Prototyping |
| SCIG | Squirrel Cage Induction Generator |
| SMES | Superconducting Magnetic Energy Storage |
| TES | Thermal Energy Storage |
| TSO | Transmission System Operator |
| TSR | Tip Speed Ratio |
| O&M | Operations and Maintenance |
| UWCAES | Underwater Compressed Air Energy Storage |
| VAWT | Vertical Axis Wind Turbine |
| WRIG | Wound Rotor Induction Generator |
| ZnBr | Zinc bromide |

# *Chapter 1 - Introduction*

## *1.1 Background*

Global concerns over climate change and the limitations of fossil energy resources have spawned international legislations which commit countries to reducing greenhouse gas emissions and to building a low-carbon economy. For example, the Climate Change Act of 2008 states that it is the duty of the United Kingdom (UK) to ensure that net carbon emissions in 2050 are at least 80% lower than the 1990 baseline [1]. Furthermore, leaders of the European Union (EU) established a *Climate and Energy* Package, which was enacted into legislation in 2009 [2]. It commits the EU to three targets for 2020; a) that the EU's greenhouse gas emission must be reduced by 20% compared to 1990; b) that 20% of the EU's gross energy consumption must originate from renewable energy resources; c) an increase of energy efficiency by 20% from 2007 levels must be achieved. In particular, one of the initiatives originating from these "20-20-20" targets is the *Renewable Energy Directive* which sets a target for the UK to achieve 15% energy consumption from renewables by 2020 [3].

Based on these targets, projections for renewable power deployment were made. The *Gone Green Energy Scenario* is a projection made by National Grid Plc. stating that the UK requires an installed wind power capacity of 22GW by 2020 and 48GW by 2030 to meet its aforementioned targets [4]. The total UK wind power capacity in 2015 stands at 13.3GW [5], subsequently wind power deployment must increase by approximately 60% by 2020. Figure 1:1 illustrates the UK's installed wind power until 2015 and the projected wind power capacity in 2020 and 2030, according to National Grid's *Gone Green Scenario*.

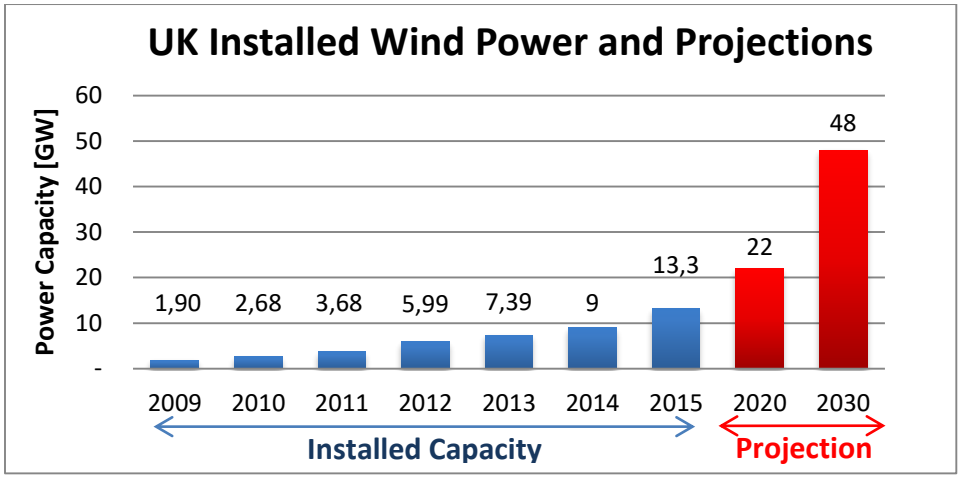


**Figure 1:1: UK Installed Wind Power Capacity and Projections**

However, wind power is variable in nature and increased shares of variable energy resources can pose great challenges regarding integration into the power network. Additionally, the wind power generation at a future point cannot be determined with certainty due to inaccuracies in weather forecasts. In a power network, it has to be ensured that the electricity generation matches the electricity demand at all times. With the increased exploitation of variable wind power in the near future, the balancing act between electricity generation and demand will become more challenging. Network capacity constraints, system stability, and security issues can lead to undesired wind power curtailment. A worst case scenario sees the Transmission System Operator (TSO) pay renewable generators to reduce power output, although they have been contracted to provide power, and potentially pay another generator to supply the amount curtailed.

To date, the TSO has been able to maintain a balanced power flow in the grid, despite sudden changes in demand (e.g. a television break during a popular live sports event), generator shortfalls or storms. Market regulations and interconnectors to import and export electricity are common options to increase the flexibility of the operation of the power network, and are enacted to help balance the power flow in the grid. However, a more flexible system operation will be required if the energy targets for 2020 and 2030 are

to be met [2]. Further flexibility can be attained by utilising power generation solutions such as quick responding gas turbines or Combined Cycle Gas Turbines (CCGT). However, these measures would be implemented at the expense of further reliance on fossil fuels. The load side can also enable flexibility by allowing for industrial or residential demand side response (DSR). DSR means that electricity users change their demand patterns according to financial incentives, and is one of the options eligible for Government support introduced by the 2013 Energy Act [6].

In addition to the options described above, Energy Storage (ES) is another viable option for achieving more power network flexibility, since it can provide a back-up to the variable and uncertain renewable energy supply [7]. ES enables the decoupling of energy generation and demand, also referred to as energy time-shift. Excess energy can be stored in moments of power oversupply and can be used at later times, whilst the operation of the power network can be improved in various scales. The most commonly used ES technology globally is pumped-hydro storage, which represents 99% of currently installed electricity storage capacity [8]. From the remaining technologies, mainly electro-chemical batteries and Compressed Air Energy Storage (CAES) are employed. Figure 1:2 shows the division of ES deployment with respect to the technology.

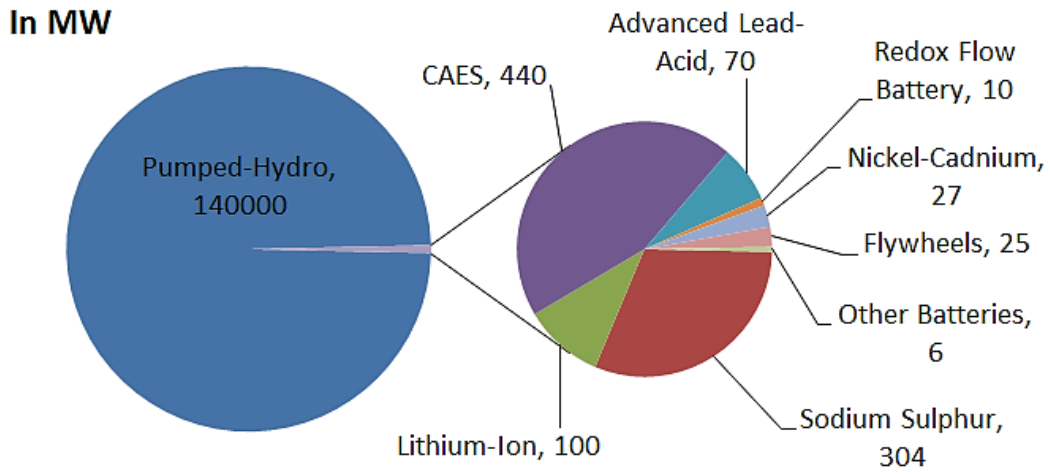


**Figure 1:2: Share of energy storage technologies globally (in MW)**

CAES is a mature technology. Electricity is used to compress air which is stored in underground caverns or storage tanks. When the compressed air energy is required for power generation, the air is released through a combustor in a gas turbine or through an air expander. CAES offers scalability alongside low maintenance and low operational costs whilst providing an environmental friendly storage medium with long lasting life time.

This research project proposes an exploration of the potential that CAES has to help smooth wind power output whilst mitigating the undesired impacts on the power network operation through increased wind power exploitation. The aim is to study a novel wind turbine structure augmented with intrinsic CAES provision designed to increase flexibility for wind power integration. The CAES concept is proposed to work on the turbine level, meaning that an air compressor/expander unit is mechanically linked to the wind turbine rotor shaft via a mechanical power split device. The proposed hybrid connection of the wind turbine with CAES exhibits a major difference to conventional CAES balancing services because large scale CAES plants are sited near an aggregated wind farm to stabilise power fluctuations. The proposed hybrid wind turbine is to support the operation of the power network in megawatt scale, whilst serving as a step towards building a dispatchable wind power generator with capabilities comparable to a gas fired power station. Furthermore, the hybrid wind turbine utilises CAES without the conventional combustion of natural gas during the air expansion, thus the proposed system is a valuable asset for wind power integration into the power network.

## *1.2 Objectives*

The anticipated challenges of wind power integration to the power network gave rise to the motivation which produced this research project. The variable and unpredictable nature of wind will cause wind power curtailment if no sufficient means of power network

flexibility is in place. The main objective of the project is to design a hybrid wind turbine with a novel flexible mechanical transmission concept that merges the wind turbine with an air expander/compressor machine that can swap roles, so that the wind turbine can be augmented with CAES. The hybrid wind turbine must be able to generate the desired power, while being subject to wind speed variations. The turbine must also allow for direct compression from the wind turbine power to compressed air energy stored, without energy transfer to electricity prior to the compression. Lastly, the hybrid wind turbine must provide standalone CAES provision that can take electrical energy off the grid and return whatever amount of energy that can be restored at a later time.

A feasibility study of the hybrid wind turbine is conducted based on the maturity of technologies utilised. To prove and analyse the wind turbine transmission concept, a dynamic mathematical model is to be generated and validated by means of a small scale laboratory sized test rig. A control algorithm is introduced to ensure desired power generation under fluctuating wind speed conditions. In addition, efficiency analysis and the practicability for large scale wind turbine applications are carried out.

## *1.3 Thesis Structure*

The remainder of this thesis is structured as described below:

In **Chapter 2** the background literature pertaining to the work of the project is reviewed. It covers basic wind turbine technologies and an overview of the current situation in leading countries in renewable power capacity per capita. Then the properties of wind power are explained, followed by a discussion on the impacts of increased wind power shares on the power network operation. An overview of ES technologies is given with a detailed analysis of how CAES can support wind power integration into the network. It also covers other means of creating flexibility to power network operation.

In **Chapter 3** the proposed hybrid wind turbine design is explained after other hybrid wind turbines are investigated with respect to CAES. The chapter concludes with a description of the working principle and features of the hybrid wind turbine.

In **Chapter 4** the dynamic mathematical models of the relevant hybrid wind turbine components are derived and the overall hybrid wind turbine model is described. The modelling part is conducted on a small scale hybrid wind turbine for model validation purposes by means of an experimental test set up.

In **Chapter 5** the test rig design, selection of components and instrumentation as well as the manufacturing process is described.

In **Chapter 6** the hybrid wind turbine model validation is described. The control strategy for achieving a stabilised power output is explained and tested under various wind speed scenarios. The system efficiencies are also analysed and a feasibility study on a 1$MW$ hybrid wind turbine is given. The chapter closes with remarks on potential applications for the hybrid wind turbine system.

In **Chapter 7** the work done in this project is concluded and suggestions for further work are presented.

# *Chapter 2 - Overview of Wind Power and Energy Storage*

In this chapter, the wind turbine technologies are described, followed by a presentation of the up to date wind power generation data in the UK, Germany and Denmark; three of the leading nations in wind power generation. The properties of wind power are described and then the impacts on the power network operation caused by the rapid increase of wind power generation are explained to highlight the challenges to be addressed in the research. One of the potential solutions, energy storage, is introduced and a brief overview of energy storage technologies is given with focus on Compressed Air Energy Storage (CAES). How CAES can support wind power integration into the power network is explained and an overview of other options for supporting wind power integration is introduced. A study on the compressed air storage potential in the UK is also reported in the last part of the chapter.

## *2.1 Wind Turbine Technologies*

Wind turbine technologies can be organised into two categories based on their structure, that is, horizontal axis wind turbines (HAWT) and vertical axis wind turbines (VAWT). These two types are briefly explained in the following with focus on HAWTs and their control.

### *2.1.1 Horizontal Axis vs Vertical Axis Wind Turbines*

VAWTs can be classified into H-type, Darrieus type and Savonius type turbines [9], of which examples are shown in Figure 2:1. Except for some prototypes in the 1980s and 1990s, the only commercial exploitation of VAWT was by FloWind Inc. in 1987, California, with 500 turbines installed, representing a total rated power capacity of 100*MW*. However, the design of these turbines was not competitive with HAWT and eventually FloWind went

bankrupt in 1997 [9]. Nowadays, large VAWT are still not commercially competitive and are not manufactured in large numbers [10].


**Figure 2:1: H-Type (left), Darrieus Type (middle) and Savonius Type (right) VAWTs [9, 11]**

VAWTs have many advantages over HAWTs. They accept wind from any angle and do not need a yaw system. Components such as the generator can be mounted at ground level, which eases maintenance and leads to lighter towers. They can also sustain higher wind speeds and are silent in their operation. However, rotors are mounted near ground where wind conditions are poorer. They generally suffer from poor self-starting capabilities and need support at the top of the turbine rotor such as strings to the ground. The most important disadvantage is the overall poor performance in converting wind power to mechanical rotational power, which is why HAWTs are preferred over VAWTs. VAWTs are predominantly drag based devices, although some VAWTs can be both drag and lift based.

HAWTs are mounted on high towers, meaning that they are exposed to higher wind speeds. This technology, in contrast to VAWTs, was subject to profound research which led to better technologies. The drawback of HAWTs is the required yaw system to point the turbine towards the wind as well as the fact that they need to be stalled at high wind

speeds in order to protect them from self-destruction. They also generate noise, which negatively affects the environment. An example of a HAWT is shown in Figure 2:2

**Figure 2:2: HAWT [10]**

HAWTs can be found in various power scales and can generate up to about 7.5*MW* of power for a single unit [8]. Within the development of wind turbines, many improvements have been incorporated into the design such as rotor aerodynamics, enhanced materials for higher towers, adjustable rotor speed through pitch angle control, improved generator systems, voltage and frequency control etc. Nowadays, the trend for wind power generation is towards larger and higher turbines, driven by successful companies such as GE, Siemens, Enercon, Repower, Alstom. Currently, over 6500 turbines are operational in the UK, accumulating a rated power capacity of around 13.3*GW* [12]. The onshore Enercon E126 with a rotor diameter of 126 metres is currently the wind turbine with the highest power rating of 7.5*MW*, followed by the 6.15*MW* offshore wind turbine produced by Repower. The largest wind turbine in terms of size is the 6*MW* turbine made by Siemens with a rotor diameter of 150 metres [13]. Siemens also contributed to the London Array Project- the world's largest offshore wind farm encompassing 175 Siemens turbines with 3.6*MW* rated power each. In total this amounts to 630*MW* capacity [14, 15].

Due to the fact that HAWTs are dominant in the world, the focus in the following research will be on HAWTS. The main components of wind turbines that are of interest for this research are the generator, the drive train transmission and the power electronics. These components will be discussed further in the following subsections. Components such as rotors and their design structures, the tower, the yaw and pitch mechanism as well as their wind speed & direction monitoring are not further discussed due to the project research focus.

### *2.1.2 Structure of HAWTs*

Figure 2:3 illustrates a generic turbine nacelle and hub.

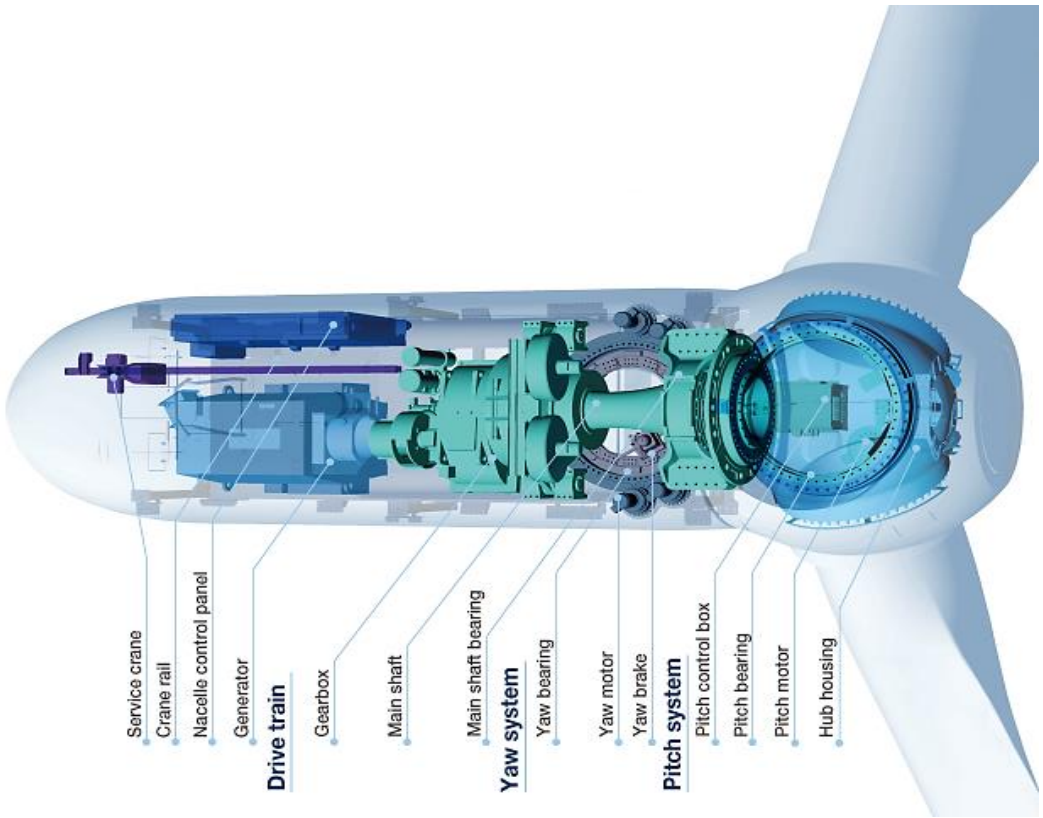


**Figure 2:3: Generic Nacelle and Hub [16]**

The rotors are attached to the hub and are equipped with pitch control in modern turbines. The pitch control enables the rotors to change their pitch angle to modify power output at high wind speeds and by doing so to protect the turbine from excessive rotational speeds.

The turbine shaft is kept in place via bearings while enabling rotation. The conventional turbine design features gear boxes to match the torque and speed characteristics of the wind turbine rotor with those of the generator. In order to make sure that the turbine faces the wind, a yaw system is installed including bearings, motors and a yaw brake. A control panel monitors wind speed, nacelle position, vibration, temperature, pitch angle etc. to ensure efficient and safe operation. Whereas the topology shown in Figure 2:3 is kept general for explanation purposes, wind turbine technologies are usually versatile. The flowchart in Figure 2:4 gives an outline of the most common design structures with the focus on transmission, generator and grid connection.

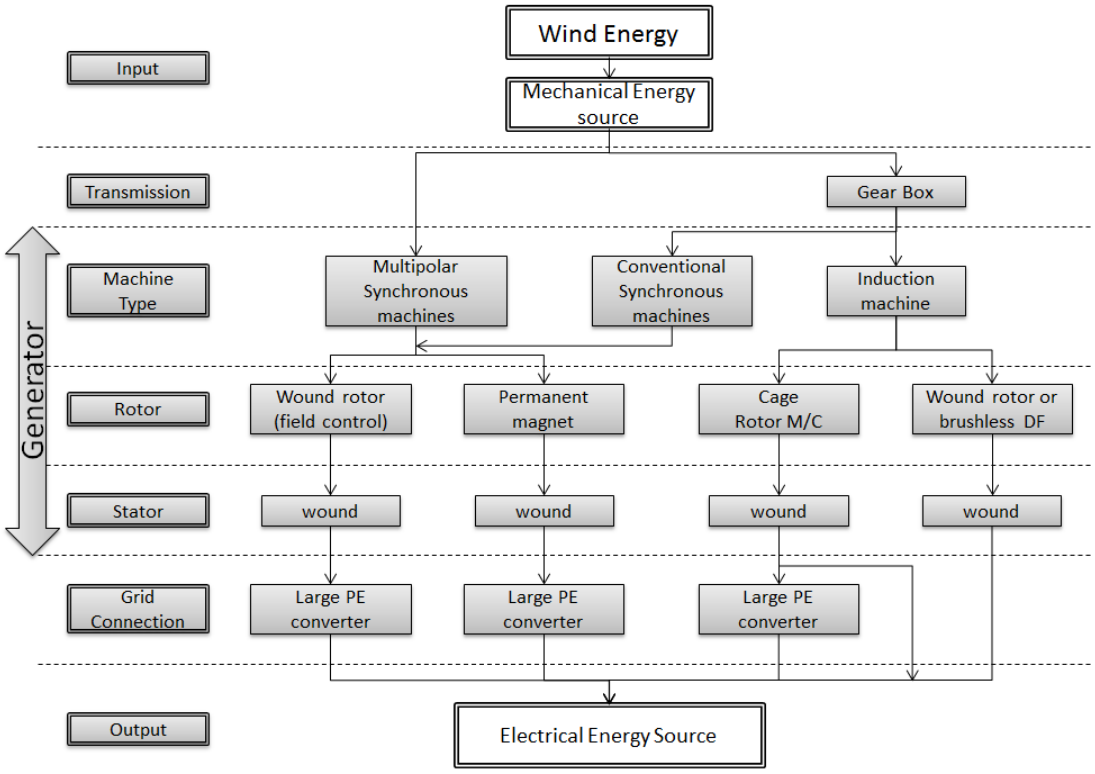


**Figure 2:4: Wind Turbine Energy Conversion. PE: Power Electronics. DF: Doubly-fed**

The flow chart shows the distinction of transmission, generator types (machine type, rotor and stator winding) and grid connection. These three topics will be discussed in this chapter.

### *A. Generators and Grid Connection*

Wind turbines predominantly employ induction generators [10, 17]. Induction and synchronous generators have similar winding arrangements on the stator [18]. However, the rotors of the generator types are different. The synchronous machine has either electromagnets or permanent magnets on the rotor and generates a revolving magnetic field in the stator by rotating the rotor. Although the stator field rotates with the same speed as the rotor field, the rotor field leads the stator field by an angle dependent on the torque applied. In contrast to synchronous machines, the induction machine has either a squirrel cage rotor, in which current is induced when cutting through the stator's magnetic field, or a wound rotor, which is used for doubly-fed generators. The induction machine can only generate electricity if the rotor speed is higher than the rotational speed of the stator field, leading to a so called negative slip. By finding an analogy, the synchronous generator acts like a torsional spring (angle between rotor and stator field), whereas the induction generator acts like a torsional damper (slip speed). The mechanical damping in conjunction with the induction generator slip reduces the stress and wear on the gear box, especially in early years where induction machines were directly connected to the grid, which in turn inherits a large amount of inertia [19]. These so called fixed speed turbines were only controlled aerodynamically (pitch control) and without power electronics. However, damping also causes losses as it dissipates heat [10]. The reactive power necessary to energise the magnetic field of the stator was drawn from the grid and fixed speed turbines do not provide direct control over terminal voltage or reactive power flow. Induction generators in combination with fixed speed turbines were a practical solution in the beginning of commercially used turbines, but could not satisfy the need for higher efficiencies coming along with new wind turbine technologies in the 1990s and the

beginning of the 21st century [20]. Nowadays, the most notable technologies are as follows[19, 21]:

1. **Variable Speed Operation**
2. **Full Power Converter**

*Variable speed operation* can be realised by variable slip induction generators and is achieved by introducing an external resistance to the rotor circuit. Having this controlled resistor, the reaction torque can be maintained while allowing variable turbine speed to a speed range of 2-5% [19]. As this method works to the expense of losses through the additional resistor, another way of variable speed operation was developed, namely, the doubly fed induction generator (DFIG). The wound rotor is connected to a frequency converter that applies variable voltage at the slip frequency and so allows operation above and below synchronous speed. In this way a speed variation of ±30% can be achieved, while controlling both active ($P_{ref}$) and reactive ($Q_{ref}$) power. Figure 2:5 shows the two methods for variable speed operation (top: control with resistor; bottom: DFIG).

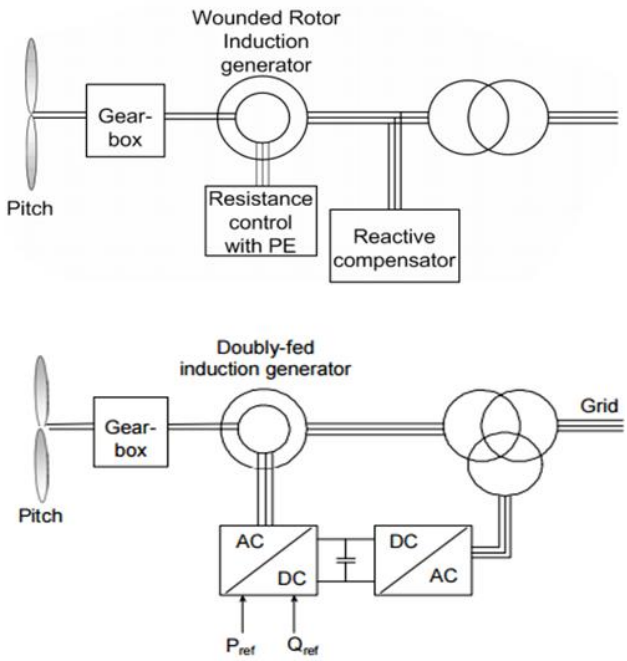


**Figure 2:5: Top: Variable Speed Resistors, Bottom: Variable Speed DFIG [19]**

In contrast to variable speed operation, *full power converters* are implemented in most of the modern wind turbines such as the Siemens turbines of the London Array [8]. All power from the generator is rectified to DC and then again converted to AC with grid compatibility. This structure can be used with a range of generators: Induction motors with gearboxes for higher speeds, wound rotor or permanent magnet synchronous rotors with or without gear box. An example structure is shown in Figure 2:6.

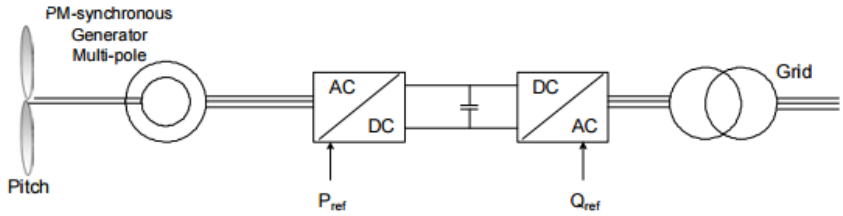


**Figure 2:6: Permanent Magnet Synchronous Generator with Full Power Converter [19]**

The load torque can be controlled, thus making it possible to operate the wind turbine at its peak efficiency for a given wind speed. As of the example shown above, a gearless turbine rotor is connected straight to a multi-pole permanent magnet synchronous generator (PMSG). The multi-pole generators are large in diameter and operate at low speed and high torque because of the large number of pole pairs on the rotor.

## *B. Gearboxes*

The purpose of the gearboxes is to step up the rotational speed from the wind turbine rotor to a value suitable for standard induction generators, which is usually around 1500*RPM*, whereas the rotational speed of large scale wind turbines can vary around 17 to 48*RPM* [10]. Therefore, gear ratios of up to 1:88 are not uncommon and are achieved by means of three separate stages with ratios of between 1:3 and 1:5 each. Apart from geared wind turbines, gearless wind turbines have gained increasing popularity in recent years [22]. The so called direct drive turbines (example shown in Figure 2:6) are characterised

through a direct connection of the wind turbine rotor and a multiple poles PMSG. These direct drive systems reduce moving parts, reduce the weight of the wind turbine and increase the mechanical transmission efficiency in comparison to geared wind turbines [22]. However, to achieve a higher power density, the generators are made bigger in terms of the radius, rather than length and contain permanent magnets with a large number of pole pairs. Using permanent magnets introduces one more problem. There is ongoing concern regarding the future supply of the rare earth metal neodymium. Using wound rotors instead would mean that the generators become even larger and heavier as copper coils produce around 10 times less energy compared to permanent magnets at given conditions [23].

### *2.1.3 Wind Turbine Control*

At any given wind speed between the cut-in and cut-off wind speed, the wind turbine can be operated at its maximum efficiency. This efficiency is referred to as power coefficient $C_p$ and is dependent on the ratio of tangential rotor speed and incoming wind speed, also called tip speed ratio (TSR). The $C_p$ also relies on the shape of the turbine blades; however, it has a theoretical maximum of 59.3% [10]. That means that a perfect wind turbine can extract only 59.3% mechanical power from the incoming wind power. As described in the previous subsection, modern turbines use full power converters. Through the decoupling of generator speed and grid frequency, maximum power point tracking (MPPT) control can be achieved over a range of wind speeds. A typical power vs generator speed plot is shown Figure 2:7.

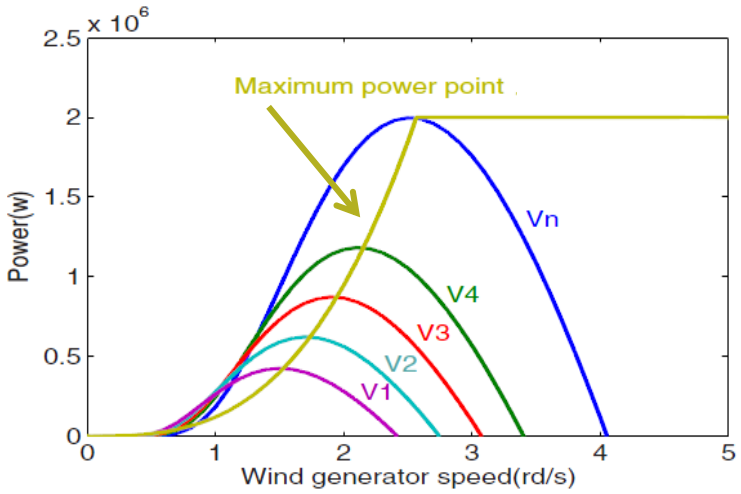


**Figure 2:7: Wind Generator Power Curves at various Wind Speeds ($v_{1\text{-}n}$) [24]**

As can be seen, the power output varies for a constant wind speed $v_{1\text{-}n}$ with respect to the generator speed, whereby $v_1<v_2<\ldots<v_n$. In theory, a maximum power output, which is proportional to the $C_p$ value, can be found for every wind speed. The yellow curve in Figure 2:7 shows the desired operating point to which the wind turbine is controlled via torque control (MPPT). At rated power (2*MW* in the example above) and high wind speeds, the wind turbine is throttled via pitch control in order to protect the turbine from excessive rotational speed and self-destruction as well as to meet the rated generator power.

## *2.2 Overview of the Current Wind Power Generation Capacity*

This section summarises recent developments in wind power capacity and provides an up to date overview of the installed wind power capacity in the UK, Germany and Denmark based on data from the year 2014. These countries are three of the leading countries in wind power generation due to their installed wind power capacity and their share of wind power to the nationwide electricity demand. A summary of important energy data is presented, followed by a more in depth explanation of wind developments in the countries mentioned above.

### 2.2.1 *Overview of the State of Wind Power Generation in 2014*

The total energy consumption, the electric energy consumption and the energy generated from wind power in the three countries are shown in Figure 2:8, based on data from 2014.

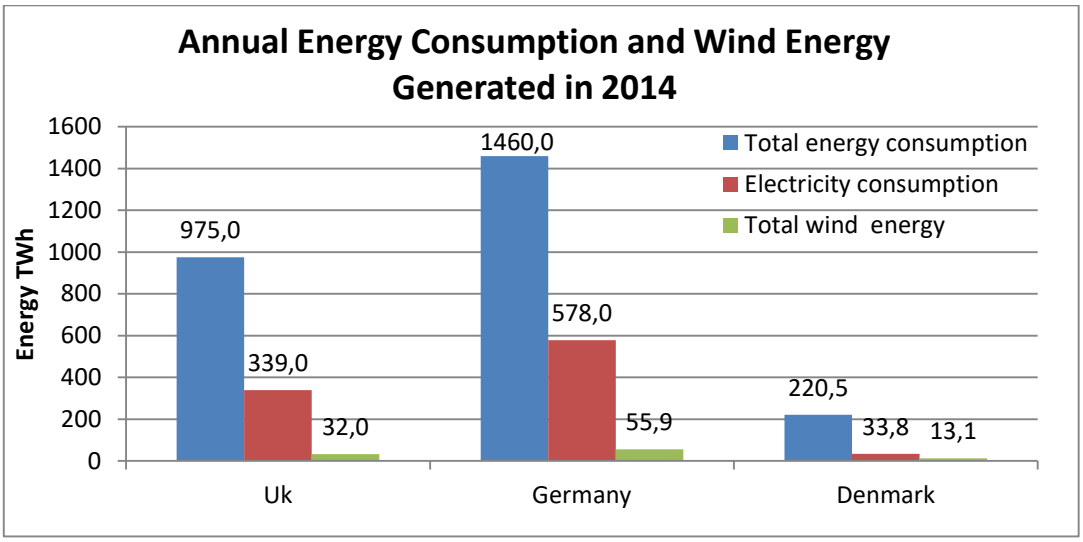


**Figure 2:8: Annual Total Energy and Electric Energy Consumption as well as Wind Energy Generated in 2014**

Another important figure is the peak electricity demand in comparison to the installed wind power capacity, see Figure 2:9. The ratio of these two values is referred to as penetration level.

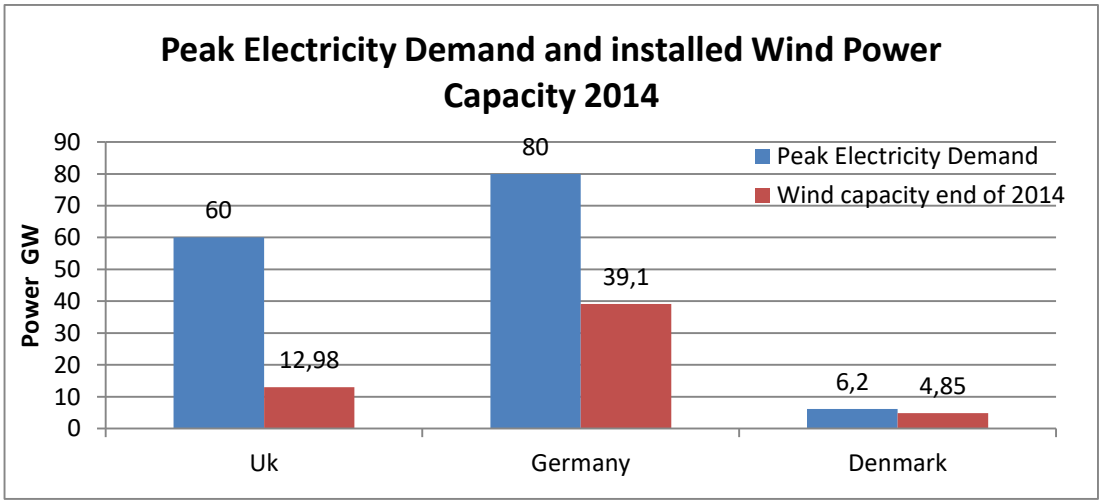


**Figure 2:9: Peak power and installed Wind Power Capacity**

Figure 2:10 shows data from 2014 regarding the shares of wind energy to the countrywide electricity consumption in percentage. It also shows the share of wind energy to renewable energy as well as the share of renewable energy to electricity consumption.

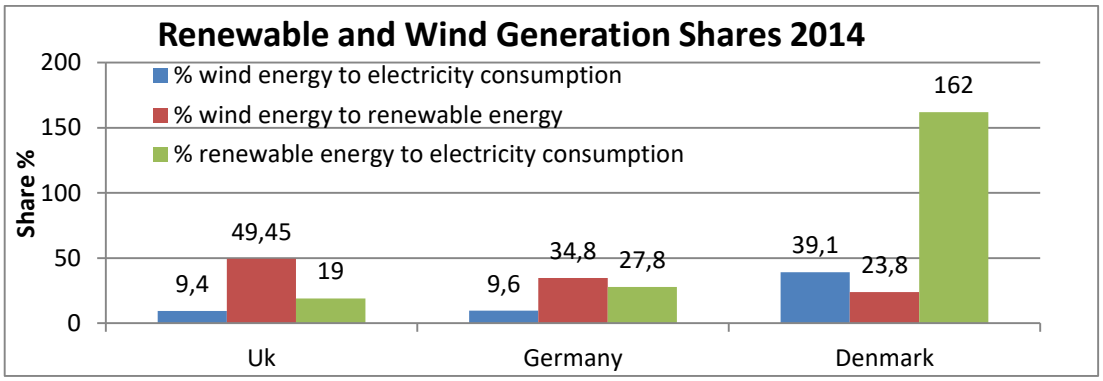


**Figure 2:10: Renewable and Wind Power Generation Shares 2014**

All data are summarised in Table 2:I.

**Table 2:I: Annual Summary of Energy Data in the UK, Germany and Denmark in 2014**

| | UK | Germany | Denmark |
|---|---|---|---|
| Total energy demand [TWh] | 975 | 1460 | 220.5 |
| Electricity demand [TWh] | 339 | 578 | 33.8 |
| Total renewable energy [TWh] | 64.7 | 160.6 | 55 |
| Total wind generation energy [TWh] | 32 | 55.9 | 13.1 |
| | | | |
| Peak Demand [GW] | 60 | 80 | 6.2 |
| Wind capacity end of 2014 [GW] | 12.98 | 39.1 | 4.85 |
| | | | |
| Penetration Level [%] | 21.6 | 49 | 75 |
| % renewables to electricity demand | 19 | 27.8 | 162 |
| % renewables to total energy demand | 6.6 | 11 | 25 |
| % wind to renewables | 49.5 | 34.8 | 23.8 |
| % wind to electricity demand | 9.4 | 9.6 | 39.1 |
| Literature used | [4, 5, 25, 26] | [27-32] | [33-39] |

### *2.2.2 United Kingdom*

According to the Department of Energy & Climate Change (DECC), the installed wind power capacity in the UK is estimated to be 8.58GW onshore and 4.75GW offshore in the first quarter of 2015 [5], and totals 13.3GW. The growth in onshore and offshore capacity

compared to the equivalent data in early 2014 shows 12.1% and 26.2%, respectively. The average load factor[1] in 2014 was around 30%, resulting in a wind energy share of 32TWh. According to National Grid Plc. the average electricity demand in the UK in 2014 was 33.5GW, summing up 339TWh [4, 25, 26]. The resulting wind power generation share to the electricity consumption, based on the figures above, is around 9.4% assuming that all wind power was utilised. In contrast, the share of all renewable energy generation was 64.7TWh and totals 19% of the electricity consumption in the UK. However, the UK's total energy consumption is 975TWh, whereby a share of renewables accounts to 6.6% in 2014 (to be increased to 15% by 2020). Another important parameter is the penetration level of wind power. With a peak demand of 60GW, the penetration level for 2014 can be computed to 21.6% and to 22.5% in 2015.

The development of renewable power capacity, and especially wind power, cannot be accurately estimated. National Grid Plc. has created a set of scenarios, which have been approved by the system regulator *Ofgem*. The scenarios are *Consumer Power, Gone Green, No Progression* and *Slow Progression*. As to the gone green scenario, it is estimated 15% renewable energy share by 2020 in order to meet the target set by the European Commission. Among the renewables, wind power will have a capacity of 22.2GW and an annual energy generation of around 61.5TWh by 2020. In 2030 a wind capacity of 48GW and an energy generation of 141.8TWh are estimated. Given these figures, the penetration level from wind power to peak demand will be 37% in 2020 and 72% in 2030 [4].

### *2.2.3 Denmark*

Denmark's target for the share of renewables in gross energy consumption is 30% and, therefore, twice the share compared to the UK [39]. Denmark is the leading country in

[1] The load factor describes the ratio of energy generated from a generator to energy it could have generated per year if operated at rated power throughout.

renewable power capacity per capita. In the evening of July 15th 2015, 116% of its national electricity needs were covered by wind power alone, although not even operating at full capacity [36]. At 3am on the following day when wind speed picked up and the demand dropped, the share from wind power to the electricity demand was 140%. 80% of the surplus power was exported through interconnectors. Denmark is a smaller country compared to the UK and Germany and has less energy needs. The current amount of renewable power generation, especially wind, already exceeds the target penetration levels from other countries and makes Denmark an important nation to investigate. Denmark's total energy consumption is only 220TWh with a renewable energy share of 25% in 2014 [38]. 13.1TWh came from wind turbines with an installed capacity of 4.85GW. The electricity consumption in 2014 was about 33.8TWh, of which 39% was provided by wind power [33]. Denmark aims to supply 35% of its annual energy consumption from renewables by 2020 and 100% by 2050 [36].

### *2.2.4 Germany*

Germany is another leading country in renewable energy generation, especially through wind, solar and biomass. Renewable energy generation accounted for 160.6TWh in 2014, which is 27.8% share to the electricity consumption and around 11% to the overall energy consumption [27, 30]. Among them, wind generation accounted to 55.9TWh and is with 34.8% the largest contributor of renewables. The currently installed wind capacity is 39.1GW and leads to a penetration level of approximately 50%, whereas the load factor is only 18% on average in recent years (compared to around 30% in the UK) [29].

The German Ministry of Economic Affairs and Environment estimates an increase to 100.3TWh wind generation by 2020 and 143.3TWh by 2030 in order to meet the energy targets [40]. That means the future wind capacity will rise to approximately 63.6GW by 2020 and 91GW by 2030, assuming a load factor of 18%. Given these estimations, the

penetration level will be at around 80% and 113.8%, respectively, assuming a peak demand of 80GW.

## 2.3 Properties of Wind Power and Impacts on Power Network Operation

The properties of wind power are explained in this section, followed by a discussion on the impacts of increased wind power shares on the power network operation.

### 2.3.1 Properties of Wind Power

Wind power sources benefit from high priority in dispatch due to low marginal costs and the aim of increasing the energy share from renewable energy sources in order to meet the energy targets [41]. However, wind power and other variable renewable energy sources pose great challenges on the power network operation in both technological and economic aspects. From the analysis presented in [8], six key properties of variable renewable power generation are presented:

A. Variability
B. Uncertainty
C. Non-Synchronous generation
D. Location constraints
E. Modularity
F. Low short-run cost

These six key properties affect the power network operation and influence the integration of variable renewable energy sources such as wind power to the power network.

### *A. Variability*

Variability in wind power generation is predominantly determined by changes in weather conditions and can occur in multiple timescales, for instance from minute-to-minute changes to seasonal or even inter-year changes (e.g. windy and calm years) [8]. However, there are differences between the variability of a single wind turbine and variability of an aggregate wind turbine fleet, which is spread over a large geographical area. On a system level (i.e. aggregate fleet of wind turbines), wind power will not experience an immediate, abrupt loss or onset of power. However, when aggregated to a larger system, aggregate wind power will still show variability in power generation [8].

### *B. Uncertainty*

Although weather forecasts have been improved, it is not possible to accurately predict wind speeds. Therefore, the power generation of a wind turbine or wind farm at a future point cannot be determined with certainty. The level of uncertainty changes with length of time forecast. However, the shorter the forecast period is, the more accurate the forecast. Uncertainty differs from the other properties, since it is tied to the accuracy of the wind forecast, rather than being a characteristic of the variable wind power itself.

### *C. Non-Synchronous Generation*

Conventional power plants in a synchronous power system use synchronous generators, whereby the rotation of all generators is kept precisely at the same speed [8]. Therefore, all generators have a direct electro-mechanical link to the grid and contribute to a large system wide inertia. This inertia is important as it resists to sudden load or supply deviations, thus making the grid more reliable and robust. Wind power generators (if not directly connected to the grid but through power electronics) do not connect to the grid synchronously. If connected through power electronics, which is commonly the case in the

majority of modern wind turbines, the direct electro-mechanical link is not present and no contribution to the system inertia is made [8].

### *D. Location Constraints*

Potential wind power generation sites that are rich in wind resources may not coincide with areas of high electricity demand, for instance offshore wind power. Furthermore, wind resources are not evenly distributed geographically, so that costly transmission lines need to be built or upgraded.

### *E. Modularity*

The deployment of wind turbines occurs at a scale that is much smaller in comparison to conventional thermal power plants. Typical modern wind turbines have nameplate capacities of 1$MW$ to 7$MW$, whereby thermal power plants are usually rated to 100$MW$ to 1$GW$ [8]. However, wind turbines can be grouped together to build a wind farm, so that several hundred Megawatt capacity is formed. Smaller installations are connected to the distribution grid rather than the transmission grid. This can cause several problems since the traditional role of the distribution grid was to supply electricity to the consumer, whereas it now hosts power generation in the form of many small power plants. The power flow from transmission grid to distribution grid becomes bi-directional and smarter approaches for the distribution network operation are required (such as energy storage, smart grid).

### *F. Low short-run cost*

This property of variable energy resources differs from the others in the sense that it is not a technical property, but is linked to the electricity market. Once installed, wind power generates energy at very little cost. The low short-run costs imply that wind power will

likely be among the first technologies in the merit-order and will, therefore, displace more costly generation from other resources.

### *2.3.2 Impacts on Power Network Operation*

An increased amount of variable power generation can pose constraints on transmission and distribution networks (depending on the location, power capacity and modularity). In the worst case, the system operator has to pay renewable generators to reduce power output, although they had been contracted to provide power, and potentially pay another generator to supply the amount curtailed. Curtailment is often the only measure to ensure a stable network, if no other means of flexibility such as storage, interconnections or market regulations are available [42]. To date, curtailment data are very low; for example 0.93% in Germany in 2013 (555GWh), 1.9% in North Ireland in 2012 (24GWh) and nearly zero in Denmark except for the years 2008 and 2010 due to a fault in one of the interconnectors [30, 41, 43]. In general it can be said that curtailment occurs mainly as a *consequence of network constraints*, but also due to *system security and stability* reasons in both transmission and distribution networks [41, 43, 44]. On the other hand, allowing for curtailment can be the most cost-effective solution, as will be explained below.

#### *A. Power Network Constraints*

Power network constraints are the most common reasons for curtailment. Network cables are insufficiently designed to transport large amounts of power flows in both transmission and distribution lines. Especially in local networks this can lead to the utilisation of higher marginal-priced power sources over wind or solar in order to maintain system stability and security. Wind farms are often placed in remote areas and their development proceeds much more quickly than the transmission system can be upgraded (2-3 years for wind farms, but up to 10 years for transmission enhancements) [44]. Hand in hand with

transmission congestion, curtailment can occur in moments when the generated power is higher than the load demand. The excess power may be exported or transported to nearby storage plants. However, transmission capacity constrains may prove barriers.

### *B. System Security and Stability*

Here it is not a capacity limit that causes the curtailment, but limitations in other factors such as risks of fast change in variable power generation or reactive power. It occurs at times of high risks that large amounts of wind power generators may fall out during storms or network faults. Curtailment is often used as a precaution at times of high wind power shares and expected storms, which becomes a system reserves problem. In that case, wind generators often need curtailment hours in advance [45]. Furthermore, countries have raised their own maximum permissible level of wind power generation in order to ensure a safe and stable network. In Ireland, for instance, wind power is constrained to a maximum of 50% of electricity generation at all times [41].

In distribution networks, high wind penetration can lead to back-feeding to the transmission network when more power is generated than it is consumed on the distribution level [43]. This can lead to voltage control issues if the system is not sufficiently protected or adapted to such scenarios.

Furthermore, the increase of non-synchronous power generation through wind turbines increases the sensitivity of the grid [43]. Large amounts of wind power, especially in isolated smaller grids, replace conventional synchronous generators that provide system inertia. More non-synchronous generation may cause higher rates of change in system frequency and larger frequency deviations. Thus, the grid is more prone to instability.

Lastly, conventional thermal power plants have minimum permissible power operating levels [43]. In moments of strong wind and low demand, such as night time, base load plants can be pushed down against their minimum operation constraints.

### *C. Positive Economic Value of Curtailment*

Curtailment is often regarded negative, because potential renewable energy is unused, yet it can be the most cost-effective solution. Therefore, it is worth explaining how curtailment can contribute to an optimal solution with regards to total costs of providing electricity. Future curtailment will increase along with an increased share of renewable power generation [46]. Two socio-economic benefits can be invoked by curtailment, which are avoided *investment costs* (CAPEX) and avoided *operational costs* (OPEX) [47]. With regards to CAPEX, building additional grid capacity in order to avoid curtailment would be a costly undertaking if only used a few hours per year [46]. The wind farm investor often finances the connection to the grid, which is a considerable part of the investment, especially for offshore wind farms. The investor often accepts a low margin of curtailment, since avoided curtailment may only be a minor benefit in comparison to additional transmission capacity costs. Concerning OPEX, curtailment can avoid operational costs, which means lower system reserves procurement and buying less regulating energy from partly inflexible conventional units. Furthermore, the work in [48] shows that by allowing 2% curtailment, the capacity of variable power supply such as wind power in the distribution grid can be doubled and still be accommodated. Similar results were found in [8].

## *2.4 Overview of Energy Storage Technologies*

A brief overview of energy storage technologies is given in this section. The main characteristics, working principles, benefits and disadvantages are described. The

information used in this section is predominantly gained from the work in [49] and references therein.

### *2.4.1 Overview*

There are a number of energy storage technologies that enable the storage of energy in various ways such as mechanical, chemical, electrochemical, thermal, thermochemical or electrical. Figure 2:11 illustrated an overview of the most common energy storage technologies to be discussed in this section.

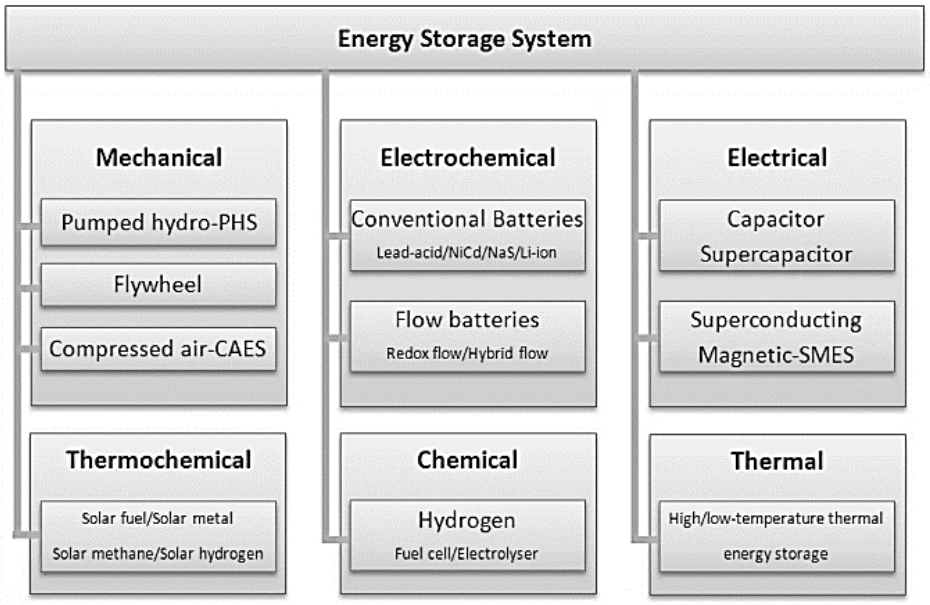


**Figure 2:11: Classification of Energy Storage Systems [49]**

The criteria by which energy storage technologies are evaluated are numerous. The following list gives an overview of the most commonly used and analysed characteristics:

- Technical maturity
- Energy and power density
- Specific energy and power
- Power rating, rated capacity
- Response time and discharge duration time

- Cycle efficiency (electricity to electricity)
- Self-discharge and storage duration
- Cycling times and lifetime
- Costs

A frequently used plot for comparison among energy storage technologies is the rated power versus rated capacity graph, shown in Figure 2:12.

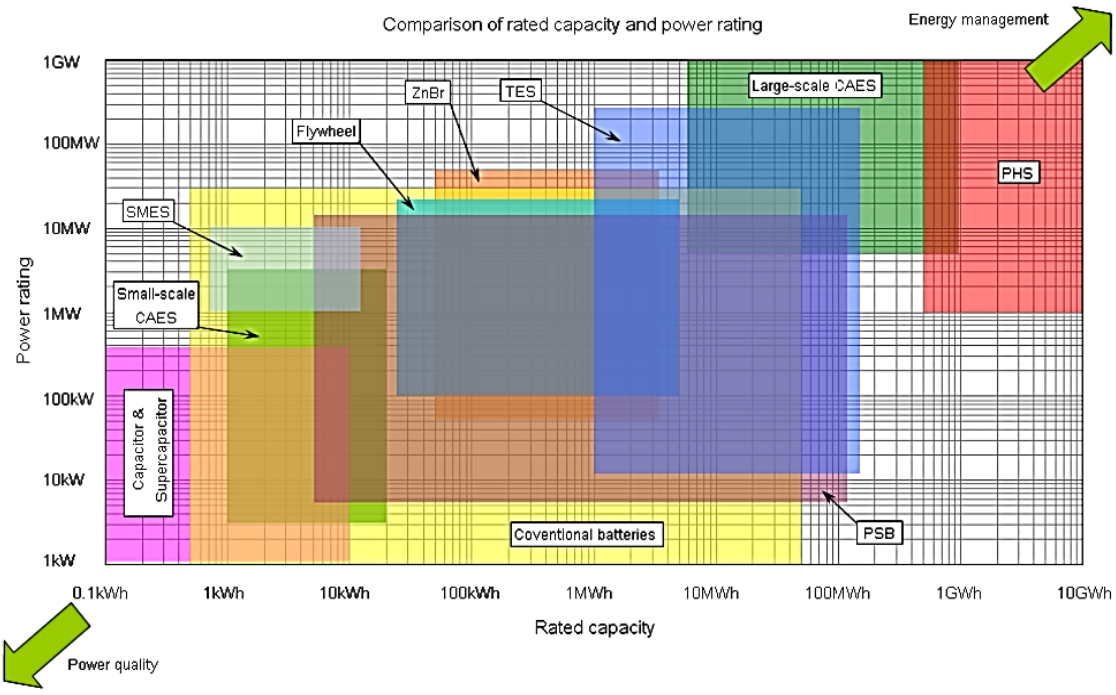


**Figure 2:12: Power Rating versus Rated Capacity [49] (see abbreviation list)**

It is clear that pumped hydro storage (PHS) and compressed air energy storage (CAES) are adequate for large scale applications with large power rating and vast storage capabilities. On the other hand, capacitors and supercapacitors are characterised by moderate power ratings and limited storage capacity. In the following subsections, the main energy storage technologies are briefly explained.

### 2.4.2 Pumped Hydro Storage

Pumped Hydro Storage (PHS) is one of the most mature, large-scale storage technologies. It dominates the energy storage sector with 99% of the total storage capacity worldwide. The largest PHS plant can be found in Virginia, USA, comprising approximately 3GW rated power.

Two water reservoirs are separated by different elevations, whereby water is pumped to a higher reservoir using pumps and electrical energy from the grid. The water on the higher reservoir contains more potential energy with respect to the lower reservoir. If energy from the store is needed, the water is released through turbines, which are connected to generators. Figure 2:13 illustrates the principle.

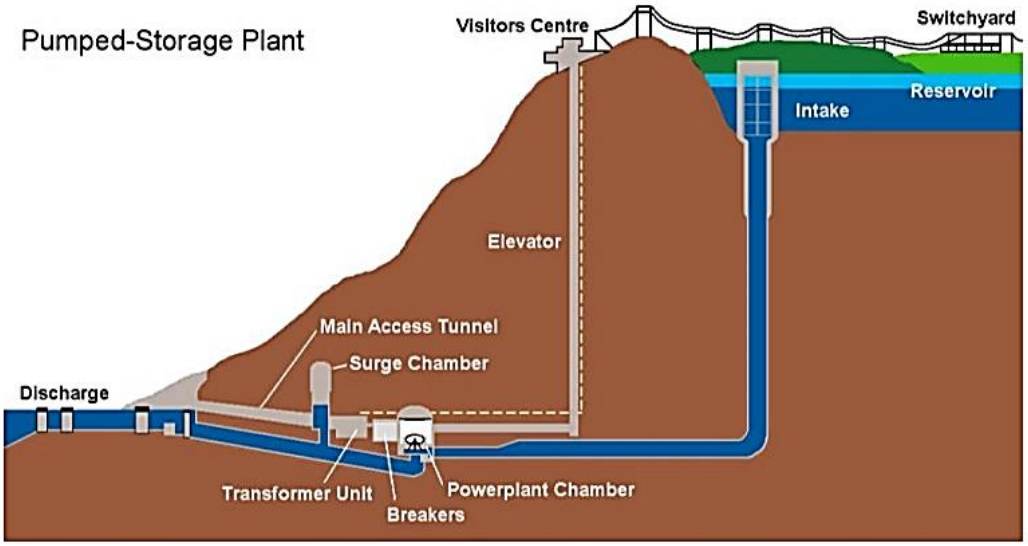


**Figure 2:13: Pumped Hydro Energy Storage Layout [50]**

The advantage of PHS is its maturity, its long lifetime and its low self-discharge rate. It benefits from relatively high cycle efficiencies usually being around 70 to 85%. On the other hand, it is bound to geological suitable areas and takes about 10 years to construct. Furthermore, large land areas are used, which may conflict with the environment. Since the storage capacity is large and the ramp-up time short (several seconds), PHS can be used for

many network services, electricity supply applications and balancing services (see Figure 2:24).

### *2.4.3 Compressed Air Energy Storage*

CAES is suitable for long term and multi-scale energy storage applications. Currently there are three CAES plants in operation. The first CAES plant was built in Huntorf, Germany, in 1978 and comprises a 320*MW* generator. The second plant was built in McIntosh, Alabama, with a power rating of 110*MW* and an increased efficiency due to a heat recovery process during the combustion with natural gas. Lastly and only recently commissioned, the Texas Dispatchable Wind project comprises a 2*MW* wind turbine in combination with CAES.

An electric motor is used to drive a compressor that compresses air to be stored in underground caverns (i.e. made of salt or rock) or aboveground vessels, after the air was cooled down. If energy is required from the store, the compressed air is released through a turbine while combusted with natural gas. The released heat energy during the combustion of natural gas may (McIntosh) or may not (Huntorf) be used to pre-heat the incoming air, see Figure 2:14.

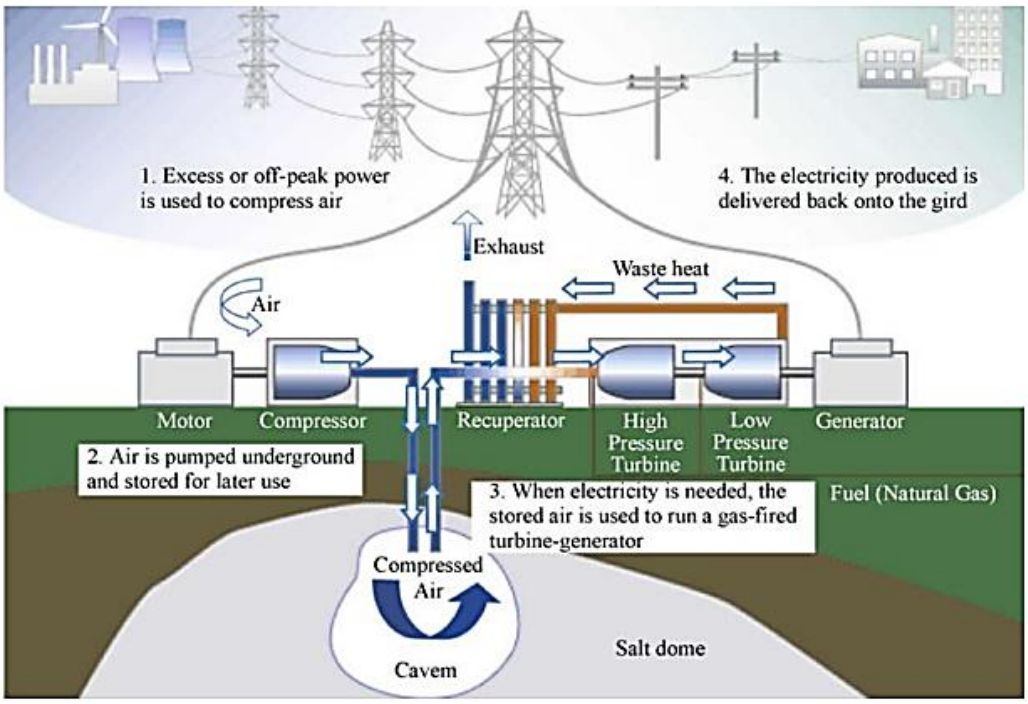


**Figure 2:14 Schematic Diagram of a Compressed Air Energy Storage System [51]**

CAES is increasingly considered among the energy storage technologies due to its lower capital cost and its scalability. It has proven reliability and compatible efficiencies ranging up to 70%. The disadvantage is the geographical restrictions if underground caverns are considered. Furthermore, emissions are produced if CAES is used in its conventional format, in which fuel is combusted. However, research is ongoing towards Advanced Adiabatic CAES (AA-CAES), aiming to utilise the heat created during the compression. The heat can then be released for the turbine operation in order to avoid the combustion of fossil fuels. More on AA-CAES and other CAES variations are described in the following subsection.

### *2.4.4 Variations of CAES*

While the previous subsection focused on the conventional CAES technology, there is more research ongoing to improve the efficiency of CAES. CAES is considered for small scale as well as large scale operations, both being of particular interest for this project. In the

following subsections the concept of Advanced-Adiabatic – CAES is explained as well as other smaller scale CAES applications.

#### *2.4.4.1 Advanced Adiabatic – CAES*

The functionality of AA-CAES is similar to the conventional CAES. Air is adiabatically compressed in several stages. The air must be cooled down before it can be accumulated into the cavern. In contrast to conventional CAES, the heat is now stored away via heat exchangers and in form of thermal storage (see Subsection 2.4.8 Thermal Energy Storage). When the compressed air is released it is merged with the heat from the heat storage prior to the expansion process in the turbine. Therefore, no combustion is needed and the electricity to electricity cycle is emission free, see Figure 2:15.

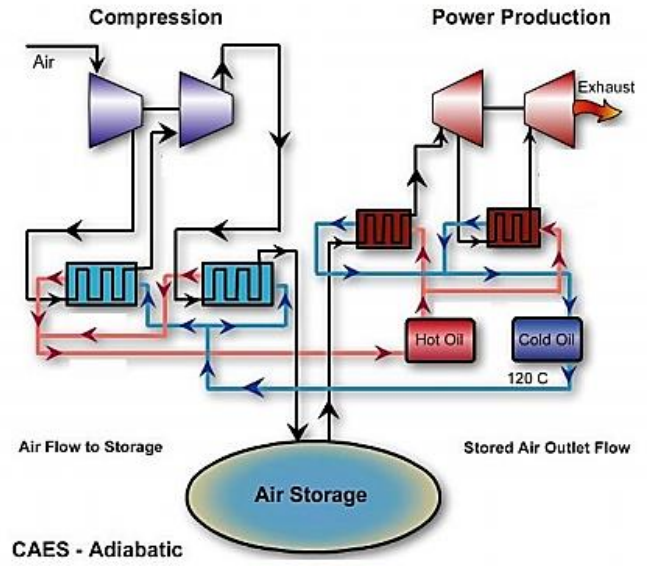


**Figure 2:15: AA-CAES Topology [49]**

If the compression takes place in several stages, the heat storage medium can be operated at manageable temperatures, e.g. around 700°C. Challenges occur when considering the heat storage medium itself. It needs to charge and discharge quickly under varying temperatures. The heat exchangers, pipelines and insulation costs put further financial strains on the technology. The famous project “ADELE” in Germany was discontinued due

to higher risks in their financial analysis. The efficiency that was claimed lies around 70%. However, a 1.5*MW* demonstration project by the Chinese Academy of Sciences is now operational after successfully demonstrating a 15*kW* plant. The overall efficiency of the plant was reported to be around 55%, but is yet to be improved.

#### *2.4.4.2 Small Scale CAES Facilities*

Flowgroup Plc employs small scale CAES under their branch called *Flowbattery*. The products are compressed air batteries for uninterruptable power supply (UPS) [52]. High pressure air tanks of up to 300*bar* are employed. The input air pressure to the scroll air expander is regulated according to the electric power demand, but does not exceed 14*bar*. A generator is driven, whereby further power electronics ensure grid compatible electricity output. A simplified structure is shown in Figure 2:16.

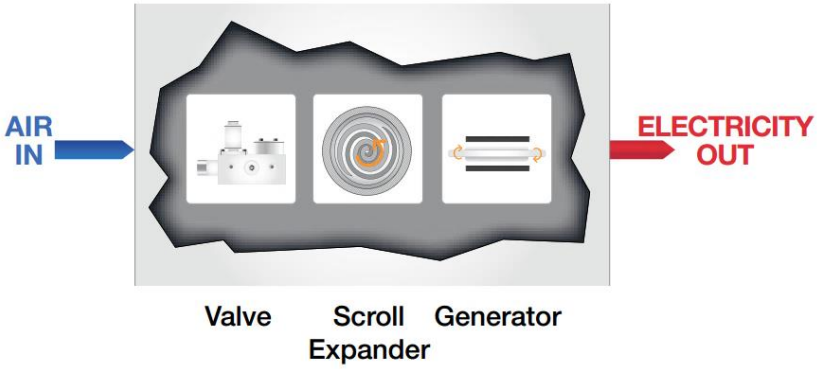


**Figure 2:16: Compressed Air Battery Principle [53]**

The scroll technology has been employed in vehicles, fridges and for stand-alone compressors. However, the working principle can be reversed to form an air expander. Flowbattery currently compiles UPS systems of up to 200*kW*. The energy capacity depends on the size of the tanks and the pressure of the working medium therein. Airsquared, an American company, have produced air expanders of up to 50*kW* driven by only 13 *bar* air

pressure input, while claiming an efficiency of up to 80%[2]. The scroll design has many advantages over other compressors/expanders. They run smoother, ramp up quicker, have fewer rotating parts and vibrations can be balanced out easier. They benefit from continuously expansion/compression and exhibit comparably high volumetric efficiencies [54-57]. Flowbattery claims high reliability, high efficiencies and lower maintenance and investment costs compared to batteries. The first CAES UPS system was employed at the Cooperative Bank's Pyramid building in Stockport, U.K., and has since become a competitor for chemical battery and flywheel back up power technologies.

The difference to conventional CAES such as the Huntorf plant is not only the power rating and intended application, but also the machinery used. The UPS system described does not use a combustion process or any other heat source. Pressure tanks are employed instead of underground caverns. These pressure tanks are usually filled with several hundred bars, as opposed to underground cavern pressures with 60 to 70*bar*.

#### *2.4.4.3 Constant Volume versus Constant Pressure*

As to underground storage technologies, two operations can be considered; constant pressure and constant volume storage [58-60]. As the name suggests, at constant volume operation, the volume of the compressed air store does not change and the air pressure varies according to the state of charge of the store. Usually, the storage air pressure is restricted, which limits the energy capacity. The pressure is then regulated downstream for the high pressure turbine's pressure intake. Both units in McIntosh and Huntorf use this operation principle. Secondly, during the constant pressure operation the volume of the cavern can be adjusted by flooding with water [61]. Figure 2:17 shows the principle.

[2] The type of efficiency could not be clarified with the company. Therefore, it is assumed isentropic efficiency.

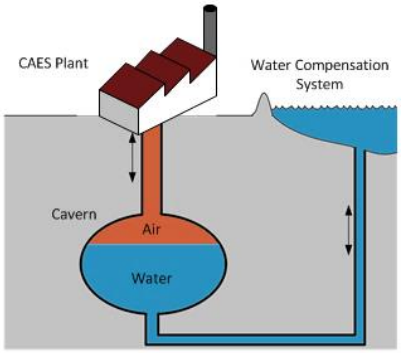


**Figure 2:17: Schematic of Constant Pressure CAES**

The disadvantage of this structure is that it cannot be used for salt caverns since the water would further solution mine the cavern. Furthermore, the flow of water must be controlled which proves difficulties, called champagne effect [61]. Although investigated in research, the constant pressure operation has to date not been found industrial application for CAES.

Another notable option is underwater compressed air energy storage (UWCAES), which takes advantage of the hydrostatic pressure of the water [62]. The water acts as the pressure restraint, just as the salt or rock does in an underground cavern. If the pressure inside the air storage container is kept close to the hydrostatic pressure, the container requirements, such as the wall thickness, can be kept minimal since the stresses at the container walls are low. Moreover, flexible energy bags can be utilised that can change in volume and pressure as they inflate or deflate.

### *2.4.5 Flywheel*

The earliest records of flywheels are dated back to 2400 BCE, which makes flywheels the first energy storage technology in history. During the 19$^{th}$ century flywheels made of steel were employed in propulsion, steam engines and electrical power generation. The applications of flywheels are wide-spread, from providing balanced torque in engines, load levelling in vehicles, busses and aircrafts, energy recuperation for railway to small and large scale grid energy storage. Advances in research such as magnetic bearings, high tensile

strength materials, advanced control strategies and power electronics make flywheels attractive for industry. Considering a flywheel as an energy storage device, it is spun up to several thousand revolutions per minute by an integrated electric motor/generator. The flywheel stores kinetic energy which is related to its moment of inertia and its rotational speed. If required, the kinetic energy can be returned back to electrical energy via a generator. Moreover, modern flywheels can reach up to more than 60,000*RPM* in a vacuum enclosure, while showing electricity to electricity efficiencies of up to 95%. Figure 2:18 illustrates the design principle.

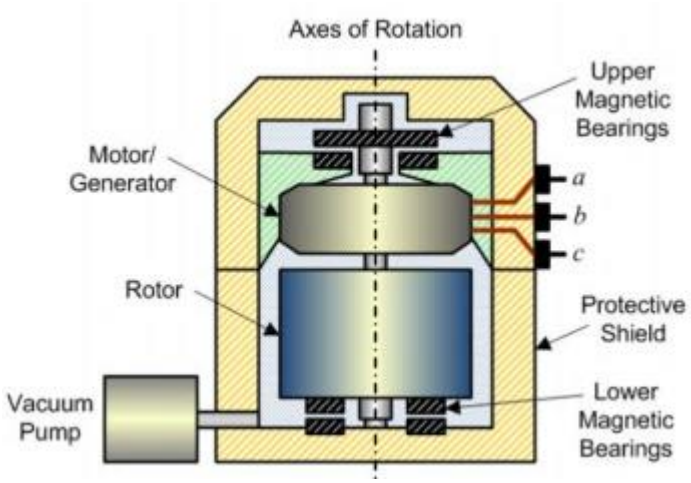


**Figure 2:18: Simplified Structure of a Flywheel [63, 64]**

The benefits of flywheels are high efficiencies at rated speed and the long cycling lifetime. They are simple and reliable, providing high power and energy density. On the other hand, they suffer from self-discharge and cannot provide rated power at lower rotational speed. Flywheels are usually used for relatively short-term energy supply and back-up power systems. Power quality improvement and stabilisation of distributed generation systems are also common applications as well as smoothing the irregularities in wind power generation or energy recovery in electrically powered mass transit systems.

### 2.4.6 Conventional Electrochemical Battery

The conventional electrochemical battery is one of the most common energy storage devices used in industry and daily life. It uses chemical reactions to generate an electrical current if connected to a load. Applications vary from small house devices to electric vehicles and grid energy storage to balance fluctuations in power generation from variable renewable power sources. Whereas batteries in electric vehicles comprise around 20 to 50*kWh* energy capacity, the battery in Fairbanks, Alaska can deliver 40*MW* for 7 minutes (4.7*MWh*). The general design of a battery is displayed in Figure 2:19.

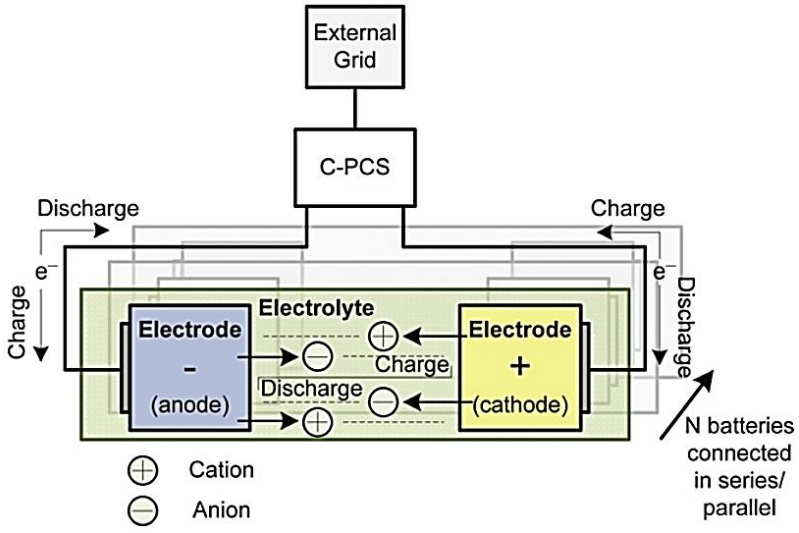


**Figure 2:19: Operation Principle of Battery Energy Storage System [64]**

Two conducting electrodes, the anode (negative terminal) and cathode (positive terminal) are placed in a container filled with liquid or solid electrolyte. The anode and cathode are connected externally to a power source (charging) or load (discharging). During charging, the anode receives electrons once voltage is applied to the battery. At the same time the cathode rejects electrons to the external circuit. A difference in potential builds up. During the discharging, the process reverses. These cells can be stacked up in parallel or series according to design parameters. A Control-Power Conditioning System is used to monitor and protect the system as well as converting DC voltage to AC voltage.

Batteries benefit from fast response times, relatively high efficiencies of up to 95% and short construction times. However, they suffer from high maintenance costs, limited cycling and relatively small power capacity if compared to other grid scale storage technologies. Furthermore, chemical and toxic waste material may have negative impacts on the environment. The most common battery technologies are lead-acid, Nickel-Cadmium (NiCd), Sodium-Sulphur (NaS), and Lithium-ion (li-ion).

### *2.4.7 Flow Battery*

A flow battery or redox flow battery is a two-electrolyte system. The main difference to conventional electrochemical batteries is that the electrolyte is not stored within the battery itself, but externally. Flow batteries can be dated back to about 1880, however, the first modern flow battery was built in the early 1970s by scientists at NASA. The technology is considered for storage capacities of about 1*kWh* to 10*MWh* for power ratings of 3*0kW* to 3*MW*. Two chemical electrolytes are dissolved in liquids and pumped through a cell, while being separated through a membrane. Within the cell, oxidation-reduction takes place, which is a chemical reaction that transfers electrons between two species, see Figure 2:20.

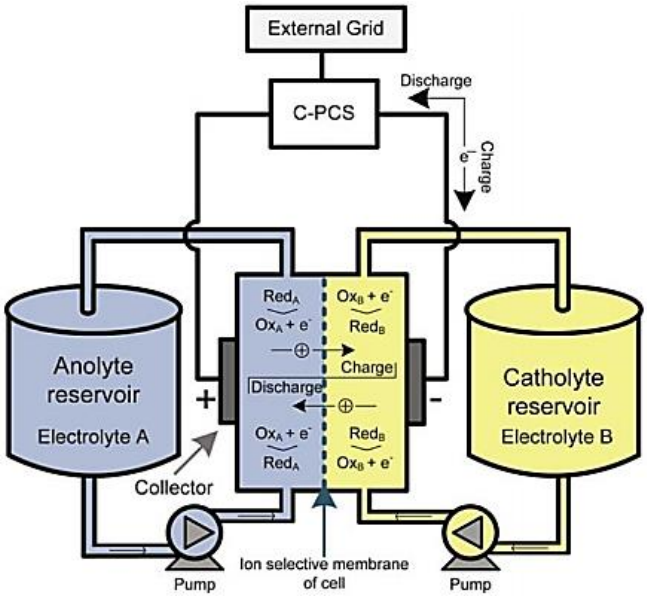


**Figure 2:20: Operation Principle of Flow Battery Systems [64]**

During the charging phase, the electrolyte A is oxidised at the anode and electrolyte B is reduced at the cathode, therefore building a difference in electrical potential. During the discharging, the process is reversed. The size of the electrode and the number of cells stacked up determine the power rating. The storage size can be kept flexible, since the containers containing the electrolyte can be exchanged or increased in size. Flow batteries benefit from low self-discharge, relatively high efficiencies, long life-time and the possibility to discharge completely (unlike conventional batteries). On the other hand, increased manufacturing costs and comparably complicated system requirements such as pumps, sensors and power management are disadvantages. The main applications for flow batteries are balancing services to the grid, uninterrupted power supply units or electric vehicles.

### *2.4.8 Thermal Energy Storage*

Thermal Energy Storage has received much attention in the past decades for domestic and industrial applications. Heat energy can be stored in a medium in a tank or reservoir. The setup usually consists of heating elements or a refrigeration cycle as well as piping, pumps and control units. Two different principles can be distinguished, namely, *Sensible Heat Storage* and *Latent Heat Storage*.

#### *A. Sensible Heat Storage*

The storage medium can be molten salt, pressurised water, thermo-oil or other solid mediums such as rock or brick. The thermal energy needed to change the medium's temperature is called *Sensible Heat*. Temperatures for storage vary between -200°C and 700°C, whereby no phase change of the medium occurs. The energy capacity depends on the specific heat capacity of the medium, the size of the store and the temperature variation range. Depending on the insulation, the heat can be stored with only minor losses and up to 95% round-trip efficiency. The heat energy can be used for either heating or

generating electricity via vaporising water, which can be fed to a steam turbine. The principle is visualised in Figure 2:21.

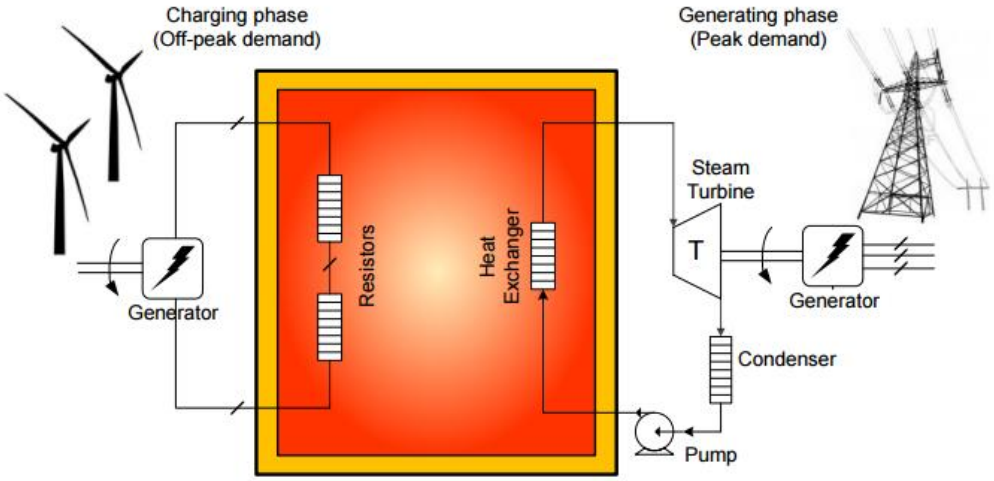


**Figure 2:21: An Example of Sensible Heat Storage [49]**

### *B. Latent Heat Storage*

Latent heat storage employs phase change materials (PCMs) and is the energy exchanged during the phase change of the storage medium. Usually turning from liquid to solid phase, the temperature change through heat transfer is not obvious and therefore called latent heat exchange. The advantage over sensible heat storage is the capability to store large amounts of energy in small volumes without large temperature changes. However, the technology is still in development stage.

In summation it can be noted that thermal heat storage has comparably low efficiencies considering electricity to electricity applications (30-60 %). However, with respect to heat to heat it can reach efficiencies of up to 95%. The self-discharge rate is low and the energy density very high. It can also be combined with power plants forming Combined Heat and Power (CHP). The heat captured from steam turbines can be used to heat nearby buildings and homes as well as providing hot water.

### *2.4.9 Capacitors and Supercapacitors*

Capacitors are the most direct way to store electrical energy and are widely used as passive components in electrical circuits. Supercapacitors are electro-chemical devices that use the topology of both batteries and conventional capacitors. Capacitors and supercapacitors are explained separately below.

#### *A. Capacitors*

Capacitors are usually made of 2 electrical conductors (e.g. metal foil), separated by a thin layer of dielectric or insulator such as air, ceramic or plastic. If charged with direct current, an electric field develops across the dielectric since one conductor is positively charged, whereas the other conductor is negatively charged. Figure 2:22 visualises a simplified capacitor structure.

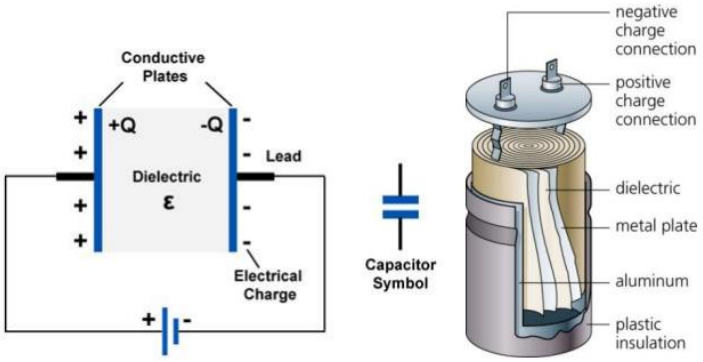


**Figure 2:22: Capacitor in Circuit and Construction [49]**

A large range of capacitors are available, depending on material, structure and size. In general, the energy capacity depends on the voltage applied to the capacitor and its capacitance. However, the voltage is limited by the breakdown characteristic of the dielectric. Since they can be charged quicker than batteries and last longer, while having efficiencies of about 75-85%, they are commonly used in electric circuits, in power quality applications, in filter networks and in energy recuperation in mass transit systems. The drawbacks of capacitors are their high self-discharge rate and relatively low energy density.

## *B. Supercapacitors*

Supercapacitors, also known as ultracapacitors or Electric Double-Layer Capacitor (EDLC), combine characteristics of conventional electrochemical batteries and conventional capacitors. Two electrodes are separated by an ion-permeable membrane (separator), whereby an electrolyte connects both electrodes (unlike the insulator in capacitors). If DC voltage is applied, the electrodes polarise and ions will form a double layer of opposite polarity to the electrodes' polarity. Therefore, the supercapacitors can be seen as two capacitors in parallel, hence the name electric double-layer capacitor. The electrodes are usually made of porous carbon. See Figure 2:23 for illustration.

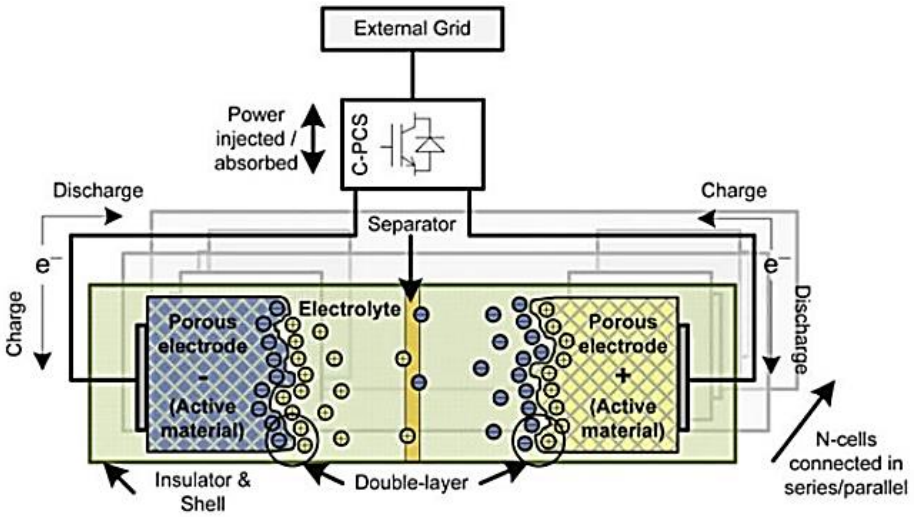


**Figure 2:23: Supercapacitor Structure**

The power density of supercapacitors can be up to 10 times higher compared to conventional electrochemical batteries, whereas they suffer from lower energy density, which makes them heavy and large if higher energy capacities are required. Their efficiencies are reported to 65-95%, while exhibiting long life times. Further drawbacks are high costs and the significant self-discharge which can reach around 20% of the rated capacity in 12 hours. Supercapacitors find applications in industrial factories for solenoid

valves, uninterrupted power supply units and short-term electrical energy storage systems for energy recuperation in vehicles.

## *2.5 Options for CAES for Supporting Wind Power Integration*

The objective of this section is to find the suitable domains in which CAES can provide services to help integrate variable wind power to the power network. In general, ES technologies can provide a wide range of network services to the system operator, such as electricity supply applications, balancing services, transmission network support etc. These network services become more important as wind power exploitation increases. The way in which CAES can be used to help integrate wind power to the power network hinges upon the intended services it can provide. CAES can either be operated in the whole-sale market and/or be operated in conjunction with a nearby wind farm to claim additional revenue streams. Regarding the former, the CAES plant in Huntorf, Germany, is decoupled from wind power and is used for tertiary frequency response, while operating only 2 to 3 times per week, although the plant is surrounded by wind turbines in *MW* scale. In that case, the CAES plant can be considered as one more option to help balance power generation with demand in general, while operating in the whole-sale market. The benefits of the CAES unit in Huntorf are, therefore, not predominantly related to wind power resources per se, but are disseminated to the market as a whole. Moreover, it can often not be quantified whether the stored energy comes either from wind resources or other power plants or both. In contrast to the Huntorf plant, the Iowa Stored Energy Park was a project that intended, not only but foremost, to build a 270*MW* CAES facility to be coordinated with regional wind energy sources [65]. In that way, additional revenue streams in relation to wind power were sought on top of the network services. From the two aforementioned examples it can be deduced that it is difficult to identify if a CAES plant serves a specific nearby wind farm or whether it operates within the market as a whole, or even both. It

depends on the intention of the owner and the objectives of the plant. More about that topic can be found in the Appendix A.

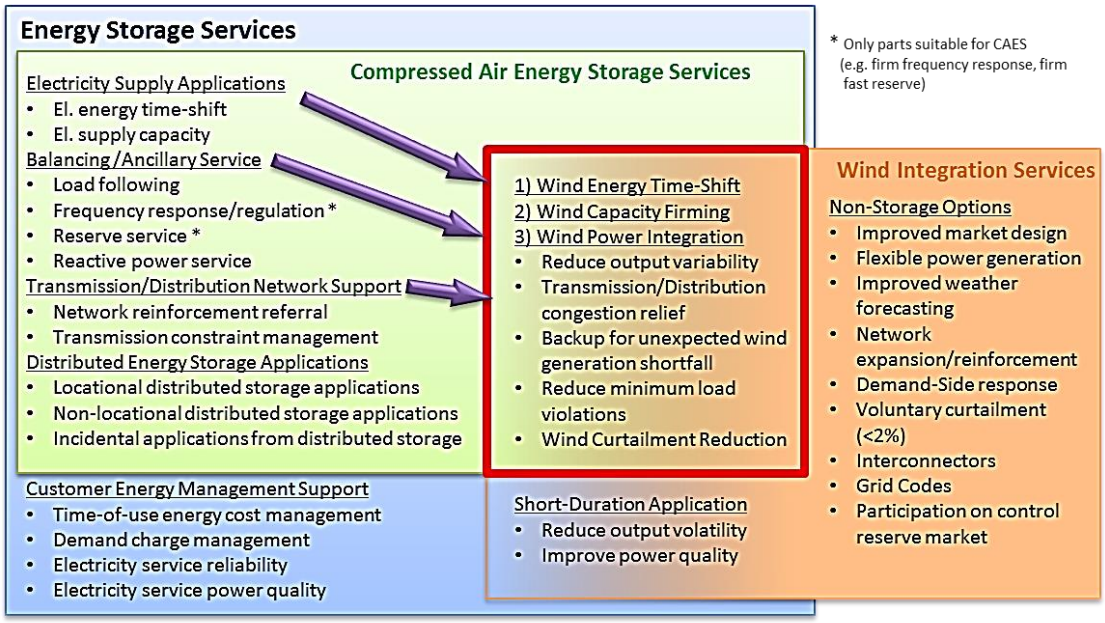


**Figure 2:24 ES and CAES Applications and Wind Integration Services**

The blue box in Figure 2:24 gives the most common applications for energy storage in general, of which more information based on U.S. applications can be found in [66]. The green box encompasses those applications that can be provided by CAES. The orange coloured box describes wind integration services that can be provided by CAES and other storage technologies as well as non-storage options. The applications within the thick red frame are the possible services identified for CAES in order to help integrate variable wind power generation to the power network. These applications will be discussed further in this section. Note that electricity supply applications, balancing services and transmission/distribution network support can be considered for wind power integration services as wind power generation increases and is highlighted by the purple coloured arrows. In the following it is focused on the applications written in the red box in Figure 2:24.

### *2.5.1 Wind Energy Time-Shift*

In brief, wind power time-shift involves enhancing the value of energy in order to increase profits. The reduction of the use of expensive fuel and operation and maintenance (O&M) of fossil fuelled power plants are of primary interest. Wind power generation often peaks in times when demand is low. For instance, wind power generation in Denmark reached 140% of the electricity demand at 3am. The store could be charged using low-price energy and sold when more expensive. The price of energy is low at off-peak times when demand is low (night, early morning) and high at peak times when demand is high. The energy could be bought by the storage owner and sold on the whole sale market, via Power Purchase Agreements or Feed-in Tariffs [67]. Note that this idea is not as attractive for solar power generation, because solar power is generated during the day when energy prices are higher.

The storage plant can be built either near to a wind farm or near to the load, which also depends on transmission capacity limitations. The stored energy discharge time for time-shift ranges from about 4 to 6 hours and depends mostly on the duration of off-peak and peak moments and peak to off-peak price differences. Figure 2:25 illustrates the idea of wind power time-shift.

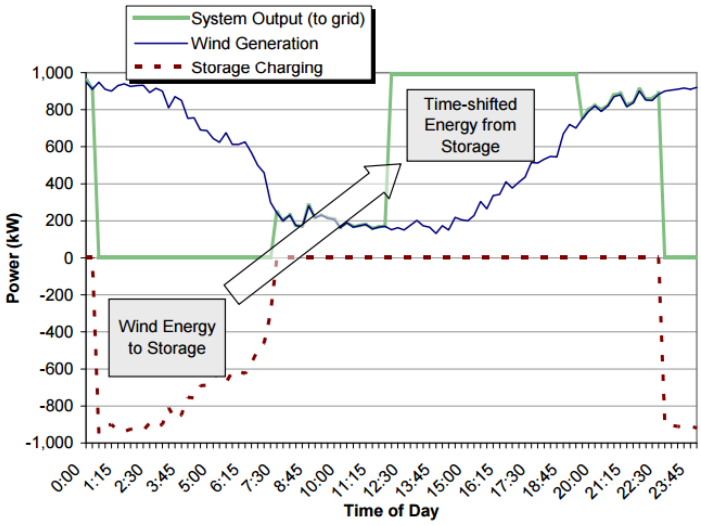


**Figure 2:25: Wind generation Energy Time-Shift [66]**

### *2.5.2 Wind Capacity Firming*

Wind capacity firming means that the variable wind power can be maintained at a committed level for a period of time. The objective is to use CAES in combination with wind power to smooth the power output. Wind capacity firming can be classified as short-term and long-term. Wind power generation often tends to ramp down when demand increases and vice versa, making "firming" valuable as a way to reduce load following resources from conventional fossil fuelled power plants. For capacity firming a time period of 2 to 3 hours is considered, which is not to be confused with wind power time-shift. The difference is that for capacity firming a controlled power supply profile can be achieved from variable wind power sources, which offsets the need for expensive equipment investments such as transformers and cables and also reduces the need for other fossil fuelled *dispatchable* power generation. Wind power time-shift and wind power capacity firming can go hand-in-hand resulting in combined benefits.

### *2.5.3 Wind Power Integration into the Power Network*

Energy Storage, and CAES in particular, can help manage the challenging effects to the power network operation from high wind penetration levels. It can be distinguished

between short-duration and long-duration applications. Based on Figure 2:24, the services are *reduced output variability, transmission congestion relief*, *back-up for unexpected wind generation shortfall* and *reduced minimum load violation*.

### *A. Reduce Output Variability*

This application is related to the need to offset variable wind power generation over durations of several minutes to a few hours. It is analogous to the load following balancing service due to the time-scale and the operational profiles. Especially at times of mismatching wind power generation and demand, load following mechanisms are needed, which CAES can be used for.

### *B. Transmission Congestion Relief*

Wind power may be curtailed as a consequence of network capacity constraints or system stability and security issues. CAES may store energy at times when the grid reaches its capacity limits and returns it to the grid in a controllable manner. This is especially of interest when wind power is connected to a grid with little power capacity. The results can be reduced wind curtailment, reduced need for back-up power, reduced transmission losses, network enhancement deferral, management constraint and improved security of power supply. Note that it is important that the link between wind power resources and the storage are sufficiently sized to avoid constraints between them.

### *C. Back-Up for Unexpected Wind Generation Shortfall*

In Texas 2008, an unexpected drop in wind power of 1700*MW* coincided with a sudden increase in demand and loss of a conventional generator [66]. Although to date being a rare scenario, the effect on the grid may increase as wind penetration levels increases. The grid operator responded by asking customers to reduce power output by 1GW in total for 90 minutes. Additionally, dispatchable generation needed to be ramped up. A CAES plant nearby can compensate for the drop in wind power.

### *D. Reduce Minimum Load Violations*

Conventional power plants have minimum operating levels, which can be reached in moments of high wind power penetration and low load. If not otherwise overcome (e.g. export of electricity), CAES can store the excess energy so that minimum operating levels are not violated. In that way, curtailment can be reduced, while providing more system inertia.

## *2.6 Flexibility in Power Network Operation*

Energy Storage is not the only solution for providing flexible power network operation. To date, TSOs have been able to balance the power supply with power demand, while taking into account sudden changes in demand (e.g. television break during a popular live sports event), generator shortfalls or storms. The increased amount of variable renewable energy sources can be seen as one more variable to deal with. Market regulations and interconnectors to import and export electricity are common methods to help balance the grid. More flexible power plants, network capacity extension and demand-side response are further methods. All the possible solutions aim for an increase in flexibility in power network operation and is described in this section.

Flexibility can be defined as the extent to which a power system can increase/decrease electricity production or consumption in response to variability, expected or otherwise [68]. Across the literature, the suggested means for successfully integrating variable wind power are overlapping, whereby costs are hard to quantify as costs are system specific.

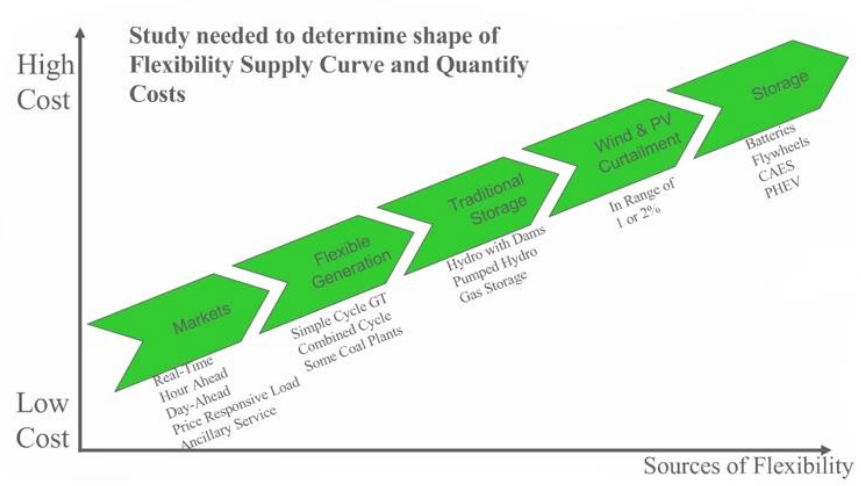


**Figure 2:26: Flexibility Supply Curve [68]**

Figure 2:26 shows some means of flexibility in accordance with costs qualitatively, presented by Alstom. The extensions of the grid infrastructure as well as demand-side response are not mentioned in this plot. It can be seen that storage options are considered last. A study from Germany's *Agora Energiewende* states that energy storage should be considered when the variable energy share exceeds 70% and until then grids are cheaper than storage facilities [69]. It concludes that large and strong grids and interconnection to neighbouring countries can increase flexibility because fluctuations are spread over large areas. Even the upgrade of distribution and transmission grids is cheaper than energy storage since it is more profitable to export excess energy especially to countries with beneficial flexibility options such as pumped hydro storage and adequate market regulations. Buying electricity from abroad may even be cheaper than using the own power plants, for instance in moments of wind troughs. These viewpoints are supported by the "Fraunhofer Institute for Wind and Energy System Technology" in Germany. Besides advocating the strong need in extending the grid infrastructure with both HVDC and AC lines, wind power delivering network services is also suggested [30]. Since 2012, renewable power such as biogas and hydro power have entered the market for system reserves. For wind power the access to that market is to date not permitted since wind power does not

fulfil the necessary regulations yet. What that means is that curtailment of renewable power would be incentivised in order to avoid expensive ramping up and down of conventional power units and to avoid expensive storage facilities.

Figure 2:27, compared to Figure 2:26, again demonstrates integration options, while emphasizing that costs are illustrative, as actual costs are system dependent.

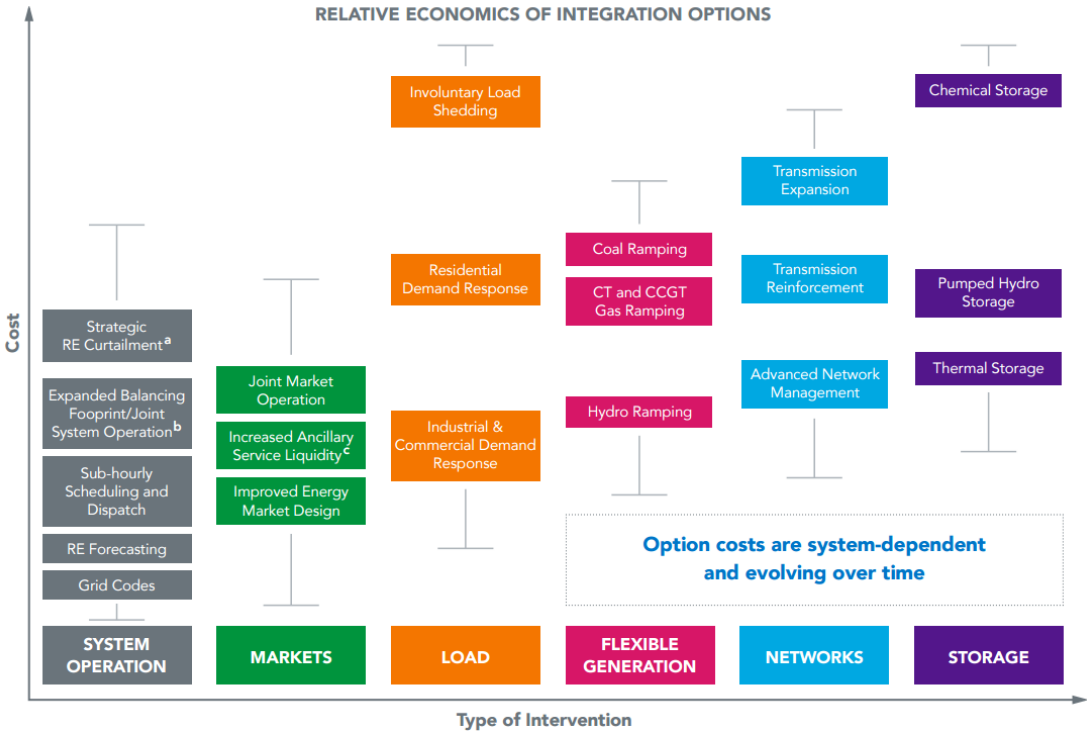


**Figure 2:27: Relative Economics of Integration Options [70]**

In contrast to the information from Figure 2:26, Figure 2:27 shows an overlap of *networks* (that is, transmission reinforcements/expansion and advanced management) and *storage* (that is, thermal, pumped hydro and chemical storage). Nevertheless, an overall rising trend in costs can be noticed as it is moved towards energy storage.

During the time of the research, substantial information is found among industry favouring demand-side response and interconnectors over energy storage in the very near future. On the other hand, energy storage is subject to research and considered beneficial in the

future as costs for storing energy are expected to decrease. A case study on Denmark has shown how large amounts of variable wind power can be accommodated by many means other than storage, but mainly exporting and importing energy (see Appendix B). However, Denmark is a small country with advantageous neighbours that can be used as sinks to balance power supply and demand. In fact, Denmark uses energy storage indirectly in Norway and Sweden, which further helps balancing power supply with demand (Norway and Sweden have a storage potential of 116TWh [71]). Energy storage becomes inevitable by considering that other European countries increase their share of variable power supply towards their specific targets in 2020 and 2050 [7]. In fact, a mix of strong interconnectors, demand side response and energy storage on different levels of the power network system must be considered [7].

## *2.7 Underground Compressed Air Storage Potential in the UK*

It is beneficial to investigate the potential underground storage capacity for CAES in the UK. The majority of the information in this section is taken from the work conducted by the British Geological Survey (BGS). The report presented in [72] can be found on the IMAGES webpage [73] and summarises natural gas underground storage facilities and salt beds across the UK that can be used for CAES caverns. However, the study is yet ongoing and not finalised, so that preliminary results are presented. In the UK the main salt beds, comprising halite, can be found offshore and onshore, whereby onshore salt beds are more suitable since they are shallower and less costly concerning the solution mining process. In the UK, numerous underground natural gas storage facilities are already in place, however, for CAES no caverns exist. The key parameters when assessing caverns are the depth, wall thickness and purity of the salt bed. The volume is of interest as well as the potential operational pressure ranges. Furthermore, the operational storage cycles and aboveground

infrastructure are important factors when considering a new cavern for a store. The work in [72] distinguishes between already existing/planned caverns for natural gas and potential salt beds that can be utilised to build caverns for CAES. These two subjects are described in the following.

### *2.7.1 Natural Gas Storage Caverns*

Five locations were identified in the UK that host natural gas storage caverns. The regions are:

- Aldbrough and Hornsea (East Yorkshire)
- Rough (offshore North Sea)
- Hatfield Moors (Yorkshire)
- Humbly Grove (Weald)
- Holford and Hole House Farm (Cheshire)

In addition, some estimated 20 new locations are currently considered for natural gas storage and are either in planning or construction phase. The total cavern volume from existing caverns for natural gas storage can be estimated to around 13.3mcm. Assuming an operational pressure range of 46-66*bar* (example Huntorf) and a storage temperature of 20°C, the caverns can storage around 30.9*GW*h of compressed air.

| Air energy (GWh) STP: 273.15 K and $10^5$ Pa | | Stored air pressure | | | | | | |
|---|---|---|---|---|---|---|---|---|
| | | 80 *bar* (Ref STP) | 100 *bar* (Ref STP) | When operating, available transfer energy to electricity | Operating pressure range | | | |
| | | | | | 40-66 *bar* | 40-76 *bar* | 46-66 *bar* | 46-76 *bar* |
| Stored air temperature | 233 K (-40°C) | 133.5 | 178.2 | | 47.0 | 66.9 | 36.8 | 56.7 |
| | 253 K (-20°C) | 125.3 | 164.8 | | 43.6 | 61.6 | 33.9 | 52.0 |
| | 273 K (0°C) | 119.9 | 156.7 | | 41.3 | 58.1 | 32.1 | 48.9 |
| | 293K (+20°C) | 116.1 | 151.1 | | 39.9 | 56.0 | 30.9 | 47.1 |
| | 313K (+40°C) | 113.5 | 144.0 | | 38.8 | 54.4 | 30.1 | 45.6 |

**Figure 2:28: Storage Capacity for Existing Natural Gas Caverns for 13.3mcm**

Figure 2:28 shows a number of storage capacities for the existing natural gas cavern volumes if they were used for CAES and by taking into account different temperatures as well as pressures and pressure ranges. In comparison, the total electricity consumption in the UK was around 339*TWh* in 2014. Therefore, by taking a realistic storage capacity of 30.9*GWh* as an example, the storage capacity of existing natural gas caverns would amount to a share of 0.01% of the nationwide electricity consumption. Furthermore, estimations show that if all planned natural gas storage caverns were commissioned and utilised for CAES, a total storage volume of around 76.1mcm would be available. Operated at a pressure range of 46-66*bar* and 20°C would uncover a storage capacity of 176.4*GWh*. Figure 2:29 shows more information.

| Air energy (GWh) STP: 273.15 K and $10^5$ Pa | | Stored air pressure | | | | | | |
|---|---|---|---|---|---|---|---|---|
| | | 80 *bar* (Ref STP) | 100 *bar* (Ref STP) | When operating, available transfer energy to electricity | Operating pressure range | | | |
| | | | | | 40-66 *bar* | 40-76 *bar* | 46-66 *bar* | 46-76 *bar* |
| Stored air temperature | 233 K (-40°C) | 761.2 | 1011.2 | | 268.4 | 382.0 | 210.1 | 323.8 |
| | 253 K (-20°C) | 715.7 | 941.0 | | 249.0 | 351.7 | 193.6 | 296.9 |
| | 273 K (0°C) | 684.8 | 895.0 | | 235.8 | 331.7 | 183.3 | 279.2 |
| | 293K (+20°C) | 662.8 | 862.9 | | 227.8 | 319.8 | 176.4 | 268.9 |
| | 313K (+40°C) | 646.8 | 821.1 | | 221.6 | 310.6 | 171.9 | 260.4 |

**Figure 2:29: Capacity for planned Natural Gas Caverns if utilised for CAES for 76.1mcm**

Summing up both existing and planned storage caverns, a total energy capacity of around 207GWh could be available assuming an operational pressure range from 46-66*bar*. That would amount to a share of 0.06% of the UK's annual electricity need.

### *2.7.2 Potential Storage Volume in UK Salt Beds*

Apart from the idea to exploit natural gas storage caverns for CAES, new caverns can also be built. As mentioned before, the UK is rich in salt beds that can be used for CAES. The map in Figure 2:30 shows suitable salt beds for CAES in the UK.

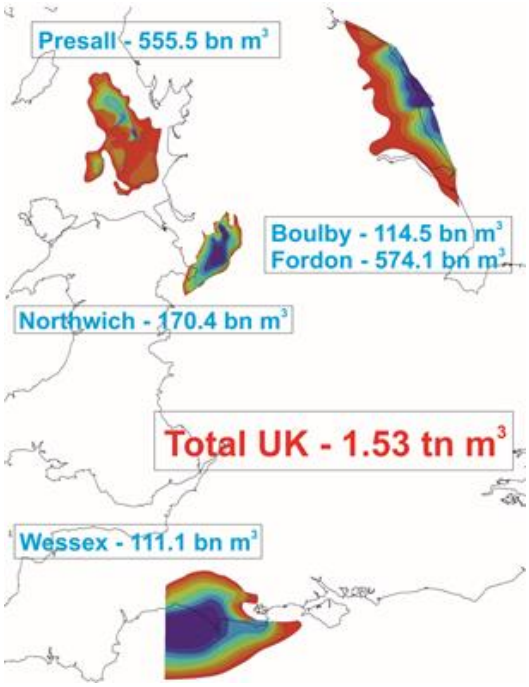


**Figure 2:30: Suitable Salt Beds for CAES in the UK**

To give a comparison, if it was possible to utilise 1.53tcm, a total storage capacity of 363TWh would be available, which almost coincides with the UK's annual electricity consumption. However, only a fraction of the available salt bed volume can be made accessible. Criteria such as wall thickness, depth, infrastructure etc. limit the utilisation of the available storage volume drastically. An estimation based on the Northwich salt bed near Cheshire was made in [72]. Applying all constraints to the salt bed, the maximum exploitable volume for CAES is about 33.7mcm (0.2% of the available 170bcm). The storage capacity for a pressure range of 44 to 66*bar* equals approximately 78GWh. Further study is currently ongoing as to whether storage caverns can be made available for CAES in other regions such as Wessex, Boulby, Fordon and Presall.

To sum up, the UK offers large amounts of salt beds suitable for CAES. Combining the storage volumes of the natural gas caverns (operating and in planning/construction) plus the available storage volume in Cheshire, a total energy capacity of 285GWh would be

made available, which is 10 times the storage capacity of the UK's pumped hydro storage capacity.

## *2.8 Summary*

HAWTs are favoured over VAWTs in industry due to their distinct advantages such as higher efficiencies and the fact that they are mounted on high towers, meaning that they are exposed to higher wind speeds. Modern wind turbine systems commonly contain full power converters so that the rotational speed of the rotor shaft and generator shaft are disassociated from the grid frequency. In that way, the wind turbine can be controlled to operate at its maximum efficiency at given wind speed.

An overview of the up to date installed wind power capacity in the UK, Germany and Denmark was given along with projections for future wind power development. It was shown that for the UK, the currently installed wind power capacity of 13.3GW must increase to about 22GW to achieve 15% energy consumption from renewables by 2020.

With the increase in wind power penetration in the near future, great challenges regarding integration into the power network are expected to occur. Wind, by nature, is variable and uncertain. Furthermore, the low short-run costs of wind power, the modularity, the location constraints and the non-synchronous generation are properties identified to contribute to the challenges of wind power integration into the power network.

Energy storage technologies were explained, while focusing on the options for CAES to support wind power integration into the power network. Wind energy time shift, wind capacity firming and wind power integration (i.e. reduced output variability, transmission congestion relief, back-up for unexpected wind generation shortfall and reduced minimum load violation) were identified to be appropriate applications.

Lastly, recent findings regarding the underground CAES potential were reported. If existing natural gas underground storage facilities were exploited, a total energy capacity of around 207GWh could be available assuming an operational pressure range from 46-66*bar*. In addition, if it was possible to utilise the UK salt deposits of 1.53tcm, a total storage capacity of 363TWh would be available. However, only a minor fraction of this potential can be utilised due to limitations such as wall thickness, depth, infrastructure etc.

# *Chapter 3 - Hybrid Wind Turbine Design*

The aim of this chapter is to provide an overview of existing technologies in the literature and industry regarding the combination of wind power and CAES. Following the literature review, the design idea of the proposed hybrid wind turbine is introduced. The components for the hybrid wind turbine are discussed and the selection of the components is made. Lastly, the working principle and the operating modes of the proposed hybrid wind turbine are explained.

## *3.1 Existing Hybridisation Systems for Wind Turbines and CAES*

The literature shows a number of hybrid applications, combining both energy storage and wind turbines, whereby it is primarily looked at applications that include compressed air energy storage. Among them, Wind-Diesel Hybrid Systems (WDS), wind turbines directly connected to pneumatic and hydraulic pumps, hybrid compressed air with supercapacitors, and scroll type air expanders connected to the wind turbine drive train are found to be the most relevant. These technologies are discussed in the following subsections.

### *3.1.1 Wind-Diesel Hybrid Systems*

WDSs are used in remote areas, whereby a diesel generator complements one or more wind turbines with the aim to increase the share of environmental friendly power generation. However, two main problems occur due to the variability of wind power. The diesel generator either needs to undergo undesired frequent starts and stops, or the share of wind power must be reduced so that the diesel generator can operate in its recommended power range [74, 75]. Both issues suggest that a standalone wind turbine and diesel generator is not sufficient for an efficient operation. In order to reach more

flexible operation and an increase of wind power exploitation, energy storage is applied in the form of thermal storage, batteries and CAES. It is difficult to convert thermal energy back to electricity so it is often used for heating nearby building spaces instead. Batteries are commonly deployed to facilitate the DC-link between the rectifier and inverter unit that are part of the power electronics units. Therefore, the battery serves as an energy storage unit that helps improve the transient performance of the system in moments of wind drops or gusts. However, batteries are expensive [76], difficult to recycle, a source of pollution and limited in power and lifecycle. The benefits of using batteries for this application are the high energy density and the relatively high cycle efficiency. Figure 3:1 illustrates an example of a WDS, in which a battery is used to smooth power fluctuations.

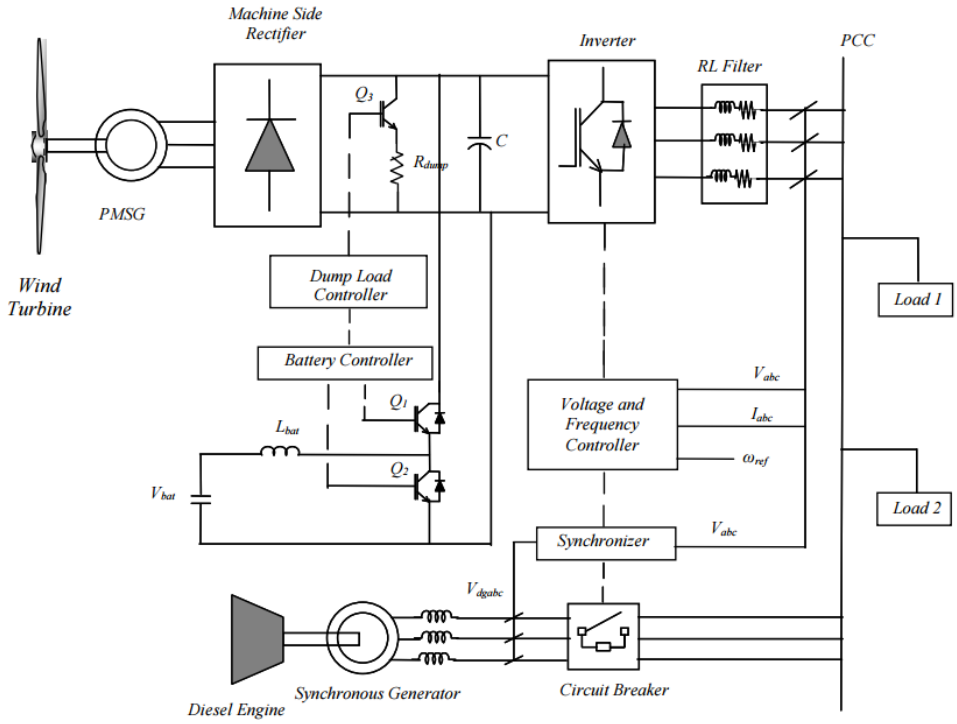


**Figure 3:1: Wind-Diesel Hybrid System[74]**

The battery is connected to the DC-link between the rectifier and the inverter. An additional diesel generator is employed to further supply electricity when wind speeds are not high enough to meet the power demand. It is noticed that the system requires complex control and sensible sizing of the wind turbine, the battery and the diesel engine.

An alternative design structure to the wind-diesel hybridisation is shown in Figure 3:1 is a WDS with continuous diesel generator power output, whereby the wind turbine balances fluctuations using variable blade pitch control [77]. However, this is not preferable since renewable power is throttled. Furthermore, WDS comprising CAES can be found in industry [75]. A typical WDS with a CAES system is shown in Figure 3:2.

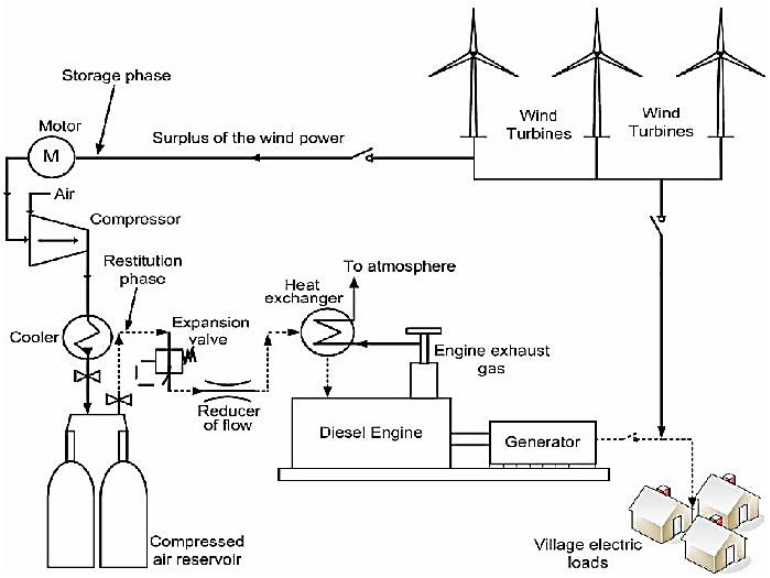


**Figure 3:2: Illustration of WDS with CAES [75]**

Wind turbines generate intermittent power which is balanced via the diesel generator. In times of excessive wind power generation over the demand, the excess power can be used to drive a compressor to store high pressure air. The compressed air is then used to charge the diesel engine to achieve higher efficiencies and reduce fuel consumption. In that way, more wind power can be exploited while maintaining stable electricity supply. Based upon the structure in Figure 3:2, variations exist in the way the compressed air is generated (more information is given in [75]).

To sum up, WDS are common and provide secure power supply in rural areas. However, fossil fuel is used as a source of energy, which is not ideal for a clean energy supply.

### *3.1.2 Wind Turbines in connection with CAES or Hydraulic Power*

In [78], an off-shore wind turbine in connection with an energy storage system is presented. The system is capable of smoothing power fluctuations from wind power. It also addresses the inefficiencies through heat losses during the compression stage, as well as the under-utilisation of electrical components due to low capacity factors. The system is depicted in Figure 3:3.

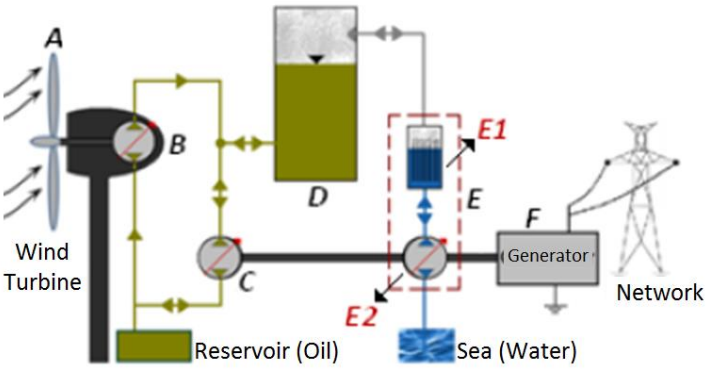


**Figure 3:3:** ***Wind Turbine in connection with CAES and Hydraulic Power [78]***

The wind turbine is directly connected to a hydraulic pump (B), which drives a hydraulic motor (C). The hydraulic motor drives a nearly isothermal liquid piston air compressor/expander (E) and a fixed speed induction generator (F). The storage vessel (D) is charged with compressed air via the piston pump (E1) or with oil via the turbine pump (B), respectively. E1 is a liquid piston pump that uses honeycomb porous material. The porous material is used to increase the heat transfer surface area. During excessive wind speeds, power is taken off the main drive shaft via E2. E2 pumps seawater into the expansion/compression chamber of E1 to pressurise air and to charge the storage vessel (D). The heat during the compression is transferred to the sea water to maintain nearly isothermal compression. For discharging, the compressed air from the vessel (D) is moved to the piston pump (E1), which then drives the hydraulic motor (E2) so that torque can be added to the main drive shaft. Heat energy is injected to the expansion process from the

porous material to prevent the air from getting too cold. With this configuration the air pressure in the vessel can be maintained while regulating the amount of oil in the vessel.

For the system described above, simulation study is conducted in [78] and the results are presented and analysed. It is shown that the power generation can be kept constant under varying wind speeds, while the hydraulic pumps (B, E) and the hydraulic motor (C) are operating individually. Wind power can be captured beyond the rated power of the generator, so that capacity factors can be increased. The capacity factor is also increased through downsizing of the electrical components in comparison to conventional wind turbines which only reach nameplate power rating at high wind speeds. Although the capacity factor can be increased with the proposed design, it is not quantified how much more energy is produced [78]. Furthermore, neither the capability of maximum power point tracking is investigated in the paper, nor is the system experimentally verified. The heat storage process and associated efficiencies are not explained. On the other hand, it can be said that the system does balance fluctuations in wind speed, which increases flexibility in operation.

The work in [79] describes a wind turbine system directly connected to a compressor. The pressurised air circulates in a closed loop system and drives an expander, which in turn drives a generator. The system is illustrated in Figure 3:4.

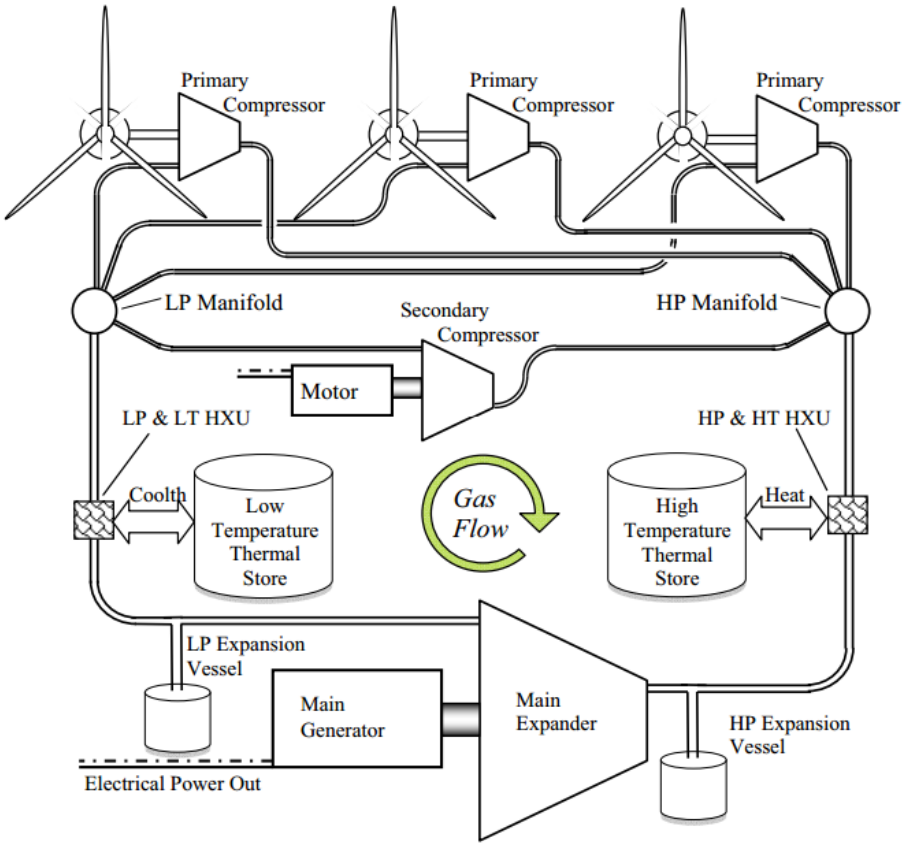


**Figure 3:4: Schematic of the Wind Turbine System with intrinsic Thermal Storage [79]**

The system utilises thermal storage and compressors directly driven by wind turbines. The right hand side of Figure 3:4 describes the high pressure and high temperature side (after air compression), whereas the left hand side describes the low pressure and low temperature side (after air expansion). The air flows in a closed loop, whereby heat and coolth can be added or extracted to/from the compressed air flow from the thermal store. Therefore, by adding heat energy to and taking heat energy out of the system, the expander can either draw more energy than the compressor delivers or vice versa. Five modes are described in [79]:

- Mode A: Direct power transmission from primary compressor to the expander
- Mode B: Transmission from primary compressor to expander with some heat energy going into storage

- Mode C: Transmission from primary compressor to expander with some energy returning from heat storage
- Mode D: Power insertion via secondary compressor towards expander with some energy going into storage
- Mode E: Power insertion via secondary compressor towards expander with some energy returning from storage

Modes B and D can be operated at the same time as can mode C and E. If operated in mode D and E, the system can be regarded as standalone, taking electricity off the grid for storage. A core component of that proposed system is the novel compressor design for which an isentropic efficiency is believed to achieve 98%. The application is claimed practicable for on- and offshore, whereby a wind fleet shares the same expander/generator set. Pipe losses are considered and are deemed to be negligible if pipes are sized adequately.

Critically reviewed, the authors of [79] mention high turnaround efficiencies of up to 85% (which is the ratio of electrical energy delivered from the system after it has passed through storage to the amount of electrical energy it would have produced if it had not been passed through storage). Concerning the commercial argument, the proposed system is considered favourable in comparison to conventional wind farms and storage in time scales of hours. The limitations of the systems are the low time constant of an hour when considering a change in the operation mode. A maximum of 60% of the energy being harvested by wind can be put into the storage (using mode B only).

### *3.1.3 Hybrid Wind Turbine with Scroll Air Expander on Turbine Shaft*

A small scale hybrid wind turbine is introduced in [80-82] which is the predecessor project of the research in this study. It utilises a scroll type air expander that is connected to the

wind turbine shaft. In that way, torque can be added to the wind turbine drive train. Scroll type air expanders originate from scroll type air compressors and have recently gained interest from industry for Uninterruptable Power Supply units (UPS) and waste heat recovery systems [52, 83]. Power ratings can be found from several *kW* up to 50*kW* [52].

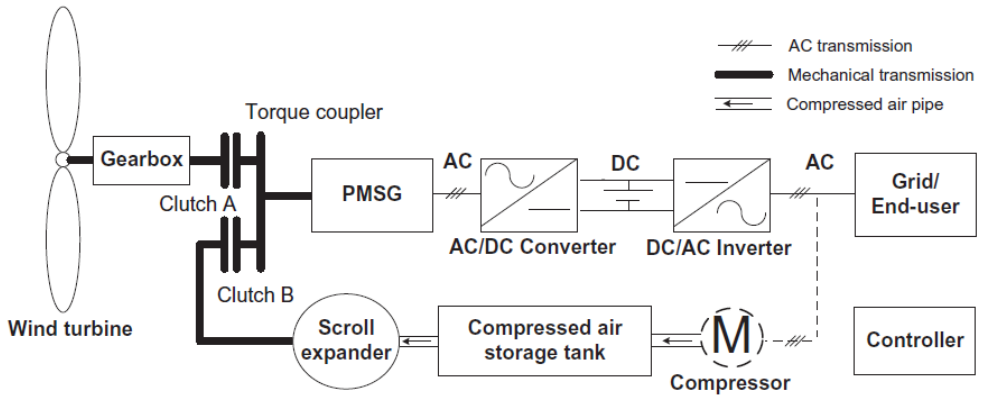


**Figure 3:5: Hybrid Wind Turbine with CAES and Scroll Type Expander [82]**

The system topology is shown in Figure 3:5. The turbine drive train speed is increased via the gear box. A torque coupler allows the scroll type air expander to add torque to the drive train. If wind speeds are not high enough so that the generator power does not satisfy the demand, the scroll expander can be engaged via a magnetic clutch, and add power to the system. The scroll expander is driven by compressed air, which is taken from an air tank which is filled by an external compressor. The research shows that wind power can be smoothed since power is added from CAES in moments of wind troughs. Likewise, excess electrical power generation over the demand can be extracted from the grid and used to compress air. The system is simple in its design and offers more flexibility by using CAES. However, the research does not state roundtrip efficiencies from electricity to electricity via compressed air energy storage. No information is given about thermal losses during the compression or expansion and the compression stage is not studied at all. Instead the peak efficiency of the scroll expander, i.e. the ratio of the mechanical power from the scroll expander to the input air power, is computed to around 55%. Although the system offers

more flexibility in electric power generation, it is not flexible in itself. The scroll air expander's rotational speed is tied to the turbine drive train's rotational speed. The hybrid wind turbine is investigated based on a small scale 1-2*kW* wind turbine system and the scalability to *MW* levels it not explored. After all, the added torque to the wind turbine drive shaft also propels the wind turbine, which has undesired effects on the wind turbine power coefficient.

## *3.2 Proposed Design of the Hybrid Wind Turbine System*

The motivation for designing a hybrid wind turbine system is to add flexibility in power generation by utilising CAES and to find a more efficient method to generate compressed air directly through the wind turbine's mechanical power. The need for flexibility is outlined in Section 2.5 and Section 2.6. Concerning CAES, research has mainly been concentrating on large scale storage and only a few hybrid wind turbine technologies in connection with CAES were found (see Section 3.1). However, as shown in Subsection 2.4.4, CAES is not limited to large scale applications only, but can as well be considered for small scale applications, making it suitable for storage applications on a wind turbine level.

The hybrid system presented in Subsection 3.1.3 shows that a scroll air expander is used to support the turbine drive shaft. The drawbacks of the system have motivated this research work to innovate the hybrid wind turbine to improve the system performance with regards to the following aspects:

- More flexible mechanical power transmission
- Reduced amount of components
- Increase in efficiency
- Increased power rating
- Standalone energy storage provision

- No negative influence on the wind turbine's power coefficient

### 3.2.1 Design Idea

It is intended to combine the wind turbine with an expander/compressor unit mechanically though a transmission device/technique. Both, the wind turbine and the expander must be able to drive the generator independently or together. It must also be possible to compress air directly through the wind turbine and/or the electric motor.

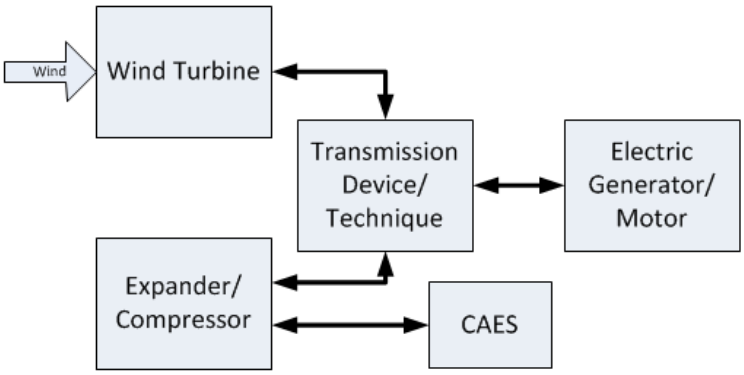


**Figure 3:6: Initial Design Idea of the Hybrid Wind Turbine**

Figure 3:6 shows the schematic of the initial design idea. The key aspect of the wind turbine is the mechanical transmission to meet the aforementioned requirements. The selected transmission device is explained in the following, along with a choice of the system components (wind turbine type, expander/compressor type and motor/generator type).

### 3.2.2 Transmission Device

The hybrid wind turbine must accommodate three shafts, i.e. the wind turbine shaft, the air expander/compressor shaft and the electric generator/motor shaft. The device should be compact in size and efficient in operation. Inspiration is sought in the automotive industry, especially hybrid vehicles that use more than one propulsion technique. It can be distinguished between *series*, *parallel* and a combination of series and parallel connections, called power split devices (PSD) [84]. Concerning the series connection, a combustion engine is used to charge a battery via a generator, while operating at peak efficiency. An

electric motor is then used to draw power from the battery. As to the parallel configuration, both the combustion engine and the electric motor are fitted on the same drive train. In both the series and parallel case the electric machine can be used as a motor and a generator. Figure 3:7 illustrates these two configurations.

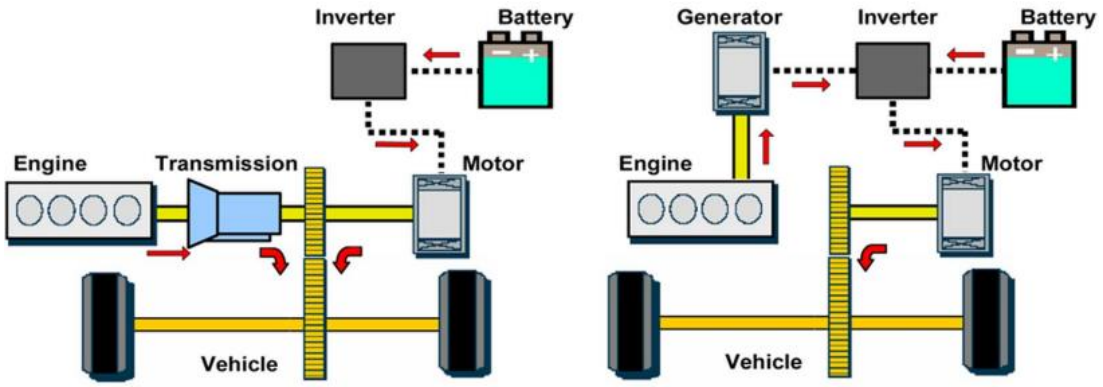


**Figure 3:7: Hybrid Vehicle Configuration. Left: parallel. Right: series.[84]**

### *A. Parallel Configuration*

The parallel configuration is similar to the configuration of the hybrid wind turbine system described in Figure 3:5 on page 64. The benefit is that two power streams can be used separately or simultaneously. For example the electric machine and/or the combustion machine can propel the hybrid vehicle. Concerning the hybrid wind turbine, the wind turbine and/or the air expander can drive the generator. The parallel configuration is beneficial for the hybrid vehicle since the strong starting torque of electric motors offsets the weaker and less efficient torque generation from the combustion engines at low shaft speed. Furthermore, the electric machine can act as a motor and generator whilst driving and being driven in the same direction. Clutches can be used to decouple and merge the combustion engine and the electric machine according to purpose. With regards to the hybrid wind turbine, the aforementioned benefits do not apply. The wind turbine spins continuously and does not undergo vast changes in rotational speed (no high acceleration torque). Most importantly, however, the air expander cannot be run in reverse in moments

of excessive wind speeds so that air can be compressed. This is one of the major limitations of the parallel connection if utilised for the hybrid wind turbine. Furthermore, the rotational shaft speeds of the wind turbine and the expander are synchronised at all times, which limits the flexibility.

### *B. Series Configuration*

The series configuration of a hybrid vehicle is used to drive a generator for electricity via the combustion engine. The electricity is either used to drive the electric motor directly or to charge the battery. The benefit is the option to decouple the combustion engine from the electric motor so that the combustion engine can operate at high efficiency at all times. Concerning the hybrid wind turbine, similarities can be found in the system idea shown in Figure 3:4 on page 62, where the wind turbines generate compressed air directly through compressors. The compressed air is used to drive the expander, while heat energy can be added or extracted to/from the thermal store. The disadvantage of the series connection is that there is no direct link between the wind turbine shaft and the generator. All power goes through the compression and expansion process which inherits losses mainly due to thermal implications.

### *C. Power Split Devices*

PSDs are commonly used in industry and date back to the 1970s [85]. They usually consist of a three-shaft planetary gear box and are compact and efficient transmission devices. Furthermore, the PSD offers continuously variable transmission and, therefore, it is suitable for hybrid vehicles. PSDs are found in many well-known vehicle manufacturers such as Toyota and Honda [84]. Toyota released the famous and successful hybrid vehicle called *Prius* in 1997, which further proves the reliability of the PSD. Additionally, PSDs have been suggested for wind turbines, as reported in [86-88], and led to commercial products such as the DSgen-Set® [89, 90], which will be studied more in detail in this section. The idea of

DSgen-Set® is to allow for variable speed operation of the wind turbine, while removing power electronics, such as inverters and converters, so that a straight-through connection between the generator and the grid can be realised. The system provides more mechanical system inertia as opposed to systems with inverter/converter units, which decouple the generator from the grid. The system structure of the PSD is depicted in Figure 3:8.

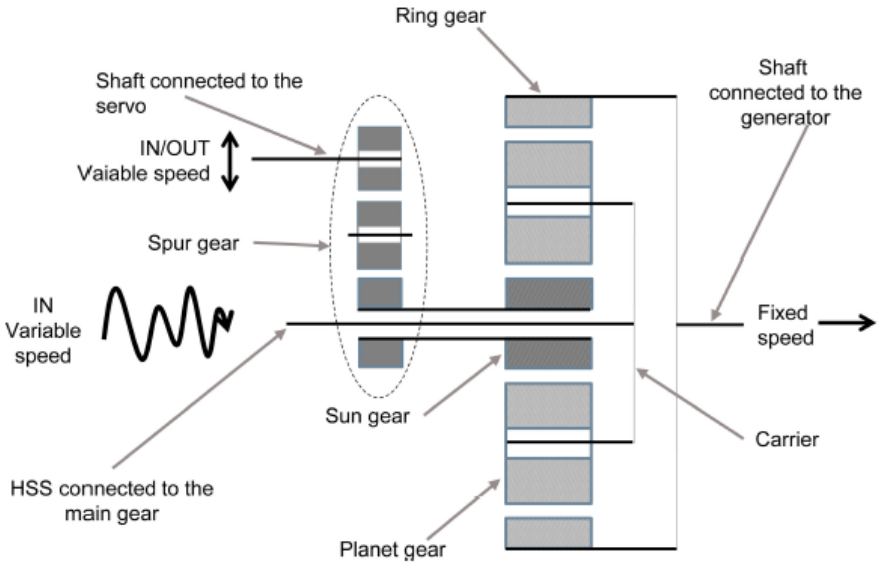


**Figure 3:8: Sectional View of the Power Split Device [88]**

The planetary gear box (PSD), consists of a ring gear, a sun gear and a carrier that holds the planet gears. All three components are movable and interact with each other depending on the torque acting on them. The turbine shaft is connected to the carrier and provides the main torque input to the system. An electric servo motor is connected to the sun gear via several spur gear transmissions and provides additional in- and output. The resultant torque is transmitted through the ring gear to the main generator of the system. Through the PSD a constant output generator speed can be maintained while the turbine rotor is changing its rotational speed according to wind speed variations. The main actuator for the control is the servo machine, which operates as a motor or generator according to the control design. The system described above is modelled and experimentally verified by means of a 2.7*MW* wind turbine generator and a 250*kW* servo motor [88]. The advantage

of the system is its simplicity and high efficiency of the planetary gear box (up to 95% [91]). The authors claim a cost reduction of up to 50% in comparison to a permanent magnet synchronous generator with a full-scale converter. An important benefit is offered through the PSD in which it is possible to reverse the sun gear's direction of rotation. Concerning the hybrid wind turbine, the air expander/compressor can be connected to the sun gear so that expansion and compression modes can be realised. The system structure of the PSD reveals that the device is a sound solution for the intended hybrid wind turbine application. Similar applications for the PSD can be found in further publications [86, 87, 92, 93].

### *3.2.3 Air Expander/Compressor*

The air expander/compressor for the hybrid wind turbine is required to be compact in size with low weight, low maintenance, high efficiencies and scalability from several kilowatts to several hundreds of kilowatts. Based on the idea of the PSD, the air expander can be connected to the sun gear shaft, which is suited for moderate speeds (several thousands of *RPM* rotational speed) and low torques. The torque and rotational speed depend on the overall gear ratio of the PSD and will be covered more in detail in Section 4.8 (mathematical modelling) and Section 5.3 (determination of gear ratio).

Commercially available expanders/compressors can be classified in reciprocating, rotary positive displacement and turbo machines. Turbo machines, such as axial turbines can be considered too large for the application since they are used for several hundreds of *MW* rated power plants [94]. Reciprocating machines are used for various scales from micro scale to several hundred kilowatts and are characterised through their high single stage pressure ratios (up to some 20*bar*) and low air mass flow rates [94]. They benefit from relatively inexpensive design and high volumetric efficiencies[3] due to their large volume ratios. On the other hand, reciprocating machines are noisy, require high oil content in the

[3] Volumetric efficiency is defined as the ratio of the ideal flow rate based on the intake stroke volume to the actual flow rate

air and suffer from re-expansion losses due to the clearance volume. Most importantly, these machines have many moving parts, cause vibration and are large and bulky in design while requiring high maintenance effort in comparison to other machine types. These drawbacks lead to the decision that reciprocation machines are not further considered for the hybrid wind turbine design.

The rotary positive displacement machines that are considered here are screw and scroll expanders/compressors. Both types have similar advantages and disadvantages. They are light, quiet in operation and work smoother with less vibration in comparison to reciprocating machines [95]. They also tend to have lower clearance volumes and benefit from higher efficiencies compared to reciprocation machines [94]. The main advantage that makes them attractive for the hybrid wind turbine design is the compact size, while reaching up to around 65% isentropic efficiency[4] for screw machines and up to 70% isentropic efficiency for scroll machines [83, 96]. The low maintenance and reliability further increase their potential for the use in the hybrid wind turbine. The fundamental difference between these two machine types is the design and size with increase of rated power. Whereas scroll machines need to increase in radius in order to increase power rating, screw machines increase in length. Therefore, screw machines are more suited for larger scale applications since the scroll machine is limited in size by increased centrifugal forces. The largest scroll compressor can be found in the UPS system by *FlowBattery*, housing a rated scroll expander of 50*kW*, while requiring a maximum air pressure input of around 14*bar* [52]. A large screw type expander was found in [94], with a power rating of up to 200*kW*. Both machine types can be considered for the hybrid wind turbine design. The compact design of both machine types makes it possible to engage more than one machine to the sun gear of the PSD. This is especially beneficial with respect to the

[4] Isentropic efficiency is defined as the ratio of isentropic work to mechanical work output

compression mode, since the maximum achievable pressure can be increased with a series connection of the compressors while being driven by the same shaft.

Lastly, radial turbo machines are widely used in industry and can be found for various applications reaching up to 85% isentropic efficiency [97, 98]. Power ratings are reported from several Watts up to Megawatts, while being very compact. For instance, according to [98] a 27.9$MW$ turbine would have a diameter of 1m. However, the pressure ratios are reported to be below 5$bar$, which is why the power is generated from high rotational speed, rather than torque. Typical rotational speeds are in the range of 6000 up to 80,000$RPM$. In fact, the high rotational speeds and, therefore, the comparable large amount of air consumption would make this turbine type unattractive for the intended hybrid wind turbine.

To conclude, screw and scroll air machines are best suited for the hybrid wind turbine application for the reasons given above. With respect to a larger scale wind turbine in Megawatt region, screw machines are more adequate. For smaller scale applications in the region from several Kilowatts to hundreds of Kilowatts, scroll machines may be more suited. For this project, a scroll machine is considered for the small scale experimental test rig.

### *3.2.4 Wind Turbine*

The difference between HAWTs and VAWTs were examined in Subsection 2.1.1, concluding that the benefits of HAWTs outweigh the benefits of VAWTs. HAWTs are more efficient in terms of energy conversion from kinetic wind energy to mechanical shaft energy [99], and are widely used for commercial applications. A HAWT is considered for the final hybrid wind turbine proposal. However, concerning the set-up of a small scale experimental test rig, a HAWT is more difficult to accommodate compared to a VAWT. A small scale 1$kW$ VAWT-Generator assembly was available prior to the beginning of this research and the

unit was initially considered to be adequate to use. A VAWT can be placed on a ground level hub that also contains the generator, the scroll air expander/compressor, the PSD and various instrumentation apparatuses. However, as the project progressed it transpired that the VAWT was not large enough to match the generator's rated power of 1*kW* even under strong wind conditions. For example, wind tunnel tests at 17m/s wind speed led to only 130W electrical power output from the unit, despite the VAWT operating at maximum efficiency (the maximum efficiency of that VAWT is 8%). Therefore, it was concluded that the VAWT should not be used. Further research into the use of VAWTs and HAWTs for the test rig concluded that they were not feasible for the following reasons:

- High costs of wind turbines
- Limited feasibility to implement a sufficiently scaled wind turbine (either HAWT or VAWT) for a laboratory scaled test rig due to the size of the potential wind turbine
- Health & Safety constraints
- Dependency on outdoor wind conditions

A further solution was seen in wind turbine emulators, where electric motors are controlled in a manner to mimic the behaviour of any wind turbine. This is regarded suitable for laboratory purposes because electric motors are small, compact, high in power density, controllable, low cost, and they do not require wind resources. Wind turbine emulators are widely used in industry and research for the purpose of developing and testing of new wind turbine systems [100, 101]. Aachen University, Germany, for example employs a 1*MW* and 4*MW* wind turbine emulator at the *Center for Wind Power Drives* [102]. It is the above mentioned reasons that led to the decision to employ wind turbine emulators for the test rig.

### *3.2.5 Electric Generator*

The electric generator for the intended hybrid wind turbine does not require strict characteristics. Power electronic units such as bidirectional converters/inverters are

desired so that the generator can also be utilised as a motor. To use the wind turbine generator as a motor is important for standalone energy storage provision (operating Mode C). The electric motor can use electricity from the grid to drive the compressor via the PSD independently from the HAWT operation.

Wind power generation systems predominantly use induction and synchronous generators [24]. The wind energy conversion types were outlined in Subsection 2.1.2, but were discussed only briefly. Figure 3:9 illustrates the wind conversion system, whereby the generator types are highlighted in blue.

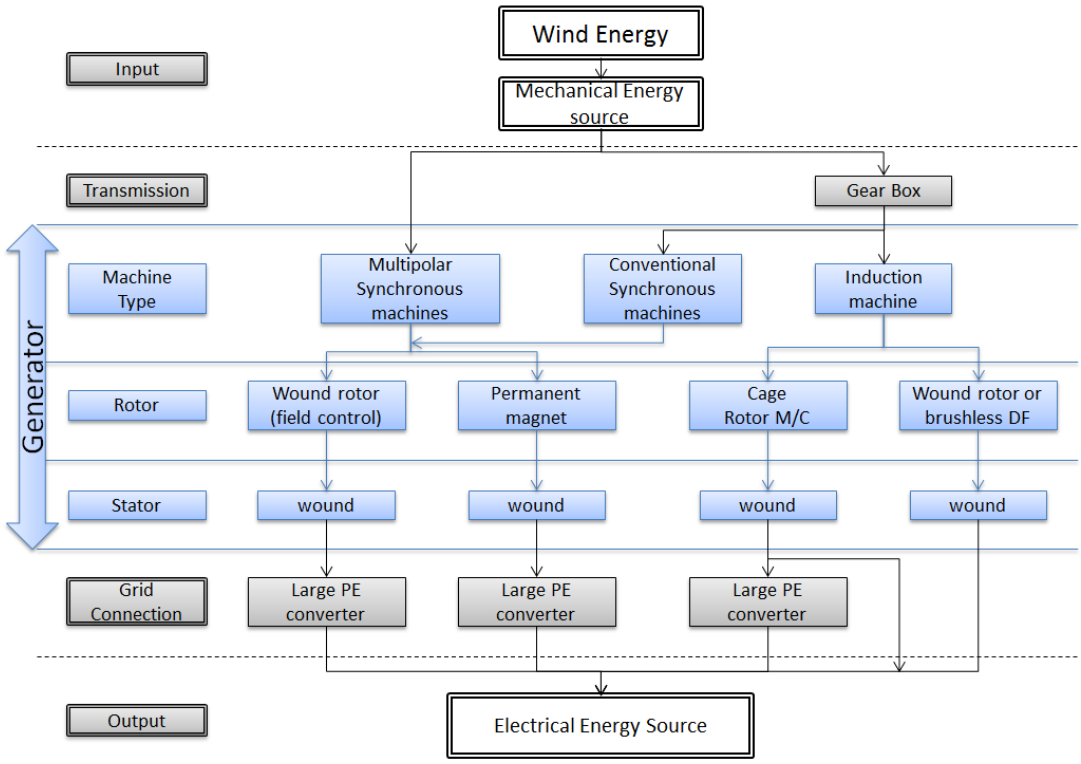


**Figure 3:9: Wind Energy Conversion Outline (PE: Power Electronics)**

The synchronous generator is classified by wound/electrically excited rotors (EESG) and permanent magnet rotors (PMSG), whereas the induction machine is classified by squirrel cage (SCIG) and wound rotor generators (WRIG). The benefits and disadvantages of the generator types with respect to wind power applications are listed in the Table 3:1.

**Table 3:1: Generator Comparison for Wind Turbine Applications [24, 103, 104]**

| *Generator Type* | *Advantage* | *Disadvantage* |
|---|---|---|
| EESG | - cheaper compared to PMSGs<br>- higher efficiency in generator mode compared to induction machines | - lower power density compared to PMSG<br>- needs field excitation circuitry |
| PMSG | - high efficiency<br>- no field excitation required<br>- can be used for direct drive (offsetting the need for gear boxes)<br>- improved thermal characteristic due to absence of field losses in rotor<br>- no slip rings, higher reliability<br>- Lighter than EESG, high power density | - higher costs due to permanent magnet material<br>- limited rare earth material used (neodymium)<br>- large in diameter if direct driven (large number of pole pairs)<br>- less mechanical damping compared to induction generator |
| SCIG | - robust, cheap and simple<br>- good performances of reactive power compensation<br>- smooth grid connection<br>- damps harmonic disturbances<br>- no brushes | - high losses due to full scale converter in comparison to synchronous machines<br>- gear box needed<br>- reactive power compensation required<br>- lower efficiency compared to synchronous machine<br>- poor voltage regulation |
| WRIG | - rotor energy can be fed back to the grid through converter<br>- damps harmonic disturbances | - excitation needed<br>- gear box needed<br>- losses through slip rings<br>- lower efficiency compared to synchronous machine<br>- poor voltage regulation |

Either of the types mentioned above is suitable for the hybrid wind turbine. However, since the PMSGs can be built to have high torque and low speed characteristics, they are suitable for direct drive applications. In the case of the hybrid wind turbine, lower rotational speeds and high torques are expected on the PSD's ring gear, so that a direct connection of the PMSG with the ring gear is sensible. The higher efficiency and absence of any excitation circuitry make the PMSG a suitable and favourable option for the hybrid wind turbine.

### 3.2.6 Storage

The main energy storage technologies were briefly discussed in Section 2.4, outlining the benefits and suitable applications for each technology. Potential storage technologies for the hybrid wind turbine application are batteries, flow batteries and CAES. Flow batteries and other electro-chemical batteries benefit from high energy densities, suitable scalability and descending costs in the future [105]. Additionally, efficient and proven electric machines (and associated drives) could be used for the aforementioned PSD's sun gear input. The main disadvantage of batteries is the limited cycle life and the limited discharge and charge ranges. Flow batteries can overcome this issue, but in contrast invoke more complicated control equipment such as pumps, instrumentation etc., which add maintenance costs and complexity to the design. Both electro-chemical batteries and flow batteries share the problems of the chemical waste disposal. In contrast, CAES offers scalability, low maintenance and low operational costs and provides an environmental friendly storage medium with long lasting life time [7]. The technology in conjunction with scroll air expanders/compressors is a proven concept which can be found in industrial applications [83]. The storage capacity depends on the volume and pressure of the stored medium, whereby storage vessels or underground caverns can be exploited. Compared to electro-chemical batteries, CAES has lower energy efficiencies due to thermal losses. However, the low efficiency drawback has not stopped the exploitation of CAES to work with renewable energy; this is due to its distinguished advantages. The project is particularly to explore how CAES can work with HAWTs.

### 3.2.7 Final Design

The proposed design is a novel combination of a HAWT, a scroll air expander/compressor in connection with CAES, a permanent magnet synchronous generator/motor (PMSG/PMSM) and a power split device (PSD) in the form of a planetary gear box. Figure 3:10 shows the design structure in block diagram.

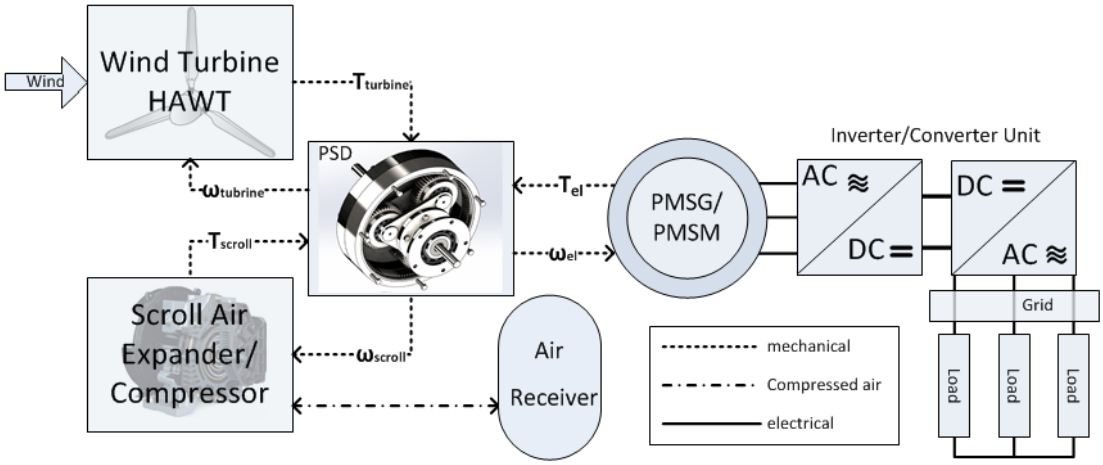


**Figure 3:10: Proposed Hybrid Wind Turbine Design Structure**

The PSD has three rotating shafts to be connected to the HAWT, the scroll air expander/compressor and the PMSG/PMSM. Torque can be added to the system via the scroll expander in moments of wind troughs and high electricity demand. In moments of excessive wind speeds, power can be extracted from the PSD to drive the compressor and to store compressed air. The hybrid wind turbine can operate in standalone mode, in which the HAWT drives the PMSG only. The inverter/converter unit enables maximum power point tracking (see Section 2.1.1). The Hybrid wind turbine can also work as a standalone energy storage system independently from the HAWT operation.

To sum up, the system offers more flexibility in operation, while reducing the amount of components needed. The system is simple and efficient with respect to the mechanical transmission. It also offers the possibility of intrinsic CAES through direct compression from the HAWT, thus eliminating the conversion from mechanical power to electrical power prior to the compression. The working principle and all possible operating modes are explained in the following section.

## 3.3 Working Principle and Operating Modes of the Hybrid Wind Turbine

The hybrid wind turbine benefits from its flexibility in operation. Three operating modes are identified, which can be further organised into two operating modes each. Figure 3:11 visualises the operating modes.

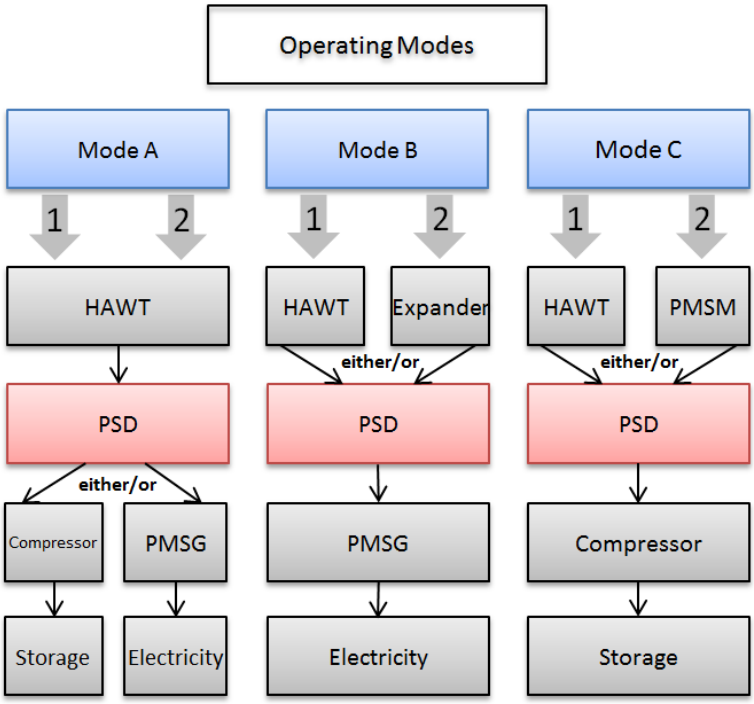


**Figure 3:11: Operating Modes of Hybrid Wind Turbine**

In *Mode A*, the HAWT can drive the compressor (Mode A1), the PMSG (Mode A2), or both at the same time (Mode A12). Regarding the Mode A12, the mechanical power from the HAWT is split between the compressor and the PMSG through the PSD. Mode A12 is applicable at times of power oversupply, so that excess power from the HAWT can be utilised to compress air. It can be seen that Mode A2 represents the standalone wind turbine with no engagement of the expander/compressor unit. In contrast, *Mode B* involves the air expander unit. The PMSG can be driven by the HAWT (Mode B1), by the air expander (Mode B2) or by both the HAWT and the air expander at the same time (Mode B12). It is clear that Mode B1 is the analogous to Mode A1. These modes will be referred to

as *Standalone Mode* from now on. Mode B12 is applicable in times of wind troughs and high electricity demand. The expander can add power to the system to meet the electricity demand or to smooth the power supply under fluctuating wind power. Furthermore, *Mode C* defines two operating modes in which the compressor is utilised. The compressor can be driven by the HAWT (Mode C1), the PMSM (Mode C2) or both the HAWT and the PMSM at the same time (Mode C12). Again, Mode C1 equals Mode A1 and they will be referred to as *Direct Compression Mode* from now on. Mode C12 is of interest when no electricity is needed. In fact, electricity can be drawn *from* the grid to drive the PMSM, which in turn drives the compressor.

Within all operating modes, the PSD is the enabling device. The rotational direction of the sun gear, planet carrier and ring gear are crucial to enable all operating modes. Table 3:2 shows the three operating modes by means of the PSD.

**Table 3:2: Operating Modes with Respect to the PSD**

| *Mode* | *Description* | *PSD* |
|---|---|---|
| Mode A | The sun gear, the ring gear and the planet carrier spin in the same direction. The HAWT, which is connected to the planet carrier ($\omega_c$) drives both the PMSG (ring gear $\omega_R$) and the compressor (sun gear $\omega_s$). If the HAWT drives the compressor alone, the PMSG must be mechanically locked. If the hybrid wind turbine operates in standalone mode, the air expander must be mechanically locked. | 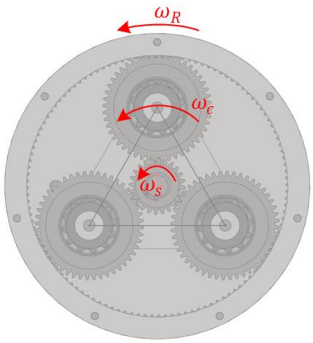 |
| Mode B | The difference to Mode A is that the compressor operates as an air expander. The PMSG is driven by the HAWT or/and by the expander. For that, the sun gear spins in reverse direction in comparison to Mode A. If the HAWT is at stand still and the expander drives the PMSG, then the HAWT needs to be secured against spinning backwards. The same applies to the air expander for the standalone mode. | 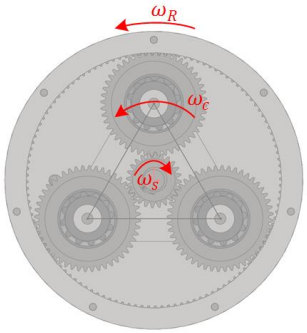 |
| Mode C | The PMSG becomes a PMSM and the rotational direction of its drive shaft changes. The HAWT can drive the compressor alone (direct compression operation) or the HAWT is supported by the PMSM. Likewise, the PMSM can drive the compressor alone if no wind is present. In that case, the HAWT must be locked against spinning backwards. | 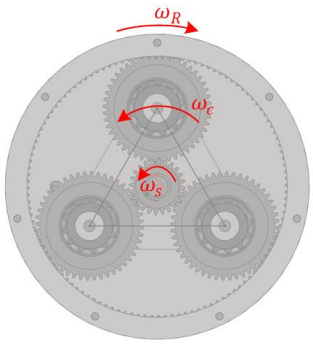 |

## *3.4 Summary*

Existing hybridisation systems regarding the combination of wind power and CAES were critically reviewed. Wind-diesel hybrid systems are commonly augmented with CAES to reach more flexible operation and to increase the exploitation of wind power.

Furthermore, wind turbines with hydraulic and pneumatic pumps along with hybrid wind turbines in connection with CAES and super-capacitors were investigated.

The proposed hybrid wind turbine structure with intrinsic CAES provision was then introduced, beginning with the investigation of flexible and efficient mechanical transmission mechanisms. The wind turbine structure comprises of a power split device in the form of a planetary gear box that merges the drive shaft of a Horizontal Axis Wind Turbine (HAWT), a Permanent Magnet Synchronous Generator/Motor (PMSG/PMSM), and a scroll expander/compressor machine. The hybrid wind turbine can operate in standalone mode, i.e. the direct connection of the wind turbine shaft with the generator, while exhibiting the opportunity to control the generator output power by engaging CAES. Additionally, the hybrid wind turbine offers standalone energy storage provision, meaning that the turbine generator can be operated as a motor to compress air for storage, while taking electricity from the grid.

Three main operating modes were introduced; a) Mode A: the HAWT drives the compressor (Mode A1), the PMSG (Mode A2), or both at the same time (Mode A12); b) Mode B: the PMSG is driven by the HAWT (Mode B1), by the air expander (Mode B2) or by both the HAWT and the air expander at the same time (Mode B12); c) Mode C: the compressor is driven by the HAWT (Mode C1), the PMSM (Mode C2) or both the HAWT and the PMSM at the same time (Mode C12).

# *Chapter 4 - Modelling Study of the Hybrid Wind Turbine*

The essential components to form the proposed hybrid wind turbine system are discussed in Chapter 3 and suitable components are selected. The focus of this chapter lies on the mathematical modelling of the hybrid wind turbine system. It begins with the description of the system components' mathematical model and ends with the overall hybrid wind turbine mathematical model.

In addition to the main components that are discussed in Chapter 3, further ancillary units such as the air pressure regulator, the heat exchanger and the VAWT as well as drive train dynamics are studied and the associated mathematical models are derived, which are explained in the Appendix C.

## *4.1 Scroll Air Expander*

The scroll air expander is one of the key components of the proposed hybrid system, since it is the device that converts the compressed air energy to mechanical energy to be added to the PSD. Dynamic mathematical modelling of scroll expanders and compressors is described in a number of publications such as [55-57, 106, 107], which enable a foundation for the modelling of the expander as well as the compressor. The modelling procedure is organised into mathematical descriptions of geometric, thermodynamic and associated mechanical working principles. The geometric modelling encompasses the shape of the spirals, and the volume of the chambers which are formed by the interactions of the two spirals. The geometric modelling is also relevant for the determination of the spiral's wall thicknesses. The thermodynamic modelling comprises the chamber air pressure and temperature variations as well as air mass flow calculations with respect to the scroll air

expander's angular movement. With the model derived, the driving torque can be obtained. Figure 4:1 shows a dismantled scroll air expander/compressor.

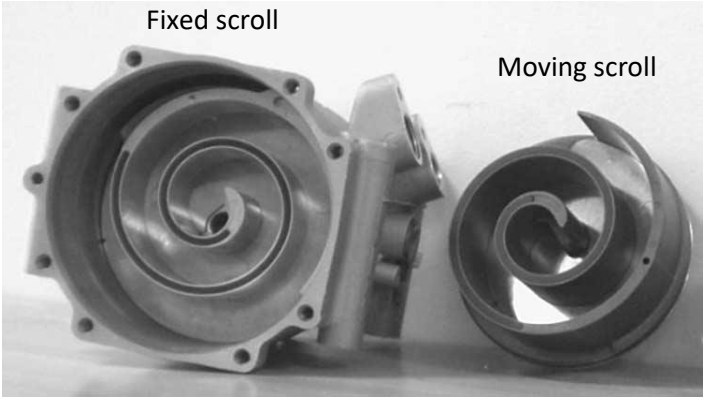


**Figure 4:1: Illustration of the mechanical structure of a Sanden Scroll TRSA09 [106]**

A scroll air expander consists of two scrolls - a fixed and a moving scroll. The moving scroll is connected to a crankshaft, allowing for eccentric motion following a fixed path with respect to the fixed scroll. While orbiting, the chamber volumes formed by the fixed and the moving scrolls are gradually increasing, beginning with the central chamber volume towards the exhaust chamber volume. The process repeats with every 360° rotation of the drive shaft. Comprehensive modelling study is reported in [56, 106], including geometric, thermodynamic and mechanical analysis. Therefore, the entire derivation of the scroll expander model will not be repeated in this thesis but a brief description of the modelling process is given. The scroll air expander used in the system is a modified Sanden TRSA09 *compressor* with 2.1 wraps, from which its internal reed-valve was removed. This valve acts as a spring-loaded non-return valve on the central orifice of the fixed scroll. The reed-valve has the purpose to prevent air flow back into the scroll compressor from the downstream high pressure reservoir if the compressor stops running. Removing this valve allows the air to flow in both directions and enables the expander operating mode.

The modelling work is based on the block diagram shown in Figure 4:2.

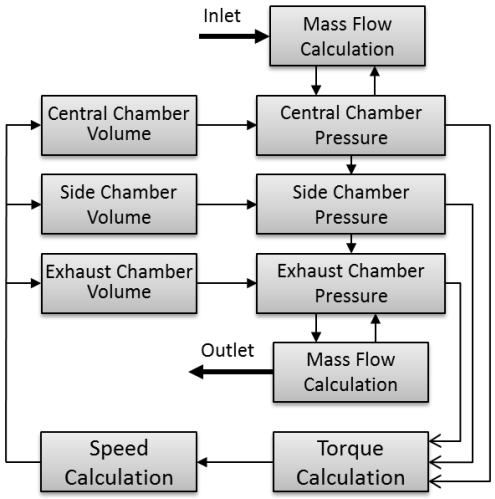


**Figure 4:2: Block diagram for Scroll Air Expander Mathematical Model**

The volume of each chamber needs to be found at every angle of the shaft rotation. Based on the volume and the air mass flow in and out of the scroll expander, the pressure in the chambers, and the resulting torque can be deduced. The torque leads to the eccentric movement of the moving scroll and results in shaft rotation, whereby the angular speed depends on the mechanical load connected to the scroll shaft. The resulting angular speed is then used to derive the angular position of the moving scroll so the chamber volumes can be calculated simultaneously. For this analysis, isothermal expansion is considered, due to the fact that temperature changes were found to have only a minor effect on the torque/speed characteristic of the expander in low pressure regions (1 to 5*bar*). For example, based on experimental results and exergy analysis, the reduction in output power was calculated to a maximum of 2.5% if polytropic expansion is considered instead of isothermal expansion. More information is given in the Appendix C.4. For the modelling work the following simplifications are made:

- Air leakage is ignored at this stage of analysis
- Heat transfer through the expander walls is neglected
- Ideal gas law holds
- Time invariant static and viscous friction coefficients are assumed

### A. Chamber Volume Calculation

Figure 4:3 shows the central shape of the spirals of a scroll expander with the orbit circle.

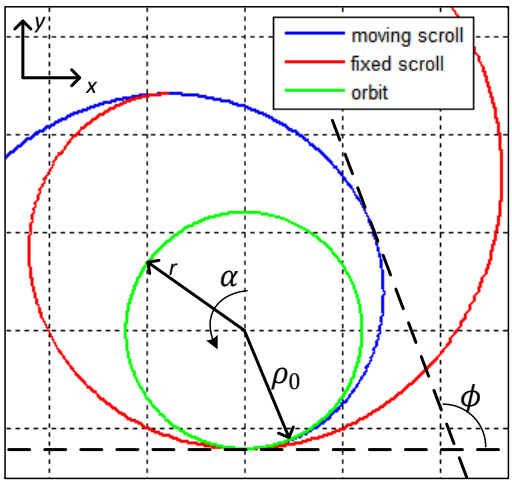


**Figure 4:3: Illustration of the Spiral**

With respect to the coordinate system illustrated in Figure 4:3, it can be shown that the following two equations can be derived for the *moving scroll* (subscript *m*) [106].

$$X_m(\phi,\alpha) = (\rho_0 + k\phi)sin\phi + kcos\phi - k + rsin\alpha \qquad \textbf{Eq. 4:1}$$

$$Y_m(\phi,\alpha) = -(\rho_0 + k\phi)cos\phi + ksin\phi + \rho_0 - rcos\alpha \qquad \textbf{Eq. 4:2}$$

with

| | | | |
|---|---|---|---|
| $X_m$ | = | X coordinate of curvature | $[m]$ |
| $Y_m$ | = | Y coordinate of curvature | $[m]$ |
| $\phi$ | = | Angle see Figure 4:3 | $[rad]$ |
| $\alpha$ | = | Orbit angle | $[rad]$ |
| $\rho_0$ | = | Initial radius of curvature | $[m]$ |
| $k$ | = | Opening value for curvature | $[-]$ |
| $r$ | = | Radius orbit | $[m]$ |

With the coordinates $X_m$ and $Y_m$, every point of the curvature can be described with respect to the rotating angle $\alpha$. Furthermore, the following two equations are used to determine the coordinates of the fixed scroll (subscript *f*):

$$X_f(\phi,\alpha) = (\rho_0 + k(\phi+\pi))\sin(\phi+\pi) + kcos(\phi+\pi) - k + rsin\phi \quad \textbf{Eq. 4:3}$$

$$X_f(\phi,\alpha) = -(\rho_0 + k(\phi+\pi))\cos(\phi+\pi) + kcos(\phi+\pi) + \rho_0 + rcos\phi \quad \textbf{Eq. 4:4}$$

The equations for the fixed and moving scroll are used to plot Figure 4:4, which illustrates a full cycle of the moving scroll in four moments beginning with $\alpha = 0$.

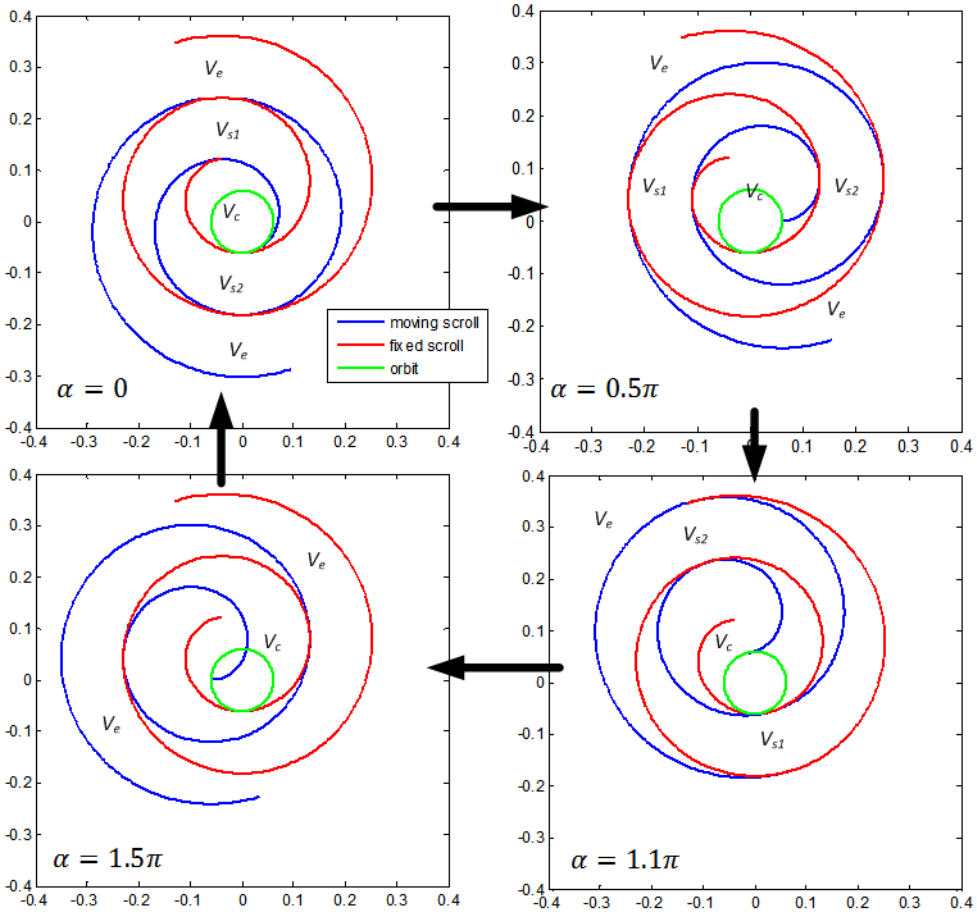


**Figure 4:4: Scroll Chamber Volume Changes**

The central chamber increases from $\alpha = 0$ to $\alpha = 2\pi$ at which the central chamber splits into two side chambers and a new central chamber is formed. The side chambers keep increasing until $\alpha = 1.1\pi$, where they reach the maximum volume and eventually merge with the exhaust chamber. For $1.1\pi < \alpha < 2\pi$, the side chambers can be considered non-existent. In contrast, the exhaust chambers reach their maximum chamber volume at $\alpha = 0$ and volume decreases from that point onwards. Note that the scroll air expander used in

this study comprises only one pair of side chambers. It can be shown that the volume of the central chamber, side chambers and exhaust chambers follow Eq. 4:5 to Eq. 4:7 [108].

$$V_c(\alpha) = z\Big[(kr - k^2\pi)cos\alpha + (kr\rho\pi - r\rho_0)sin\alpha + (kr\pi + 2k\rho\pi)\alpha + k^2\pi\alpha^2 - kr + \frac{1}{3}k^2\pi^3 - \frac{1}{2}kr\pi^2 + \rho r\pi + \frac{1}{2}r^2\pi + \rho^2\pi\Big] \quad \textbf{Eq. 4:5}$$

$$V_s(\alpha) = \pi r^2 + 2\pi r\big(\rho_0 + k(\alpha + \pi)\big) \quad \textbf{Eq. 4:6}$$

$$V_e(\alpha) = V_{total} - V_c(\alpha) - V_s(\alpha) \quad \textbf{Eq. 4:7}$$

with

| | | | |
|---|---|---|---|
| $z$ | = | Height of scroll walls | $[m]$ |
| $V_c$ | = | Central chamber volume | $[m^3]$ |
| $V_s$ | = | Total side chamber volume | $[m^3]$ |
| $V_e$ | = | Exhaust chamber volume | $[m^3]$ |
| $V_{total}$ | = | Total scroll expander volume | $[m^3]$ |

### *B. Chamber Air Pressure Calculation*

The air pressure in the chambers are associated with the air mass flow rate $\dot{m}$, the rate of volume changes $\dot{V}$ and the chamber air temperature $T$, described by the following three equations [108].

$$\dot{p}_c = \frac{1}{V_c}\left(\dot{m}_c R T_c - \dot{V}_c p_c\right) \quad \textbf{Eq. 4:8}$$

$$\dot{p}_s = \frac{1}{V_s}\left(-\dot{V}_s p_s\right) \quad \textbf{Eq. 4:9}$$

$$\dot{p}_e = \frac{1}{V_e}\left(\dot{m}_e R T_e - \dot{V}_e p_e\right) \quad \textbf{Eq. 4:10}$$

with $p_i$ being the air pressure inside the respective chamber. For example, the air pressure in the central chamber increases as air enters the central chamber. However, at the same time the air pressure tends to decrease due to the fact that the chamber volume increases as the scroll expander's shaft rotates. For the calculation of the air mass flow rate it is resorted to the orifice theory [109].

$$\dot{m}_i = A_i \frac{c_d c_0 p_u}{\sqrt{T}} f(p_u, p_d) \qquad \textbf{Eq. 4:11}$$

$$f(p_u, p_d) = \begin{cases} 1 & , \frac{p_d}{p_u} \leq c_r \\ c_k \left( \left(\frac{p_d}{p_u}\right)^{\frac{2}{\gamma}} - \left(\frac{p_d}{p_u}\right)^{\frac{\gamma+1}{\gamma}} \right)^{\frac{1}{2}} & , \frac{p_d}{p_u} < 1 \end{cases} \qquad \textbf{Eq. 4:12}$$

with

| | | | |
|---|---|---|---|
| $\dot{m}_i$ | = | Air mass flow rate | $[kg/s]$ |
| $A_i$ | = | Orifice opening | $[m^3]$ |
| $c_d$ | = | Discharge coefficient see Appendix D | $[-]$ |
| $c_0$ | = | Flow constant see Appendix D | $[-]$ |
| $T$ | = | Temperature | $[K]$ |
| $p_u$ | = | Upstream pressure | $[Pa]$ |
| $p_d$ | = | Downstream pressure | $[Pa]$ |
| $c_k$ | = | 3.864 see Appendix D | $[-]$ |
| $\gamma$ | = | Ratio of specific heats | $[-]$ |
| $c_r$ | = | 0.528 see Appendix D | $[-]$ |

### *C. Driving Torque Calculation*

The total driving torque generated by the scroll expander dependents on the pressure difference across the adjacent chambers from the central chamber towards the exhaust

chamber, and the depth of the scroll. The principle of torque generation is illustrated in Figure 4:5, whereby the orbit angle $\alpha$ is set to *0*.

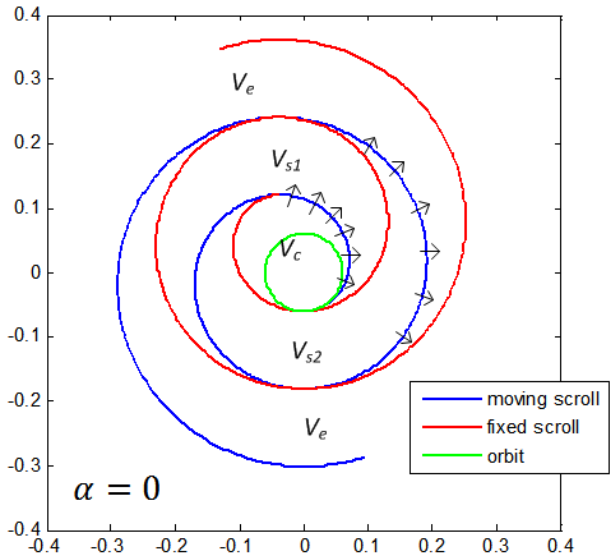


**Figure 4:5: Illustration of driving chambers for torque derivation**

It can be seen that forces act only on the segments of the moving scroll, which are defined by a pressure difference greater than zero in adjacent chambers ($V_c \rightarrow V_{s1}$and $V_{s2} \rightarrow V_e$). It can be shown that the final torque follows the Eq. 4:13 [108].

$$\tau_{scroll}(\alpha) = \sum zr(2\rho_0 + 2k\alpha + (4j+1)k\pi)\Delta p \qquad \textbf{Eq. 4:13}$$

with

| | | | |
|---|---|---|---|
| $\tau_{scroll}$ | = | Overall driving torque | $[Nm]$ |
| $\Delta p$ | = | Pressure difference across driving segments | $[Pa]$ |
| $j$ | = | Counter, number of driving segments | $[-]$ |

The counter $j$ increases from *0* with the number of driving segments. In the case of the scroll air expander/compressor used in this study, only two driving segments occur at the same time. Therefore, $j = 0{,}1$.

## *4.2 Scroll Air Compressor*

The dynamic mathematical modelling process of the scroll compressor closely resembles the model of the scroll expander. Only minor changes are conducted to derive the compressor's mathematical model. These changes include:

a) Reversed order of the volume calculation of all chambers
b) Compression instead of expansion; air pressure and temperature increase
c) Discharge chamber (central chamber) volume depends on the reed valve position and, therefore, the compression ratio is affected by it
d) Suction occurs in the intake chamber

Regarding point c); the reed valve was removed from the scroll air compressor to allow for the expander operation. The reed valve's position, however, is crucial to the compressor performance. Removing it and replacing it by an ordinary non-return valve at the outlet of the scroll machine makes the device functional as a compressor; however, the discharge volume is significantly increased which affects the compression ratio and, therefore, the maximum achievable downstream air pressure. Furthermore, two compression cycles occur for the scroll compressor as it undergoes one full movement around the orbit. These are the compression within the side chambers and the compression within the central chamber. To compress the air from the side chambers to the outlet, more than one full revolution is required.

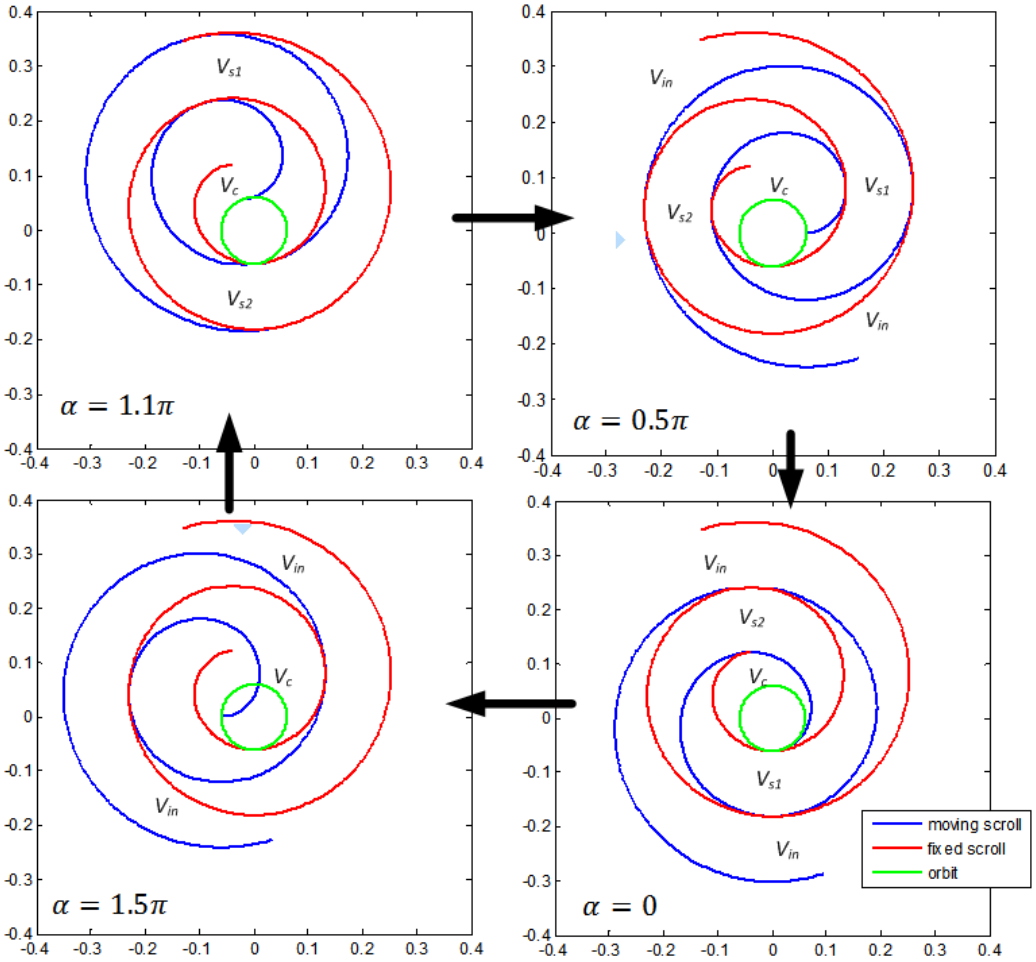


**Figure 4:6: Scroll Compression Illustration**

Figure 4:6 illustrates the compression cycle of the scroll air compressor at four different angular positions. Beginning at $\alpha = 1.1\pi$, the side chambers are at the state of maximum volume. The scroll air compressor is now driven clockwise (the opposite direction in comparison to the expander's motion), meaning that the side chamber volumes reduce in size and continuously compress air. At the angle $\alpha = 0$, the side chambers are about to merge with the central chamber, whereupon the central chamber keeps compressing the air. From that point onwards, the side chambers do not exist anymore. The intake chamber increases continuously, which means that air is being sucked in. At $\alpha = 3.1\pi = 1.1\pi$, new side chambers are created and the central chamber keeps compressing the air that was compressed by the side chambers in the previous cycle. As soon as the air pressure in the

central chamber exceeds the downstream pressure and the torsional stiffness of the reed valve, the valve opens and air streams out towards the air receiver.

The equations for the chamber volumes can be reused from the expander model, whereby the sign of the angle $\alpha$ is reverted:

$$V_c(\alpha) = z\Big[(kr - k^2\pi)\cos(-\alpha) + (kr\rho\pi - r\rho_0)\sin(-\alpha) - (kr\pi + 2k\rho\pi)\alpha + k^2\pi\alpha^2 - kr + \frac{1}{3}k^2\pi^3 - \frac{1}{2}kr\pi^2 + \rho r\pi + \frac{1}{2}r^2\pi + \rho^2\pi\Big] \quad \textbf{Eq. 4:14}$$

$$V_s(\alpha) = \pi r^2 + 2\pi r\big(\rho_0 + k(-\alpha + \pi)\big) \quad \textbf{Eq. 4:15}$$

$$V_{in}(\alpha) = V_{total} - V_c(\alpha) - V_s(\alpha) \quad \textbf{Eq. 4:16}$$

Based on the volume calculations, the air pressure and temperature in each chamber can be calculated, whereby only the side chambers and the central chamber account for compression. The pressure in the intake chamber decreases below the ambient pressure so that air is sucked in as the scroll compressor shaft rotates. Before the thermodynamic modelling work is described, the following simplifications are made:

- Air leakage is small enough to be ignored
- Polytropic compression holds
- Temperature change during suction is neglected

The air pressure in the intake, side and central chambers are derived. In Eq. 4:17 to Eq. 4:19, the subscript *in, s* and *c* stand for the intake, side and central chamber respectively.

$$\dot{p}_{in} = \frac{1}{V_{in}}\big(\dot{m}_{in}RT_{in} - \dot{V}_{in}p_{in}\big) \quad \textbf{Eq. 4:17}$$

$$\dot{p}_s = \frac{1}{V_s}\big(m_sR\dot{T}_s - \dot{V}_sp_s\big) \quad \textbf{Eq. 4:18}$$

$$\dot{p}_c = \frac{1}{V_c}\left(-\dot{V}_c p_c + m_c R\dot{T}_c - \dot{m}_{out} R T_c\right) \quad \textbf{Eq. 4:19}$$

whereby the mass $m_s, m_c$ can be derived from the ideal gas law ($PV = mRT$). The subscript $out$ stands for *outlet*. To solve Eq. 4:18 and Eq. 4:19, the change in temperature is required. In an ideal polytropic process the following is yielded:

$$T_s(V_s) = \left(\frac{V_{s,max}}{V_s(\alpha)}\right)^{n-1} T_{in} \quad \textbf{Eq. 4:20}$$

$$T_c(V_c) = \left(\frac{V_{c,max}}{V_c(\alpha)}\right)^{n-1} T_{s,\alpha=0} \quad \textbf{Eq. 4:21}$$

with $n$ defining the polytropic index. $T_{in}$ describes the constant temperature of the inlet air. $T_{s,\alpha=o}$ defines the temperature of the air at the moment when the side chambers merge with the central chamber. $V_{s,max}$ and $V_{c,max}$ are the maximum volume of the side chamber and central chamber, respectively. However, Eq. 4:20 and Eq. 4:21 describe an ideal steady state process. To satisfy Eq. 4:18 and Eq. 4:19, the derivative of Eq. 4:20 and Eq. 4:21 is taken with respect to time as described by Eq. 4:22 and Eq. 4:23:

$$\dot{T}_s(V_s) = -(n-1)V_{s,max}\left(\frac{V_{s,max}}{V_s(\alpha)}\right)^{n-2} T_{in}\frac{\dot{V}_s}{V_s^2} \quad \textbf{Eq. 4:22}$$

$$\dot{T}_c(V_c) = -(n-1)V_{c,max}\left(\frac{V_{c,max}}{V_c(\alpha)}\right)^{n-2} T_s\frac{\dot{V}_c}{V_c^2} \quad \textbf{Eq. 4:23}$$

The torque equation remains unchanged in comparison to the scroll expander model, but is given again below for convenience:

$$\tau_{scroll}(\alpha) = \sum zr(2\rho_0 + 2k\alpha + (4j+1)k\pi)\Delta p \quad \textbf{Eq. 4:24}$$

## *4.3 Compressed Air Storage*

It is necessary to study the thermodynamic characteristics of compressed air energy storage during the charging/discharging process. Solutions for the storage temperature and pressure variations are derived from the energy conservation equations, whereby isentropic storage can be assumed [110]. Consider a constant storage volume *V* and air flows in and out at quasi-equilibrium conditions which will increase/decrease the stored air pressure, whereby the pressure and temperature is evenly distributed in the reservoir. Assuming the storage walls as the boundary of the control volume and applying the mass and energy conservation equations, the following equations are obtained [110]:

$$V\left(\frac{d\rho}{dt}\right) = \dot{m}_{in} + \dot{m}_{out} \qquad \textbf{Eq. 4:25}$$

$$V\left(\frac{d(\rho e)}{dt}\right) = \dot{m}_{in}\left(h_{in} + \frac{v_{in}^2}{2} + gz_{in}\right) + \dot{m}_{out}\left(h_{out} + \frac{v_{out}^2}{2} + gz_{out}\right) \qquad \textbf{Eq. 4:26}$$

where:

$$e = u + \frac{v^2}{2} + gz \qquad \textbf{Eq. 4:27}$$

with:

| | | | |
|---|---|---|---|
| $V$ | = | Storage volume | $[m^3]$ |
| $\dot{m}$ | = | Air mass flow rate | $[kg/s]$ |
| $\rho$ | = | Air density | $[kg/m^3]$ |
| $e$ | = | Specific energy of storage air | $[J/kg]$ |
| $h$ | = | Specific enthalpy | $[J/kg]$ |
| $v_i$ | = | Specific air velocity | $[m/kgs]$ |
| $g$ | = | Acceleration of gravity | $[m/s^2]$ |
| $u$ | = | Specific internal energy | $[J/kg]$ |
| $z$ | = | Elevation | $[m]$ |

The subscript *in* denotes the inlet air conditions and the subscript *out* stands for the outlet air conditions of the control volume. Furthermore, Eq. 4:28 describes the ideal gas law and Eq. 4:29 shows the derivative of the product $\rho e$, whereby it can be assumed that $e$ equals $u$ for the reasons that the height $z$ can be neglected and the velocity of air has a negligibly small effect as shown in [110].

$$p = \rho RT \qquad \textbf{Eq. 4:28}$$

$$\frac{d(\rho e)}{dt} = \rho\left(\frac{du}{dt}\right) + u\left(\frac{d\rho}{dt}\right) = \rho c_v\left(\frac{dT}{dt}\right) + u\left(\frac{d\rho}{dt}\right) \qquad \textbf{Eq. 4:29}$$

where $c_v$ is the specific heat at constant volume. If Eq. 4:29 is substituted into Eq. 4:26, the following is yielded:

$$V\left(\rho\left(\frac{du}{dt}\right) + u\left(\frac{d\rho}{dt}\right)\right) = \dot{m}_{in}\left(h_{in} + \frac{v_{in}^2}{2} + gz_{in}\right) + \dot{m}_{out}\left(h_{out} + \frac{v_{out}^2}{2} + gz_{out}\right) \qquad \textbf{Eq. 4:30}$$

If Eq. 4:25 is put into Eq. 4:30, the following can be deduced:

$$V\rho\left(\frac{du}{dt}\right) + u(\dot{m}_{in} + \dot{m}_{out}) = \dot{m}_i\left(h_{in} + \frac{v_{in}^2}{2} + gz_{in}\right) + \dot{m}_{out}\left(h_{out} + \frac{v_{out}^2}{2} + gz_{out}\right) \qquad \textbf{Eq. 4:31}$$

Knowing that

$$u = h - pv \qquad \textbf{Eq. 4:32}$$

with $v$ being the specific volume, Eq. 4:31 can be rearranged and extended with Eq. 4:32 and Eq. 4:28 to the following:

$$V\rho c_v\left(\frac{dT}{dt}\right) = \dot{m}_{in}\left(h_{in} - h + RT + \frac{v_{in}^2}{2} + gz_{in}\right) + \dot{m}_{out}\left(h_{out} - h + \frac{v_{out}^2}{2} + gz_{out} + RT\right) \qquad \textbf{Eq. 4:33}$$

with $h_{in} - h = c_p(T_{in} - T)$ and $h_{out} - h = c_p(T_{out} - T)$ and $c_p$ being the specific heat at constant pressure. $T$ is the temperature in the storage reservoir. $T_{in}$ is the temperature of the incoming air, whereby $T_{out}$ is the temperature of the outgoing air from the reservoir. In fact, $T$ and $T_{out}$ are the same. The kinetic and potential energy part of the air can be neglected, due to the little impact brought to system as is shown in [110]. Eq. 4:33 can be simplified to:

$$\frac{dT}{dt} = \frac{1}{V\rho c_v}\left(\dot{m}_{in}\left(c_p(T_{in} - T) + RT\right) + \dot{m}_{out}RT\right) \qquad \textbf{Eq. 4:34}$$

With Eq. 4:34, the temperature in the reservoir can be computed as air enters and leaves the storage reservoir, and with help of Eq. 4:28 the pressure in the reservoir can be obtained. Note that because $\dot{m}_{out}$ leaves the reservoir it must have a negative sign.

## *4.4 Permanent Magnet Synchronous Generator*

The permanent magnet synchronous generator (PMSG) converts the mechanical energy into electrical energy. The mathematical model can be deduced from simplified equivalent circuit diagrams (see Figure 4:8), whereby the circuitry is converted to the commonly used d-q coordinate system, which is a two-phase equivalent representation of the three-phase system. The methodology is explained in the following based on Figure 4:7.

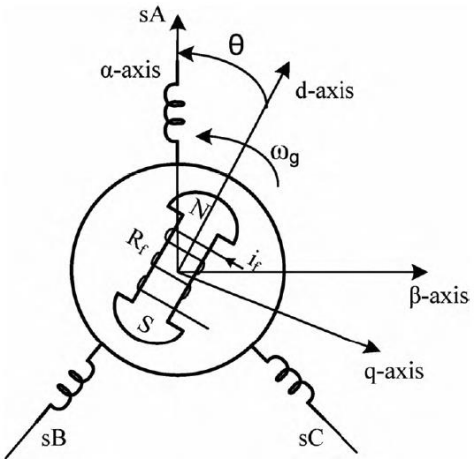


**Figure 4:7: d-q and α-β reference frame for a electrical synchronous machine [111]**

The α-β reference frame is a fixed two-phase coordinate system obtained from the three-phase stator winding (*sA, sB, sC*) via the well-known *clarke transformation*. The method is based on the fact that by having two voltages, the third voltage can be worked out. The *clarke transformation* is not discussed in this research. The d-q transformation, also known as *park transformation*, is used to transform the fixed α-β coordinate system into a coordinate system that is fixed to the moving rotor's coordinate system. The d-axis is positioned along the magnetic field direction of the rotor and the q-axis is perpendicular to the d-axis. The following simplifications are made:

- Linear magnetising characteristics
- Symmetric stator winding
- No iron losses

Based on the d-q coordinate system, the following two equivalent circuit diagrams can be deduced, shown in Figure 4:8 [111].

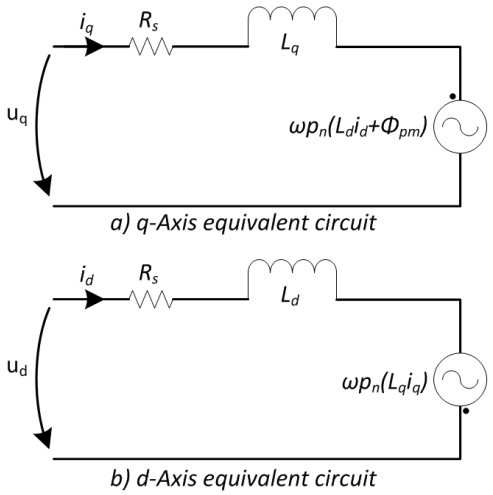


**Figure 4:8: Equivalent circuit diagrams in the d,q- reference frame**

Applying Kirchhoff's voltage law, the following two equations can be derived [111]:

$$u_q = R_s i_q + L_q \left(\frac{di_q}{dt}\right) + \omega p_n (L_d i_d + \Phi_{\mathrm{pm}}) \qquad \textbf{Eq. 4:35}$$

$$u_d = R_s i_d + L_d \left(\frac{di_d}{dt}\right) - \omega p_n L_q i_q \qquad \textbf{Eq. 4:36}$$

with:

| | | | |
|---|---|---|---|
| $u_{d,q}$ | = | Voltage in d and q frame | $[V]$ |
| $R_s$ | = | Armature resistance | $[\Omega]$ |
| $i_{d,q}$ | = | Current in d and q frame | $[A]$ |
| $L_{d,q}$ | = | Inductance in d and q frame | $[H]$ |
| $\Phi_{\mathrm{pm}}$ | = | Magnetic flux | $[Wb]$ |
| $\omega$ | = | Mechanical angular speed | $[rad/s]$ |
| $p_n$ | = | Number pole pairs | $[-]$ |

If Eq. 4:35 and Eq. 4:36 are rearranged to the highest derivative, the following equations are yielded:

$$\frac{di_q}{dt} = \frac{1}{L_q}(u_q - R_s i_q - \omega p_n (L_d i_d + \Phi_{\mathrm{pm}})) \qquad \textbf{Eq. 4:37}$$

$$\frac{di_d}{dt} = \frac{1}{L_d}\left(u_d - R_s i_d + \omega p_n L_q i_q\right) \qquad \textbf{Eq. 4:38}$$

If a star connected resistive load is considered for the generator, the equations above can be rearranged to obtain the voltage derivatives.

$$\frac{du_q}{dt} = \frac{R_l}{L_q}\left(-u_q\left(1+\frac{R_s}{R_l}\right) - \omega L_d p_n \frac{u_d}{R_l} + \omega_{gen} p_n \Phi_{\mathrm{pm}}\right) \quad \textbf{Eq. 4:39}$$

$$\frac{du_d}{dt} = \frac{R_l}{L_d}\left(-u_d\left(1+\frac{R_s}{R_l}\right) + \omega L_q p_n \frac{u_q}{R_l}\right) \quad \textbf{Eq. 4:40}$$

with $R_l$ being the resistive load applied to the generator. Furthermore, the torque required to rotate the generator can be expressed by Eq. 4:41.

$$\tau_{gen} = \frac{3}{2} p_n\left(\Phi_{\mathrm{pm}} i_q + \left(L_d - L_q\right) i_q i_d\right) \quad \textbf{Eq. 4:41}$$

Measurements on the PMSG in use showed that $L_d \approx L_q$ so that Eq. 4:41 can be simplified to:

$$\tau_{gen} = \frac{3}{2} p_n \Phi_{\mathrm{pm}} i_q \quad \textbf{Eq. 4:42}$$

From Eq. 4:42, it can be seen that the torque is proportional to the current in the q-axis.

To sum up, the input of the model is torque and the output is the voltage in d- and q-coordinates, which can be converted to the three-phase stator voltages in its original real coordinate system.

## *4.5 Permanent Magnet Synchronous Motor*

The mathematical model for the Permanent Magnet Synchronous Motor (PMSM) is equivalent to the PMSG model described in the previous section. The difference is that the input for the PMSM is electrical energy with the input variable of voltage which leads to a mechanical torque output. In contrast, the generator requires driving torque as the input, whereby electrical energy is generated with voltage as the output variable. Therefore, Eq.

4:37, Eq. 4:38 and Eq. 4:42 can be utilised to model the PMSM. The PMSM needs to be controlled in both simulation and practice. Since the model based on Eq. 4:37 and Eq. 4:38 requires the voltages described in d-and q-coordinates, the *park-clarke transformation* is necessary to convert the three-phase stator voltages to the voltages described in d-q coordinates. The control strategy chosen to obtain three-phase voltages for the stator winding is the commonly used *U/f=const.* method. This open loop control is based on the idea that the ratio of voltage and frequency is constant until the rated speed (e.g. 50Hz) is reached. Figure 4:9 visualises the idea.

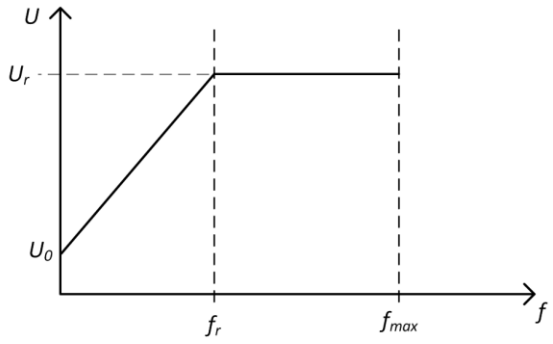


**Figure 4:9: *U/f=const*. diagram**

From Figure 4:9 the following is yielded:

$$\begin{cases} U = \dfrac{U_r - U_0}{f_r} f + U_0 & , f < f_r \\ U = U_r & , f > f_r \end{cases} \qquad \textbf{Eq. 4:43}$$

with:

| | | | |
|---|---|---|---|
| $U$ | = | RMS stator voltage | $[V]$ |
| $U_r$ | = | RMS rated stator voltage | $[V]$ |
| $U_0$ | = | Offset, usually 5% of $U_r$ | $[V]$ |
| $f$ | = | Frequency | $[Hz]$ |
| $f_r$ | = | Rated frequency | $[Hz]$ |

The stator windings have three phases with a phase angle of 120° between them as described by the following three equations:

$$U_a = Usin(\theta) \quad \textbf{Eq. 4:44}$$

$$U_b = Usin(\theta + 2/3\pi) \quad \textbf{Eq. 4:45}$$

$$U_c = Usin(\theta - 2/3\pi) \quad \textbf{Eq. 4:46}$$

with

$$\theta = \int_0^t 2\pi f dt \quad \textbf{Eq. 4:47}$$

## *4.6 Horizontal Axis Wind Turbine*

HAWTs extract kinetic energy from wind and turn it into mechanical energy. The amount of energy that can be converted from wind energy to available mechanical energy is expressed through the turbine power coefficient $C_p$, which is limited to a maximum of 59.3% according to the Betz Limit [99]. A common expression for modelling a wind turbine is given in Eq. 4:48 [112].

$$P_t = C_p(\lambda, \beta)\frac{1}{2}\rho R^2 \pi v_w^3 \quad \textbf{Eq. 4:48}$$

$$\lambda = \frac{\omega_t R}{v_w} \quad \textbf{Eq. 4:49}$$

with

| | | | |
|---|---|---|---|
| $P_t$ | = | Mechanical power | $[W]$ |
| $C_p$ | = | Power coefficient | $[-]$ |
| $\lambda$ | = | Tip speed ratio[5] | $[-]$ |
| $\beta$ | = | Blade pitch angle | $[°]$ |
| $\rho$ | = | Air density | $[kg/m^3]$ |
| $R$ | = | Rotor radius | $[m]$ |
| $v_w$ | = | Wind speed | $[m/s]$ |
| $\omega_t$ | = | Angular speed turbine rotor | $[rad/s]$ |

[5] TSR: the ratio of tangential rotor tip speed and incoming wind speed

The power coefficient $C_p$ requires aerodynamic knowledge and is calculated numerically. A generic equation is used to model the power coefficient, shown in Eq. 4:50 [112].

$$C_p(\lambda,\beta) = 0.5176\left(\frac{116}{\lambda} - 0.4\beta - 5\right)e^{-\frac{21}{\lambda_i}} + 0.0068\lambda \qquad \textbf{Eq. 4:50}$$

$$\lambda_i = \frac{1}{\lambda + 0.08\beta} - \frac{0.035}{\beta^3 + 1} \qquad \textbf{Eq. 4:51}$$

Figure 4:10 shows the power coefficient versus the tip speed ratio.

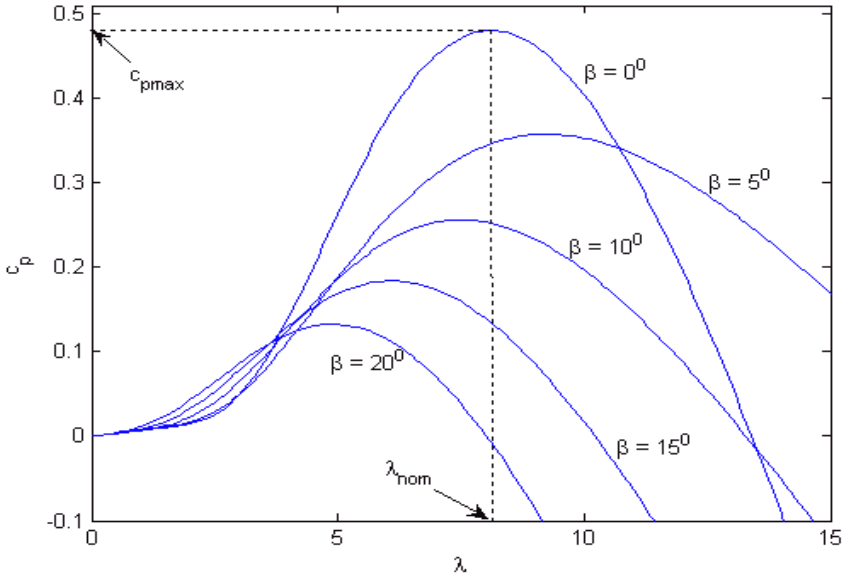


**Figure 4:10: $C_p$ Power coefficient with respect to the tip speed ratio λ [112]**

It can be seen that the power coefficient is a function of both tip speed ratio and blade pitch angle. It can be seen that the maximum power coefficient decreases as soon as the pitch angle is changed from 0°. As described in Section 2.1, the pitch angle control is only used at high wind speeds to maintain the rated power output and to protect the wind turbine from excessive rotational speeds. For every wind speed, a corresponding maximum power coefficient can be found with respect to the turbine's rotational speed. Based on Eq. 4:48, the turbine torque $T_t$ can be extracted if the angular speed $\omega_t$ is known (see Eq. 4:52).

$$T_t = P_t/\omega_t \qquad \text{Eq. 4:52}$$

## 4.7 DC Motor

Two permanent magnet DC motors are employed on the experimental test rig to mimic a HAWT. The dynamic mathematical model of the DC motor is well understood and described based on [113]. Figure 4:11 shows a simplified physical model of a permanent magnet DC motor.

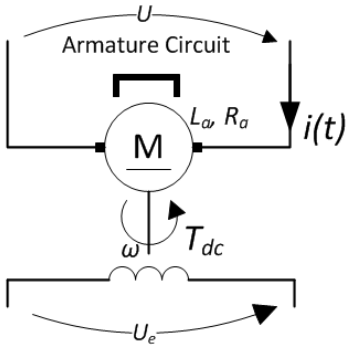


**Figure 4:11: Physical Model of a Permanent Magnet DC Motor**

A Voltage $U$ is applied to the armature winding. The armature windings are represented by a resistance $R_a$ and an inductance $L_a$ in series connection. As the DC motor rotates, it will also generate a back *emf*[6] in the form of a voltage $U_e$, which is proportional to the angular velocity and which opposes $U$. It is assumed that the magnetic field of the permanent magnet material is constant. Therefore, the torque of the motor is proportional to the armature current $i(t)$. Furthermore, the rotor and shaft are assumed to be rigid. The raise in temperature is neglected, and time-invariant viscous friction for the rotor shaft rotation can be assumed. Based on these simplifications, the mathematical model can be deduced. Eq. 4:53 shows the Kirchhoff's voltage law applied to the armature circuit.

$$U = R_a i + L_a\left(\frac{di}{dt}\right) + k_{dc}\omega \qquad \text{Eq. 4:53}$$

[6] emf – electromotive force

$$U_e = k_{dc}\omega \qquad \textbf{Eq. 4:54}$$

with:

| | | | |
|---|---|---|---|
| $U$ | = | Applied voltage | $[V]$ |
| $R_a$ | = | Armature resistance | $[\Omega]$ |
| $i$ | = | Armature current | $[A]$ |
| $L_a$ | = | Armature inductance | $[H]$ |
| $k_{dc}$ | = | Torque constant | $[Nm/A]$ |
| $\omega$ | = | Angular speed | $[rad/s]$ |
| $U_e$ | = | Back-emf | $[V]$ |

The driving torque is proportional to the armature current and is depicted in Eq. 4:55.

$$T_{dc} = k_{dc}i \qquad \textbf{Eq. 4:55}$$

The torque of the DC motor can be controlled to mimic the behaviour of a chosen HAWT.

## *4.8 Planetary Gearbox – Power Split Device*

The operating modes of the PSD were introduced in Section 3.3. In order to mathematically model the mechanics of the PSD it is resorted to the lever analogy [114]. In this section, the working principle, the kinematics and the system dynamics are explained in detail.

### *A. Working Principle of the PSD*

The structure of the drive train and the planetary gear box used in this study is shown in Figure 4:12.

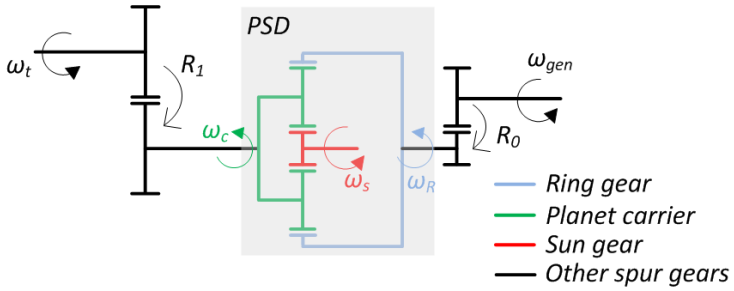


**Figure 4:12: Structure of planetary gear box**

As it can be seen in Figure 4:12; the PSD has three main shafts (highlighted in green, red and blue). The sun gear is connected to the scroll air expander/compressor (labelled by its speed $\omega_s$) and can serve as either input or output. The wind turbine ($\omega_t$) is connected to the planet carrier ($\omega_c$) via a gear transmission with the transmission ratio $R_1$. The ring gear ($\omega_R$) is connected to the generator ($\omega_{gen}$) via a further gear transmission with the ratio $R_0$. The ring gear can serve as both input (PMSM drives the ring gear) and output (PMSG is driven by ring gear). Note that the size of the gear ratios and the rotational directions of the shafts in Figure 4:12 are indicated qualitatively only. The gear transmission ratios $R_1$ and $R_0$ are integrated to better match the test rig components regarding their torque/speed characteristics (more information is given in Section 5.3).

The operating modes of the hybrid wind turbine are explained in Section 3.3. These modes are defined by the rotational direction of the sun gear, the planet carrier shaft and the ring gear. For a more detailed illustration, the operating mode B12 (HAWT and scroll expander drive the PMSG together) and operating mode A12 (the HAWT drives both the scroll compressor and PMSG) are explained in the following. Figure 4:13 shows the operating principle and the kinematics for mode B12. The kinematics are illustrated by means of the lever analogy [114], which is shown on the left hand side in Figure 4:13.

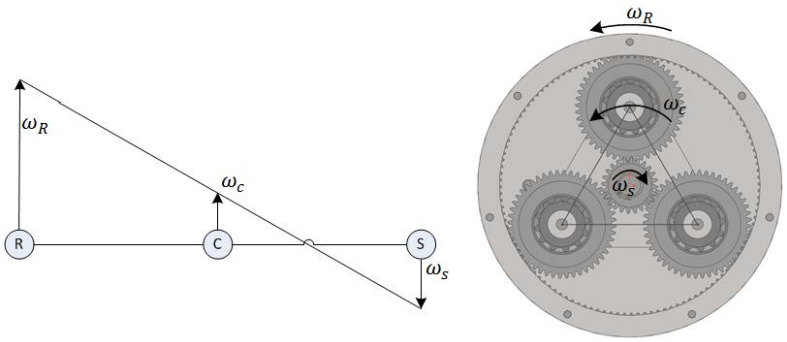


**Figure 4:13: Kinematics of PSD for Operating Mode B12 (HAWT and Scroll Expander drive PMSG)**

The sun gear (S) spins in the opposite direction compared to the planet carrier (C) and the ring gear (R). With the planet carrier and the sun gear providing torque input, it is clear that the faster the sun gear spins, the faster the ring gear will spin (indicated by the length of the arrows on the left hand side in Figure 4:13), whereby the planet carrier is used as a counter lever in the form of torque. Likewise, if the planet carrier's angular speed is increased, so will the ring gear increase in angular speed, while the sun gear provides the counter lever torque.

Concerning the operating mode A12, the scroll air compressor becomes driven so that the sun gear spins in the same direction as the ring gear and planet carrier.

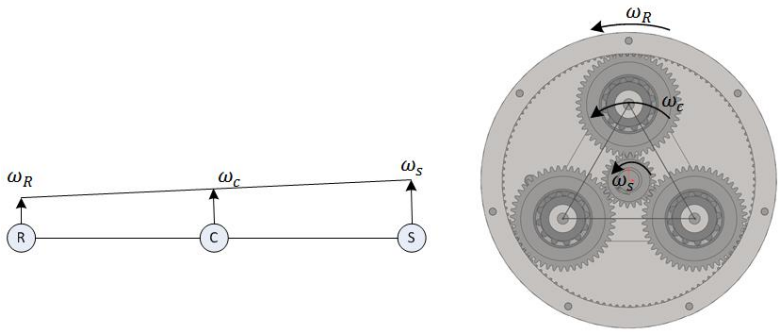


**Figure 4:14: Kinematics of PSD for Operating Mode A12 (the HAWT drives Scroll Compressor and PMSG)**

From Figure 4:14 it can be seen that all components spin in the same direction. The torque input is given to the planet carrier (C) only, whereas the ring gear (R) and the sun gear (S) become outputs. If the planet carrier's angular speed is increases, so will the ring gear and

the sun gear increase their angular speed. The magnitude of the sun gear's and the ring gear's angular speed depends on their load torques. For example, if the ring gear was held stationary, then the sun gear would be driven solely by the planet carrier.

## *B. System Dynamic Mathematical Model*

To describe the kinematics of the PSD the lever analogy and the principle of intersecting lines are applied. The kinematic relationship can be deduced from Figure 4:15.

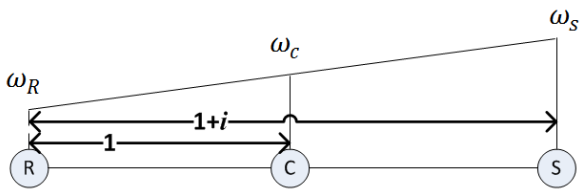


**Figure 4:15: Kinematic Relationship for the PSD**

The distance between the ring (R) and the sun gear (S), is defined to $(i + 1)$ according to [114], whereby $i$ describes the gear ratio between the sun gear and the ring gear. From Figure 4:15, the following relationship can be derived:

$$\frac{\omega_s - \omega_R}{\omega_c - \omega_R} = \frac{1 + i}{1} \qquad \textbf{Eq. 4:56}$$

If Eq. 4:56 is rearranged, the following is yielded:

$$\omega_R = \frac{\omega_c(1 + i)}{i} - \frac{\omega_s}{i} \qquad \textbf{Eq. 4:57}$$

From Eq. 4:57, if $\omega_c = 0$, meaning that the planet carrier stands still, the transmission ratio between the ring gear $\omega_R$ and the sun gear $\omega_s$ is $(-i)$.

The angular speed of each component is a result of the driving and load torques acting on the PSD. The physical model is depicted in Figure 4:16, whereby the case of operating mode B12 is chosen first. The physical model is, again, based on the lever analogy, whereby

torques can be treated as forces acting on a lever. For the system model the drive train dynamics are neglected and friction values are assumed to be time-invariant.

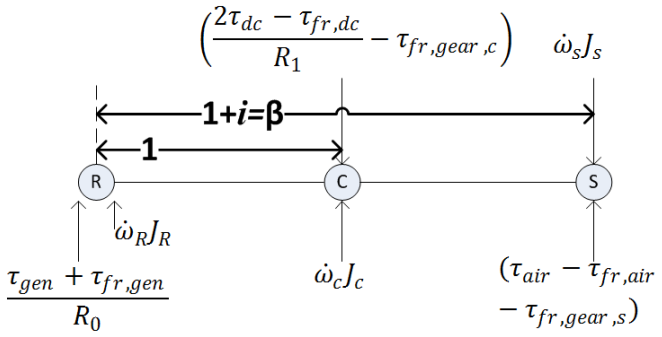


**Figure 4:16: Lever Diagram for Power Split Device with Scroll Air Expander**

It can be seen from Figure 4:16 that torques act on the sun gear, planet carrier and ring gear, whereby the planet carrier torque opposes the torque of the generator and the scroll air expander. The sun gear and planet carrier torques are the inputs to the PSD and the ring gear experiences the load torque. Furthermore, the transient reaction torques which are formed by the moment of inertia and the acceleration of the respective shafts are plotted. The DC motor torque is chosen instead of the HAWT torque. This is to simplify the comparison between the simulation and the practical experimental work at later stages (see Section 6.1). The variables and parameters are listed below:

| | | | |
|---|---|---|---|
| $\tau_{dc}$ | = | DC motor torque | $[Nm]$ |
| $\tau_{fr,dc}$ | = | DC motor friction | $[Nm]$ |
| $\tau_{fr,gear,c}$ | = | Gear box carrier friction | $[Nm]$ |
| $\tau_{gen}$ | = | Load torque generator | $[Nm]$ |
| $\tau_{fr,gen}$ | = | Generator friction | $[Nm]$ |
| $\tau_{air}$ | = | Scroll expander torque | $[Nm]$ |
| $\tau_{fr,air}$ | = | Scroll expander friction | $[Nm]$ |
| $\tau_{fr,gear,s}$ | = | Sun gear friction | $[Nm]$ |
| $\dot{\omega}_i$ | = | Angular speed | $[rad/s^2]$ |
| $R_0, R_1$ | = | Gear ratios | $[-]$ |
| $i$ | = | PSD gear ratio | $[-]$ |

| | | | |
|---|---|---|---|
| $J_i$ | = | Moment of inertia reduced to sun gear, ring gear and carrier | $[kgm^2]$ |

Two differential equations can be derived from the physical model in Figure 4:16. The sum of the moments is arbitrarily taken around the sun and ring gears, respectively, so that $\sum \tau^{sun} = 0$ and $\sum \tau^{ring} = 0$.

$$\sum \tau^{sun} = 0 = -(\beta - 1)\left(\frac{2\tau_{dc} - \tau_{fr,dc}}{R_1} - \tau_{fr,gear,c}\right) + (\beta - 1)J_c\dot{\omega}_c + \beta\frac{\tau_{gen} + \tau_{fr,gen}}{R_0} + \beta\dot{\omega}_R J_R \quad \textbf{Eq. 4:58}$$

$$\sum \tau^{ring} = 0 = \left(\frac{2\tau_{dc} - \tau_{fr,dc}}{R_1} - \tau_{fr,gear,c}\right) - \beta\left(\tau_{air} - \tau_{fr,air} - \tau_{fr,gear,s}\right) - \dot{\omega}_c J_c + \dot{\omega}_s J_s \beta \quad \textbf{Eq. 4:59}$$

Taking the derivatives of Eq. 4:57 and substituting $\dot{\omega}_R$ in Eq. 4:58 and Eq. 4:59, the following is yielded:

$$\dot{\omega}_s = \frac{1}{(1+i)J_R}\left[-i\left(\frac{2\tau_{dc} - \tau_{fr,dc}}{R_1} - \tau_{fr,gear,c}\right) + (1+i)\frac{\tau_{gen} + \tau_{fr,gen}}{R_0} + \dot{\omega}_c\left(iJ_c + \frac{(i+1)^2 J_R}{i}\right)\right] \quad \textbf{Eq. 4:60}$$

$$\dot{\omega}_c = \frac{1}{J_c}\left[\left(\frac{2\tau_{dc} - \tau_{fr,dc}}{R_1} - \tau_{fr,gear,c}\right) + (1+i)\left(\tau_{air} - \tau_{fr,air} - \tau_{fr,gear,s}\right) + \dot{\omega}_s J_s(i+1)\right] \quad \textbf{Eq. 4:61}$$

It can be seen from Eq. 4:60 and Eq. 4:61 that the equations are linked through $\dot{\omega}_s$ and $\dot{\omega}_c$. By decoupling the equations from each other, the following differential equations are yielded:

$$\dot{\omega}_c = \frac{1}{J_{k2}}\left[\left(\frac{2\tau_{dc} - \tau_{fr,dc}}{R_1} - \tau_{fr,gear,c}\right)J_{k3} - (1+i)\left(\tau_{air} - \tau_{fr,air} - \right.\right. \quad \textbf{Eq. 4:62}$$

$$\tau_{fr,gear,s}\Big) + J_{k4}\left(\frac{\tau_{gen}+\tau_{fr,gen}}{R_0}\right)\Big]$$

$$\dot{\omega}_s = \frac{1}{J_{k5}}\Big[\Big(\frac{2\tau_{dc}-\tau_{fr,dc}}{R_1} - \tau_{fr,gear,c}\Big)J_{k6} + (1+i)\left(\frac{\tau_{gen}+\tau_{fr,gen}}{R_0}\right) - \frac{J_{k1}}{J_c}(i+i)\big(\tau_{air}-\tau_{fr,air}-\tau_{fr,gear,s}\big)\Big] \quad \textbf{Eq. 4:63}$$

In the process of forming the equations described above, some terms for the moment of inertia were merged together to reduce the length of the equations. The moment of inertias $J_{k_i}$ with $i = 0,1,\dots,6$ are listed in the following table:

**Table 4:1: Inertias for PSD dynamic model**

| ***Variable*** | ***Description*** |
|---|---|
| $J_{k1}$ | $iJ_c + \frac{(1+i)^2 J_R}{i}$ |
| $J_{k2}$ | $-\frac{J_{k1}J_s i}{J_R} + J_C$ |
| $J_{k3}$ | $1 - \left(\frac{J_s i^2}{J_R}\right)$ |
| $J_{k4}$ | $\frac{J_s i}{J_R}$ |
| $J_{k5}$ | $\frac{(1+i)J_R}{i} - \frac{J_s J_{k1}}{J_c}(i+1)$ |
| $J_{k6}$ | $-i + J_{k1}/J_c$ |

The derivation above concerns the operating mode B12 only. Mode A12, however, deserves special attention and needs to be modelled as well. In general, the model based on Eq. 4:62 and Eq. 4:63 can be reused with minor changes to the scroll expander/compressor part. Figure 4:17 shows the physical model for the operating Mode A12.

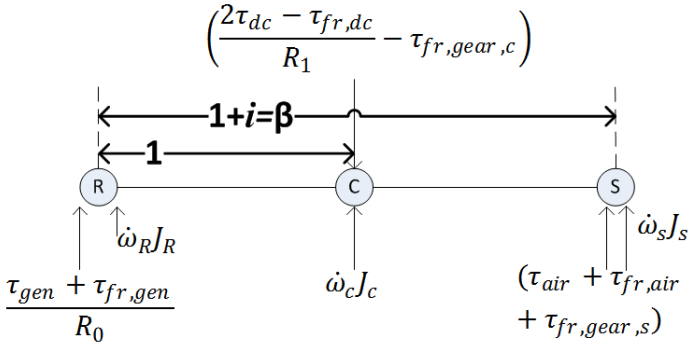


**Figure 4:17: Lever Diagram for Power Split Device with Scroll Compressor (Mode A12)**

It can be seen from Figure 4:17 that the dynamic load torque, $\dot{\omega}_s J_s$, for the scroll compressor changes its direction in comparison to Figure 4:16. This is caused by a change in direction of the angular speed. Moreover, since the scroll compressor is now a load to the HAWT/DC emulators, the friction losses are added to the load. Therefore, the HAWT/DC emulators need to account for both compression and friction losses. The two differential equations for the compression mode are as follows:

$$\dot{\omega}_c = \frac{1}{J_{k2}}\left[\left(\frac{2\tau_{dc}-\tau_{fr,dc}}{R_1}-\tau_{fr,gear,c}\right)J_{k3}-(1+i)\left(\tau_{air}+\tau_{fr,air}+\tau_{fr,gear,s}\right)+J_{k4}\left(\frac{\tau_{gen}+\tau_{fr,gen}}{R_0}\right)\right] \quad \text{Eq. 4:64}$$

$$\dot{\omega}_s = \frac{1}{J_{k5}}\left[\left(\frac{2\tau_{dc}-\tau_{fr,dc}}{R_1}-\tau_{fr,gear,c}\right)J_{k6}+(1+i)\left(\frac{\tau_{gen}+\tau_{fr,gen}}{R_0}\right)-\frac{J_{k1}}{J_c}(i+i)\left(\tau_{air}+\tau_{fr,air}+\tau_{fr,gear,s}\right)\right] \quad \text{Eq. 4:65}$$

## 4.9 Overall System Model

The overall system model is formed by interconnection of the individual models described in the previous sections. It needs to be emphasised that a single set of an overall model is inadequate to represent all possible operating modes of the hybrid wind turbine. The overall model would include the scroll expander and scroll compressor model as well as the

PMSG and PMSM model and switching between these models would be required. Therefore, three individual models, representing operating Mode A, B and C are utilised to represent the whole hybrid wind turbine system. Firstly, Figure 4:18 shows the model that is used to investigate the case in which the scroll compressor becomes a load (Mode A).

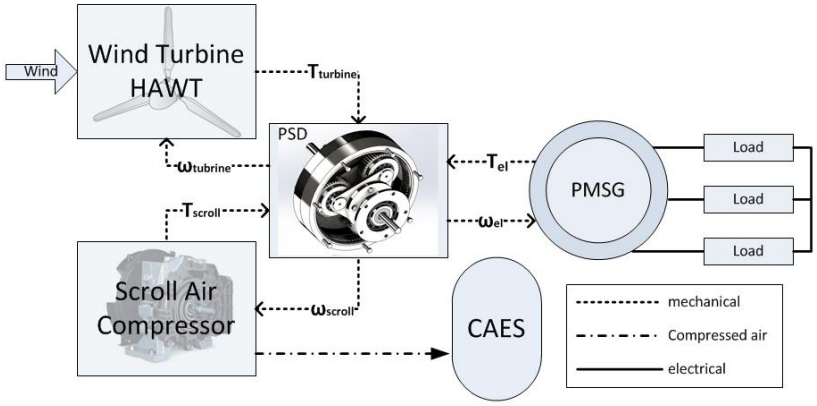


**Figure 4:18: Overall System Model for Mode A**

The dynamic mathematical model of the PSD forms the core of the overall hybrid wind turbine model. In the simulation it requires all torques from the system components acting on it and outputs the resulting angular speeds of the respective shafts. The angular speeds are necessary inputs for the PMSG, scroll air compressor and HAWT/DC motor models. A resistive load is considered only for the PMSG and the inverter/converter unit as well as the grid connection are not considered at this stage of the simulation study.

Figure 4:19 visualises the second model in which the scroll air expander can add power to the system (Mode B).

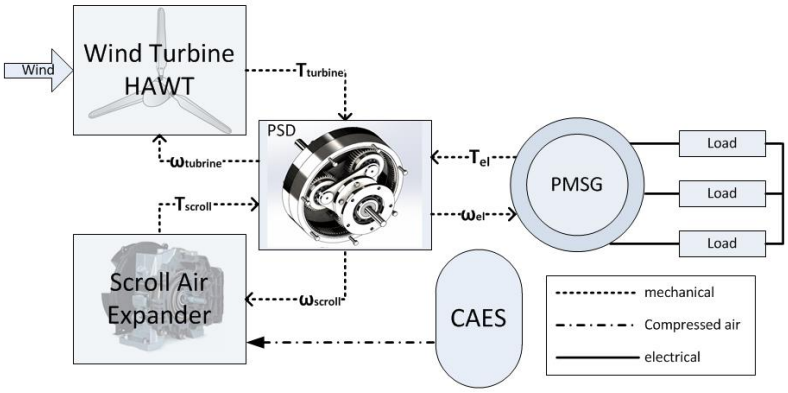


**Figure 4:19: Overall System Model for Mode B**

This model is similar to the first model in Figure 4:18, with the difference that the scroll expander model is implemented instead of the scroll compressor model.

Lastly, the Mode C represents the standalone energy storage provision application of the hybrid wind turbine. The PMSM drives the air compressor for which power electronics and an adequate control strategy is needed. The open loop *v/f=const*. control method is applied for both simulation and experimental rig. The industrial inverter unit ACS355 3*kW* from ABB is employed on the test rig to drive the PMSM. Figure 4:20 illustrates the topology for the simulation model for Mode C.

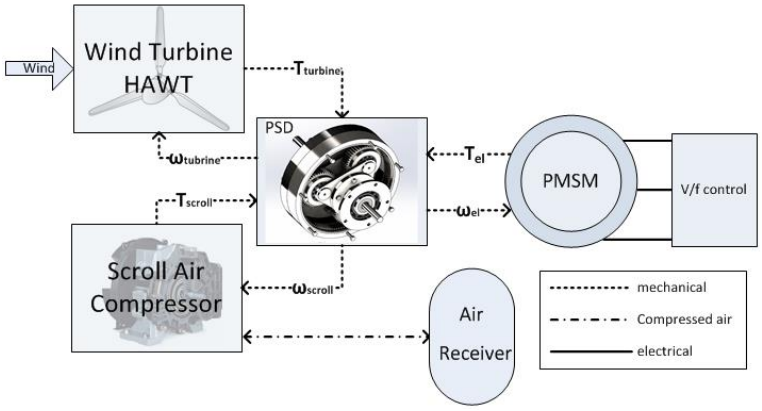


**Figure 4:20: Overall System Model for Mode C**

## *4.10 Summary*

To sum up, the relevant dynamic mathematical models for the relevant system components were derived. The models are listed below:

- Scroll air expander
- Scroll air compressor
- Compressed air storage
- Permanent magnet synchronous generator
- Permanent magnet synchronous motor and control
- Horizontal axis wind turbine
- DC motor
- Planetary gearbox/ Power split device

The models are derived based on reasonable simplifications. The mathematical models were then utilised to form the overall dynamic system model. It was concluded that a single overall model is inadequate to represent all possible operating modes of the hybrid wind turbine. Therefore, three models were presented that describe the operation Mode A, B and C.

# *Chapter 5 - Test Rig Design and Implementation*

An experimental test rig is required to validate the mathematical model described in Chapter 4 and to demonstrate the practical feasibility of the proposed hybrid wind turbine structure. In this chapter, the general design requirements of the hybrid wind turbine test rig are highlighted, followed by an explanation of the hardware and instrumentation utilised for the test rig. Next, the design of the gearbox (PSD) is explained, followed by the explanation of the turbine emulator set up. The chapter ends with an explanation of the overall wind turbine test rig design and manufacturing.

## *5.1 Test Rig Requirements*

The general requirements for the hybrid wind turbine test rig are listed in Table 5:1, and allocated as either *important* or *desired*. "*Important*" means an absolute necessity and "*desired*" means that it should be included if possible, but it is not a critical requirement. This gives an overview of what is needed and what can be expected from the test rig.

**Table 5:1: Test Rig Requirements**

| **Requirements** | **Important** | **Desired** |
|---|---|---|
| Functionality: | | |
| Power rating based on 1*kW* PMSG | • | |
| Scroll expander needs to be able to produce the PMSG's rated power when wind turbine is inactive | • | |
| Wind turbine emulator needs to be secured against back spinning | • | |
| Changeable resistive 3-phase load | • | |
| Expansion and compression mode of air machine must be possible | • | |
| PMSG needs to be able to be operated as PMSM through inverter | • | |
| PMSM and DC motor emulators must be able to drive the compressor | • | |
| Possibility to accommodate real wind turbine for future tests | • | |
| Pressure supply of up to 7 *bar* for given scroll | • | |

| | | |
|---|---|---|
| expander | | |
| Rapid Control Prototyping with real-time capability | • | |
| Equipment with various sensors (instrumentation, data acquisition tools etc.) | • | |
| Geometry: | | |
| Laboratory sized | • | |
| Movable | • | |
| Hub that contains all key components and sensors | | • |
| External storage tank | | • |
| Heavy in weight for future turbine application | | • |
| Health & Safety: | | |
| Safety against moving mechanical parts | • | |
| Safety against electric shocks | • | |
| Safety against air pressure systems | • | |
| Safety against noise | • | |
| Manufacturing: | | |
| Single test rig | • | |
| Simplicity in manufacturing methods | | • |
| Inexpensive material | | • |
| Costs: | | |
| Inexpensive manufacturing | | • |
| Low quantity of components needed | | • |
| Avoidance of outsourcing manufacturing | | • |
| Utilisation of available components in research lab | | • |
| Maintenance free | | • |
| Utilisation of standard parts | | • |
| Application and Commissioning: | | |
| Long life-time | | • |
| Good accessibility and convertibility | • | |
| Simple assembly and disassembly | • | |
| Simple maintenance | | • |
| Low dirt susceptibility | | • |

## *5.2 Test Rig and the Associated Instrumentation*

The hardware and instrumentation is described in this section. It entails a short description of the main components, which are the PMSG/PMSM, the scroll air machine, the PSD and the turbine emulator. In addition, ancillary components such as sensors, power supplies, computers etc. are described, followed by the introduction of the electro-mechanic schematic of the test rig.

### *5.2.1 Main Components*

The main component types are discussed in Chapter 3, where the justification of the chosen component types is described. In this section, the final selection of the system components is given, see Table 5:2.

**Table 5:2: List of selected components**

| *Component* | *Description* |
|---|---|
| PMSG/PMSM | Ginlong Technologies GL-PMG 1000 (1*kW*) |
| Scroll machine | Sanden TRS090 compressor, converted to an expander and able to swap roles between expander and compressor |
| PSD | Single stage planetary gearbox, custom made |
| Turbine emulator | Two DC motors of type Callan Technology M4-2952 (1*kW*) are used to emulate a HAWT |

Figure 5:1 shows images of the PMSG. The PMSG contains 8 pole pairs, which make the unit large in diameter and cause a need for a relatively high input torque. The specifications of the PMSG are obtained partly from the datasheet and partly from experimental tests.

**Figure 5:1: Ginlong Technologies GL-PMG 1000 (1*kW*)**

The scroll air machine is shown in Figure 5:2. The unit is commonly used as a compressor in vehicles. Figure 5:2 shows the scroll air compressor as it is used in a vehicle, which is why the pulley and the thermal protection switch are shown. The pulley for the belt transmission is engaged via a magnetic clutch. In order to convert the compressor to an expander, the reed valve inside the unit was removed. The reed valve acts as a non-return

valve attached to the compressor outlet. In addition, the pulley and clutch assembly as well as the thermal protection switch were removed.


**Figure 5:2: Sanden TRS090 Scroll Air Machine**

The gearbox merges the torques of the HAWT, scroll expander/compressor and PMSG/PMSM. The device was custom made because no suitable off-the-shelf unit was found. Figure 5:3 shows an image of the gearbox's 3D model. The unit is explained more in detail in Section 5.3.

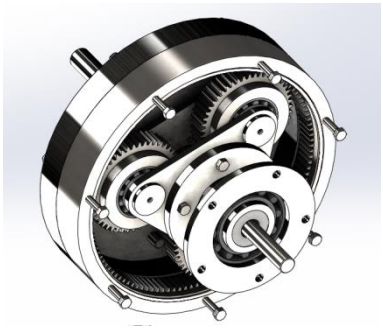

**Figure 5:3: Gearbox as 3D Model**

Lastly, the turbine emulator consists of two permanent magnet DC motors, type Callan Technology M4-2952, rated at 1*kW* each. The choice of the motors and the integration into the test rig are explained more in detail in Section 5.4 *Turbine Emulator.* Figure 5:4 shows one DC motor.

**Figure 5:4: Callan Technology M4-2952**

### *5.2.2 Ancillary Components and Integration*

The test rig requires ancillary components for the integration of the main components described in the previous subsection. It is essential to place a sufficient amount of sensors to measure the system variables that are of interest. Concerning the mechanical system, it is necessary to measure the torques acting on all three PSD shafts as well as the rotational speeds. Torque sensors with integrated encoders for angular speed measurements were mounted to the scroll expander/compressor shaft and generator shaft. The torque of the DC motors can be estimated by means of the armature current and, therefore, less costly current transducers are implemented. A rotational encoder is placed on one of the DC motors to measure its angular speed. With regards to the PMSG-load system, two current and voltage transducers are in place to measure current and phase voltage to determine the electrical power generated. Air temperature, air pressure and volumetric flow rate sensors are installed for the scroll compressor/expander operation. An OPAL-RT 5600 real-time target was chosen as the interface between Matlab/Simulink and the test rig. Further devices such as analogue voltage amplifiers, a solenoid pressure regulator, power supply units, load resistors, compressed air conditioning equipment and a personal computer with Matlab/Simulink software are in place to complete the test rig. A list of components and instruments of the test rig is given in the Appendix E.3.

Figure 5:5 shows the electro-mechanic diagram in which all the components mentioned above are visualised for Mode B (DC motors and scroll air expander drive the PMSG).

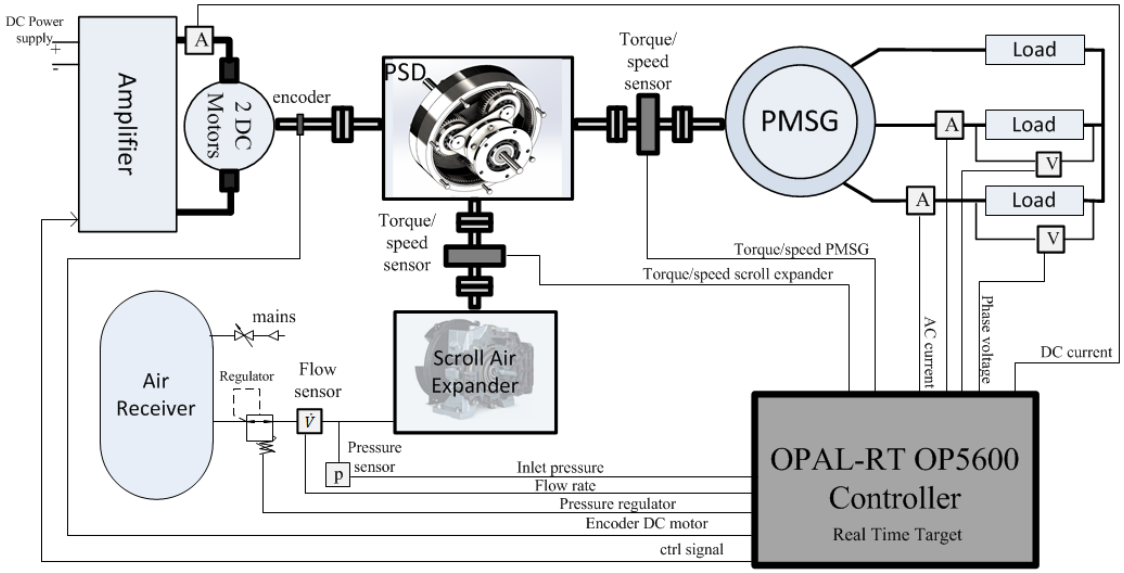


**Figure 5:5: Electro-Mechanic Schematic Diagram of Test Rig and RCP Mode B**

The compression mode, in which air is compressed and stored in the air receiver, is realised by reconfiguring the compressed air lines. Furthermore, if the PMSG is operated as a motor (PMSM), the resistive load is removed and a 3 phase inverter is put in place. Figure 5:6 shows the electro-mechanic diagram for Mode C (PMSM and/or DC motors drive the scroll air compressor).

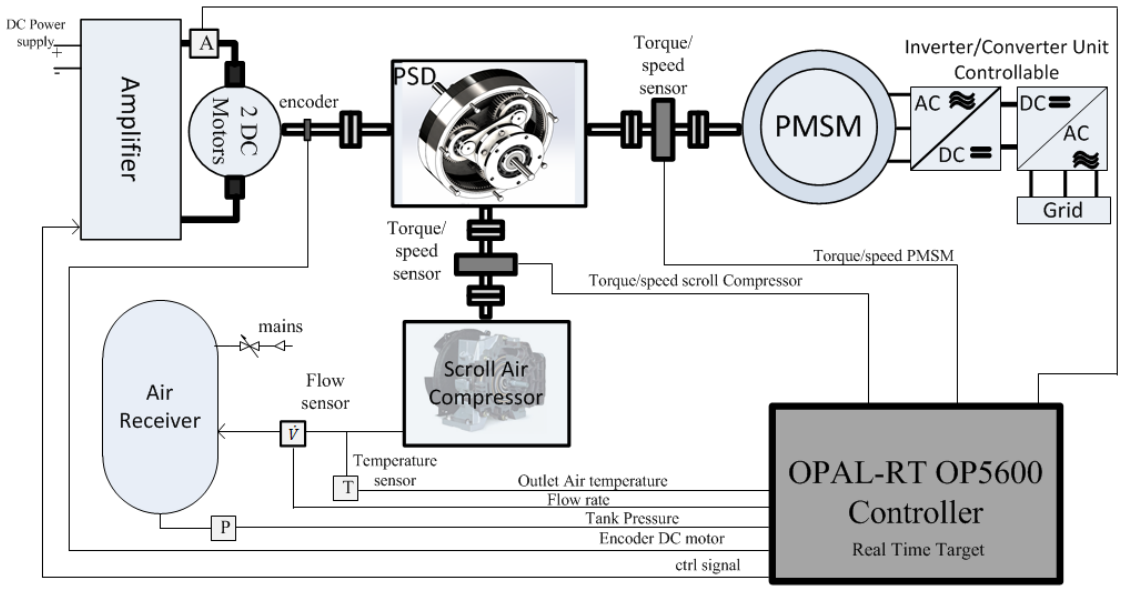


**Figure 5:6: Electro-Mechanic Schematic Diagram of Test Rig and RCP Mode C**

## *5.3 Gearbox Design*

In this section, the method of determining the gear ratio of the PSD is described, which is supported by experimental test results from the scroll air machine when used as an expander. Once the decision for the transmission ratio is made, a brief description of the design and manufacturing process of the device is given.

### *5.3.1 Determination of Gear Ratio*

The main challenge in the design of the gearbox is to determine the gearbox ratio, i.e. the ratio between the sun gear and the ring gear. Two of the requirements outlined in Table 5:1 are:

1. The scroll air expander needs to be capable of driving the PMSG by itself in moments of wind troughs.
2. The DC motors and/or the PMSM need to be capable of driving the compressor.

Concerning the first requirement, since the chosen PMSG is a relatively high torque/low speed device (due to the number of pole pairs) and the scroll air expander is a low torque/high speed device, it can be expected that their operating points differ significantly from each other. In fact, the operating point and rated power of the scroll air expander are unknown, since the device is converted from a compressor.

Firstly, the PMSG's torque/speed characteristics are taken from datasheets. Secondly, a temporary test rig is built to acquire the torque/speed characteristics of the scroll expander under varying air pressure inputs. Figure 5:7 shows a number of test results, in which the falling lines describe the torque/speed characteristics of the scroll expander under varying input gauge air pressure. The measurements are digitally filtered and approximated to straight lines. Furthermore, the rising lines represent the torque/speed characteristics of the PMSG by assuming a number of gear ratios between scroll expander and PMSG along with a transmission efficiency of 85%.

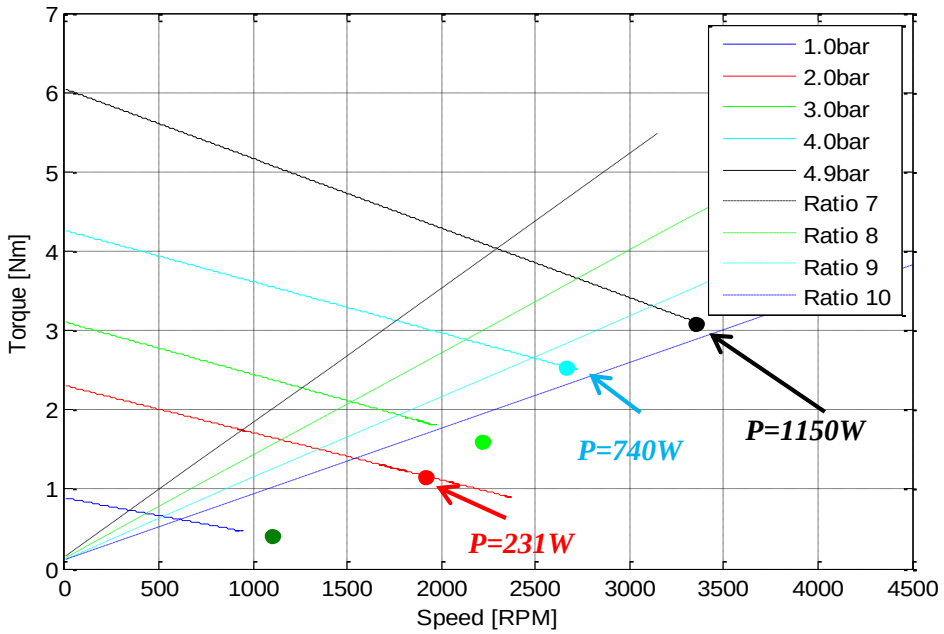


**Figure 5:7: Operating Point of Scroll Expander and PMSG with Gear Ratios and Losses**

Wherever a falling line intersects a rising line there will be the operating point of the *scroll expander-gearbox-PMSG* assembly according to the respective gear ratio and air pressure input. The maximum mechanical power produced by the scroll expander with respect to the input air pressure is shown through the solid dots in Figure 5:7. It can be concluded that in order to generate around 1150W mechanical power (black dot) for the input to the PMSG, the scroll expander needs to be driven with 4.9*bar* (gauge), while having a gear ratio of about 10 between the components. At that operating point, the scroll expander will rotate with 3350*RPM* and produce around 3Nm torque. The PMSG will experience a torque input of about 26Nm (losses included), while rotating with 335*RPM*. In general, by looking at the solid dots in Figure 5:7, it can be assumed that the gear ratio should be around 10 to ensure that maximum power is extracted at any given input air pressure and depending on the load. However, the maximum power extracted does not mean that the scroll air expander works efficiently at that operating point. Figure 5:8 shows the efficiency[7] vs. speed plot for different air gauge pressure inputs.

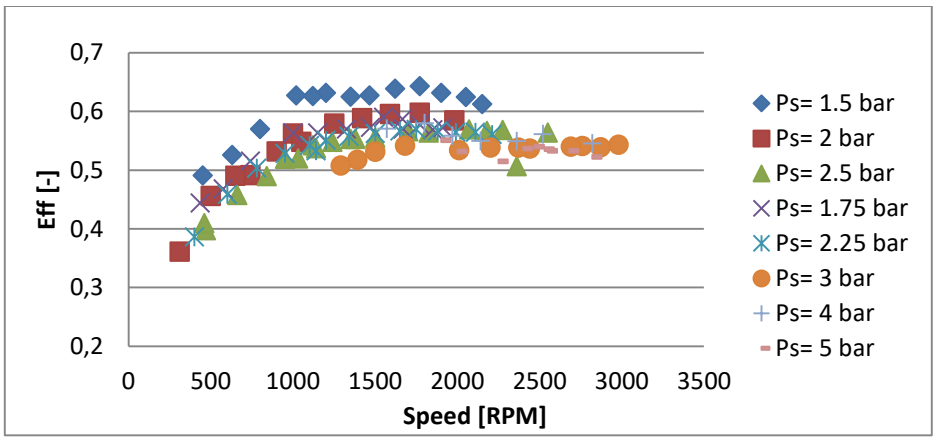


**Figure 5:8: Efficiency vs. *RPM* plot Scroll air expander**

It can be seen that the maximum efficiency can be achieved at around 1500 to 2000 *RPM* for an air pressure input of 1,5 bar (gauge). At the time of research it was not possible to increase the input air pressure to above 5 *bar* (gauge). Figure 5:8 shows a decreasing trend

[7] Ratio of mechanical shaft power over flow exergy of compressed air (see Section 6.4.1)

in efficiency at higher speeds, which can be explained by the large amount of air consumed. The plot in Figure 5:8 can be confirmed by means of the study reported in [115].

Having accumulated the information from Figure 5:7 and Figure 5:8, the final transmission ratio can now be discussed. It has to be taken into account that the scroll air expander will operate over a range of speed, which is the intended application and which is why a PSD is utilised. Therefore, a range of air pressure inputs and load torques will occur according to the power needed from the scroll air expander and, hence, the speed will vary accordingly. On the one hand, large transmission ratios are desired to ensure maximum mechanical power extracted, meaning that the scroll expander will operate at high speeds. However, in order to operate more efficiently with respect to the amount of air consumed, angular speeds such as 1500 to 2000*RPM* for a pressure range of about 2 to 4 *bar* are desired. Moreover, a large transmission ratio such as 10 for a single stage planetary gearbox is rather uncommon and a 2-stage gearbox would be considered, which in turn increases the design effort. A decision was made to choose a gear ratio of 5 for the gearbox. Additionally, a belt transmission from the gearbox to the PMSG is implemented with a transmission ratio of 1.5. Therefore, the overall gear transmission from the scroll air expander to the PMSG is 7.5.

To conclude, the kinematics of the gearbox can be expressed as follows:

$$\omega_R = \frac{\omega_c(1+i)}{i} - \frac{\omega_s}{i} = \frac{6}{5}\omega_c - \frac{\omega_s}{5} \qquad \textbf{Eq. 5:1}$$

If the planet carrier is held still, i.e. $\omega_c = 0$ (turbine does not spin), the following is yielded:

$$\frac{\omega_s}{\omega_R} = -5 \qquad \textbf{Eq. 5:2}$$

Moreover, if the sun gear is held still, i.e. $\omega_s = 0$ (scroll machine does not spin), the transmission from the planet carrier to the ring gear is:

$$\frac{\omega_c}{\omega_R} = \frac{5}{6} \quad \textbf{Eq. 5:3}$$

If the ring gear is held stationary, i.e. $\omega_R = 0$ (PMSG does not spin), the transmission ratio from the sun gear to the planet carrier is:

$$\frac{\omega_s}{\omega_c} = 6 \quad \textbf{Eq. 5:4}$$

Lastly, a belt with a transmission ratio of 1.5 is used to connect the ring gear to the generator shaft. Therefore:

$$\frac{\omega_R}{\omega_{gen}} = 1.5 \quad \textbf{Eq. 5:5}$$

so that:

$$\frac{\omega_s}{\omega_{gen}} = -7.5 \quad \textbf{Eq. 5:6}$$

As well as the expander mode, the compression mode must be considered for the gearbox design. The scroll machine can be driven as a compressor by either the HAWT (DC emulators) or the PMSM (e.g. at high wind speeds and low electricity demand). Therefore, the selected gear ratios need to be confirmed for the case that the compressor is driven. Again, no detailed datasheets for the scroll compressor are available so that experimental tests needed to be conducted in which:

a) The DC emulators drive the scroll compressor

b) The PMSM drives the scroll compressor

This work is not described in this section because it follows the same principles described for the expander operation. The suitability of the gear ratios for the PSD described in Eq. 5:1 to Eq. 5:6 were confirmed for the cases described in *a.)* and *b.)*. More information and test results can be found in Section 6.1, where the mathematical system model for these two cases is validated with experimental results.

### *5.3.2 Gearbox Design*

Having established the final transmission ratio, the gearbox can now be designed. Note that for the planetary gearbox, all three gear components need to be able to revolve (sun-, carrier- and ring gear). An off-the-shelf unit that matches the specifications needed was not found. Since the costs of outsourcing the design and construction was prohibitive, the gearbox was designed in-house. The main guidance used for the gearbox design can be found in [91]. A number of design factors need to be taken into account prior to the actual design. The design factors are as follows:

- Gear ratio (see Subsection 5.3.1)
- Rotational speed and torque (see Subsection 5.3.1)
- Operating factor (takes into account the type of load, e.g. peak shock load, type of driving machines etc.)
- Shaft diameters and material
- Selection of basic tooth data
- Geometries of gears
- Selection and design of the link between shaft and gear
- Strength and stress analysis on shafts and gears
- Selection of bearings and their stress analysis
- Lubrication
- Manufacturing and assembly

The design of a planetary gearbox is a complex task and many factors, as shown above, need to be taken into account. Most importantly, the gearbox is a costly custom-made one off product and a flawless design had to be ensured. In this section, only the final design is presented. The software used for the design task is *SolidWorks*. Figure 5:9 shows the

gearbox model from the top, whereby its view is sectioned so that the inside gears can be seen.

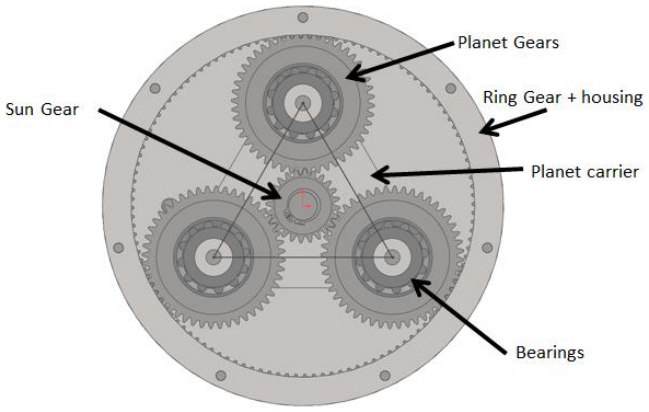


**Figure 5:9: Gearbox Top View-Sectioned**

Figure 5:10 presents the side view of the gearbox model.

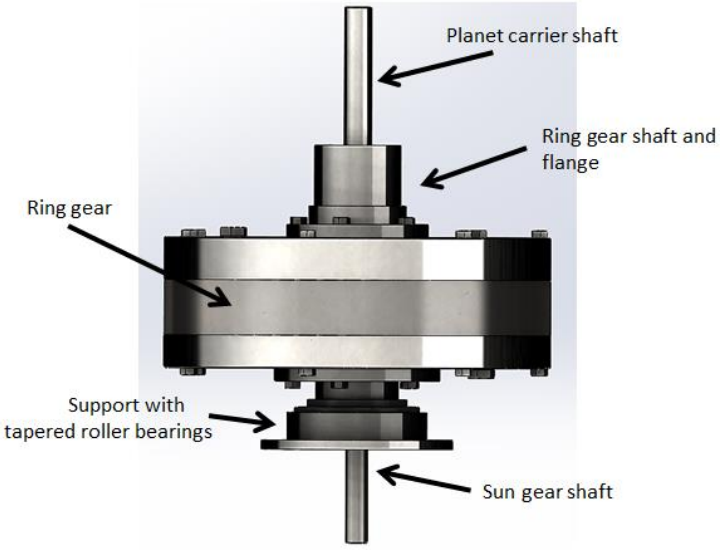


**Figure 5:10: Gearbox Side View**

Table 5:3 gives an overview of the key parameters of the gear box:

**Table 5:3: Overview of Gearbox Key Parameters**

| ***Entity*** | ***Value*** |
|---|---|
| Circular module | 1.5 *mm* |
| Teeth pressure Angle | 20° |
| Face width of gears | 15 *mm* |

| | |
|---|---|
| Circular pitch ring gear | 180 *mm* |
| Circular pitch planet gear | 72 *mm* |
| Circular pitch diameter sun gear | 36 *mm* |
| Number of teeth ring gear | 120 |
| Number of teeth planet gear | 48 |
| Number of teeth sun gear | 24 |
| Outside diameter | 210 *mm* |
| Total height | 291 *mm* |
| Weight | 8.3 *kg* |
| Material gears | 20MnCr5 |

Figure 5:11 shows a technical drawing, sectioned from B to B as indicated within the figure. The sectioning cuts two of the planet gears in the middle. The sectioning A-A is not shown here.

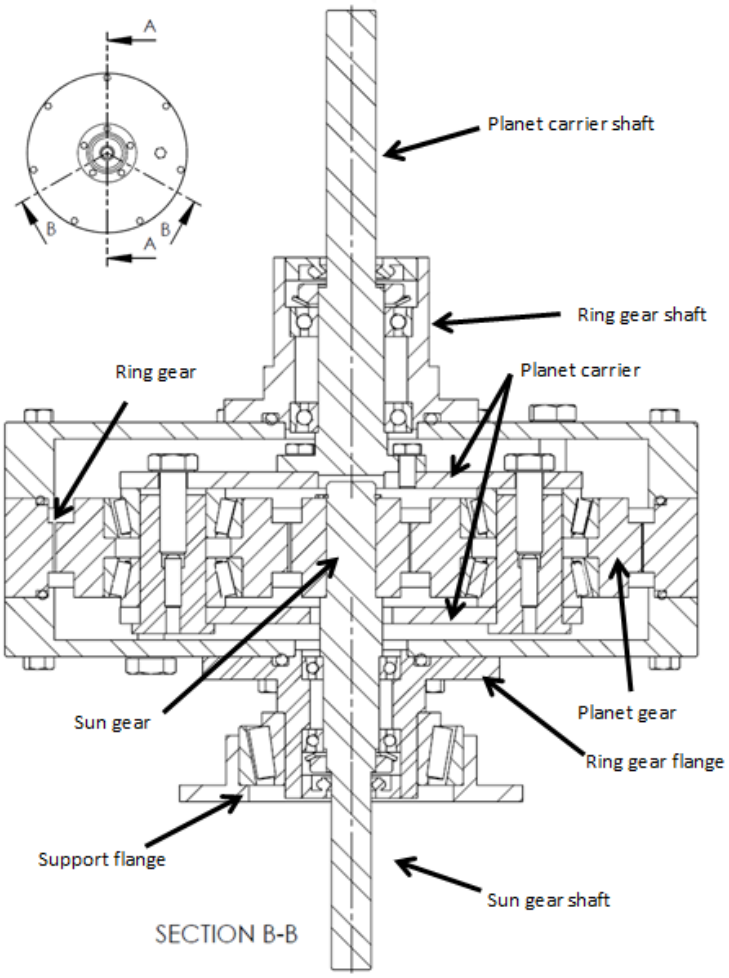


**Figure 5:11: Technical Drawing Sectioned View B-B**

Both the planet carrier shaft and the sun gear shaft are running on two sets of angular ball bearings that keep the shafts in place and prevent them from moving vertically. The planet gears are running on tapered roller bearings and are held in place by means of the planet carriers. The planet carrier is connected to the planet carrier shaft. The ring gear is connected to the housing, which is also connected to the ring gear shaft (top of gearbox) and ring gear flange (bottom of gearbox). This configuration prevents vertical movement of any of the rotating components. The gearbox rests on the support flange, running on tapered rolling bearings. This means that the gearbox is placed vertically on the test rig as it is shown in Figure 5:11. Furthermore, the gearbox requires radial support on the top, which is realised by an additional bearing block mounted to the carrier shaft and the test rig (a clearer illustration of the bearing block is shown in Figure 5:15 on page 134). 2D technical drawings of each component of the gearbox can be found in the Appendix E.

### *5.3.3 Manufacturing*

2D drawings and the list of parts for the gearbox was sent to the manufacturing company (*Dongguan Zhuolan Automation Equipment Co., Ltd.*, China) so that the gearbox could be manufactured, assembled and tested with the intended parts before shipment. Appendix E.1 entails all 32 parts of the gearbox such as bearings, seals, lock nuts, bolts etc. The final product is shown in Figure 5:12.

**Figure 5:12: Opened and Assembled Gearbox**

The gearbox is shown without the top lid and the carrier shaft (left picture of Figure 5:12). The planet gears are visible and held in place via the planet carrier. Figure 5:12 also shows the assembled gearbox, whereby the tapered roller bearing and support flange can also be seen (right picture).

## *5.4 Turbine Emulator*

As discussed in earlier sections, the VAWT available to this project was too small and inefficient to operate within the hybrid wind turbine system. Instead, an electric motor emulator is used, which is a proven method in academia and industry [102]. To successfully engage an electric motor, several design aspects such as the choice of motors, transmission ratios and hardware implementation need to be taken into account.

### *5.4.1 Selection of Motors and Drives*

Suitable electric motors have to be selected. Two 1*kW* DC motors of the type M4 2952 made by Callan Technology and two analogue amplifiers also made by Callan Technology were selected for the HAWT emulator. Table 5:4 shows the DC motor specifications.

**Table 5:4: DC Motor Specifications**

| ***Description*** | ***Value*** |
|---|---|
| Rated power | 1044 *W* |
| Max Speed | 4000 *RPM* |
| Max Voltage | 115 *Vdc* |
| Cont. Torque | 4.1 *Nm* |
| Peak Torque | 20.3 *Nm* |
| Current at Cont. Torque | 16.10 *A* |
| Current at peak torque | 90 *A* |
| Torque Constant | 0.252 *Nm/A* |
| Resistance | 0.25 *Ω* |
| Inductance | 0.78 *mH* |

Important parameters are the power rating, but also the torque values and the electric current required for that torque. Furthermore, the motor amplifiers must be analysed. The specifications of the amplifiers are shown in Table 5:5.

**Table 5:5: DC Motor Analogue Amplifier**

| ***Description*** | ***Value*** |
|---|---|
| DC supply Voltage | 24-100 *V* |
| Peak Current | 20 *A* |
| Switching Frequency | 33 *KHz* |
| Bandwidth | Greater than 1 *kHz* |

Based on these DC motors and amplifiers, the simulation model can be investigated with respect to the suitability of the components and possible gear ratios.

### *5.4.2 Determination of Transmission Ratio and Number of Motors*

In this subsection, the process of choosing the number of motors and the gear ratio is explained. Given the maximum current of 20*A* for one voltage amplifier, the motor delivers a torque of about 5*Nm* at a speed depending on the load. To meet the power rating of the 1*kW* PMSG, an input torque to the PMSG of about 30*Nm* is required (assuming a resistive load of 20Ω). Therefore, it was chosen to utilise two DC motors and to implement an additional gear ratio of 3.33. With this configuration, a maximum torque of about $(10Nm \cdot 3.33/0.8) = 42Nm$[8] at the PMSG shaft can be achieved and is considered sufficient. The gear ratio is realised using spur gears, which are chosen due to space available, costs, manufacturing effort and safety requirements. With that gear ratio and two DC motors, sufficient power can be produced under consideration of a small scale HAWT. The simulation study was conducted using a HAWT with 2*m* and 3*m* diameter. Table 5:6 shows an example of the simulation study.

[8] 0.8 in the equation is the transmission ratio from the planet carrier to the generator shaft

**Table 5:6: Emulator Simulation Study Example**

| ***Conditions*** | ***Turbine 1*** | ***Turbine 2*** |
|---|---|---|
| HAWT diameter | **2 *m*** | **3 *m*** |
| Wind speed | 12 *m/s* | 12 *m/s* |
| Resistive load | 87.5 $\Omega$ | 30 $\Omega$ |
| ***Results:*** | | |
| Torque turbine | 16 *Nm* | 32 *Nm* |
| Combined torque DC motor | 4.6 *Nm* | 9.5 *Nm* |
| Speed turbine | 800 *RPM* | 660 *RPM* |
| Speed DC motor | 2700 *RPM* | 2240 *RPM* |
| $C_p$ value turbine | 0.4 | 0.3 |
| Total DC current drawn | 18.5 $A < 40$ *A* | 38 $A < 40$ *A* |
| DC voltage | 75 *V* | 60 *V* |
| Transmission losses assumed | 30 % | 30 % |
| Power generated | 880 *W* | 1300 $W$ |

It can be seen that the emulator can reproduce the behaviour of a small scale HAWT as shown by the example of a 2m and 3m diameter HAWT. The torque can be matched under acceptable current and voltage requirements. It is suggested to keep the wind turbine size below 3 metres diameter, to allow for higher torques during transient areas.

Finally, the design of the turbine emulator is shown in Figure 5:13, where it can be seen that the two DC motors are mounted vertically.

**Figure 5:13: DC Motors for HAWT Emulator**

It is shown that the two DC motors are connected to the turbine shaft via spur gears. In that way the torque of both motors are added together and increased through the gear ratio. The encoder for speed measurement is mounted on the top of the right motor. The motors are controlled via the analogue voltage amplifiers, which in turn are controlled by OPAL-RT hardware.

## 5.5 Test Rig Design

The primary requirements of the test rig, the main components and the gearbox design as well as the emulator were discussed in the previous sections. The design and manufacturing of the whole test rig is explained in the following. This section begins with the CAD design and ends with the manufacturing and assembly of the experimental test rig.

### 5.5.1 Test Rig CAD Design

The CAD software *SolidWorks* was utilised for the task, in which a 3D model of the test rig was designed and 2D drawings for the manufacturing were derived. For the 3D model, only the main components that need specific mechanical design considerations are implemented. The following components are modelled:

- DC motors
- Scroll air machine and gearbox assembly with torque/speed sensor
- Generator and torque/speed sensor assembly
- Turbine drive train assembly
- Frame of test rig
- Timing belt transmission

The final test rig with the DC motor emulators is shown in Figure 5:14. The front was sectioned to better see the inside of the test rig.

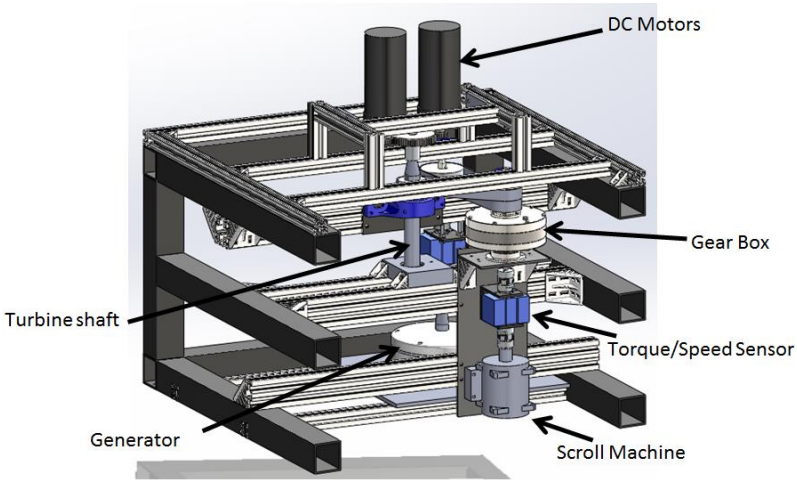


**Figure 5:14: Hybrid Wind Turbine Test Rig Design with Emulators**

The test rig was designed to be able to house a real wind turbine by removing the DC motors so that the turbine shaft is accessible. In the following, more components and assemblies within the test rig are explained in detail.

The first assembly is the *scroll air machine to PSD unit*, shown in Figure 5:15.

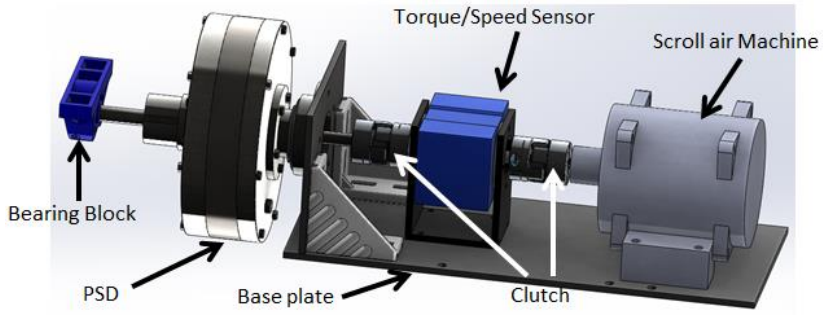


**Figure 5:15: Scroll Air Machine, Torque/Speed Sensor and PSD**

It shows the scroll air machine and how it is connected to the torque/speed sensor via an off-the-shelf claw clutch. The clutch allows for angular deviation to minor extents. The same clutch is fitted between the gearbox and the torque/speed sensor. Accurate design and manufacturing is required to guarantee near perfect alignment of the components shown above. The bearing block gives support to the gearbox since it connects the planet

carrier shaft to the frame of the test rig. Furthermore, Figure 5:16 shows the generator unit and the torque/speed sensor.

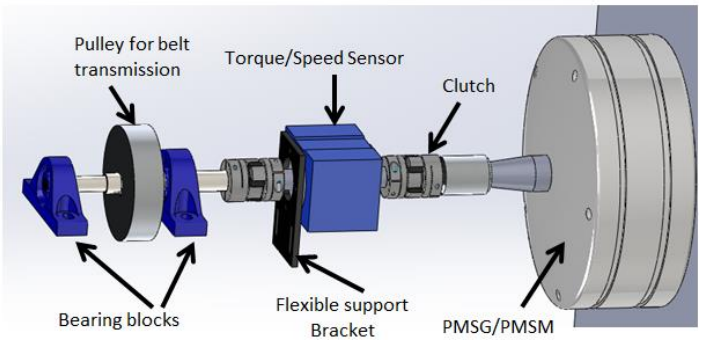


**Figure 5:16: Generator and Torque/Speed Sensor Assembly**

A flexible support bracket for the torque/speed sensor is fitted which keeps the sensor flexibly in place. Due to the number of parts within the assembly and the number of coupling points it cannot be guaranteed that all shafts are perfectly aligned. Therefore, the sensor is flexibly connected to the frame while allowing for small movements so that torque measurement deviations due to shaft tensions are avoided. A timing belt pulley is utilised to connect the generator shaft to the gearbox. The connection between the pulley and the shaft is made through keyways.

Figure 5:17 shows the DC motor and the main drive shaft assembly.

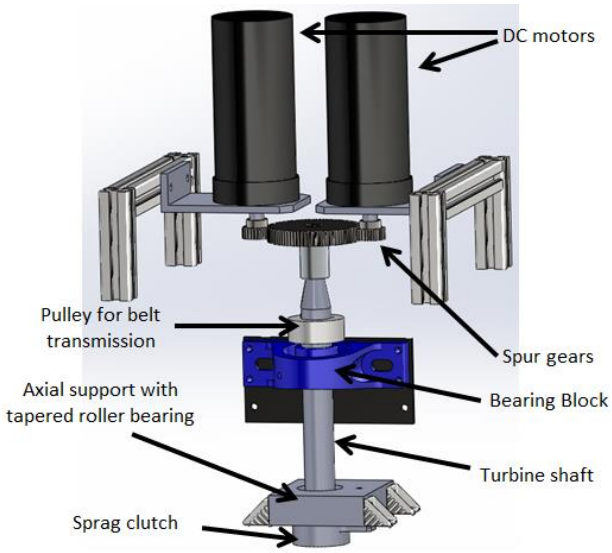


**Figure 5:17: DC Motor Emulator and Main Driving Shaft Assembly**

A gear ratio using spur gears is implemented to better fit the DC motors' torque/speed characteristics to the PMSG's while taking into account the maximum electric current of the DC motors. The turbine shaft is supported in the radial and axial directions. The bearing block houses ordinary ball bearings, whereas the axial support block has inbuilt tapered roller bearings, which take account for radial and axial forces. The dimensions of the shaft and its material as well as the dimensions of the bearings were determined based on maximum forces that can occur assuming the operation with the VAWT, which was initially intended to be used. A sprag clutch connected to the axial support block is fitted in order to prevent the turbine shaft from spinning backwards. Lastly, a timing belt pulley is employed that will be used in conjunction with a timing belt to connect the drive shafts to the gearbox. The timing belt design is shown in Figure 5:18.

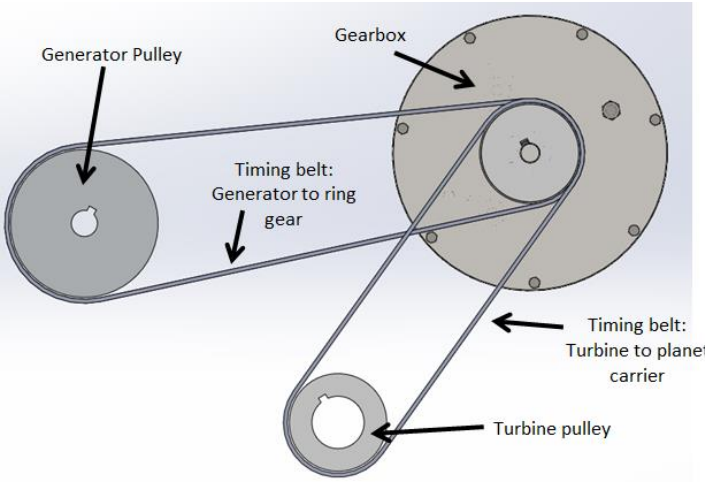


**Figure 5:18: Timing Belts and Transmission Ratios**

It can be seen that two timing belts are employed to connect the generator shaft and the turbine shaft to the gearbox. The gear ratio between the ring gear and the generator shaft is designed to be 1.5. The gear ratio between turbine shaft and the ring carrier of the gearbox is 1. It can also be seen that the pulleys entail keyways to ensure secure mechanical connection to the respective shafts. The timing belt transmission is an efficient and flexible way of connecting two or more shafts. The gear ratios can be altered by changing the diameters of the pulleys. Moreover, the location of the aforementioned assemblies and shafts is not critical, since the belts can be tightened using adequate rollers (not shown in Figure 5:18). The dimensions of the timing belts are determined based on [91].

### *5.5.2 Test Rig Manufacturing and Assembly*

In this section, the manufacturing of the test rig is explained step by step. As opposed to the 3D model, more system components are needed, which are as follows:

- DC power supply for sensors
- DC power supply for DC motors
- Analogue voltage amplifiers for DC motors

- Rapid Control Prototyping hardware
- Voltage and Current sensor board
- Encoder for DC motors
- Pressure sensors, temperature sensors, flow rate sensors and pressure regulators as well as air conditioning units such as filters and lubricators
- Air receiver
- Tubing and cabling
- Inverter unit
- Host computer
- Safety circuitry

All the above mentioned components need to be implemented to guarantee the functionality of the system. For more information about the components it is referred to Appendix E.3. The manufacturing process is briefly described in the following; beginning with the frame of the test rig, see Figure 5:19.

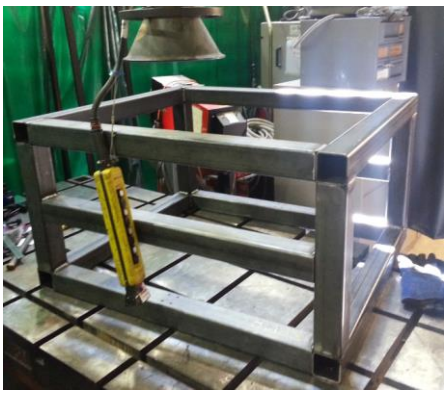

**Figure 5:19: Steal Frame**

The box-sections were welded together after they were processed to length and predefined tapped holes were inserted. The frame was then painted black and wheels as well as aluminium Bosch-sections were added so that the generator and turbine drive train could be fitted, see Figure 5:20.

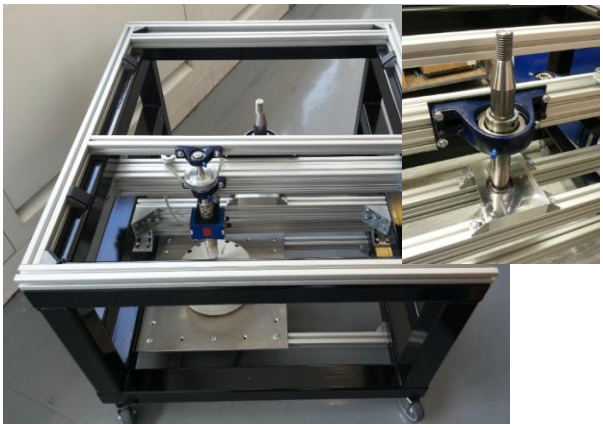

**Figure 5:20: Frame with Aluminium Bosch-Section and Generator and Turbine Shaft Assembly**

Then, the scroll air machine and gearbox assembly were built and mounted along with sensors and actuators as shown in Figure 5:21.

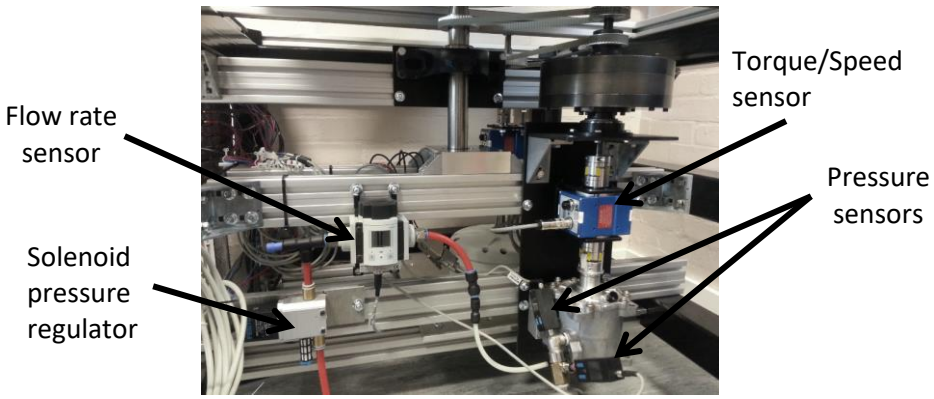


**Figure 5:21: Installation of Scroll and Gearbox Assembly and Sensors**

Two pressure sensors are fitted to the inlet and outlet of the scroll air machine. The volumetric flow rate is measured via a flow rate sensor. The actuator to control the input air pressure to the scroll air expander is a solenoid pressure regulator. A thermocouple is designed to measure the temperature of the compressed air flow. However, the thermocouple is not shown in Figure 5:21.

All sensor signals as well as the inputs for actuators are integrated on the interface panel on the test rig. The interface panel is shown in Figure 5:22.

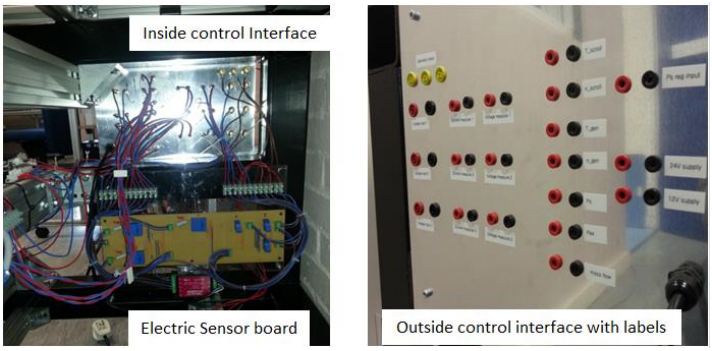


**Figure 5:22: Electrical Sensor Board mounted and inside/outside View of Signal Interface**

A resistive load bank serves as electrical load for the generator and was designed and built for the test rig, see Figure 5:23.

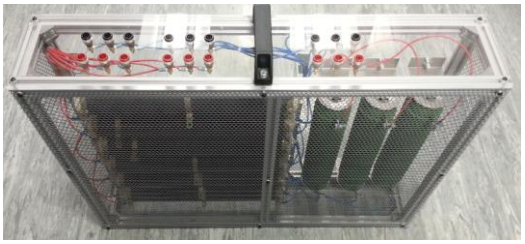

**Figure 5:23: Resistive Load Bank**

The load bank is held flexible and portable and comprises 9 resistors in total (6x60Ω and 3x22Ω) so that multiple resistive load variations can be applied to the PMSG. Finally, the test set up is shown in Figure 5:24.

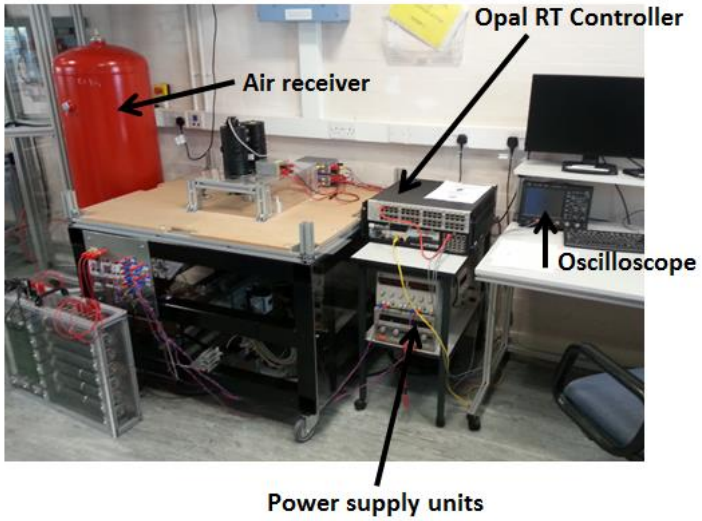


**Figure 5:24: Hybrid Wind Turbine Test Rig**

An oscilloscope is used to visualise sensor signals and for troubleshooting purposes. The Opal-RT controller is the interface between Matlab/Simulink and the hardware and is connected to the host computer via LAN connection.

## *5.6 Summary*

The requirements, the design and manufacturing of the 1*kW* hybrid wind turbine test rig were described in this chapter. The test rig is held flexible so that all operating modes can be realised. In-depth explanations on the design of the PSD with respect to the gear ratio were given. Based on the torque/speed characteristics of the system components, a gear ratio for the PSD of $i = 5$ was regarded adequate. Further gear ratios prior to the PSD are put in place via timing belts to add flexibility to the test rig.

The complete test rig is utilised to validate the system mathematical model and to demonstrate the working principle of the proposed hybrid wind turbine. These two aspects will be described in Chapter 6, along with the system analysis, the control of the system, the efficiency analysis and a feasibility study of a *MW* scale hybrid wind turbine.

# *Chapter 6 - System Analysis and Results*

The working principle of the hybrid wind turbine is explained in this chapter. First, the validation of the hybrid wind turbine's mathematical model is described by comparing the measurement data from the experimental test rig with the simulation results. With the validated model, the controller design is described and the performance of the hybrid wind turbine is investigated. The efficiency analysis of the overall hybrid wind turbine is conducted, which is based on the currently reported individual component efficiencies. The analysis is then extended from the 1*kW* demonstration system to a potential 1*MW* hybrid wind turbine. The chapter ends with a discussion about the potential application of the hybrid wind turbine.

## *6.1 Comparison between Experiment and Simulation Results*

The validation of the whole system mathematical model is described in this section. For doing so, it is essential to know the parameters of the main system components, being the scroll air machine, the PMSG, the Emulator and the PSD. Some parameters were found from the datasheets if available. Further unknown parameters were identified by using measurement data from the component under test (e.g. geometry, electrical resistance/inductance etc.). However, some system parameters are difficult if not impossible to measure directly, such as viscous friction values, so that experimental test rigs are utilised to measure data which will enable the analytical determination of parameters. The experimental test rig and the simulation model are run with the same input signals. Then, the responses of the experimental test and the simulation model are compared against each other, whereas parameters in the simulation model are adjusted to improve the fit between the simulation and the experimental results. The determination of the parameters were conducted manually (trial and error) and automatically through

optimisation algorithms (such as *Genetic Algorithms*). The parameters for the PMSG, scroll air machine, PSD and DC motors are listed in the Appendix D.

In the following subsections the validation results for the mathematical model of the whole hybrid wind turbine are described. The following operating modes are chosen for the validation process:

1.) Direct Compression Mode (HAWT drives the compressor)
2.) Mode A12 (HAWT drives the compressor and PMSG)
3.) Mode B12 (HAWT and air expander drive the PMSG)
4.) Mode C2 (PMSM drives the compressor)

Although these four modes are not all of the possible modes of the hybrid wind turbine, it can be assumed that if the four modes above can be validated, the mathematical model is valid for all possible modes.

### *6.1.1 Direct Compression Mode-HAWT drives the Compressor*

For the *direct compression mode*, the scroll air compressor is driven by the DC motors, which mimics the HAWT. The scroll air compressor charges the air receiver and the pressure in the reservoir builds up over time. As the air pressure in the air receiver increases, so increases the torque required to drive the compressor. The scenario is simulated and tested experimentally under the same input conditions. The input voltage profile to the DC motors is shown in Figure 6:1.

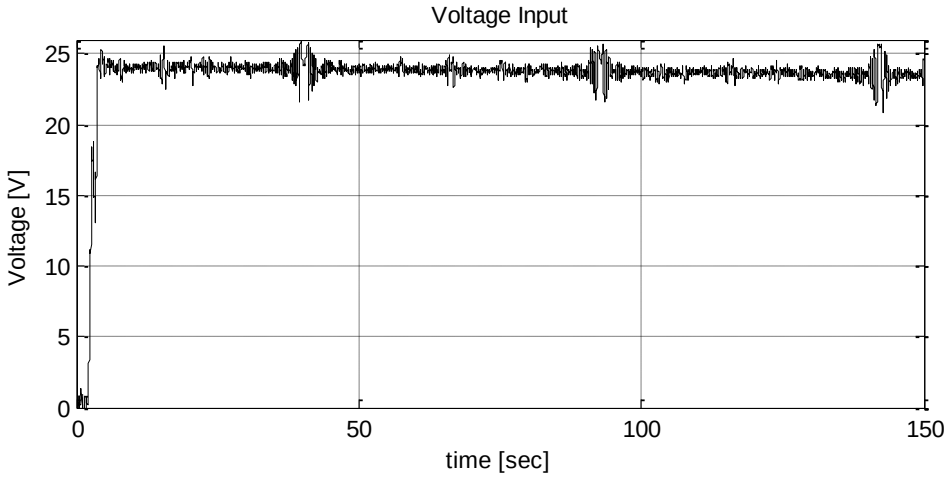


**Figure 6:1: Voltage Input for Direct Compression Mode**

The curve shown in Figure 6:1 is the measured voltage, which was digitally filtered with a low pass filter with a cut-off frequency of $f_c = 2Hz$ to reduce the noise level. It is noticeable that the signal is not even, which was likely be caused by electromagnetic interferences (EMI) within the measurement circuitry. This signal is used as the input signal for the simulation.

The resulting torques of the scroll compressor and DC motors are illustrated in Figure 6:2.

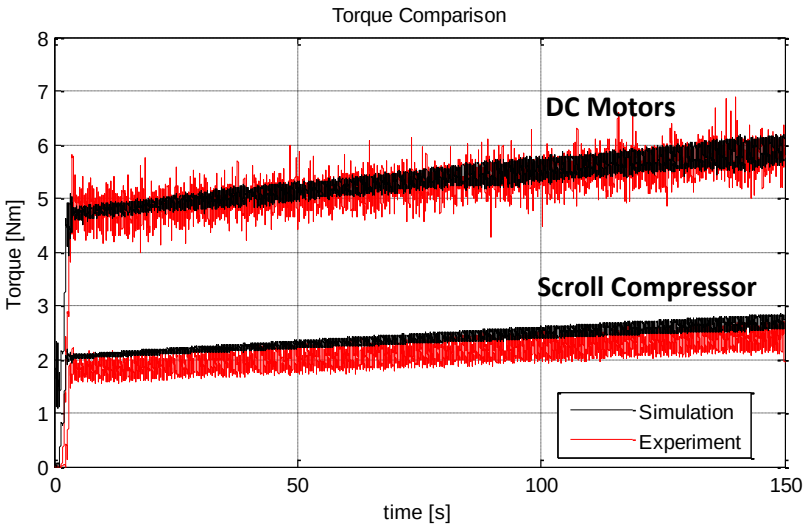


**Figure 6:2: Torque Comparison for Direct Compression Mode**

It can be seen that a reasonable fit between the simulation and experimental results is achieved. The experimental and simulation results were digitally filtered with a low pass

filter with a cut-off frequency of $f_c = 50Hz$ to reduce the noise level while maintaining the system dynamics. The average absolute error, $e_{abs,avg}$, and the average relative error, $e_{rel,avg}$, between the experimental and simulation results are calculated according to Eq. 6:1 and Eq. 6:2:

$$e_{abs,avg} = \frac{|\Psi_{exp} - \Psi_{sim}|}{n} \quad \textbf{Eq. 6:1}$$

$$e_{rel,avg} = \frac{|\Psi_{exp} - \Psi_{sim}|}{n \cdot \Psi_{exp,max}} \cdot 100\% \quad \textbf{Eq. 6:2}$$

with $\Psi_{exp}$, $\Psi_{sim}$ and $n$ representing the experimental data, simulation data and number of samples taken, respectively. $\Psi_{exp,max}$ describes the maximum experimental data value within the time frame given in the test. The average absolute error for the torque response is 0.21*Nm* and 0.3*Nm* for the DC motor torque and scroll compressor torque, respectively. The average relative error accounts to 3.5% and 12%.

It can also be seen that the torque increases over time, which is due to the rising pressure in the air receiver, shown in Figure 6:3.

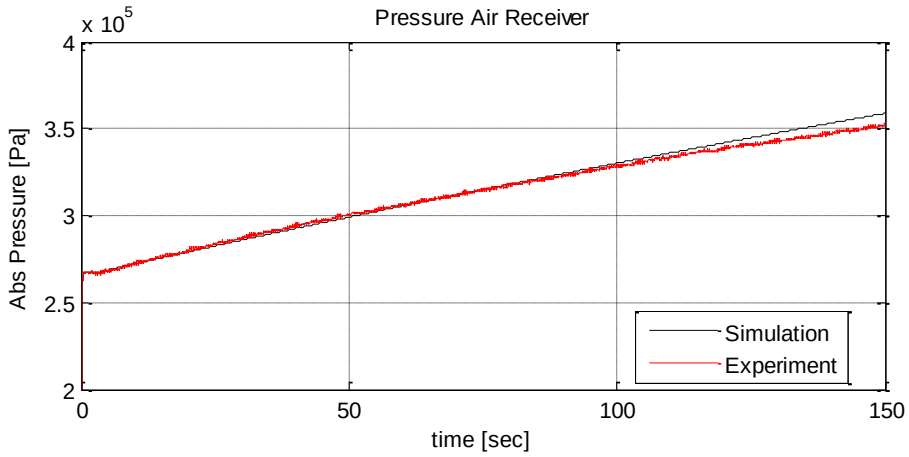


**Figure 6:3: Air Receiver Charging Process with 2.7bar Initial Pressure**

The pressure rise is due to the mass of air that accumulates in the air receiver. The average absolute and relative errors are 2000*Pa* and 0.57%. The maximum achievable air pressure

in the air receiver from the experimental and simulation result was determined to 4.6*bar* and 4.4*bar*, respectively. A deviation of the pressure is noticed at the end of the time frame, which can be explained by the differences in the air mass flow rate between experimental and simulation results. Figure 6:4 shows the air mass flow rate over time.

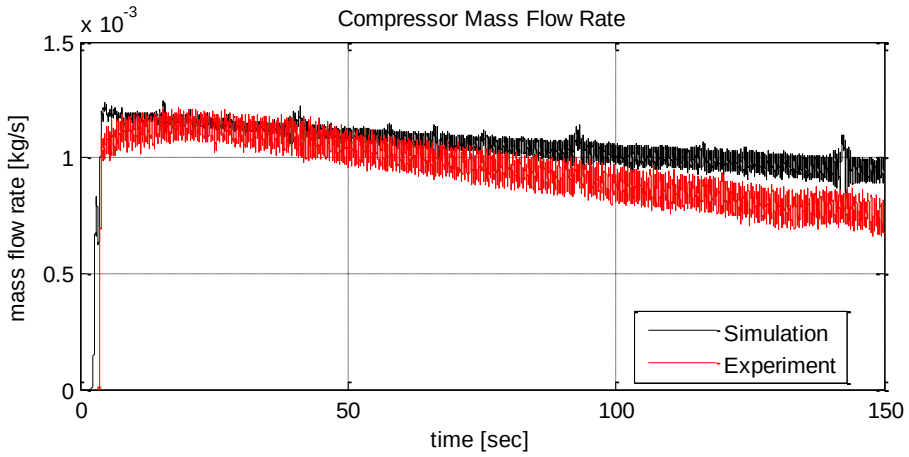


**Figure 6:4: Air mass flow Rate of Compressor**

The air mass flow rate decreases because the increased torque load causes the DC motors to slow down and since the air mass flow rate during the compression is a function of the angular speed, it can be expected that the air mass flow rate decreases with decreasing angular speed. The difference between the experimental and simulation results can be explained by imperfect parameterisation and the air leakage, which was not considered in the simulation. With decreasing speed, the amount of air leaked increases, which might explain the fact why the measured flow rate decreases more in comparison to the simulated air mass flow rate [115]. The average absolute and relative errors of the air mass flow rate between experimental and simulation results are $1.2 \times 10^{-4}$ kg/s and 10%.

The angular speed of the system components is visualised in Figure 6:5.

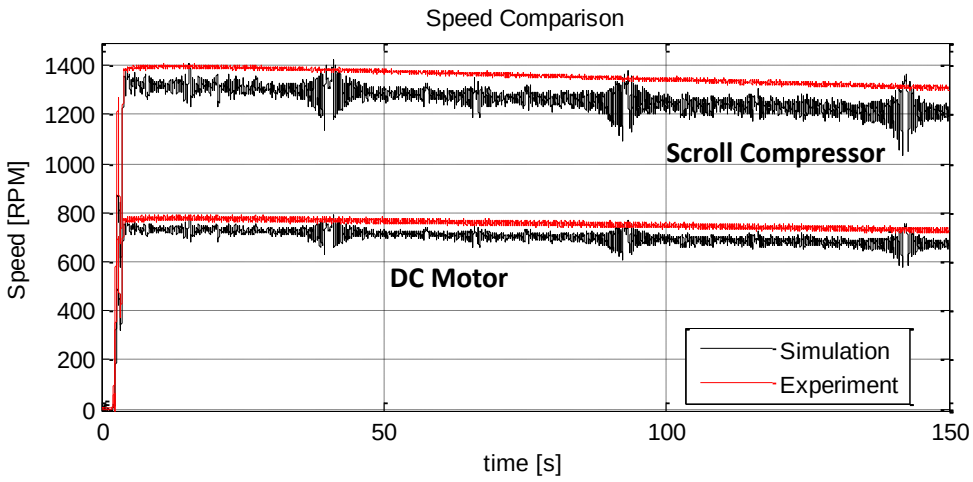


**Figure 6:5: Rotational Speed Comparison DC Motor and Compressor for Direct Compression Mode**

It is noticed that the angular speed decreases as predicted. The noise level from the measured voltage input is also noticeable on the simulation result. The average absolute error for the speed response is 54*RPM* and 93*RPM* for the DC motor speed and scroll compressor speed, respectively. The average relative errors account to 6.7% and 6.6%. A closer view at the transient speed response is given in Figure 6:6.

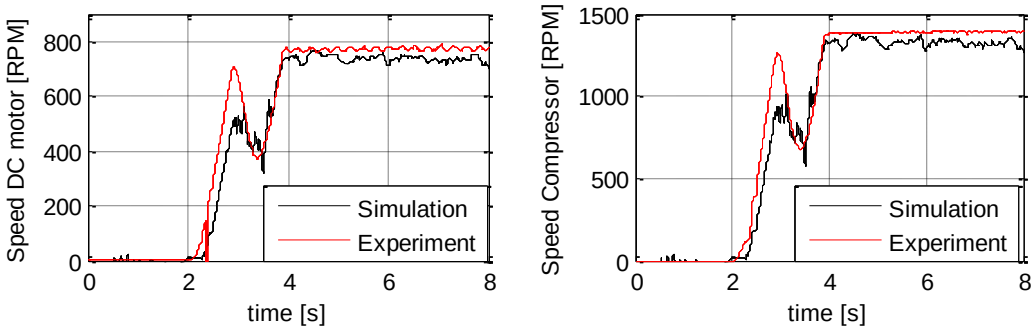


**Figure 6:6: Transient Speed Response for Direct Compression Mode**

An acceptable fit between experimental and simulation result is achieved for both DC motors and compressor. The oscillation during the transient response is caused by the oscillation of the voltage input during the transient area (see Figure 6:1). The experimental results show a greater deflection during the oscillation which might be caused by the belt transmission system that introduces a spring-damper system to the drive train dynamics.

These drive train dynamics were not modelled (see Appendix C.3 for more information regarding drive train dynamics).

Lastly, the temperature of the air exiting the compressor was measured. The measurements and simulation results are shown in Figure 6:7.

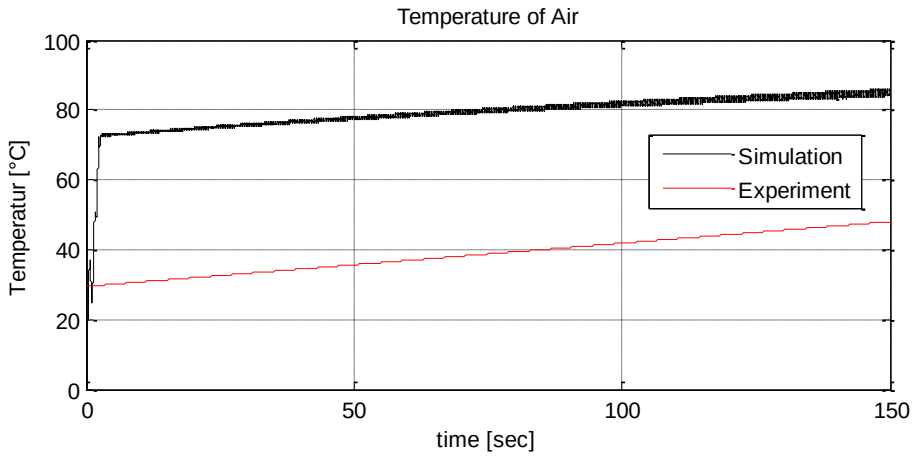


**Figure 6:7: Exhaust Air Temperature Measurement and Simulation Result**

A steady rise in temperature can be seen in both simulation and experiment. A nearly constant deviation of about 40°C is notable, which is due to multiple reasons. The temperature was measured outside the compressor and not within the compressor as done in the simulation model. Additionally, the simulation model does not consider heat losses, which makes the temperature appear higher. Therefore, the experimental and simulated temperature responses are not expected to match. The raise in temperature can be explained by the increasing downstream pressure over time. Higher compression ratios occur within the compressor, which cause the temperature to increase over time.

### *6.1.1 Mode A12-HAWT Drives Compressor and PMSG*

In Mode A12, the power from the DC motors (HAWT) is split into two streams, being the compression stream and PMSG stream. It mimics the scenario in which power oversupply is experienced. The excess power can be used to compress air and store energy for later use.

To validate the mathematical model, a scenario is created with the DC motors powered by a nearly constant voltage of 25V, see Figure 6:8.

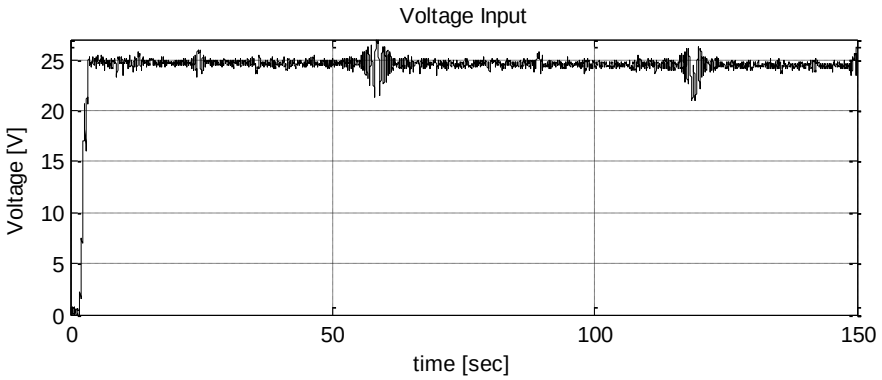


**Figure 6:8: Voltage Input for Mode A12**

The three phases of the PMSG are short circuited to ensure high torque load. To begin with, the torque of the DC motors and the reaction torques from the PMSG and the scroll compressor are shown in Figure 6:9. It needs to be emphasised that the system components' torques are shown and not the torque acting on the PSD.

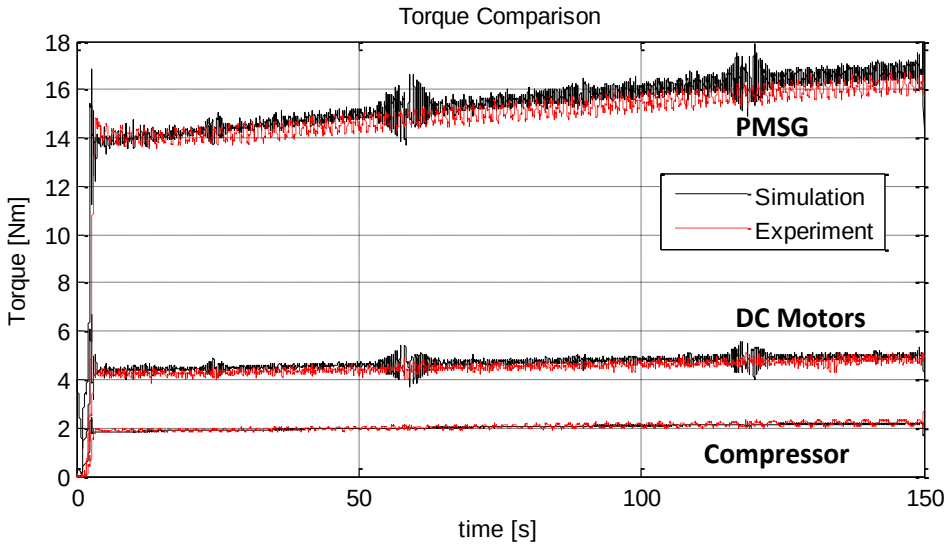


**Figure 6:9: Torque Comparison for Mode A12**

A rising trend in torque for all three components can be observed. This is due to the fact that the compressor charges the air receiver, with the result that the pressure in the air receiver builds up and the load torque of the compressor increases. As the compressor

torque increases, the DC motors start to draw more electric current (torque increases). As a reaction, the PMSG load torque increases, too. The average absolute and relative errors are given in Table 6:1.

**Table 6:1: Errors for Torque Comparison for Mode A12**

| Component | Average Absolute Error | Average Relative Error |
|---|---|---|
| PMSG | 0.99 *Nm* | 6.25 % |
| Scroll Compressor | 0.14 *Nm* | 7 % |
| DC Motors | 0.39 *Nm* | 7.8 % |

The pressure in the air receiver is shown in Figure 6:10.

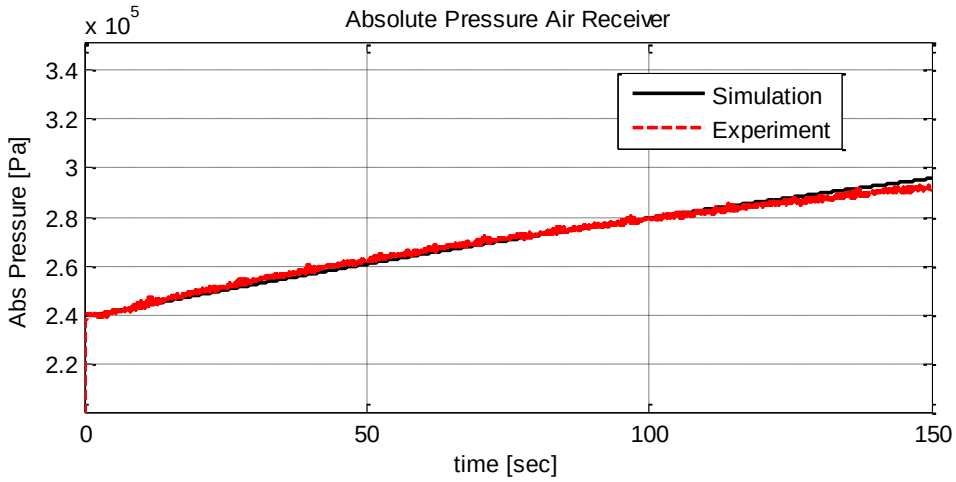


**Figure 6:10: Charging of Air Receiver with 2.4bar Initial Pressure**

The initial pressure at the beginning of the experiment was set to $2.4 \times 10^5 Pa$ (absolute) and over the course of 150sec, the pressure in the receiver increased by approximately $0.6 \times 10^5 Pa$. The average absolute and relative errors are $1400 Pa$ and 0.4%. The increasing load torque during the charging process causes a decreasing angular speed of the system components, whereby the higher the load on the PMSG, the more torque will be

transferred to the compressor and vice versa. The speed comparison is illustrated in Figure 6:11.

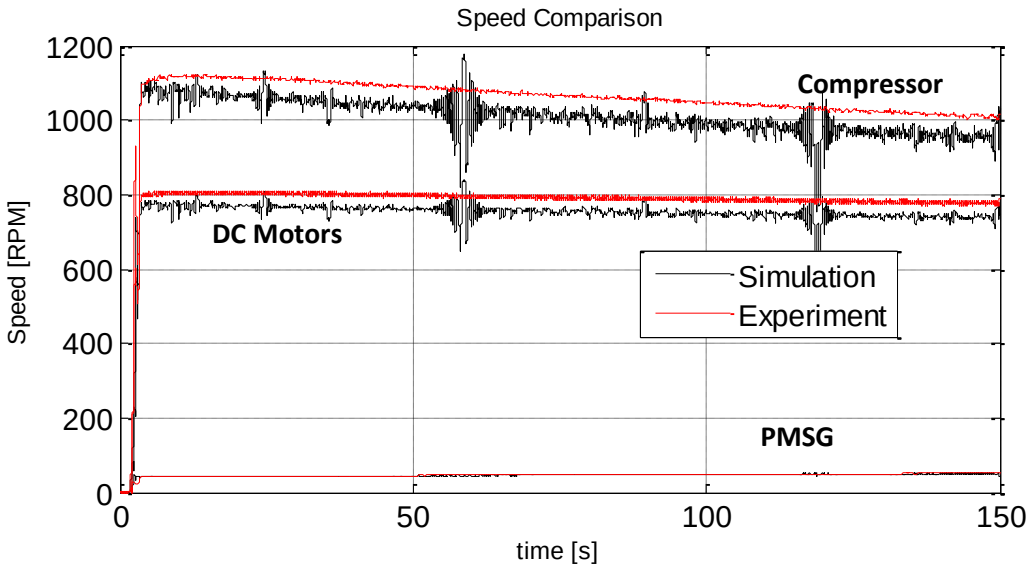


**Figure 6:11: Speed Comparison for Mode A12**

The respective errors are shown in Table 6:2

**Table 6:2: Errors for Speed Comparison for Mode A12**

| Component | Average Absolute Error | Average Relative Error |
|---|---|---|
| PMSG | 1.9 *RPM* | 6 % |
| Scroll Compressor | 87 *RPM* | 7.9 % |
| DC Motors | 48 *RPM* | 7.8 % |

The transient speed response is highlighted in Figure 6:12 to better highlight the system dynamics of the hybrid wind turbine system.

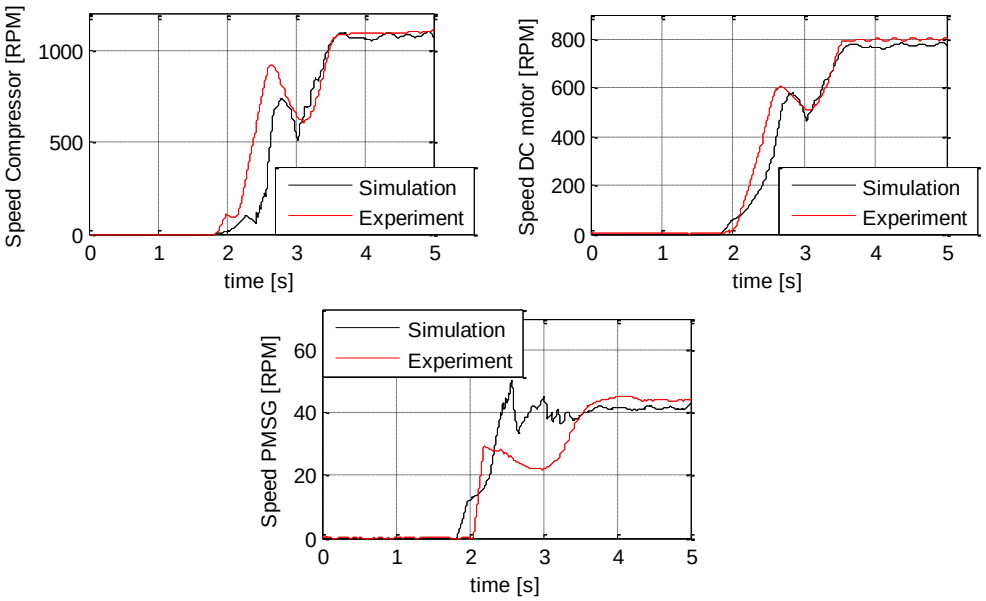


**Figure 6:12: Transient Speed Response for Mode A12**

It can be seen that the simulation results for the compressor speed and DC motor speed represent the real system response relatively well. However, the dynamic speed response of the PMSG shows a significant deviation between experimental and simulation result. The simulated result of the PMSG's speed in the transient area is higher in comparison to the experimental result and is caused by the lower simulated speed response of the scroll compressor. Under given DC motor speed; the slower the scroll compressor rotates, the faster the PMSG's rotational speed.

The plots above show that the mathematical model of the hybrid wind turbine is valid for Mode A12. The incoming power from the DC motors (which mimics the wind turbine) can be split into the compression and PMSG stream so that the air receiver can be charged while electricity is generated.

### *6.1.2 Mode B12- HAWT and Air Expander Drive the PMSG*

In this subsection, it is aimed at the validation of the torque and speed characteristics of the PSD, whereby the scroll expander and the DC motors apply the driving torque to the PSD simultaneously. To illustrate the working principle of Mode B12, various voltage and

air pressure inputs are given to the DC motors and to the scroll air expander, while constant resistive load of 64Ω is applied to the PMSG. The input signals can be seen in Figure 6:13.

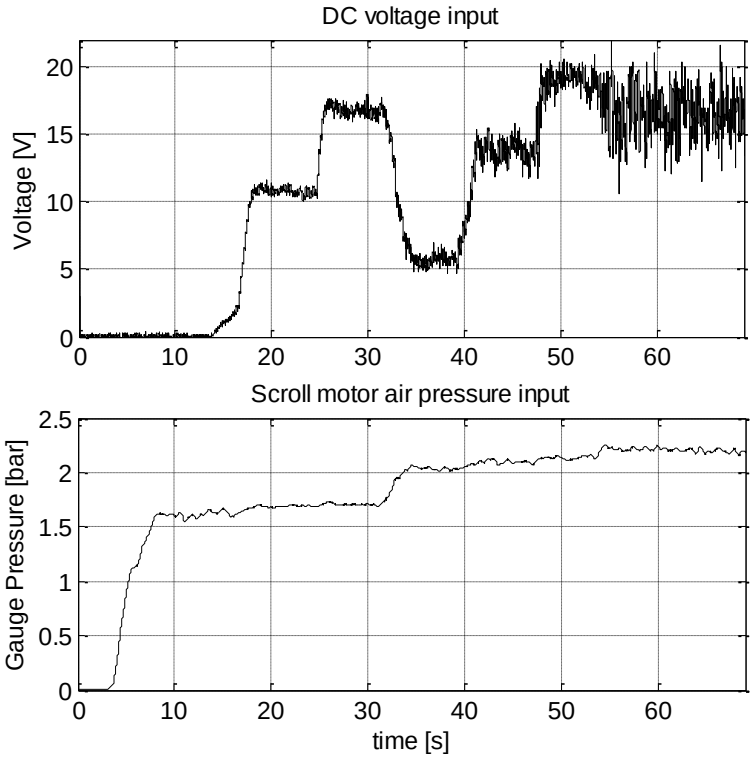


**Figure 6:13: Voltage and Gauge Air Pressure Input**

The input voltage and air pressure were created on the hybrid wind turbine test rig, recorded, digitally filtered and then used as inputs for the simulation study. It can be seen from Figure 6:13 that the input voltage is applied at around $t = 14sec$ and the air pressure is supplied at around $t = 4sec$, meaning that at the beginning the scroll expander drives the PMSG by itself. The corresponding torque and speed of the DC motors, the scroll air expander and the PMSG are measured, so that the experimental and simulation results can be compared. Figure 6:14 shows the torque response of all the three components from the experiment and simulation.

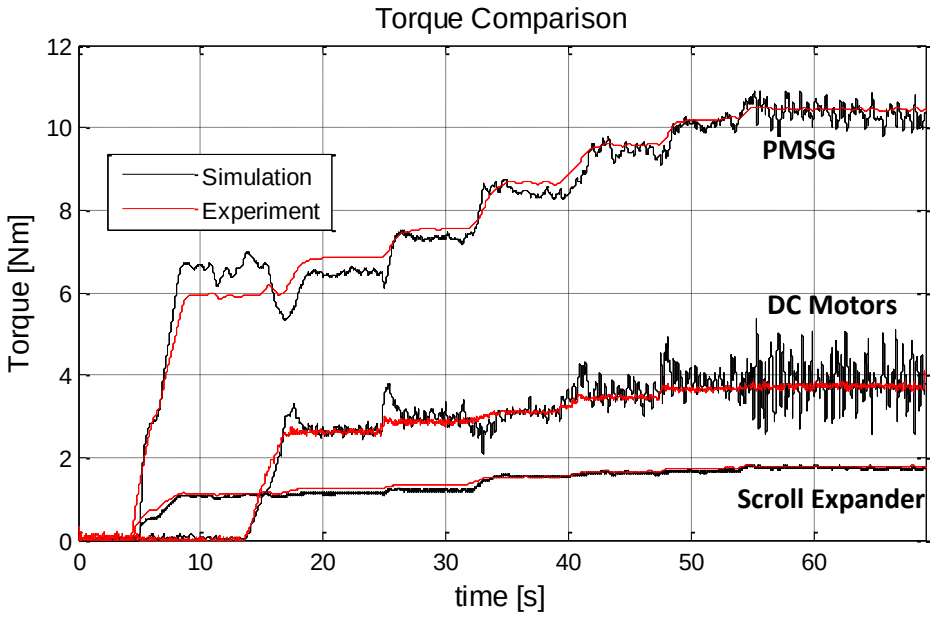


**Figure 6:14: Torque Comparison Simulation and Experimental Test for Mode B12**

From Figure 6:14 it can be seen that a reasonably good fit between the simulation and experimental results are achieved. Table 6:3 shows the average absolute and relative errors between the experimental and simulation results.

**Table 6:3: Errors for Torque Comparison for Mode B12**

| Component | Average Absolute Error | Average Relative Error |
|---|---|---|
| PMSG | 0.28 *Nm* | 2.6 % |
| Scroll Expander | 0.12 *Nm* | 6.3 % |
| DC Motors | 0.19 *Nm* | 4.9 % |

The corresponding angular speeds are shown in Figure 6:15.

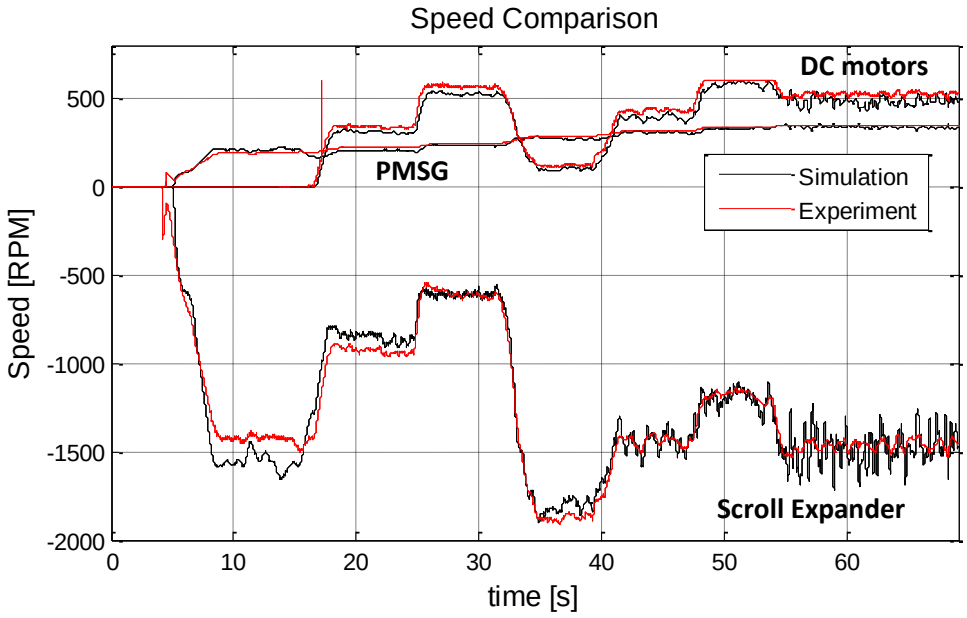


**Figure 6:15: Speed Comparison Simulation and Experimental Test Mode B12**

It can be seen that the scroll air expander's angular speed is negative for Mode B12. The scroll air expander's speed changes significantly within the first 30sec although the input air pressure is kept nearly constant. This is due to the DC motors, which become engaged and add torque to the system. It can also be seen that the DC motor's angular speed decreases at around $t = 32sec$, which is due to the drop in supplied voltage and increase in air pressure at the same time. The scroll air expander speeds up and the system finds its new equilibrium point where all the torques acting on the PSD are balanced. The generator's angular speed and torque increase throughout the experiment, meaning that the power increases constantly. Not only do the torque and speed plots show the interaction between the system components under variable inputs, they also show a good match between the simulation and real physical system performance. The respective errors are shown in Table 6:4

**Table 6:4: Errors for Speed Comparison for Mode B12**

| Component | Average Absolute Error | Average Relative Error |
|---|---|---|
| PMSG | 11.53 *RPM* | 3.8 % |
| Scroll Expander | 58.3 *RPM* | 3.2 % |
| DC Motors | 21.7 *RPM* | 3.9 % |

### *6.1.3 Mode C2-PMSM Drives Compressor*

The aim is to use the PMSG as a motor (PMSM) to drive the compressor, while the wind turbine does not deliver power. It can be expected that the torques on the PSD will cause the wind turbine to spin backwards. For that reason, a sprag clutch is permanently installed on the test rig, which prevents the turbine from spinning backwards.

The difference to the direct compression mode is that the compressor is now driven by the PMSM and not by the DC motors (HAWT). For the test rig, the industrial inverter ABB ACS355 is employed to control the speed of the PMSM. It is important that the PMSM rotates in the opposite direction in comparison to the PMSG operation so that the scroll machine is operated as a compressor. In order to show the functionality of this mode the speed of the PMSM was manually increased through the inverter. The control method of the inverter, $U/f = const.$, which is explained in Section 4.5, is applied in the simulation to mimic the industrial inverter. Figure 6:16 shows the speed of the scroll compressor and the PMSM for both simulation and experiment.

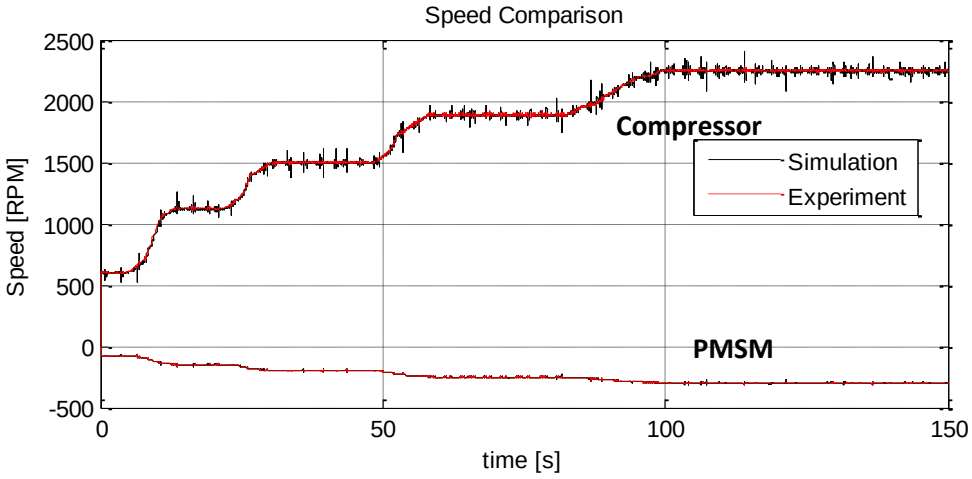


**Figure 6:16: Rotational Speed for Mode C2**

The simulation and experimental results overlap, since the speed of the PMSM is controlled in both simulation and test rig. The gear ratio between the PMSM and the scroll compressor is (-7.5). Note that the PMSM and the scroll compressor rotate in opposite directions.

Since the speed of the PMSM is controlled to a desired level, the PMSM draws electric current according to the load torque. The load is defined by the state of charge of the air receiver. The torque of the PMSM and the load torque of the compressor are illustrated in Figure 6:17.

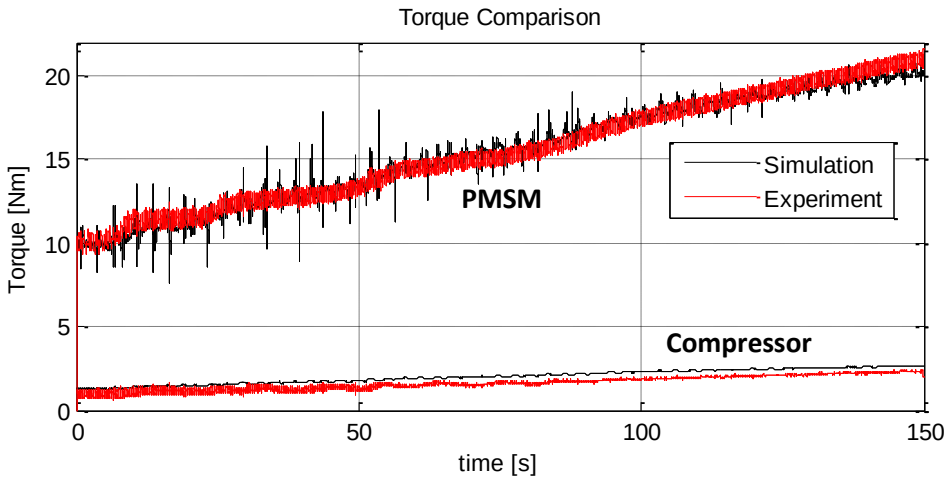


**Figure 6:17: Torque Comparison for Mode C2**

The torque for the PMSM has to account for the compressor's load torque (while taking into account the gear ratio of the PSD) as well as losses that occur within the transmission. The average absolute error for the torque values is 0.47$Nm$ and 0.36$Nm$ for the PMSM torque and the scroll compressor torque, respectively. The average relative errors account to 2.3% and 12%. A rising torque for the time period $t > 100sec$ is noticeable, even though the angular speed of both PMSM and compressor is kept constant. This, again, is due to the increase in air pressure in the air receiver, which causes a higher load torque. The air receiver's air pressure is shown in Figure 6:18.

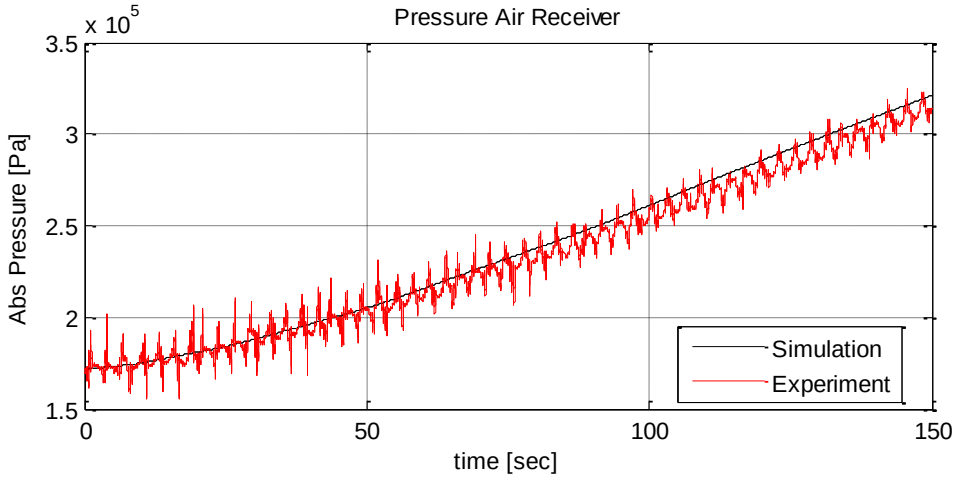


**Figure 6:18: Charging Air receiver for Mode C2**

The experimental result closely matches the simulation result, while showing an average absolute and relative error of 4200$Pa$ and 1.3%.

## *6.2 Control Design*

It is the aim to smooth the electrical power generated by the PMSG under varying wind speed conditions. For example, if the wind speed is not high enough for the HAWT to generate the desired power output, then additional power needs to be added to the system. Contrarily, in moments of power oversupply, the excess power generated from the HAWT should be stored. The device for adding and subtracting power to and from the

system is the scroll air machine. A controller needs to be designed that ensures a desired electrical power generation under fluctuating wind speeds. In the following subsections, the control strategy for Mode B12 and A12 is explained. Concluding remarks are given regarding the control of Mode C.

### *6.2.1 Controller for Mode B12*

The system mathematical model consists of a number of non-linear differential equations. The non-linear properties are associated with mechanical friction, compressibility of air, electromagnetism and wind turbine aerodynamics. In order to analyse the system behaviour, the control strategy analysis starts from a PID controller which is expected to be sufficient at this stage to deliver the desired system performance. The system topology is shown in Figure 6:19.

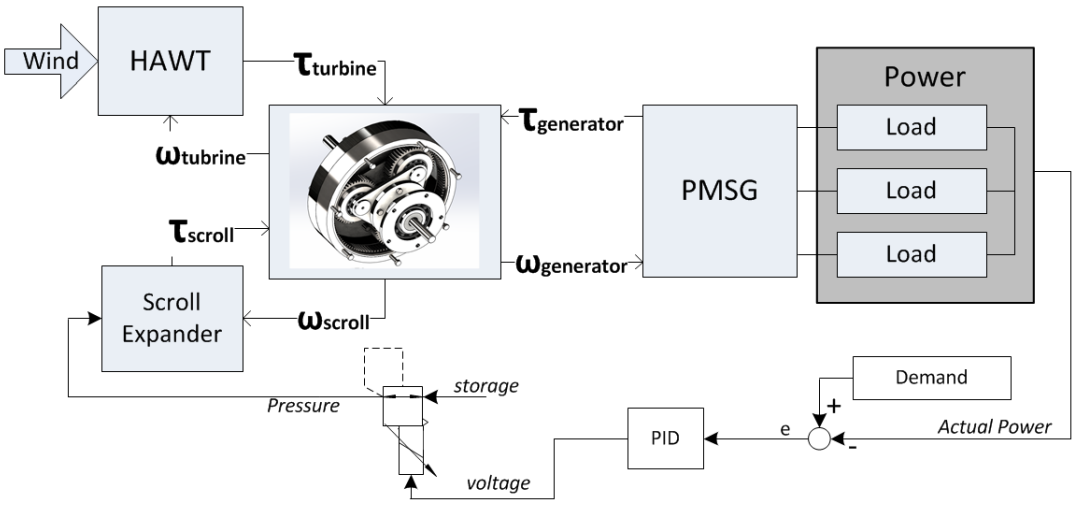


**Figure 6:19: Control Schematic Mode B12**

The electrical power generated is compared against the demand power. The resulting error (*e*) is the input for the PID controller. A solenoid pressure regulator is suggested as the actuator for the scroll expander. It regulates the downstream pressure from the upstream pressure. The pressure input to the scroll expander is regulated with the aim to regulate the scroll expanders torque output.

The control schematic has the benefit of simplicity. However, since the PID controller is designed to track the power demand, it does not take into account the operation of the wind turbine. The torque of the scroll expander is transferred to the PMSG via the planet carrier (connected to the HAWT) of the PSD, meaning that the scroll expander's torque has an impact on the HAWT's operation and power coefficient $C_p$. Further details are given in Section 6.3, where the performance of the control strategy is presented.

### *6.2.2 Controller for Mode A12*

Mode A12 is essential in moments of power oversupply due to high wind speeds. The excess power over the demand needs to be transferred to the scroll compressor. The mechanical power from the wind turbine is split into two paths: the PMSG path and the compressor path. This case is challenging, since the compressor load torque needs to be controlled. However, controlling the load torque of a compressor is uncommon, since compressors are usually designed to operate at rated power. The load torque of the compressor depends mainly on the downstream pressure (that is the pressure in the air receiver), which adds constraints to the control strategy. If the air receiver was fully charged, the torque for compression would be at its maximum and no control can take place. Furthermore, no air would enter the air receiver anymore and the energy consumed by the compressor will be lost in friction, heat, air leakage, and work done on the gas. In that case, the compressor would need to be switched off for security reasons. In the case of an empty air receiver, the load torque may be controlled via a solenoid pressure regulator which is placed downstream of the compressor. This enables the control of the downstream pressure of the compressor and, therefore, the torque required to rotate the compressor. In this way, the load torque for the compression can only be increased, based on the pressure already present in the air receiver. The control schematic is shown in Figure 6:20.

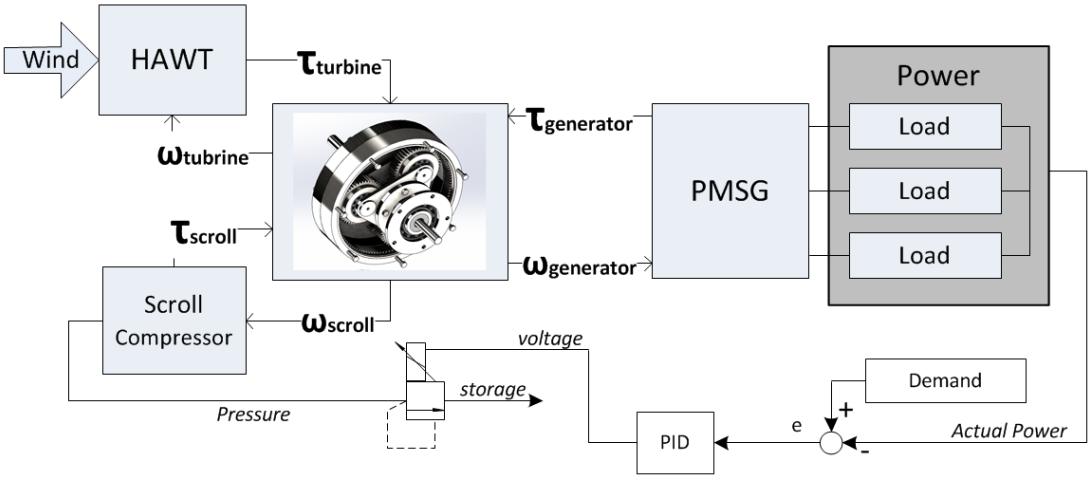


**Figure 6:20: Control Schematic Mode B12**

Figure 6:20 is similar to Figure 6:19, with the difference that a different regulator valve is used. It is important to highlight that this method is unconventional, since the compressor's downstream pressure is increased through the solenoid regulator. Further details are given in Section 6.3, where a discussion of the control strategy is given.

### *6.2.3 Direct Compression and Mode C2*

The control of the direct compression (HAWT drives scroll compressor only) and Mode C2 (PMSM drives the compressor only) are not further discussed in this research. If the compressor is driven solely by the HAWT, the commonly used pitch angle control can be utilised to regulate the power output of the wind turbine. If the compressor is driven by the PMSM, an inverter can be utilised to regulate the PMSM's power output. However, the theory is not further explored in this research.

## *6.3 Operating Scenarios*

In this section, the functionality of Mode B12 and Mode A12 under random wind speed scenarios and predefined power demand is demonstrated. The efficiencies of the system during the operation are also analysed, while highlighting the system benefits and

limitations. The operating scenarios are based on the small scale hybrid wind turbine, for which a HAWT with a rotor diameter of 2.5m is chosen.

### *6.3.1 Mode B12 Operating Scenario*

To demonstrate Mode B12, the electrical power demand must be set higher than the standalone HAWT can provide at a given wind speed. Thus, power must be added to the generator output power via the scroll air expander. The aim is to maintain a desired electric power generation under varying wind speed. The wind speed profile is based on the work reported in [116] and is shown in Figure 6:21.

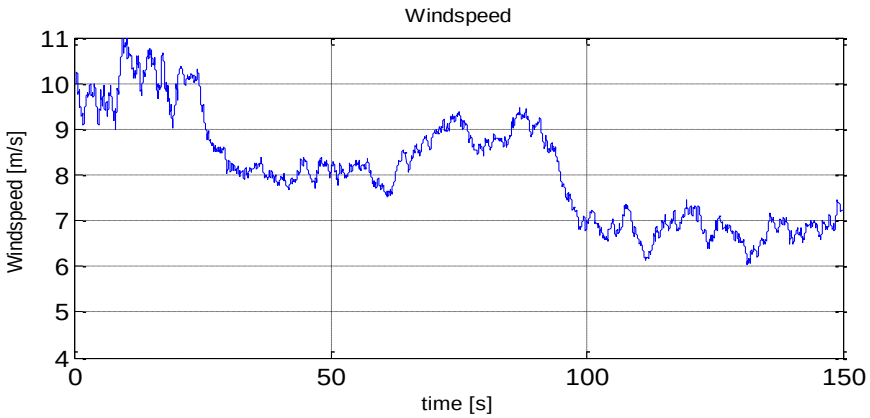


**Figure 6:21: Wind Speed Profile for Mode B12**

The response of the HAWT, scroll air expander and PMSG are of interest, whereby a desired generator power of 1000$W$ is set as the reference value for the first 100 seconds. A step change in demand power to 750$W$ is introduced at $t = 100sec$. Figure 6:22 shows the power, speed and torque responses of the controlled hybrid wind turbine's components. The resistive load for the PMSG is set to 64$\Omega$.

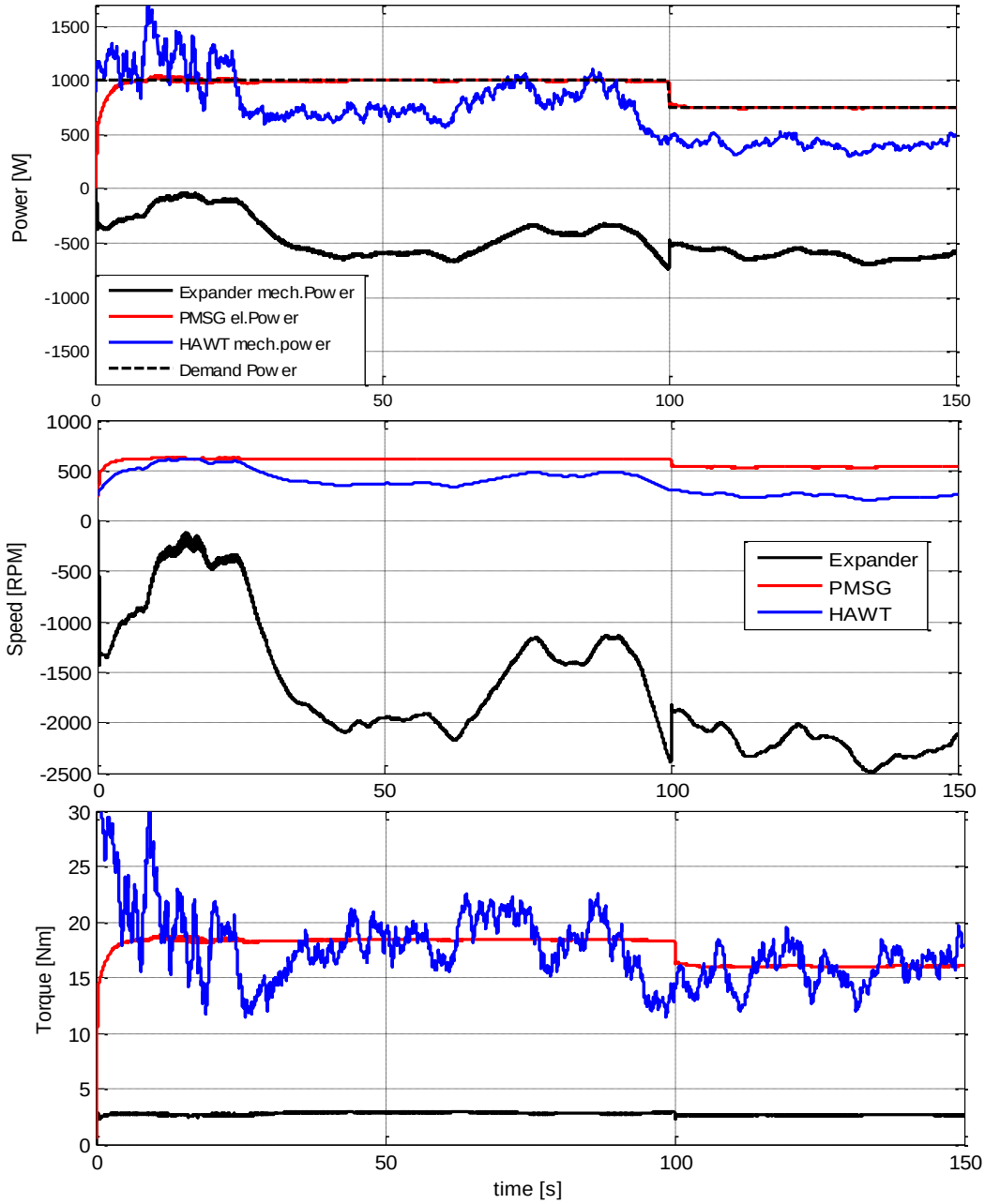


**Figure 6:22: Power, Speed and Torque of the Hybrid Wind Turbine in Mode B12**

From Figure 6:22 it can be seen that the electrical power (PMSG) follows the demand power, despite the HAWT's varying power output. It is evident that the scroll air motor compensates for the lack of wind power due to low wind speed under consideration of mechanical and electromagnetic losses. The air pressure input to the scroll expander is visualised in Figure 6:23, showing that the input pressure is kept in an acceptable range.

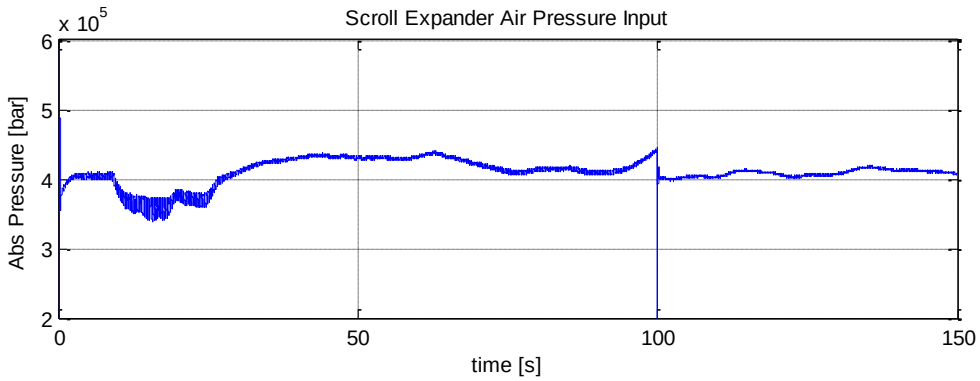


**Figure 6:23: Air Pressure Input for Scroll Expander**

Furthermore, the efficiencies of the system components and the overall efficiency can be calculated with respect to the scenario given above. The calculation of the efficiencies is shown in Subsection 6.4.1. The efficiencies of the system components are shown in Figure 6:24.

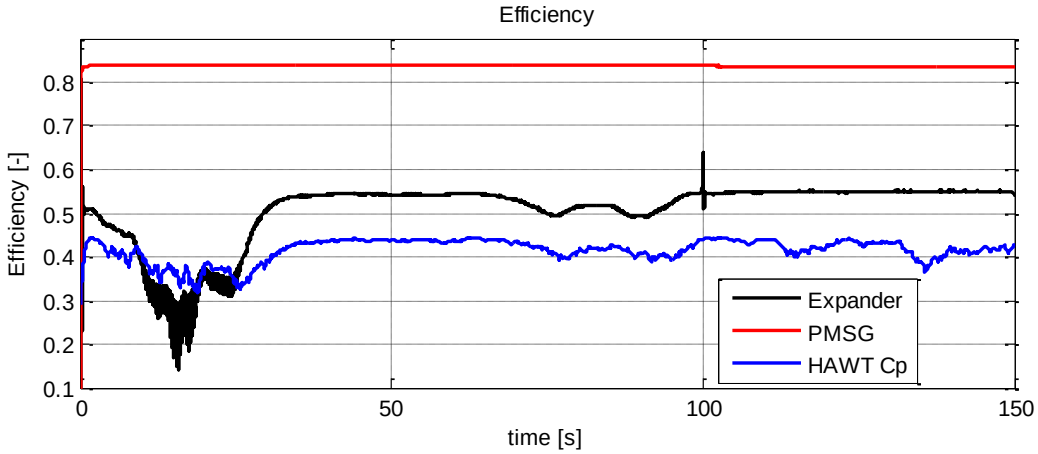


**Figure 6:24: Efficiency of System Components in Mode B12**

Since the PMSG generates the same power under constant load, its efficiency is nearly constant. It is to be highlighted that the HAWT's power coefficient ($C_p$) varies, which is due to the fluctuating wind speed and the additional torque applied to the PSD by the scroll expander. Therefore, it can be seen that the additional torque from the scroll air expander can have an effect on the HAWT's power coefficient. The scroll expander itself operates between 37% and 55% efficiency in this example.

### *Benefits of Mode B12*

Through the wind speed scenario, it is evident that the system functions as predicted. The scroll air expander can add power to the PMSG via the PSD. The scroll air expander uses the HAWT as a counter level to transfer the torque to the PMSG. Thus, the HAWT experiences a greater load torque, which can positively affect the HAWT's power coefficient $C_p$. To visualise this, the power coefficient of the hybrid wind turbine is compared to the power coefficient of a standalone HAWT under the same operating conditions. The wind speed from Figure 6:21 is utilised as the input. The hybrid wind turbine power output is controlled to 1000W for the first 100sec and 750W for the remaining 50sec, whereby the conventional standalone HAWT generates power according to the wind speed input only. The generated power and corresponding power coefficients of both hybrid wind turbine and conventional standalone HAWT are shown in Figure 6:25.

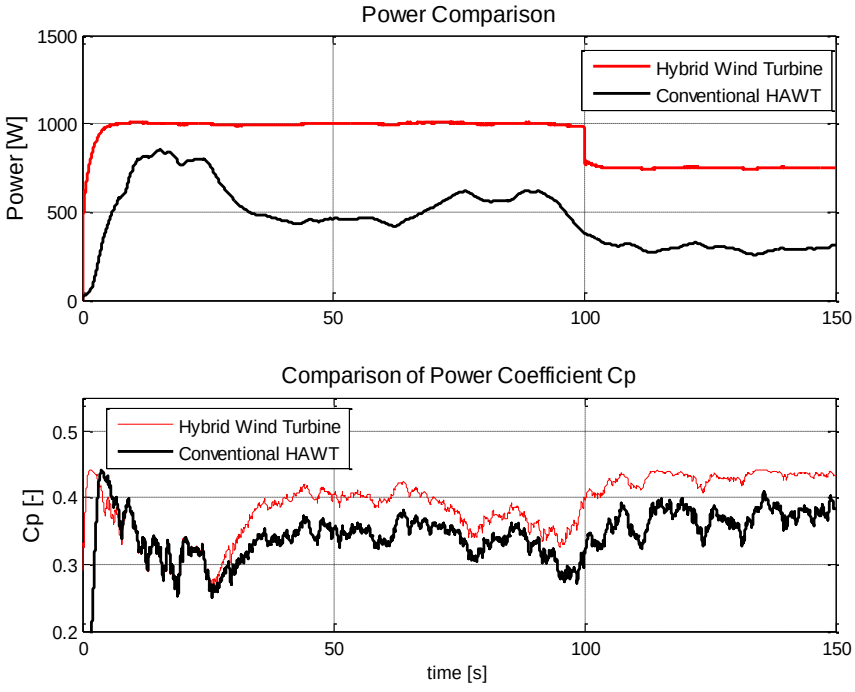


**Figure 6:25: Comparison Hybrid Wind Turbine and Conventional Standalone HAWT**

It can be seen that the hybrid wind turbine operates with a higher power coefficient for most of the time. However, the engagement of the scroll air motor is not always beneficial to the HAWT's power coefficient. Some drawbacks of the system are discussed below.

### *Limitations of Mode B12*

If the combined torque of the PMSG and the scroll expander applied to the PSD cannot be balanced by the HAWT, then the HAWT will slow down and stop rotating. Figure 6:26 shows a scenario in which the mean wind speed drops from 10$m/s$ to 5$m/s$ at $t = 20sec$, whereby the electric power output is controlled to meet 1000$W$.

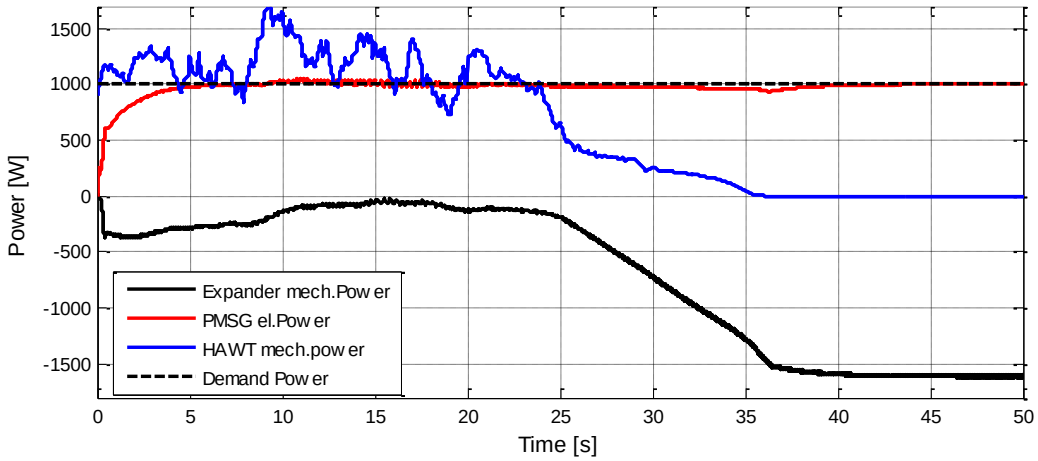


**Figure 6:26: HAWT standstill**

It can be seen that the HAWT comes to a standstill at around $t = 36sec$ and the scroll expander drives the PMSG alone to meet the power demand.

## *6.3.2 Mode A12 Operating Scenario*

To demonstrate Mode A12, the desired electrical power generation is set below the generated wind turbine mechanical power output at a given wind speed. This leads to the case that excess power is generated by the wind turbine. The excess mechanical power can be utilised to compress air through the scroll air compressor. The wind speed profile is shown in Figure 6:27.

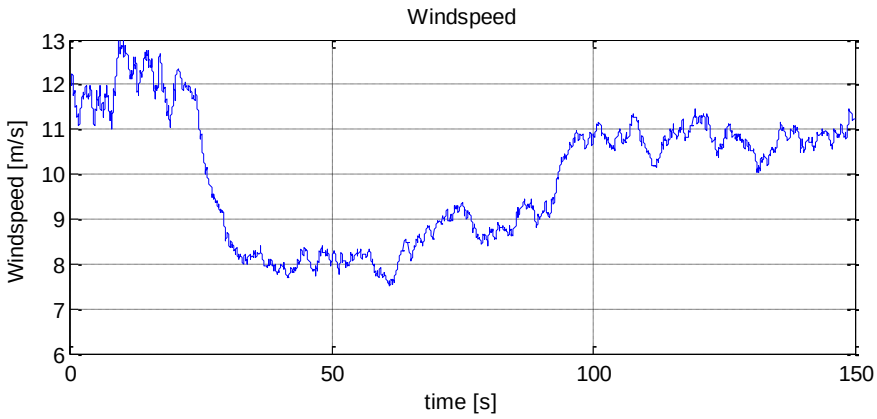


**Figure 6:27: Wind Speed Profile for Mode A12**

The electric power demand is set to 300*W*. That means that any excess power needs to be transferred to the scroll air compressor. Figure 6:28 shows the power, speed and torque response, whereby a 1000 litre air receiver is utilised. The resistive load for the PMSG is set to 22Ω.

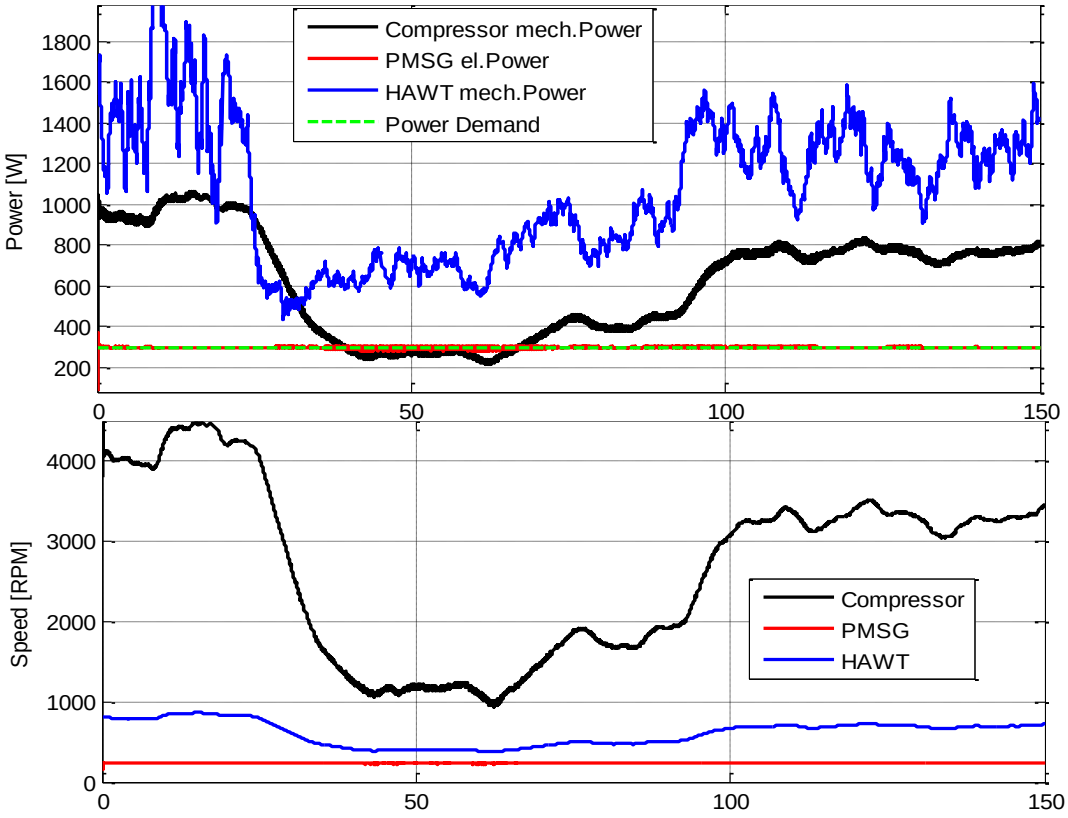

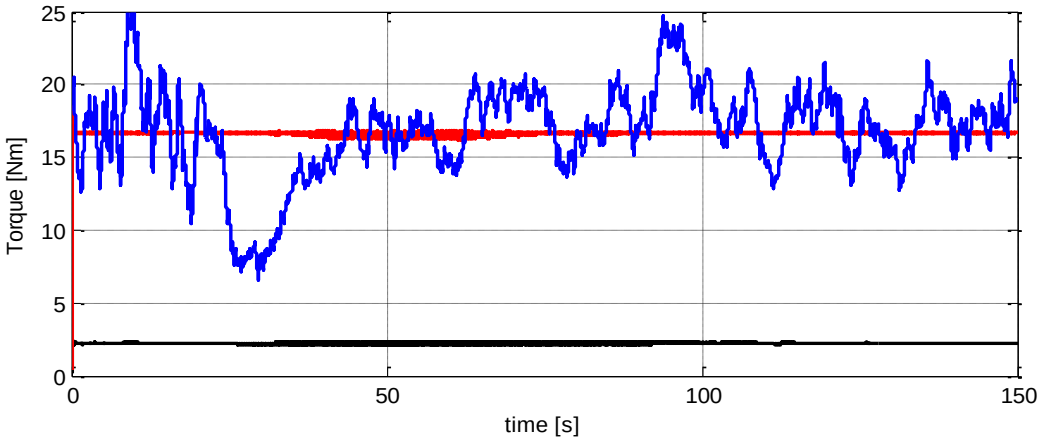


**Figure 6:28: Power, Speed and Torque of the Hybrid Wind Turbine in Mode A12**

From the power plot it can be seen that the desired electrical power generated is met throughout the scenario. The excess mechanical power is used to compress air. The torque of the wind turbine is balanced by the scroll compressor load torque and the PMSG load torque.

The efficiencies of the individual components for the scenario are shown in Figure 6:29.

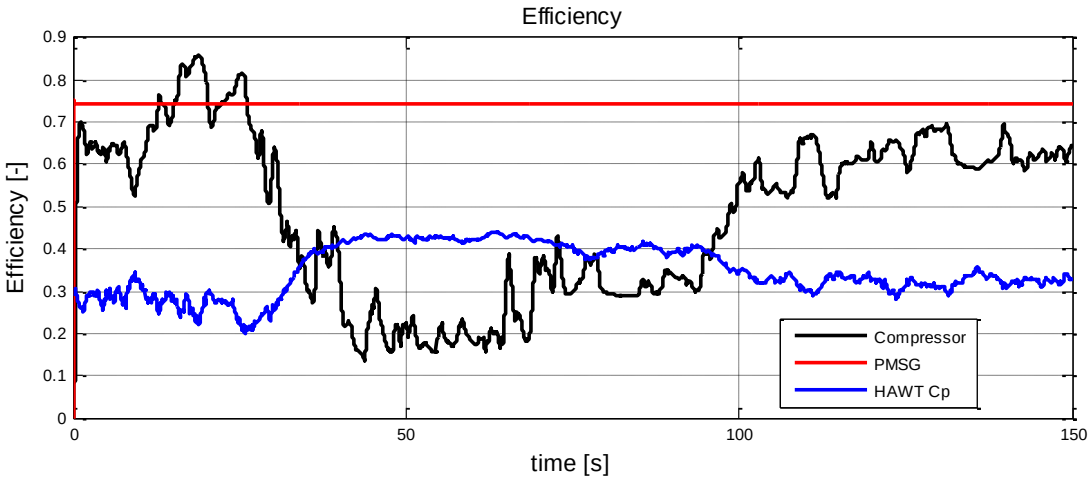


**Figure 6:29: Efficiency of System Components in in Mode A12**

It is notable that the PMSG's efficiency is comparably low; because it is operated far below rated power (rated power is 1*kW*). It can also be seen that the scroll compressor's efficiency ranges from 16% to 85%. The higher efficiencies occur at higher rotational speeds, whereas the efficiency drops significantly at lower rotational speeds (e.g. at around

$t = 50sec$). The reason is that higher volumetric air flow (=higher rotational speed) accounts for more power in compressed air flow. The HAWT's power coefficient is at its maximum from about $t = 40sec$ to $70sec$, due to the fact that the turbine operates at a more efficient tip speed ratio.

### *Mode A12 Benefits*

It has been shown that the power from the HAWT can be split into two streams, the compression stream and the electricity generation stream. Moreover, it has been shown that the PMSG's power output can be controlled by controlling the load torque of the compressor. Therefore, the excess power from the HAWT can be utilised to compress air so that curtailment can be avoided. However, Mode A12 has many disadvantages, which are explained in the following.

### *Mode A12 Limitations*

Some limitations were encountered during the analysis of Mode A12, which are listed below:

a. The control of the load torque is dependent on the state of charge of the air receiver.
b. The amount of torque to drive the compressor is defined by the PMSG's load torque. If the PMSG's load torque is low, then less torque will be available to drive the compressor and the PMSG will rotate faster.
c. Unconventional control applied, i.e. the compressor is not operated at rated design points, but controlled over a range of torque and speed input, resulting in lower efficiencies.
d. The compressor may not achieve the desired pressure ratios, if only a low amount of excess power from the HAWT is transferred to the compressor.
e. The maximum pressure in the air receiver is limited to the maximum pressure of the compressor.

### 6.3.3 Conclusions and Recommendations

It has been shown that the hybrid wind turbine system works well in Mode B12 and power can be added to the system via the expander, while having the possibility to positively impact the HAWT's power coefficient. In contrast, Mode A12 is rather limited in operation and it is suggested that Mode A12 is to be avoided. If a number of hybrid wind turbines are aggregated to form a wind farm and power oversupply is present, then it is recommended to operate a number of hybrid wind turbines in standalone mode and the remaining hybrid wind turbines in direct compression mode. The decision of how many hybrid wind turbines are operated in which mode depends on the wind speed, the electricity demand and the state of charge of the compressed air store.

A further benefit of the hybrid wind turbine is the capability to damp shock loads on the mechanical drive train during wind gusts. The system structure of the PSD allows that shock loads can be compensated through the air machine; thus less mechanical stress is imposed on the drive train. Therefore, the life-time of the hybrid wind turbine can be extended. However, this feature is not further discussed in this research.

## 6.4 Efficiency Analysis

Since the hybrid wind turbine can be operated in many different modes it is impractical to determine a single, overall efficiency for it. In the following, four energy transfer processes are explained:

1. Direct compression (HAWT to compressed air storage)
2. Mode B2 (compressed air to electric power)
3. Mode B12 (Expander and HAWT to electric power)
4. Round-trip Efficiency

In the following efficiency analysis, the best possible efficiencies for the hybrid wind turbine components are assumed to demonstrate the potential of the hybrid wind turbine. Thus, the efficiencies of the components are based on their respective rated powers. In reality, this condition is not possible to appear since the expander/compressor unit, the PMSG, the PSD and the HAWT operate over a wide range outside their designed operating point.

To begin with, the methods of calculating the component's efficiencies are explained.

### *6.4.1 Efficiency Calculation*

The formulas for the efficiency calculation for the scroll air expander/compressor, the PMSG and the HAWT are given in Table 6:5.

**Table 6:5: Efficiency Calculation**

| Description | Formula | |
|---|---|---|
| Scroll expander efficiency | $\eta_{exp} = \frac{P_{mech,s}}{P_{ca}} = \frac{\omega_{exp}\tau_{exp}}{p_a\dot{V}\left(ln\left(\frac{p}{p_a}\right) + \frac{k}{k-1}\left(\frac{T}{T_a} - 1 - \ln\left(\frac{T}{T_a}\right)\right)\right)}$ | **Eq. 6:3** |
| Scroll compressor efficiency | $\eta_{comp} = \frac{P_{ca}}{P_{mech,s}} = \frac{p_a\dot{V}\left(ln\left(\frac{p}{p_a}\right) + \frac{k}{k-1}\left(\frac{T}{T_a} - 1 - \ln\left(\frac{T}{T_a}\right)\right)\right)}{\omega_{comp}\tau_{comp}}$ | **Eq. 6:4** |
| PMSG efficiency | $\eta_{gen} = \frac{P_{el}}{P_{mech,gen}} = \frac{3\frac{u_d^2 + u_q^2}{\sqrt{2}R_{load}}}{\omega_{gen}\tau_{gen}}$ | **Eq. 6:5** |
| HAWT efficiency [9] | $\eta_t = C_p = \frac{P_{mech,t}}{P_{wind}} = \frac{\omega_t\tau_t}{0.5\rho A v^3}$ | **Eq. 6:6** |

The indices $exp, comp, gen$ and $t$ stand for the scroll expander, scroll compressor, PMSG and HAWT respectively. The system variables are explained below:

| | | | |
|---|---|---|---|
| $\eta_{exp}$ | = | Scroll expander efficiency | $[-]$ |
| $\eta_{comp}$ | = | Scroll compressor efficiency | $[-]$ |
| $\eta_{gen}$ | = | PMSG efficiency | $[-]$ |
| $\eta_t$ | = | HAWT power coefficient ($C_p$) | $[-]$ |
| $P_{mech,i}$ | = | Mechanical shaft power | $[W]$ |
| $P_{el}$ | = | Electric power PMSG | $[W]$ |
| $P_{wind}$ | = | Available power in wind | $[W]$ |
| $P_{ca}$ | = | Power in compressed air flow (flow exergy) with respect to atm. conditions | $[W]$ |
| $\omega_i$ | = | Respective shaft speed | $[rad/s]$ |
| $\tau_i$ | = | Respective shaft torque | $[Nm]$ |
| $p, p_a$ | = | Absolute and ambient pressure | $[Pa]$ |
| $T, T_a$ | = | Temperature of air | $[K]$ |
| $\dot{V}$ | = | Volumetric air flow (NAR) | $[m^3/s]$ |
| $u_d, u_q$ | = | Voltage in d-,q- reference frame | $[V]$ |
| $R_{load}$ | = | Resistive load | $[\Omega]$ |
| $\rho$ | = | Air density | $[kg/m^3]$ |
| $k$ | = | Ratio specific heat | $[-]$ |
| $A$ | = | Turbine swept area | $[m^2]$ |
| $v$ | = | Wind speed | $[m/s]$ |

In addition to the efficiencies of the individual system components, the compressed air network losses need also investigation. It is referenced to exergy analysis, whereby the pressure drop in a given pipe causes the losses.

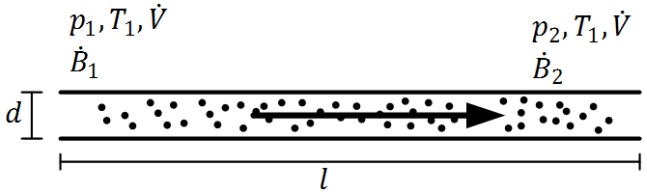


**Figure 6:30: Pipe Losses**

Figure 6:30 shows a generic pipe with a diameter $d$ and length $l$. The pressure drop across the pipe can be estimated by using the empirically established formula described by Eq. 6:7.

$$\Delta p = p_1 - p_2 = 450 \frac{\dot{V}^{1.85} \cdot l}{d^5 p_1} \qquad \textbf{Eq. 6:7}$$

with:

| | | | |
|---|---|---|---|
| $p_{1,2}$ | = | Pressure of air | $[Pa]$ |
| $p_a$ | = | Ambient pressure | $[Pa]$ |
| $\dot{V}$ | = | Volumetric air flow (NAR) | $[m^3/s]$ |
| $d$ | = | Pipe diameter | $[mm]$ |
| $l$ | = | Pipe length | $[m]$ |

Based on the pressure drop across the pipe, the flow exergy loss can be computed:

$$\dot{B}_{loss} = \dot{B}_1 - \dot{B}_2 \qquad \textbf{Eq. 6:8}$$

$$\dot{B}_1 = p_a \dot{V} \left( ln\left(\frac{p_1}{p_a}\right) + \frac{k}{k-1}\left(\frac{T_1}{T_a} - 1 - \ln\left(\frac{T_1}{T_a}\right)\right)\right) \qquad \textbf{Eq. 6:9}$$

$$\dot{B}_2 = p_a \dot{V} \left( ln\left(\frac{p_2}{p_a}\right) + \frac{k}{k-1}\left(\frac{T_2}{T_a} - 1 - \ln\left(\frac{T_2}{T_a}\right)\right)\right) \qquad \textbf{Eq. 6:10}$$

with:

| | | | |
|---|---|---|---|
| $\dot{B}_1$ | = | Flow exergy before | $[W]$ |
| $\dot{B}_2$ | = | Flow exergy after | $[W]$ |

| | | | |
|---|---|---|---|
| $p_a$ | = | Ambient pressure | $[Pa]$ |
| $T_{1,2}$ | = | Temperature of air | $[K]$ |
| $T_a$ | = | Ambient Temperature | $[K]$ |
| $k$ | = | Ratio specific heat | $[-]$ |

### *6.4.2 Maximum Efficiency for Direct Compression*

Figure 6:31 shows the energy transfer for the direct compression.

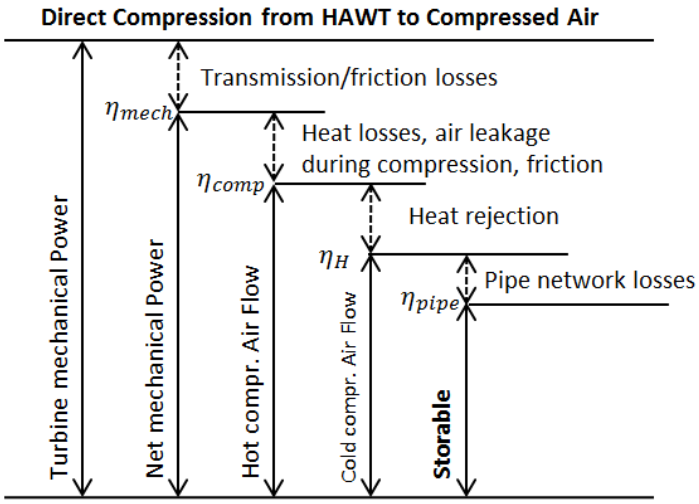


**Figure 6:31: Energy Transfer for Direct Compression from HAWT to Compressed Air**

The solid arrows define the available power after each conversion. The dashed lines represent the losses. Note that the length of the arrows does not correspond to the amount of power or losses. Based on the HAWT's available mechanical power, losses occur within the mechanical transmission due to friction in bearings and the gear box. The net mechanical power is then converted to compressed air by the compressor, where power is split into heat generation and compressed air generation, while undergoing losses due to heat flow to the surroundings, friction and air leakage. The high temperature of the compressed air must be reduced since air receivers, vessels or caverns underlie temperature limitations of the compressed gas inside it. The rejection of heat through heat exchangers reduces the available compressed air flow power. The compressed air flows

into the air receiver, while undergoing losses due to pressure drops in the piping network.

The overall efficiency for the direct compression can be summarised to the following:

$$\eta_{HAWT-store} = \eta_{mech}\eta_{comp}\eta_{H}\eta_{pipe} \quad \textbf{Eq. 6:11}$$

Realistic efficiency values are summarised in Table 6:6.

**Table 6:6: Maximum Efficiency Estimation for Direct Compression from HAWT to Compressor**

| *Name* | *Description* | *Value* | *Source* |
|---|---|---|---|
| $\eta_{mech}$ | Efficiency of mechanical transmission (bearings, gear box) | 0.95 | [91, 99] |
| $\eta_{comp}$ | Compression efficiency (heat losses, air leakage, friction), expressed as isentropic or polytropic efficiency depending on the type of compression | 0.85 | [117] |
| $\eta_{H}$ | Reduction of compressed air flow power due to the rejection of heat through heat exchangers | 0.65 | From exergy analysis |
| $\eta_{pipe}$ | Pipe network efficiency taking into account losses due to pressure drops, depending on air mass flow rate, operating pressure, length and diameter of pipes | 0.99 | [62] and exergy analysis[9] |
| $\eta_{HAWT-store}$ | Charging efficiency from HAWT to compressed air storage | 0.52 | N/A |

An overall charging efficiency from the HAWT's mechanical power to stored energy can be estimated to 52%.

### *6.4.3 Maximum Efficiency for Mode B2*

The energy transfer from the storage via the expander to electric power is shown in Figure 6:32.

[9]. For the example above the efficiency calculation is based on a 700m long pipe with a diameter of 50mm, a volumetric flow rate of 680l/s (FAD) and 56bar pressure.

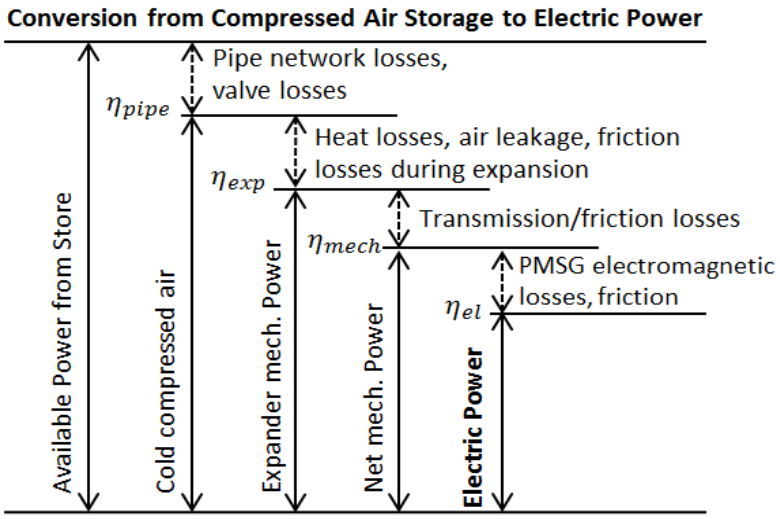


**Figure 6:32: Energy Transfer from Compressed Air to Electric Power**

The energy conversion from the compressed air storage to electric power is subject to several losses. Pipe network losses and control valve losses occur at the compressed air stage. During the conversion from compressed air flow power to mechanical power, losses occur in the form of temperature drop, air leakage and mechanical friction. Additionally, mechanical transmission losses through the gear box and bearings further reduce the available power. Finally, electromagnetic losses and mechanical friction losses within the PMSG occur. The overall efficiency of the energy transfer from compressed air energy storage to electric energy can be expressed as follows:

$$\eta_{store-el} = \eta_{pipe}\eta_{exp}\eta_{mech}\eta_{el} \qquad \textbf{Eq. 6:12}$$

**Table 6:7: Maximum Efficiency Estimation for Mode B2**

| *Name* | *Description* | *Value* | *Source* |
|---|---|---|---|
| $\eta_{pipe}$ | Pipe network and control valve efficiency, taking into account losses due to pressure drops, depending on air mass flow rate, operating pressure, length and diameter of pipes | 0.98 | From exergy analysis |
| $\eta_{exp}$ | Efficiency of compressed air flow energy to mechanical energy through expander, expressed as isentropic or polytropic efficiency depending on the type of expansion | 0.80 | [117] |
| $\eta_{mech}$ | Efficiency of mechanical transmission (bearings, gear box) | 0.95 | [91, 99] |

| | | | |
|---|---|---|---|
| $\eta_{el}$ | PMSG efficiency | 0.95 | [99] |
| $\eta_{store-el}$ | Total efficiency from store to electricity | 0.71 | N/A |

If best case efficiency values are chosen, as shown in Table 6:7, the overall efficiency for the energy conversion from stored compressed air to electric power amounts to about 71%.

### *6.4.4 Efficiency for Mode B12*

The energy transfer Mode B12 in which the expander and the HAWT contribute to the generator power output can be described my means of Figure 6:33.

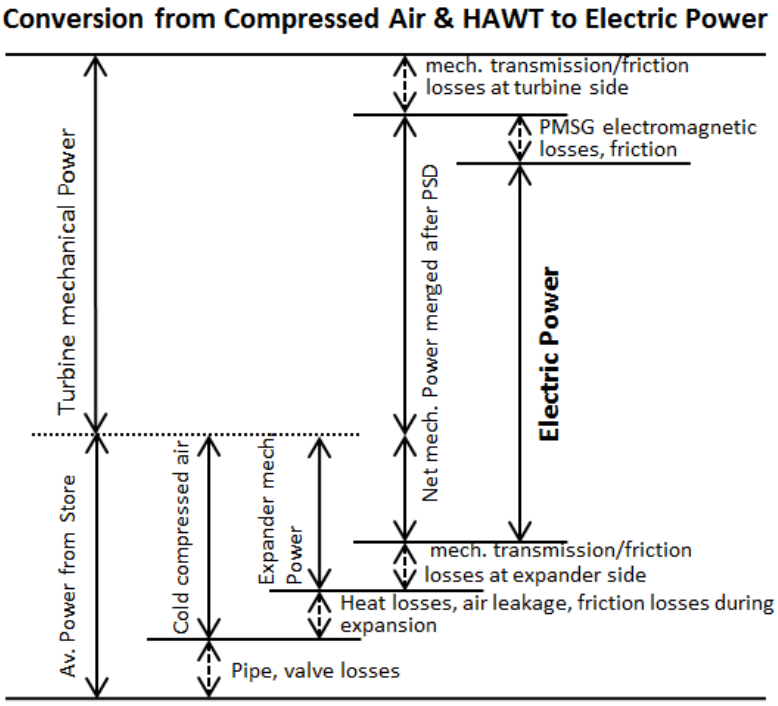


**Figure 6:33: Energy Conversion from Storage and HAWT to Electric Energy (Mode B12)**

It can be seen that the electric power is a sum of the available power from compressed air and the HAWT's mechanical power, reduced by various losses as indicated in Figure 6:33. In this case it is impractical to define an overall efficiency, since the overall efficiency depends on the ratio of the energy contribution between storage (less efficient) and HAWT mechanical energy (more efficient).

### 6.4.5 Round-Trip Efficiencies

The round-trip efficiency $\eta_{HAWT-store-el}$ from the HAWT's mechanical power to stored energy and from stored energy to electric power can be computed to:

$$\eta_{HAWT-store-el} = \eta_{HAWT-store} \cdot \eta_{store-el} \cdot 100\% = 36.8\% \quad \textbf{Eq. 6:13}$$

To give an example, the potential wind power, which otherwise would have been curtailed, can now be utilised at a later time with an overall efficiency of 36.8%, provided the system components operate at the efficiencies stated in Table 6:6 and Table 6:7.

## 6.5 Extension to 1MW Hybrid Wind Turbine

In previous sections, the small scale hybrid wind turbine application is investigated. However, the small scale versions of both mathematical simulation and experimental test rig aimed at the demonstration and validation of the hybrid wind turbine's working principle. In this section, the potential extension to a 1*MW* hybrid wind turbine is studied. The chosen components such as the generator, the HAWT and the expander/compressor unit are explained first. These components must be connected to the PSD, of which an explanation is given. At the end of this section, a performance analysis is given, describing the power and energy flow of the 1*MW* hybrid wind turbine example.

### 6.5.1 Selection of System Components

Conventional wind turbine systems have nameplate power ratings that are based on their installed generator. However, the wind turbine itself is capable of providing more power, which is throttled via pitch control as soon as the rated generator power is exceeded (see Section 2.1.1). For the hybrid wind turbine, a 1*MW* generator and an adequately sized HAWT are considered. This has the effect that the hybrid wind turbine can operate independently from the CAES facility. As to the compressed air part, the maximum size of a scroll air expander was found to be 50*kW* [83]. A single scroll air expander of that size

would not be sufficient and would contribute only 5% power in comparison to the rated generator power. As mentioned in Section 3.3.2, screw expander/compressor units are more suitable for *MW* applications and, therefore, screw air machines are considered for the 1*MW* hybrid wind turbine. The selection of the components is discussed more in detail in the following.

### *A. Generator*

For the generator, a 1*MW* PMSG is selected. Its parameters are chosen based on the work reported in [118] and are listed in Table 6:8.

**Table 6:8: 1MW PMSG Parameter**

| Parameter of 1MW PMSG | | Value |
|---|---|---|
| $\omega_{gen}$ | Rated mechanical rotational speed | $100rpm$ |
| $T_{gen}$ | Rated torque | $96kNm$ |
| $p_n$ | Number pole pairs | $60$ |

### *B. HAWT*

The data for the HAWT is extracted from the technical specifications of a WWD1 wind turbine and can be found in [119]. The main specifications are shown in Table 6:9.

**Table 6:9: HAWT Parameter**

| Parameter of HAWT | | Value |
|---|---|---|
| $\omega_t$ | Rated rotor speed | $23rpm$ |
| $T_t$ | Rated torque | $550kNm$ |
| $P_t$ | Rated Power | $1.3MW$ |
| $R_b$ | Rotor radius | $28m$ |
| $v_{in}$ | Cut-in wind speed | $3m/s$ |
| $v_{rated}$ | Rated wind speed | $12.5m/s$ |
| $v_{out}$ | Cut-out wind speed | $20m/s$ |

### *C. Air Expander/Compressor*

The air expander/compressor unit requires special attention, and knowledge from the hybrid wind turbine demonstration test rig can be utilised to select an adequate air expander/compressor for the 1*MW* hybrid wind turbine. The following aspects need to be considered:

1) The nameplate power rating of a compressor does not correspond to the power rating of the same device when used as an expander.
2) A large amount of heat energy is expected during the compression depending on the pressure ratio and the law of compression.
3) The volume ratio of the device can be assumed constant so that the maximum outlet pressure of the compressor should be the minimum inlet pressure for the expander to avoid under-expansion (if isothermal compression and expansion is considered). That also means that the pressure in the air receiver after charging will not be high enough to drive the expander.

A commercial 250$kW_{el}$ screw compressor unit made by *Atlas Copco* named G250-7.5 50Hz is taken as an example for the further investigation. The compressor technical specifications are shown in Table 6:10.

**Table 6:10: Technical Specifications of G250-7.5 50Hz**

| Parameter of 250kW Screw Compressor | | Value |
|---|---|---|
| $P_d/P_u$ | Compression ratio | 7.5 |
| $\dot{V}$ | Volumetric air flow FAD[10] | $681 l/s$ |
| $\dot{W}_{el}$ | Rated power for installed eMachine | $250 kW$ |
| $\omega_{el}$ | Rated rotational electric speed | $50 Hz$ |

To overcome the issue raised in *Point 3* described above, it is proposed to engage two screw machines to the sun gear of the PSD, whereby the compression will take place in

[10] Free Air Delivery: Actual volumetric air flow converted back to inlet conditions, i.e. 1 bar and 20°C

series. In that way a maximum pressure of $(7.5 \cdot 7.5)bar = 56.25bar$ can be achieved. Figure 6:34 shows an example calculation of the two screw compressors placed in series.

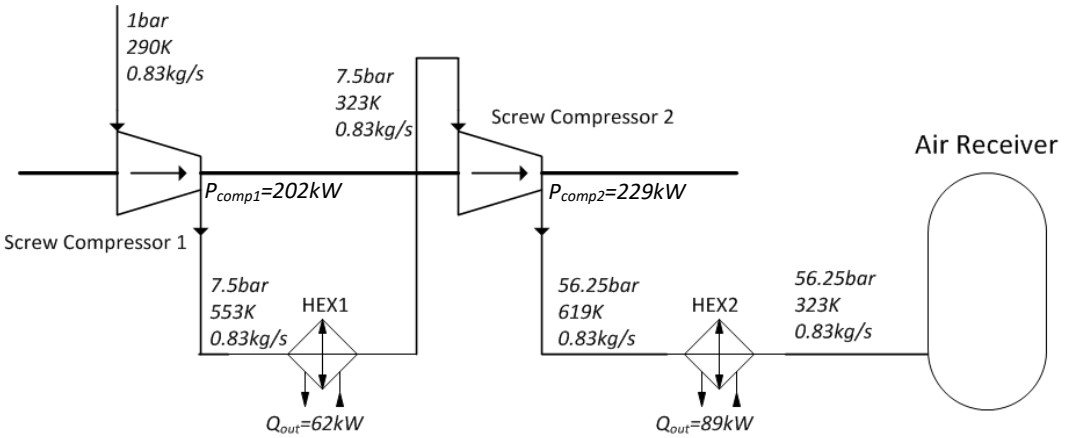


**Figure 6:34: Compressor Calculation for 1MW Hybrid Wind Turbine (HEX=Heat Exchanger)**

For the temperature and pressure values shown in Figure 6:34, isentropic compression with an isentropic efficiency of 0.85 is assumed, whereby the compressed air is cooled down to 323K after every compression stage. The power and torque to drive the compressors is listed in Table 6:11, assuming mechanical friction losses of 5%.

**Table 6:11: Performance Estimation of 2 Screw Compressors in Series**

| Performance Estimation of 2 Screw Compressors | | Value |
|---|---|---|
| $P_{comp}$ | Mechanical power to drive compressors | $490kW$ |
| $\omega_{comp}$ | Rated speed compressor | $1500rpm$ |
| $T_{comp}$ | Torque required for compression | $3130Nm$ |
| $\dot{Q}_{HEX}$ | Heat rejected at heat exchangers | $151kW$ |

The same analysis must be conducted for the expansion process. Figure 6:35 shows the diagram of the two expanders including an example calculation for an isentropic efficiency of 75%.

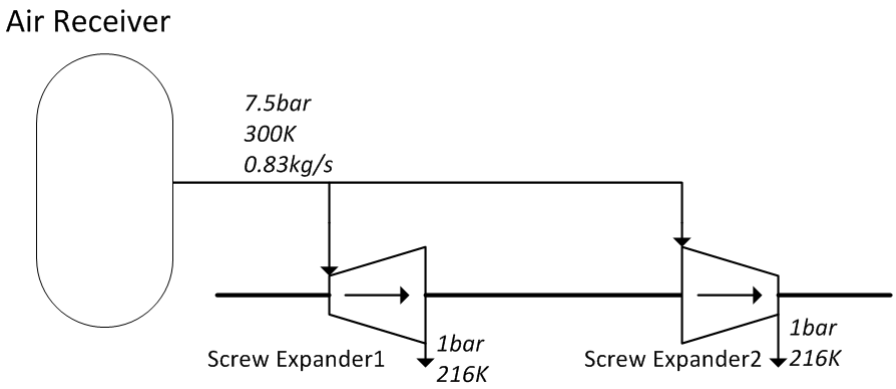


**Figure 6:35: Expander Calculation for 1MW Hybrid Wind Turbine**

Furthermore, Table 6:12 shows the performance data of the screw expanders if used in series.

**Table 6:12: Performance Estimation of 2 Screw Expanders in Series**

| Performance Estimation of 2 Screw Expanders | | Value |
|---|---|---|
| $P_{exp}$ | Mechanical power | $250kW$ |
| $\omega_{exp}$ | Speed | $1500rpm$ |
| $T_{exp}$ | Torque | $1514Nm$ |

## *D. Storage Air Receiver*

The stored energy is dependent on the volume of the store and the temperature as well as the pressure state of the air inside it. For a single hybrid wind turbine, aboveground steel storage vessels seem to be more cost effective than underground storage caverns. Commercially available air storage vessels can be found in sizes of several hundred cubic metres (see [120]). The stored energy in a compressed air vessel with respect to its volume is shown in Figure 6:36, whereby the storage temperature is assumed to be 290$K$ with a working pressure range of 7.5$bar$ to 56$bar$.

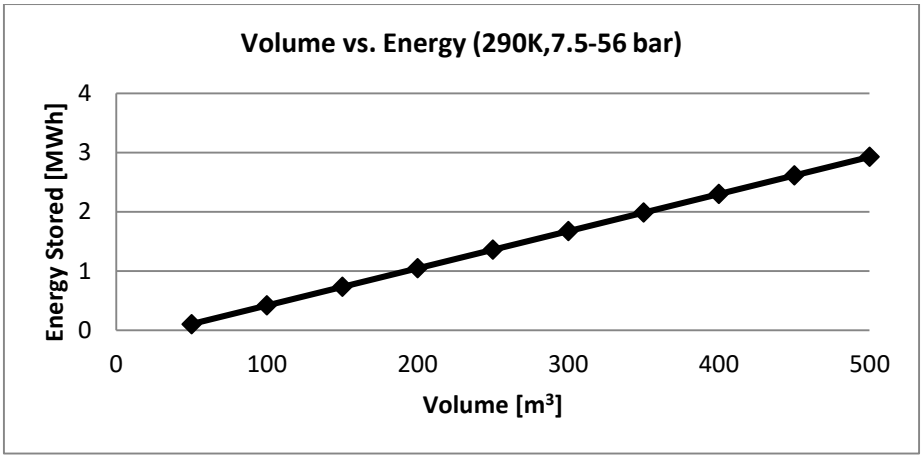


**Figure 6:36: Stored Energy vs. Storage Volume for 290K and 7.5-56bar**

As can be seen, the stored energy changes linearly with increasing storage volume. For example, if a storage volume of 500m$^3$ is chosen, a storage capacity of about 3*MWh* is available.

### *6.5.2 Mechanical Transmission System*

The gearing of the transmission system is crucial for the hybrid wind turbine's functionality. As to the PSD, the planet carrier needs to compensate for the sun gear's (expander/compressor) and the ring gear's (PMSG) torque. Since the HAWT and the expander/compressor unit as well as the PMSG have different torque/speed characteristics, various additional gearing prior to the PSD needs to be accommodated. At any time, the mechanical powers of all system components need to be balanced so that $P_{PMSG} + P_T + P_{exp/comp} = 0$, if no losses are considered. Figure 6:37 shows the chosen schematic for the 1*MW* hybrid wind turbine transmission system.

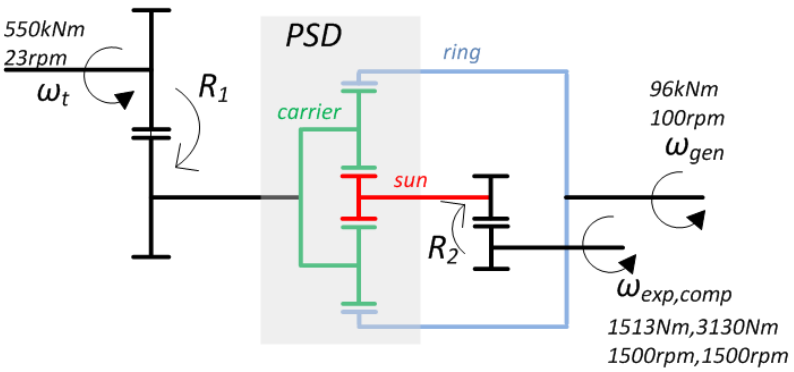


**Figure 6:37: Mechanical Transmission Structure of 1MW Hybrid Wind Turbine**

It can be seen that the rated values for the HAWT, PMSG and expander/compressor unit are labelled. The gear ratios $R_1$ and $R_2$ are determined via simulation study to 3.6 and 0.1, respectively. That means that the carrier shaft rotates 3.6 times faster than the HAWT shaft. The sun gear rotates 0.1 times as fast as the expander/compressor shaft. The PMSG is connected to the ring gear without gear ratio.

### *6.5.3 Performance Analysis*

The technical specifications of the hybrid wind turbine are summarised in Table 6:13. The gear box efficiency is set to 95%.

**Table 6:13: Technical Specifications of 1MW Hybrid Wind Turbine**

| | ***HAWT*** (at 12.5m/s) | ***PMSG*** | ***Expander*** | ***Compressor*** |
|---|---|---|---|---|
| **Rated Power** | 1.3*MW* | 1*MW* | 240*kW* | 490*kW* |
| **Rated Speed** | 23*RPM* | 100*RPM* | 1500*RPM* | 1500*RPM* |
| **Rated Torque** | 550*kNm* | 96*kNm* | 1513*Nm* | 3130*Nm* |
| **Vessel size** | 500$m^3$ | | | |
| **Storage Capacity** | 3*MWh* | | | |
| **Time Charging** | ≈ 11*hrs* (at 1500*RPM*, 626 *l/s* FAD) | | | |
| **Time Discharge** | ≈ 5*hrs* (at 1500*RPM*, 626 *l/s* FAD per expander) | | | |

Examples of operating scenarios are given below.

## *A. Standalone Wind Turbine Operation*

Steady state results are given in Table 6:14, showing the electrical power output with different wind speed inputs.

**Table 6:14: Performance Data of Hybrid Wind Turbine in Standalone Operation**

| *Wind Speed* | | *Power [kW]* | *Torque [Nm]* | *Speed [RPM]* |
|---|---|---|---|---|
| 8m/s | HAWT | 347 | 212000 | 15.6 |
| | **PMSG** | **327** | **55000** | **56** |
| 10m/s | HAWT | 659 | 289000 | 21.8 |
| | **PMSG** | **621** | **76000** | **78** |
| 12.5m/s | HAWT | 1208 | 385000 | 30 |
| | **PMSG** | **1139** | **101000** | **108** |

## *B. Mode B12*

A further example is shown for the case in which the HAWT and the expander drive the PMSG together. Table 6:15 shows the steady state results for different wind speed inputs. Note that the expander is not controlled and random power from the expander is added to the system to demonstrate the working principle. In any case, the HAWT power plus the expander power should amount to the PMSG electric power minus losses.

**Table 6:15: Performance Data of Hybrid Wind Turbine in Mode B12**

| *Wind Speed* | | *Power [kW]* | *Torque [Nm]* | *Speed [RPM]* |
|---|---|---|---|---|
| 0m/s | HAWT | - | - | - |
| | Expander | 250 | 994 | 2400 |
| | **PMSG** | **236** | **49700** | **48** |
| 8m/s | HAWT | 294 | 284000 | 11.75 |
| | Expander | 157 | 1326 | 1133 |
| | **PMSG** | **426** | **66300** | **65** |
| 10m/s | HAWT | 627 | 341000 | 17.5 |
| | Expander | 328 | 1900 | 1652 |
| | **PMSG** | **903** | **94800** | **96** |
| 11m/s | HAWT | 836 | 358000 | 22 |
| | Expander | 225 | 1992 | 1078 |
| | **PMSG** | **1003** | **99000** | **101** |

### C. Direct Compression Mode

Lastly, an example is given in which the HAWT compresses air directly without engagement of the PMSG (see Table 6:16). It shows that 12.5m/s wind speed are required to drive the compressor at full power, which occurs when the storage air receiver reaches its full capacity (56 *bar*).

**Table 6:16: Direct Compression Example**

| *Wind Speed* | | *Power [kW]* | *Torque [Nm]* | *Speed [RPM]* |
|---|---|---|---|---|
| 12.5m/s | HAWT | 1290 | 593000 | 20.7 |
| | Compressor | 1226 | 3146 | 3700 |

## 6.6 Potential Applications

The potential applications for the hybrid wind turbine are organised into technical and economic aspects, whereby it is referred back to Chapter 2, in which the challenges posed on the network operation caused by increased wind power and potential services from CAES for wind power integration are outlined. Quantitative economic analysis is not carried out in this research. The potential cost effectiveness and advantage over conventional CAES plants in combination with wind power are highlighted.

### 6.6.1 Technical Aspects

The functionality and benefits of the proposed hybrid wind turbine are demonstrated in previous sections. The hybrid wind turbine shows flexibility in operation in scales of a few *kW* up to 1*MW* and provides intrinsic CAES capability. In Section 2.4, the main properties of wind power and the impacts on the power network operation are described and in Section 2.5 the options for CAES to support wind power integration are covered. The hybrid wind turbine can help overcome the impacts on the network operation from the undesired properties of wind power (Section 2.4), while making use of the applications and services CAES can offer (Section 2.5). The undesired wind properties are *variability, uncertainty,*

*non-synchronous generation, location constraints*, *modularity* and *low short-run costs*. In some cases, wind power must be curtailed due to network constraints or stability and security issues, which are possible consequences of the increased wind power exploitation. With the hybrid wind turbine, three of the aforementioned properties of wind power can be dissolved: *variability, location constraints* and *modularity*.

### *Variability*

Variability of wind power can be reduced by aggregating conventional wind turbines over a large geographical area. However, when aggregated to a larger system, wind power will still show variability in power generation [8]. A fleet of *MW* scale hybrid wind turbines with intrinsic CAES capability can reduce the variability in wind power by controlling the power output on a turbine level. In moments of excess wind power, a number of hybrid wind turbines with a shared compressed air storage cavern or separate storage vessels can operate in direct compression mode, whereas the remaining hybrid wind turbines operate in standalone mode. This is advantageous over conventional CAES plants, since the compression is done directly through the wind turbine rotor. Switching the operating mode of the hybrid wind turbines gives more flexibility and the compression stage is assumed to be more efficient due to the fact that the compressor is driven by the HAWT's mechanical power and not electrical power. In fact, for conventional CAES applications, it cannot be determined whether the power comes either from wind resources or other power plants or both, which may pose disadvantages regarding financial revenue streams.

### *Location constraints*

The intrinsic compression of the hybrid wind turbine will relieve bottlenecks in the network so that expensive network upgrades can be avoided (also referred to as grid congestion relief). The wind farm investor often finances the connection to the grid and accepts curtailment with the aim to reduce expensive transmission capacity. With the hybrid wind

turbine, the transmission capacity could be reduced, while avoiding curtailment, since excess power could be utilised to store compressed air without converting it into electricity first. In contrast to the conventional CAES plant, the storage process often depends on the transmission capacity between the storage plant and the wind farm [65]. If the transmission between the wind farm and the CAES plant is congested, then the full potential of the CAES cannot be exploited and wind power must be curtailed.

#### *Modularity*

Smaller generators are connected to the distribution grid rather than the transmission grid. This can cause several problems since the traditional role of the distribution grid was to supply electricity to the consumer, whereas now it also hosts power generation which is rapidly increasing in form of wind power, solar power or CHP [121]. A fleet of hybrid wind turbines can support the network operation by providing more flexibility. The power output of a hybrid wind turbine fleet can be controlled, while offering storage capacity. The store can even be charged without wind power, but by utilising the wind turbine generator as a motor. Therefore, excess power can be stored using the hybrid wind turbine, thus relieving the strain especially in the distribution grid, where wind power is more likely to be employed.

To conclude, the hybrid wind turbine offers valuable flexibility from the technical viewpoint. Power supply for remote communities and industries with more predictable power demand are potential applications. Especially remote areas with poor power network connections, but that are rich in wind energy resources, can benefit from the hybrid wind turbine system.

### *6.6.2 Economic Aspects*

In terms of the commercial argument, the hybrid wind turbine in connection with CAES has the opportunity to create numerous financial benefits. Section 2.5 describes options for

CAES to support wind power integration into the network, such as wind energy time shift, wind capacity firming, reduced output variability, transmission congestion relief, back-up for unexpected wind generation shortfall and reduced minimum load violations. In addition, the hybrid wind turbine offers even more opportunities since it combines wind power with storage. Due to legislatively driven incentives for wind power development, there is an existing urge to encourage energy storage similarly. For example, a market could be created involving *firm* renewable energy. The combination of wind power and storage can be valued and priced as a premium product. Furthermore, Renewable Obligation Certificates (ROCs) could be assigned to the storage function if the storage can demonstrate the support in renewable energy development and operation. Moreover, improved operation of other generation units due to reduced cycling is a further benefit option. After all, the hybrid wind turbine can facilitate in reducing $CO_2$ emissions. This is the case if it helps the development of more renewables than would be built without the storage option. In contrast to conventional CAES plants, it depends on the resources used for the compression cycle and the resources displaced during the discharge of the storage. In a wholesale market, during off-peak it is likely that compression energy comes from baseload plants and wind whereas during on-peak times it is likely that conventional resources like coal and gas are replaced. For the hybrid wind turbine, however, it can be proven that the store was charged with wind power only.

## *6.7 Summary*

The overall mathematical system models were validated using measurements from the experimental test rig. It is concluded that the mathematical models describe the real physical system well in terms of analysing the system dynamic responses and steady state values. It has to be mentioned that a perfect fit between measurement data and simulation result is not desired, but instead correct trends and good alignments with the

measurement data are acceptable. This is due to the large number of uncertain parameters for the system components, complexity of the hybrid wind turbine system, simplifications in modelling approaches and by taking into account tolerances within sensor measurements and the data acquisitioning system. The whole system test has proven that the hybrid wind turbine system works as intended, especially with respect to the PSD.

A control strategy was then introduced for operating Mode A12 and B12. It was shown that the hybrid wind turbine system works well in Mode B12 and power can be added to the system via the expander, while having the possibility to positively impact the HAWT's power coefficient. In contrast, Mode A12 is rather limited in operation and it is suggested that Mode A12 is to be avoided.

Then, the efficiency analysis for the hybrid wind turbine was conducted based on the individual component efficiencies currently achieved. The overall round-trip efficiency, i.e. the ratio between the electric energy generated and the HAWT's mechanical energy, after all energy has passed through storage, was reported to be 36.7%.

A preliminary study was conducted concerning a 1*MW* hybrid wind turbine for which two screw expanders/compressors are utilised. Two screw machines are connected to the sun gear of the PSD, whereby the compression process must happen in series whilst the expansion process happens in parallel. The initial study indicates that the system is feasible from the mechanical transmission viewpoint for a 1*MW* hybrid wind turbine with a storage capacity of 3*MWh*.

The proposed hybrid wind turbine is particularly useful to the distributed and isolated power network. Especially remote areas with poor power network connections, but that are rich in wind energy resources, could benefit from the hybrid wind turbine system. The

variability, the modularity and location constraints of wind power could be addressed and dissolved with the proposed hybrid wind turbine.

# *Chapter 7 - Conclusions and Further Work*

## *7.1 Conclusions*

Increased electricity generation from renewable energy resources is considered as one of the top priority strategies worldwide for reducing greenhouse gas emissions. One of the "20-20-20" targets established by the European Commission is to commit the UK to achieving a share of 15% renewable energy among the gross energy consumption by 2020. Following this, the currently installed wind power capacity of 13.3*GW* in the UK will need to increase to about 22*GW* by 2020. However, wind power is variable by nature and the power generated cannot be determined with certainty due to inaccuracies in weather forecasts. The expected penetration levels of wind power will pose great challenges to the operation of the power network. In the absence of power network flexibility, wind power will experience costly curtailment due to network capacity constraints along with system stability and security reasons. Energy storage is considered as one of the possible means to provide more power network flexibility. Among various energy storage technologies, Compressed Air Energy Storage (CAES) is recommended as an environmentally friendly, scalable, and low maintenance technology with comparably low operational costs. In this project a novel hybrid wind turbine augmented with intrinsic CAES provision was designed and studied. The project was proposed to explore the potential solutions in supporting wind power generation and power network integration. The goal was to investigate whether the new structure of a hybrid wind turbine is feasible and what the added benefits are.

Literature about existing and proposed hybrid wind turbines, which are relevant to this project, has been critically reviewed. The reviewed hybrid wind turbines predominantly aim to add flexibility to the wind turbine system so that wind power can be controlled to some

extent. Following the literature review, the proposed hybrid wind turbine of this project is introduced. It comprises of a Power Split Device (PSD) in the form of a planetary gear box that merges the drive shaft of a Horizontal Axis Wind Turbine (HAWT), a Permanent Magnet Synchronous Generator/Motor (PMSG/PMSM), and a scroll expander/compressor machine. The hybrid wind turbine can operate in standalone mode, i.e. the direct connection of the wind turbine shaft with the generator, while exhibiting the opportunity to control the generator output power by engaging CAES. In moments of wind power oversupply, the surplus power can be utilised to compress air, while in moments of wind troughs and high power demand, power can be added via the air expander. Additionally, the hybrid wind turbine offers standalone energy storage provision, meaning that the turbine generator can be operated as a motor to compress air for storage, while taking electricity from the grid.

The dynamic mathematical models of the system components, being the HAWT, the PMSG, the scroll expander/compressor as well as the PSD were derived. These models, if merged together, form the overall hybrid wind turbine system model. For the validation of the system model, a laboratory sized test rig was built comprising a custom made PSD. The test rig is based on a 1*kW* PMSG and two DC motors to emulate a HAWT. At the beginning of the project the intention was to utilise a small scale Vertical Axis Wind Turbine (VAWT). However, as the project progressed it transpired that the VAWT was not large enough to match the generator's rated power of 1*kW* even under strong wind conditions. Further research into the use of a VAWT or a HAWT for the test rig concluded that they were not feasible within the scope of this project. The finalised test rig was then utilised to successfully validate the system components' mathematical model and the overall hybrid wind turbine model respectively. The fit between simulation and measurement results was discussed and it was concluded that the system mathematical model for the hybrid wind turbine can rightfully be utilised for further system analysis.

A control strategy aiming at regulating the generator power output was then introduced. The actuator for regulating power is the scroll expander/compressor to be controlled in a manner so that torque can be added or taken away to/from the PSD. If used as an expander, a conventional PID controller was suggested for the control of the scroll expander power output and, in turn, the generator's power output. The control action was realised by regulating the air pressure input to the scroll expander for which a solenoid pressure regulator was used. Under varying wind speed conditions, it was shown that a regulated power output can be achieved. If it is required that the HAWT drives both the generator and the scroll compressor, for instance in moments of excessive wind speeds and low demand, the load torque of the scroll compressor must be controlled. However, the load torque depends on the scroll compressor downstream pressure, i.e. the pressure in the air receiver. For this task, a pressure regulator was suggested to regulate the scroll compressor's downstream pressure. This is an unconventional approach and the disadvantage is that the downstream pressure can only by increased with respect to the air receiver's residual air pressure. The control strategy, augmented with a PID controller, was proven successful under varying wind speeds, yet suffers a number of limitations. Therefore, it was concluded to avoid a case in which the HAWT drives both the PMSG and the scroll compressor concurrently. As an alternative, if a fleet of hybrid wind turbines is installed, a decided number of hybrid wind turbines should be operated as standalone wind turbines, whereas the remaining hybrid wind turbines compress air directly through the HAWT.

The efficiency analysis was carried out by investigating energy losses during the hybrid wind turbine operation. The round-trip efficiency was defined as the ratio of electrical energy delivered from the generator to the mechanical energy from the wind turbine rotor after energy has passed through storage and was computed to be around 36.8% in best case scenarios. The majority of the losses can be assigned to the rejection of heat energy

after the air was polytropically compressed. Generator losses, mechanical transmission losses, and compressed air network losses were reported to be comparably low.

A feasibility study on a 1*MW* hybrid wind turbine was also given. For power ratings in megawatt scale it was suggested to utilise screw expanders/compressors due to the current limitation of 50*kW* for scroll expanders. Furthermore, the deployment of two screw expander/compressor machines is proposed. The two screw compressor/expander machines must be connected in a fashion so that a two stage compression is realised if air needs to be compressed for storage. In that way, the maximum air pressure of the storage vessel can be increased significantly. If utilised as expanders, both machines should receive the same air pressure input so that the expanders' torque will be added together. The feasibility study was conducted assuming a 1*MW* PMSG, a suitably sized HAWT, a 490*kW*/250*kW* screw compressor/expander, and a 500m$^3$ air receiver. The total storage capacity was reported to be about 3*MWh*.

A hybrid wind turbine can help mitigate the negative impacts on the network operation caused by the undesired properties of wind power, while making use of the applications and services CAES can deliver to the power network operation. A fleet of megawatt scale hybrid wind turbines with intrinsic CAES capability could reduce the variability in wind power by controlling the power output on a turbine level. The intrinsic compression would also relieve bottlenecks in the network so that expensive network upgrades could be avoided (i.e. network congestion relief), whilst also avoiding curtailment, since excess power could be utilised to store compressed air without converting it into electricity first. Concerning societal contributions, power supply for remote communities and industries with more predictable power demand are suggested as potential applications. Remote areas with poor power network connections, but with rich wind energy resources, could benefit substantially from the hybrid wind turbine system. The drawbacks of the hybrid

wind turbine are its low turnaround efficiency; this is anticipated to affect the management of the compressed air store from an economic viewpoint.

## *7.2 Further Work*

There are some elements to this project that would benefit from further research. The hybrid wind turbine can bring aforementioned societal assets to the power sector. However, detailed economic analysis need to be conducted assessing profitability from an investor's point of view. To date, energy storage is regarded as non-profitable. However, the hybrid wind turbine may open up new revenue streams from which the investor will benefit. For example, a market could be created involving *firm* renewable energy, with both energy and capacity components.

The comparably low efficiencies of both compressors and expanders and the associated thermal losses are the greatest contributors to the low turnaround efficiencies of the hybrid wind turbine. If it was possible to utilise the heat energy, which is generated during the air compression, the turnaround efficiency could be significantly improved. The heat could be stored and used at later times, e.g. to heat up the air prior to the expansion. It is also anticipated that the heat could be utilised for heating buildings for nearby communities.

The feasibility of a 1*MW* wind turbine was investigated based on industrially available components. The 1*MW* hybrid wind turbine is theoretically not the limit and even larger hybrid wind turbines are expected to be feasible. More detailed quantification could be made. For example, to date large wind turbines can reach power ratings of up to about 7*MW*.

There is reported evidence showing that gear boxes are prone to failure due to high shock loads in moments of sudden wind speed changes. The hybrid wind turbine design with the expander/compressor attached to the PSD offers intrinsic mechanical damping. Modern wind turbines often utilise PMSGs, which do not provide damping in comparison to asynchronous generators. Therefore, it is anticipated that the hybrid wind turbine structure can prolong the turbine's life-time in comparison to conventional geared wind turbines.

Lastly, further implementation of intelligent control will be required regarding the inverter/converter unit and the blade pitch angle control. As to the former, by using a bi-directional inverter/converter unit, both the generator load torque and the motor drive torque can be controlled. The blade pitch angle control is necessary for all large wind turbines for maximum power point tracking and the throttling of the wind turbine at excessive wind speeds. The pitch angle control is also important for the direct compression mode of the hybrid wind turbine.

# *References*


[1] legislation.gov.uk. (2008, 02/03/2016). *Climate Change Act 2008*. Available: http://www.legislation.gov.uk/ukpga/2008/27

[2] European Commission. (2016). *2020 climate & energy package*. Available: http://ec.europa.eu/clima/policies/strategies/2020/index_en.htm

[3] Department of Energy & Climate Change DECC, "UK Renewable Energy Roadmap," 2011.

[4] National Grid Plc, "Operating the Electricity Transmission Networks in 2020," 2011.

[5] Department of Energy & Climate Change DECC. (2015, 04/08/2015). *Digest of UK Energy Statistics (DUKES)*. Available: https://www.gov.uk/government/collections/digest-of-uk-energy-statistics-dukes

[6] Redpoint and Element Energy, "Electricity System Analysis – future system benefits from selected DSR scenarios," 2012.

[7] European Commission, "The future role and challenges of energy storage (DG ENER Working Paper)," 2015.

[8] International Energy Agency, *The Power of Transformation Wind, Sun and the Economics of Flexible Power Systems*: Organization for Economic Co-operation and Development (OECD), 2014.

[9] P. Jamieson, *Innovation in Wind Trubine Design*. Chichester: Wiley, 2011.

[10] T. Burton, N. Jenkins, D. Sharpe, and E. Bossanyi, *Wind Energy Handbook*. Chichester: Wiley, 2011.

[11] Green Living Made Easy. (2009, 10/12/2015). *Wind Turbine Systems Vertical Axis*. Available: http://green-living-made-easy.ultimate-online-services.com/wind-turbine-systems-vertical-axis.html

[12] RenewableUK. (2015, 04/08/2015). *UK Wind Energy Database (UKWED)*. Available: http://www.renewableuk.com/en/renewable-energy/wind-energy/uk-wind-energy-database/index.cfm

[13] Wind Power Monthly. (2013). *The 10 Biggest Turbines in the World*. Available: http://www.windpowermonthly.com/10-biggest-turbines

[14] London Array. (2013). *London Array*. Available: http://www.londonarray.com/

[15] N. Ames. (2013). *Kentnews.co.uk*. Available: http://www.kentnews.co.uk/news/london_array_comes_online_1_2009156

[16] Hitachi. (2013). *Nacelle and Hub*. Available: http://www.hitachi.com/products/power/wind-turbine/feature/nacelle/

[17] L. Freris, "Wind Energy Conversion," ed. London: Prentice Hall, 1990.

[18] P. C. Krause, *Analysis of Electric Machinery*. New York: McGraw Hill, 1986.

[19] F. Blaabjerg, Z. Chen, R. Teodorescu, and F. Iov, "Power electronics in wind turbine systems," in *Power Electronics and Motion Control Conference, 2006. IPEMC 2006. CES/IEEE 5th International*, 2006, pp. 1-11.

[20] S. Heier, *Grid Integration of Wind Power Conversion Systems*. New York: John Wiley & Sons Inc, 2006.

[21] Siemens, "Siemens NetConverter," ed. July: Siemens Wind Power, 2009.

[22] International Net Resources. (2013). *Power-technology.com*. Available: http://www.power-technology.com/features/feature-global-wind-energy-market-gears-growth/

[23] P. Fairley. (2010). *MIT Technology Review*. Available: http://www.technologyreview.com/news/418689/wind-turbines-shed-their-gears/

[24] H. Li and Z. Chen, "Overview of different wind generator systems and their comparisons," *IET Renewable Power Generation,* vol. 2, pp. 123-138, 2008.

[25] National Grid Plc. (2015, 07/08/2015). *Data Explorer*. Available: http://www2.nationalgrid.com/UK/Industry-information/Electricity-transmission-operational-data/Data-explorer/

[26] GridWatch. (2015, 08/08/2015). *U.K. National Grid Status*. Available: http://www.gridwatch.templar.co.uk/

[27] B. Burger, "Electricity production from solar and wind in Germany in 2014," *Fraunhofer Institute for Solar Energy Systems ISE: Freiburg, Germany,* 2014.

[28] Federal Ministry for Economic Affairs and Energy. (2015, 05/08/2015). *Erneuerbare Energien*. Available: http://bmwi.de/DE/Themen/Energie/erneuerbare-energien.html

[29] Arbeitsgruppe Erneuerbare Energien-Statistik, "Zeitreihen zur Entwicklung der erneuerbaren Energien in Deutschland," *Federal Ministry for Economic Affairs and Energy,* 2015.

[30] FRAUNHOFER-Institut für Windenergie und Energiesystemtechnik IWES, "Windenergie Report Deutschland 2014," 2015.

[31] C. Morris. (2013, 05/08/2015). *Load management in Germany – the potential*. Available: http://energytransition.de/2013/08/load-management-germany/

[32] M. Schlesinger, D. Lindenberger, and C. Lutz, "Entwicklung der Energiemärkte-Energiereferenzprognose-Projekt Nr. 57/12-Studie im Auftrag des Bundesministeriums für Wirtschaft und Technologie," *Berlin: Bundesministerium für Wirtschaft und Technologie (BMWi),* 2014.

[33] J. N. Rasmussen. (2015, 04/08). *Wind turbines reached record level in 2014*. Available: http://energinet.dk/EN/El/Nyheder/Sider/Vindmoeller-slog-rekord-i-2014.aspx

[34] International Energy Agency. (2014). *Key World Energy Statistics*. Available: http://www.iea.org/publications/freepublications/publication/KeyWorld2014.pdf

[35] REN21. (2014). *RENEWABLES 2014 GLOBAL STATUS REPORT, Key Findings 2014*. Available: http://www.ren21.net/Portals/0/documents/Resources/GSR/2014/GSR2014_KeyFindings_low%20res.pdf

[36] A. Neslen. (2015, 01/08/2015). *Wind power generates 140% of Denmark's electricity demand*. Available: http://www.theguardian.com/environment/2015/jul/10/denmark-wind-windfarm-power-exceed-electricity-demand

[37] I. B. Spliid. (2015, 08/08/2015). *Stamdataregister for vindmøller*. Available: http://www.ens.dk/info/tal-kort/statistik-noegletal/oversigt-energisektoren/stamdataregister-vindmoller

[38] H. Jeppesen. (2014, 09/08/2015). *Denmark leads the charge in renewable energy*. Available: http://www.dw.com/en/denmark-leads-the-charge-in-renewable-energy/a-17603695

[39] International Energy Agency, "Energy Policies of IEA Countries Denmark 2011 Review," 2011.

[40] EEA (European Environment Agency), "Trends and projections in Europe 2014," 2014.

[41] EirGrid and SONI, "Annual Wind Constraint and Curtailment Report 2013," 2014.

[42] H. K. Trabish. (2011, 15/12/2015). *Why Aren't Those Wind Turbines Turning?* Available: http://www.greentechmedia.com/articles/read/why-arent-those-wind-turbines-turning

[43] D. Lew, L. Bird, M. Milligan, B. Speer, X. Wang, E. M. Carlini*, et al.*, "Wind and solar curtailment," in *International Workshop on Large-Scale Integration of Wind Power Into Power Systems*, 2013.

[44] S. Fink, C. Mudd, K. Porter, and B. Morgenstern, "Wind energy curtailment case studies," *NREL subcontract report, NREL/SR-550,* vol. 46716, 2009.

[45] J. Boemer, K. Burges, and C. Nabe, "All Island TSO Facilitation of Renewables Studies," ed, 2009.

[46] H. K. Jacobsen and S. T. Schröder, "Curtailment of renewable generation: Economic optimality and incentives," *Energy Policy,* vol. 49, pp. 663-675, 2012.

[47] G. Strbac, M. Aunedi, D. Pudjianto, P. Djapic, F. Teng, A. Sturt*, et al.*, "Strategic assessment of the role and value of energy storage systems in the UK low carbon energy future," *Report for Carbon Trust,* 2012.

[48] L. F. Ochoa, C. J. Dent, and G. P. Harrison, "Distribution network capacity assessment: Variable DG and active networks," *Power Systems, IEEE Transactions on,* vol. 25, pp. 87-95, 2010.

[49] X. Luo, J. Clarke, and J. Wang, "Overview of Electrical Energy Storage Technologies," University of Warwick, Coventry2013.

[50] Wikipedia. (2015, 02/11/2015). *Pumped-storage hydroelectricity*.

[51] I. Koutsopoulos, V. Hatzi, and L. Tassiulas, "Optimal energy storage control policies for the smart power grid," in *Smart Grid Communications (SmartGridComm), 2011 IEEE International Conference on*, 2011, pp. 475-480.

[52] FlowBattery. (2015). *Compressed Air Batteries*. Available: http://www.flowbattery.co.uk/compressed-air-batteries

[53] A. Kandola. Co-operative Bank – Data Centre UPS Runs On Air! .

[54] X. Luo, N. Jia, L. Shpanin, and J. Wang, "An energy efficient pneumatic-electricity system–modelling study of the scroll expender," in *Mechatronics 2008: proceedings of the 11th Mechatronics Forum Biennial International Conference*, 2008, pp. 23-25.

[55] T. Yanagisawa, "Performance of an oil-free scroll-type expander," *Institution of Mechanical Engineers, Fluid Machinery Group, Institution of Mechanical Engineers, City University, London,* 2003.

[56] J. Wang, X. Luo, L. Yang, L. M. Shpanin, N. Jia, S. Mangan*, et al.*, "Mathematical modeling study of scroll air motors and energy efficiency analysis—part II," *Mechatronics, IEEE/ASME Transactions on,* vol. 16, pp. 122-132, 2011.

[57] Y. Chen, N. P. Halm, E. A. Groll, and J. E. Braun, "Mathematical modeling of scroll compressors—part I: compression process modeling," *International Journal of Refrigeration,* vol. 25, pp. 731-750, 2002.

[58] F. S. Barnes and J. G. Levine, *Large energy storage systems handbook*: CRC Press, 2011.

[59] S. Succar and R. H. Williams, "Compressed air energy storage: theory, resources, and applications for wind power," *Princeton Environmental Institute Report,* vol. 8, 2008.

[60] E. Bozzolani, "Techno-economic analysis of compressed air energy storage systems," 2010.

[61] A. Giramonti and E. Smith, "Control of the champagne effect in CAES power plants," in *Proc., Intersoc. Energy Convers. Eng. Conf.;(United States)*, 1981.

[62] A. J. Pimm, S. D. Garvey, and M. de Jong, "Design and testing of energy bags for underwater compressed air energy storage," *Energy,* vol. 66, pp. 496-508, 2014.

[63] M. G. Molina, *Dynamic modelling and control design of advanced energy storage for power system applications*: INTECH Open Access Publisher, 2010.

[64] F. Díaz-González, A. Sumper, O. Gomis-Bellmunt, and R. Villafáfila-Robles, "A review of energy storage technologies for wind power applications," *Renewable and Sustainable Energy Reviews,* vol. 16, pp. 2154-2171, 2012.

[65] R. H. Schulte, J. Nicholas Critelli, K. Holst, and G. Huff, "Lessons from Iowa: Development of a 270 Megawatt Compressed Air Energy Storage Project in Midwest Independent System Operator," United States of America2012.

[66] J. Eyer and G. Corey, "Energy Storage for the Electricity Grid: Benefits and Market Potential Assessment Guide " Sandia National Laboratories 2010.

[67] Energy Smartest, "Power Purchase Agreement UK | Power Purchase Agreements for Energy Generators | SmartestEnergy," vol. 2015, 2015.

[68] L. Jones, "Managing Variability, Uncertainty and Flexibility in Power Grids with High Penetration of Renewables," ALSTOM, Ed., ed: YouTube, 2014.

[69] Agora Energiewende, "12 Insights on Germany's Energiewende," 2013.

[70] C. Jaquelin, M. Mackay, Z. Owen, M. Michael, A. Doug, and P. Bryan, "Flexibility in 21st Century Power Systems," 2014.

[71] World Energy Council. (2015, 29/09/2015). *Hydropower storage abroad could support the 'Energiewende'*. Available: https://www.worldenergy.org/news-and-media/local-news/hydropower-storage-abroad-could-support-the-german-energiewende-wec-germany-report/

[72] British Geological Survey. (2015). *Operational ranges of current and proposed underground natural gas storage and CAES facilities*.

[73] IMAGES. (2015, 10/10/2015). *Integrated Market-fit and Affordable Grid Scale Energy Storage*. Available: http://www.integratedenergystorage.org/

[74] A. Haruni, A. Gargoom, M. E. Haque, and M. Negnevitsky, "Dynamic operation and control of a hybrid wind-diesel stand alone power systems," in *Applied Power Electronics Conference and Exposition (APEC), 2010 Twenty-Fifth Annual IEEE*, 2010, pp. 162-169.

[75] H. Ibrahim, A. Ilinca, R. Younes, J. Perron, and T. Basbous, "Study of a hybrid wind-diesel system with compressed air energy storage," in *Electrical Power Conference, 2007. EPC 2007. IEEE Canada*, 2007, pp. 320-325.

[76] International Energy Agency, "Technology Roadmap Energy Storage," 2014.

[77] Z. Chen and Y. Hu, "A hybrid generation system using variable speed wind turbines and diesel units," in *Industrial Electronics Society, 2003. IECON'03. The 29th Annual Conference of the IEEE*, 2003, pp. 2729-2734.

[78] M. Saadat and P. Y. Li, "Modeling and control of a novel compressed air energy storage system for offshore wind turbine," in *American Control Conference (ACC), 2012*, 2012, pp. 3032-3037.

[79] S. Garvey, A. Pimm, J. Buck, S. Woolhead, K. Liew, B. Kantharaj*, et al.*, "Analysis of a Wind Turbine Power Transmission System with Intrinsic Energy Storage Capability," *Wind Engineering,* vol. 39, pp. 149-174, 2015.

[80] S. Hao, L. Xing, and W. Jihong, "Simulation study of energy efficiency for a hybrid wind turbine system," in *Industrial Technology (ICIT), 2013 IEEE International Conference on*, 2013, pp. 781-786.

[81] S. Hao, L. Xing, and W. Jihong, "Management and control strategy study for a new hybrid wind turbine system," in *Decision and Control and European Control Conference (CDC-ECC), 2011 50th IEEE Conference on*, 2011, pp. 3671-3676.

[82] International Energy Agency, "The Power of Transformation Wind, Sun and the Economics of Flexible Power Systems," ed, 2014.

[83] AirSquared. (2015, 30/05/2015). *Oil-free scroll technology*. Available: http://airsquared.com/

[84] J. Liu and H. Peng, "Modeling and control of a power-split hybrid vehicle," *Control Systems Technology, IEEE Transactions on,* vol. 16, pp. 1242-1251, 2008.

[85] G. H. Gelb, N. Richardson, T. Wang, and B. Berman, "An electromechanical transmission for hybrid vehicle power trains-design and dynamometer testing," SAE Technical Paper1971.

[86] R. Xiaoming, l. Lin, and L. Ximei, "Fundamentals of a Power Splitting Driving Chain for Large Wind Turbines," *Proceedings of the 7th World Congress on Intelligent Control and Automation,* 2008.

[87] C. Rossi, P. Corbelli, and G. Grandi, "W-CVT continuously variable transmission for wind energy conversion system," in *Power Electronics and Machines in Wind Applications, 2009. PEMWA 2009. IEEE*, 2009, pp. 1-10.

[88] M. Waldner and I. Erlich, "Variable Speed Wind Turbines Based on Electromechanical Differential Systems," 2014.

[89] M. Waldner, "Basic Function of the DSgen-set®," SET Sustainable Energy Technologies GmbH2012.

[90] Sustainable Energy Technologies. (2014). *Wind Power*. Available: http://www.set-solutions.net/windpower-start.html

[91] W. Matek, D. Muhs, H. Wittel, and M. Becker, *Roloff/Matek Maschinenelemente: Normung Berechnung Gestaltung*: Springer-Verlag, 2013.

[92] X. Rui, L. Li, and X. Li, "Fundamentals of a power splitting driving chain for large wind turbines," in *Intelligent Control and Automation, 2008. WCICA 2008. 7th World Congress on*, 2008, pp. 9347-9350.

[93] M. Idan and D. Lior, "Continuous variable speed wind turbine: Transmission concept and robust control," *Wind engineering,* vol. 24, pp. 151-167, 2000.

[94] W. He, Y. Wu, Y. Peng, Y. Zhang, C. Ma, and G. Ma, "Influence of intake pressure on the performance of single screw expander working with compressed air," *Applied thermal engineering,* vol. 51, pp. 662-669, 2013.

[95] J. Yan, R. Boehm, and H. Yang, *Handbook of clean energy systems* vol. 2, 2015.

[96] A. Desideri, M. Van Den Broek, S. Gusev, V. Lemort, and S. Quoilin, "Experimental campaign and modeling of a low-capacity waste heat recovery system based on a single screw expander," 2014.

[97] D. Fiaschi, G. Manfrida, and F. Maraschiello, "Thermo-fluid dynamics preliminary design of turbo-expanders for ORC cycles," *Applied energy,* vol. 97, pp. 601-608, 2012.

[98] E. Sauret and A. S. Rowlands, "Candidate radial-inflow turbines and high-density working fluids for geothermal power systems," *Energy,* vol. 36, pp. 4460-4467, 2011.

[99] A. R. Jha, *Wind turbine technology*: CRC press, 2010.

[100] P. Battaiotto, R. Mantz, and P. Puleston, "A wind turbine emulator based on a dual DSP processor system," *Control Engineering Practice,* vol. 4, pp. 1261-1266, 1996.

[101] B. Rabelo, W. Hofmann, and M. Glueck, "Emulation of the static and dynamic behaviour of a wind-turbine with a DC-machine drive," in *Power Electronics Specialists Conference, 2004. PESC 04. 2004 IEEE 35th Annual*, 2004, pp. 2107-2112.

[102] RWTH Aache University. (2015, 14/05/2015). *Center for Wind Power Drives*. Available: https://www.cwd.rwth-aachen.de/1/home/

[103] C. L. Souza, L. M. Neto, G. C. Guimarães, and A. J. Moraes, "Power system transient stability analysis including synchronous and induction generators," in *Power Tech Proceedings, 2001 IEEE Porto*, 2001, p. 6 pp. vol. 2.

[104] R. Bansal, "Three-phase self-excited induction generators: an overview," *Energy Conversion, IEEE Transactions on,* vol. 20, pp. 292-299, 2005.

[105] R. Naam. (2015). *Why Energy Storage is About to Get Big – and Cheap*. Available: http://rameznaam.com/2015/04/14/energy-storage-about-to-get-big-and-cheap/

[106] J. Wang, L. Yang, X. Luo, S. Mangan, and J. W. Derby, "Mathematical Modeling Study of Scroll Air Motors and Energy Efficiency Analysis—Part I," *Mechatronics, IEEE/ASME Transactions on,* vol. 16, pp. 112-121, 2011.

[107] Y.-R. Lee and W.-F. Wu, "On the profile design of a scroll compressor," *International journal of refrigeration,* vol. 18, pp. 308-317, 1995.

[108] L. Yang, "Modelling and energy efficiency analysis of a scroll type air motor," University of Liverpool, 2008.

[109] J. Wang, D. Wang, P. R. Moore, and J. Pu, "Modelling study, analysis and robust servocontrol of pneumatic cylinder actuator systems," *IEE Proceedings-Control Theory and Applications,* vol. 148, pp. 35-42, 2001.

[110] R. Kushnir, A. Ullmann, and A. Dayan, "Thermodynamic models for the temperature and pressure variations within adiabatic caverns of compressed air energy storage plants," *Journal of Energy Resources Technology,* vol. 134, p. 021901, 2012.

[111] A. Rolan, A. Luna, G. Vazquez, D. Aguilar, and G. Azevedo, "Modeling of a variable speed wind turbine with a permanent magnet synchronous generator," in *Industrial Electronics, 2009. ISIE 2009. IEEE International Symposium on*, 2009, pp. 734-739.

[112] Mathworks. (2015, 05/05/2014). *Wind Turbine*. Available: http://uk.mathworks.com/help/physmod/sps/powersys/ref/windturbine.html

[113] Mathworks. (2016, 15/11/2015). *DC Motor Speed: System Modeling*. Available: http://ctms.engin.umich.edu/CTMS/index.php?example=MotorSpeed&section=SystemModeling

[114] H. L. Benford and M. B. Leising, "The lever analogy: A new tool in transmission analysis," SAE Technical Paper1981.

[115] B. Aoun and D. F. Clodic, "Theoretical and experimental study of an oil-free scroll vapor expander," 2008.

[116] E. Welfonder, R. Neifer, and M. Spanner, "Development and experimental identification of dynamic models for wind turbines," *Control Engineering Practice,* vol. 5, pp. 63-73, 1997.

[117] T. Eastop and A. McConkey, "Applied thermodynamics for engineering technologists, 1996," vol. 5, ed: Prentice Hall, Singapore.

[118] M. Rizo, A. Rodríguez, E. Bueno, and F. J. Rodríguez, "Robustness analysis of Wind Turbines based on PMSG with sensorless vector control," in *IECON 2010-36th Annual Conference on IEEE Industrial Electronics Society*, 2010, pp. 3103-3108.

[119] WinWinD, "WWD-1 1MW wind turbine," in *Technical Specification*, ed, 2003.

[120] Bharat Tanks And Vessels. (2015, 20/2/2016). *Pressure Vessels and Pressure Equipments*. Available: http://www.bharattanksandvessel.com/pressure-vessels-and-pressure-equipments.html

[121] E. J. Coster, J. Myrzik, B. Kruimer, and W. L. Kling, "Integration issues of distributed generation in distribution grids," *Proceedings of the IEEE,* vol. 99, pp. 28-39, 2011.

[122] E. Webborn, "Assessing the Value of Energy Storage," NationalGrid2015.

[123] M. Black and G. Strbac, "Value of storage in providing balancing services for electricity generation systems with high wind penetration," *Journal of power sources,* vol. 162, pp. 949-953, 2006.

[124] S. Gill, G. Ault, and I. Kockar, "The optimal operation of energy storage in a wind power curtailment scheme," in *Power and Energy Society General Meeting, 2012 IEEE*, 2012, pp. 1-8.

[125] A. Cavallo, "Controllable and affordable utility-scale electricity from intermittent wind resources and compressed air energy storage (CAES)," *Energy,* vol. 32, pp. 120-127, 2007.

[126] S. Kahrobaee and S. Asgarpoor, "Optimum planning and operation of compressed air energy storage with wind energy integration," in *North American Power Symposium (NAPS), 2013*, 2013, pp. 1-6.

[127] M. A. Riaz, "Feasibility of compressed air energy storage to store wind on monthly and daily basis," 2010.

[128] Energinet.dk. (2015). *Elsystemet lige nu*. Available: http://energinet.dk/Flash/Forside/index.html

[129] Low Carbon Transition Unit, "Energy Policy Toolkit on System Integration of Wind Power, Experiences from Denmark," Danish Energy Agency2014.

[130] B. Paulos, "Postcard From the Grid's Future: Record-Breaking Wind Integration in Denmark : Greentech Media," vol. 2015, 2015.

[131] P. Sorknæs, H. Mæng, T. Weiss, and A. N. Andersen, "Overview of the Danish Power system and RES integration," 2013.

[132] Energienet.dk, "Combat Climate Change," ed, 2015.

[133] Wikipedia. (2015, 02/01/2016). *Pressure regulator*. Available: https://en.wikipedia.org/wiki/Pressure_regulator

[134] F. Tatsuta, S. Takahashi, K. Suzuki, and S. Nishikata, "A wind turbine simulator for adjusting the moment of inertia of a wind power generation system using a DC motor," in *2013 International Conference on Electrical Machines and Systems (ICEMS)*, 2013.

# *Appendix A Energy Storage Revenue Streams*

CAES can be supportive for renewable energy development and can positively affect the economics of the system. The backbone of this section is based on the lessons learned from the Iowa Stored Energy Park, a $400 million CAES project, which was terminated due to geological limitations. It is a project that started in 2002 and terminated in 2011. A comprehensive report can be found in [65]. The plant comprised of two 135 *MW* turbines and a 220 *MW* compressor. The store was designed to provide 270 *MW* for 36 hours, which equates to 9.7GWh.

## *Economics*

The basic idea of CAES is to store energy and to deliver it in a controlled manner according to purpose. Applications for CAES are explained in Chapter 2 with respect to technical characteristics and with focus on wind farm applications. The applications, however, are mostly defined by financial revenue streams. In general, energy storage can generate revenue in three ways:

1.) Buying and selling in an energy market (wholesale market or spot market)

2.) Providing services to National Grid Plc.

3.) Government subsidies by combining CAES with a wind farm or other renewables

As to number 1); this is usually the primary focus of traditional storage economic studies, where inexpensive off-peak electricity is bought and sold at later times when electricity prices are higher, thus taking advantage of the price difference in the electricity market (also referred to as price arbitrage). Secondly, the management of the store can benefit from providing services to the TSO, such as balancing services (frequency response, reserve power, voltage support etc.) or network services (transmission constraint management, network reinforcement deferral). Lastly, due to legislatively driven incentives for wind

power development, there is an existing urge to encourage energy storage similarly. For example, a market could be created involving *firm* renewable energy, with both energy and capacity components. The combination of wind power and storage should be valued and priced as a premium product. Furthermore, Renewable Obligation Certificates (ROCs) could be assigned to the storage function if the storage can demonstrate the support in renewable development and operation.

In addition to the revenue streams mentioned above, literature can be found that deals with system specific cases. The author of [122] assesses the value of energy storage (and CAES in particular) through multiple revenue streams such as market actions (price arbitrage) and network services to the TSO (Short-term Operation Reserve, Firm Fast Reserve and Firm Frequency Response). By combining different services, the potential value of CAES can be increased, whereby the study showed that by tendering only one service it would not be able to recover from capital costs. In [123] the potential value of storage in providing balancing services based on 26GW wind capacity is investigated and it is shown how storage can increase efficiency of system operation and how it can reduce curtailment. Furthermore, in [124] an optimisation algorithm to maximise the revenue of an energy storage system in combination with a wind farm is investigated. More literature regarding wind power integration and energy storage (and CAES in particular) can be found in [125-127] and references therein. A comprehensive report about the potential value storage brings to the system can be found in [47].

### *Case Study: Iowa Stored Energy Park*

From the Iowa Stored Energy Park (ISEP) project, a number of financial benefits for a CAES plant have been investigated, which are organised into two streams; Phase I and Phase II. Economic analysis for Phase I entail intrinsic and extrinsic benefits (i.e. wholesale market

operations). Phase II is an extension to Phase I in order to assess further benefits alongside the coordination of a CAES unit with regional wind energy resources.

### *Phase I*

Intrinsic benefits are based on average hourly off-peak to peak price arbitrage and are often the primary focus of storage economic studies. The extrinsic value represents the option value of energy to address future load quantity and price volatility. The extrinsic analysis showed that the CAES plant would see wider price spreads over more hours annually. The ability to operate within the wholesale market allows for avoiding curtailment of wind resources, improving the ability to match load with wind power output and allows for providing balancing services. Based on intrinsic and extrinsic values, a positive net benefit comparable to combustion turbine plants was determined. Further sensitivity analysis showed that the net benefit would rise if fuel costs increased, since the CAES plant has better heat rates (fuel efficiency) compared to combustion turbines.

### *Phase II*

Phase II considers additional benefits by taking into account nearby wind power resources. Two challenges have to be mentioned upfront:

1.) Need of innovation, contract arrangements and changes in tariffs and legislation

2.) Ownership; capturing benefits

In order to accomplish additional benefits it will take innovation, contract arrangements and changes in tariffs and legislation. A further major problem is the ownership. Many of the benefits need a mechanism to capture them for the owner of the store, since otherwise dispersed to the market as a whole. Examples are given below.

It is sensible to coordinate variable wind resources and fully dispatchable load like CAES, which would benefit the market as a whole. The realisation, however, is difficult. A storage

owner has no incentive to buy energy from a wind farm and not from the wholesale market. Likewise, wind power generators do not have incentives to sell power to the storage owner specifically. A bilateral contract between wind generator and storage owner could be an option and was discussed within the planning stage of ISEP. The idea is to focus the benefits of the dispatchable load of the storage on particular wind turbines, rather than allowing the same benefits through the wholesale market. Furthermore, such a link between storage and wind generation may enable the storage to qualify for credits such as Renewable Obligation Credits (ROCs), since storage enables more wind power development.

Furthermore, curtailment can be avoided by utilising storage. Two options were examined.

Firstly, the storage can supply additional dispatchable load at times of generation oversupply. ISEP calculated for Iowa that by 1% reduction in curtailment, the benefit would be $5 million per year. If only a fraction can be captured from the CAES plant, considerable benefits can be made. However, the ownership issue applies here. If no mechanisms are in place to capture the benefits for the storage owner, the benefits would be dispersed in the wholesale market.

Secondly, storage can absorb energy at times of transmission constraints. This applies only if the transmission lines between storage and wind farm are not congested. Concerning the transmission reinforcement deferral, Iowa experienced significant transmission constraints at the time of the project planning. Since the CAES unit would be located on the transmission system with a nearby 800 *MW* wind farm, it would appear to be an opportunity to gain benefits. However, detailed analysis was not conducted since it was "beyond the scope of the Phase II and funding".

Improved operation of other generation units is a further benefit option. ISEP estimated significant costs of increased cycling of conventional power units in the near future ($24 million per year), due to increasing costs in O&M. It was estimated that the CAES plant can help reduce cycling by 30%. Alongside the cycling improvement, capacity factors of baseload plants can also be improved. However, unless the owner of the conventional power plant also owns the store, there is no current method for transferring these benefits to the storage owner.

Energy storage can facilitate in reducing $CO_2$ emissions. This is the case if it helps the development of more renewables than would be built without storage. It depends on the resources used for the compression cycle and the resources displaced during the discharge of the storage. In a wholesale market, during off-peak it is likely that compression energy comes from baseload plants and wind whereas during on-peak times it is likely that conventional resources like coal and gas are replaced. Since it was assumed that any $CO_2$ benefit would be reflected in the price of compression energy offered by the wind producer, no actual savings would go towards the storage owner.

The benefits mentioned above are summarised in the following:

1.) Bilateral contracts between storage owner and wind farm generator (market design)
2.) Getting storage in on ROCs through demonstrating that storage helps develop more wind power
3.) Avoiding Curtailment
4.) Improved Baseload Profit
5.) Reduced Baseload Cycling
6.) Net $CO_2$ benefits

# *Appendix B Case Study on Denmark's Wind Power*

In 2005 Denmark had already nearly twice the share of wind power to the nationwide energy consumption compared to the UK today. As the leading nation of wind power generation per capita, Denmark has been monitored by energy planners and funders worldwide. With a wind power share of 39% to the electricity demand, no operational problems have occurred during the past few years. Even in moments of peak wind power generation in Denmark and Germany, the grid stability was maintained. Wind power curtailment is near zero percent in Denmark, with exceptions in 2008 and 2010 due to an outage of one of the interconnection lines to neighbouring countries. It has to be mentioned that Denmark is a comparably small country and well located with a diverse climate over the interconnected countries. The energy consumption is low in comparison to the UK or Germany, making it easier to reach higher shares in wind power. However, key to Denmark's successful integration of large amounts of variable power is the amount of interconnection and efficient system operation working hand in hand with the Nordic power market. In total, the interconnection capacity almost equals the peak electric power demand, meaning high voltage direct current (HVDC) and AC transmission lines are installed from West Denmark to Germany (1500*MW* southbound and 250*MW* northbound, AC), Norway (1040*MW* DC) and Sweden (740*MW* DC). East Denmark, comprising a separate grid, is connected to Sweden via four AC lines totalling 1900*MW* and to Germany with 600*MW* DC. More interconnection lines are being built that will connect the wind farm Kriegers Flak (600*MW*) in the Baltic Sea, which power is then shared among Denmark, Sweden and Germany. The connection to Norway and Sweden allows the utilisation of hydro power to spread out the fluctuation in wind power. Equally, Germany is a larger country and can absorb Denmark's surplus power generation. The export of excess energy, which totalled 8.3*TWh* in 2014, decreases the electricity price in the country where it flows

to. The implementation of negative prices has allowed incentives to increase demand and reduce power generation in hours of high wind power supply. Furthermore, negative prices help reduce the need for wind power curtailment. An online power flow of Denmark's interconnectors can be seen in the link provided in [128].

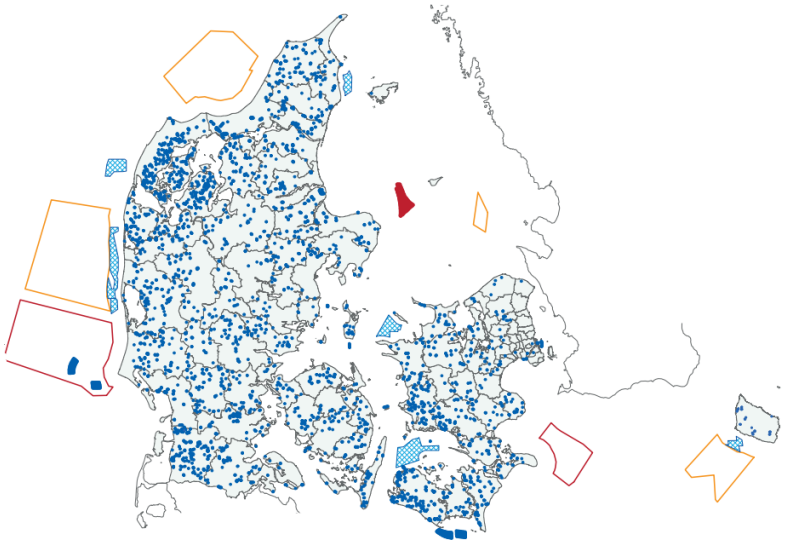

**Figure B:1 Wind Power Distribution in Denmark (blue: wind turbines; orange and red: planned wind farm areas) [129]**

A further positive feature of Denmark's wind integration is the wind farm distribution all over the country, as seen in Figure B:1. If aggregated over large geographic areas, the entire wind power supply is less variable. For example, a cluster of Denmark's wind farms might fluctuate around 3% whereas a single 5*MW* turbine fluctuates around 12% under the same conditions. A strong distribution and transmission network is installed in Denmark to accommodate wind power more easily.

Energinet.dk, the Danish TSO, states that the weather forecast in Denmark is very accurate and is used to calculate the wind power output on a minute by minute basis. The weather forecast is updated every 6 hours and is used for hour-to-hour as well as day-to-day

planning and system operation. The forecast is also linked to the marketplace and is an integrated part of the functioning of the market.

Another key aspect is the Danish Grid Code, which is updated on a regular basis with respect to the technology advances. It sets technical regulations and defines generator requirements e.g. to disconnect during abnormal voltage and frequency events. It states that wind turbines should remain connected to the grid in case of faults, should be controlled remotely and be able to be curtailed if necessary. It also includes regulations regarding power gradient limitations, output of reactive power and more.

In addition, efficient reserves with adequate capacity, such as dispatchable and fast acting power plants, such as gas turbines, are in place for frequency and voltage regulation. The demand side adapts automatically in situations when there is too little or excess wind power generation through direct load control and demand-side response using electric vehicles as manageable and flexible demand.

Little has been found in the literature about the use of energy storage in Denmark. To date, the operator dealt very well with fluctuating wind power as it is seen as only one more variable among others, e.g. fluctuating demand which occurs due to social events, industrial operations or even weather uncertainties or time of the day. Likewise, operators maintained system stability very well when power plants failed unexpectedly [130].

Looking ahead, the Energinet.dk established a list of priorities for integrating variable wind power to the power system in the future. The TSO distinguishes between means of integrating wind power into the power system and means of integrating renewable power into other sectors (e.g. transport). Figure B:2 illustrates the actions.

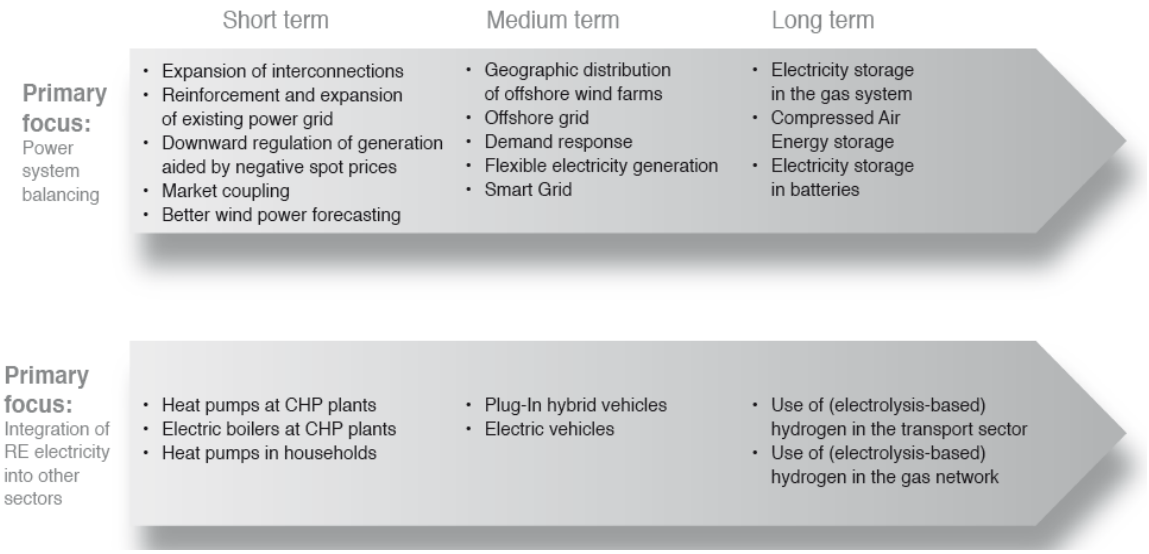


**Figure B:2: Integration of Renewable Power in Power Systems and other Sectors [131]**

It can also be seen that Denmark moves towards heat pumps and the electrification of transport, whereby electric vehicles are used as energy storage and demand-side response [132].

# *Appendix C Auxiliary Mathematical Models*

## *C.1 Pressure Regulator*

A generic manually controlled pressure regulator is shown in Figure C:.

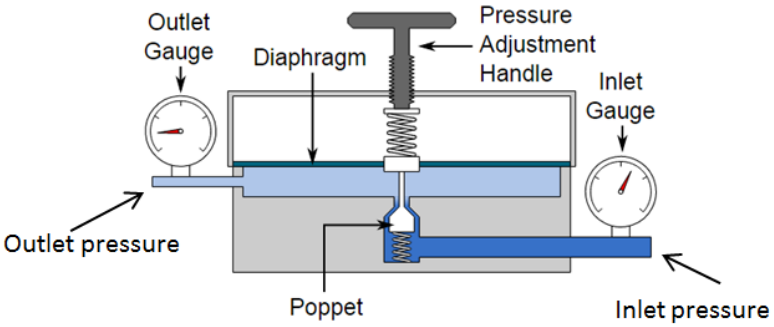


**Figure C:1: Single Stage Pressure Regulator [133]**

The purpose of the pressure regulator is to reduce the inlet pressure to a lower and stable pressure. The air enters the inlet and passes through the poppet valve to the outlet. The outlet chamber consists of a diaphragm upon which the outlet air pressure acts. The diaphragm is spring-loaded and can be adjusted via the pressure adjustment handle to set the desired outlet pressure. If air flows out of the outlet chamber, the pressure in it will eventually decrease, resulting in the poppet valve to move down. That allows the air flow into the outlet chamber causing the pressure to rise again. If the outlet air flow is zero, the poppet valve will close the orifice at the desired outlet pressure. Many different variants exist such as multistage pressure regulators, spring-loaded regulators, solenoid regulators etc. In order to model the system mathematically, an equivalent physical model is developed, which is shown in Figure C:2.

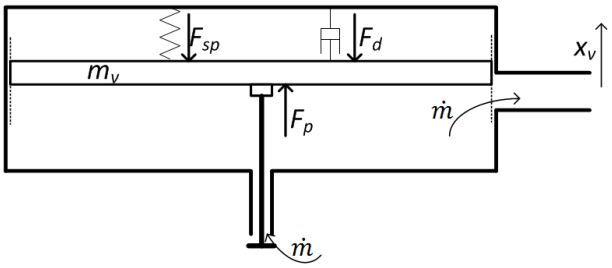


**Figure C:2: Physical Model of Pressure Regulator**

A pressure regulator can be mathematically modelled by means of a second order mass-spring-damper system.

$$m_v\ddot{x_v} = F_p - F_{sp} - F_d = A_v p_d - k_{sp}x_v - d_v x_v \qquad \textbf{Eq. C:1}$$

with:

| | | | |
|---|---|---|---|
| $m_v$ | = | Mass of moving element | $[kg]$ |
| $x_v$ | = | Distance | $[m]$ |
| $F_p$ | = | Force due to pressure | $[N]$ |
| $F_{sp}$ | = | Spring force | $[N]$ |
| $F_d$ | = | Damper force | $[N]$ |
| $A_v$ | = | Area on which pressure acts | $[m^2]$ |
| $p_d$ | = | Downstream pressure | $[Pa]$ |
| $k_{sp}$ | = | Spring constant | $[N/m]$ |
| $d_v$ | = | Damper constant | $[Ns/m]$ |

If the orifice opening depends on the position of the distance $x_v$, then the air mass flow rate can be computed based on the orifice theory. In order to adjust the desired downstream pressure, the spring constant $k_{sp}$ has to be varied. This value can be used as a control input. The lower the value of $k_{sp}$, the higher the downstream pressure and vice versa.

## *C.2 Heat Exchanger*

One of the main disadvantages of the current compressed air energy storage technology is the significant losses that occur during the compression. The heat energy, if stored and

utilised, can contribute to an increased overall efficiency. The recently proposed Advanced-Adiabatic Compressed Air Energy Storage is to find the way of storing and reutilising the heat energy and is an active research area, as explained in Section 2.4.

Although thermal energy storage is not the major focus in this research, the heat generated by the system during the compression has the potential to increase the overall system efficiency of the proposed hybrid wind turbine if the heat energy is used to benefit the system operation. The mathematical model described in this section is based on steady state equations since the dynamics of a heat exchanger depends on specific technology used and the geometry of it. Undertaking dynamic modelling of a chosen heat exchanger would, therefore, exceed the scope of this research.

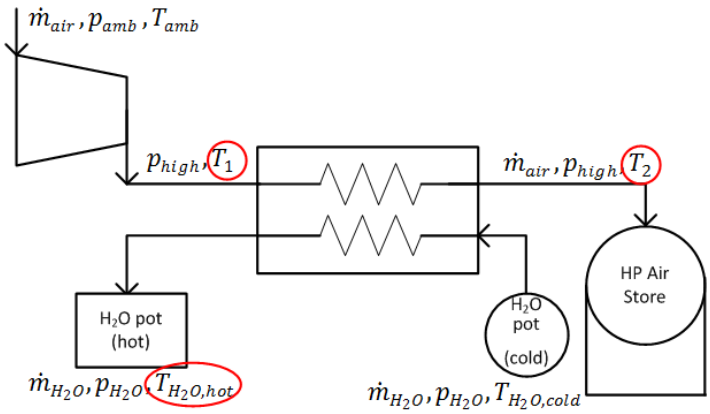


**Figure C:3: Heat Exchanger Physical Model**

Figure C:3 shows a generic heat exchanger model assuming two mediums, being air and water that exchange the heat to each other, with $\dot{m}$, $p$ and $T$ being the air mass flow rate, pressure and temperature of the air and water, respectively. The variables in red circles are unknown and need to be determined. All other variables are assumed known from the system. Therefore, three equations are needed to determine the unknown variables. Ideal gas can be assumed. Presuming ideal isentropic compression, the temperature-pressure relationship is as follows:

$$T_1 = \left(\frac{p_{amb}}{p_{high}}\right)^{\frac{\gamma-1}{\gamma}} T_{amb} \qquad \textbf{Eq. C:2}$$

with $\gamma$ being *1.4*. Furthermore, it is assumed that no heat leaves the system so that

$$\dot{Q}_{hot} - \dot{Q}_{cold} = 0 \qquad \textbf{Eq. C:3}$$

with $\dot{Q} = \dot{m}c_p(\Delta T)$. Rearranged, Eq. C:3 becomes the following:

$$T_{H_2O_{hot}} = \left(\frac{1}{\dot{m}_{H_2O}c_{p_{H2O}}}\dot{m}_{air}c_{p_{air}}(T_1 - T_2)\right) + T_{H_2O_{cold}} \qquad \textbf{Eq. C:4}$$

$T_2$ is determined via the efficiency analysis, see the following equation:

$$\eta - \frac{\dot{Q}_{hot}}{\dot{Q}_{max}} = 0 \qquad \textbf{Eq. C:5}$$

Assuming a perfect heat exchanger, then $\eta = 1$. $\dot{Q}_{max}$ is defined as follows:

$$\begin{aligned} \dot{Q}_{max} &= \min(\dot{m}c_p)\left(T_{H_2O_{cold}} - T_1\right) \\ &= \dot{m}_{air}c_{p_{air}}\left(T_{H_2O_{cold}} - T_1\right) \end{aligned} \qquad \textbf{Eq. C:6}$$

By substituting Eq. C:6 into Eq. C:5, the following equation is yielded:

$$T_2 = \dot{m}_{air}c_{p_{air}}\left(T_{H_2O_{cold}} - T_1\right)\frac{1}{\dot{m}_{air}c_{p_{air}}} + T_1 \qquad \textbf{Eq. C:7}$$

For a perfect heat exchanger, the term $\dot{m}c_p$for both fluids (air and water) must be the same. Therefore, if $\dot{m}_{air}$ is given through the scroll air compressor, the air mass flow of the water can be determined to:

$$\dot{m}_{H_2O} = \frac{\dot{m}_{air}c_{p_{air}}}{c_{p_{H2O}}} \qquad \textbf{Eq. C:8}$$

To sum up, with Eq. C:2, Eq. C:4 and Eq. C:7 all unknowns can be determined for the heat exchanger. Furthermore, the maximum heat flow (as a form of power) can be estimated based on Eq. C:6.

## *C.3 Drive Train Dynamics*

During wind gusts or other shock torque inputs, the drive train is exposed to mechanical strain. The torsional stiffness of the propulsion drive train is an important factor to determine the life-time of the wind turbine. Although it is not the primary focus of this research to investigate the drive train dynamics in depth, an exemplarily mathematical model is given that describes the torsional oscillation during shock-like torque inputs to the drive train. The main reason for the study is the fact that during tests on the hybrid wind turbine test rig (explained in Chapter 5) torsional oscillation was observed, mainly caused by the timing belt transmission that was chosen for the test rig. The second motivation for the modelling work is the fact that gear boxes tend to be a weak component within the drive train and, therefore, tend to fail first. The PSD offers the potential to increase the life-time of the wind turbine system. However, the idea is not further investigated and there are no quantified results to show how long the life-time can be prolonged.

In general, torsional oscillation can be modelled by introducing a spring-damper system, which mimics a twisting shaft and therefore an angular deviation along the shaft. The angular deflection is affected by the torsional stiffness of the materials used and/or by components used such as solid drive shafts, clutches or other transmission components. Figure C:4 shows the physical model.

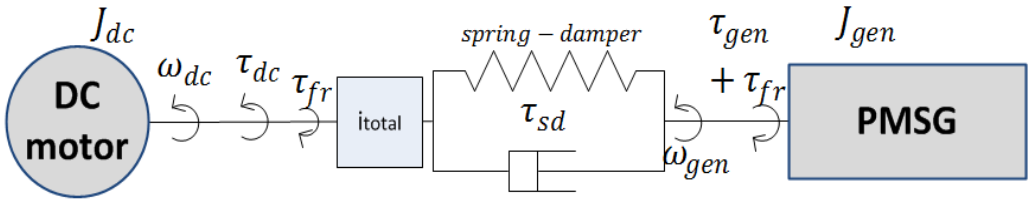


**Figure C:4: Drive Train Dynamics from DC motors to PMSG**

It can be seen that the system can be decoupled through $\tau_{sd}$, which is the dynamic torque that accounts for the spring- and damper-effect. The following two second order systems can be derived:

$$\dot{\omega}_{dc} J_{dc} = 2\tau_{dc} - \tau_{fr,dc} - \frac{1}{i_{total}} \tau_{sd} - \tau_{fr,gear} \qquad \textbf{Eq. C:9}$$

$$\dot{\omega}_{gen} J_{gen} = \tau_{sd} - \tau_{gen} - \tau_{fr,gen} \qquad \textbf{Eq. C:10}$$

with:

$$\tau_{sd} = s\left(\frac{\phi_{dc}}{i_{total}} - \phi_{gear}\right) + d\left(\frac{\omega_{dc}}{i_{total}} - \omega_{gen}\right) \qquad \textbf{Eq. C:11}$$

and with:

| | | | |
|---|---|---|---|
| $i_{total}$ | = | Transmission ratio from DC motors to PMSG | $[-]$ |
| $\phi_{dc}$ | = | Rotor angle DC motor | $[rad]$ |
| $\phi_{gear}$ | = | Rotor angle PMSG motor | $[rad]$ |
| $s$ | = | Spring coefficient | $[Nm/rad]$ |
| $d$ | = | Damping coefficient | $[Nms/rad]$ |

From Figure C:4 it can be seen that the spring-damping torque $\tau_{sd}$ is only present when a difference between the rotor angle of the DC motor and the PMSG exists. The torsional stiffness of the system is defined by the constants $s$ and $d$. The greater the angle between

DC motor shaft and generator shaft, the greater the spring force and the greater the derivative of the angular difference the more damping is added to the system.

To better understand the system's mechanical oscillation, a smoothed voltage step input was used as input to cancel out the electrical power supply's disturbances[11]. Figure C:5 shows the comparison between simulation and experiment of the DC motor step input after parameter identification was completed.

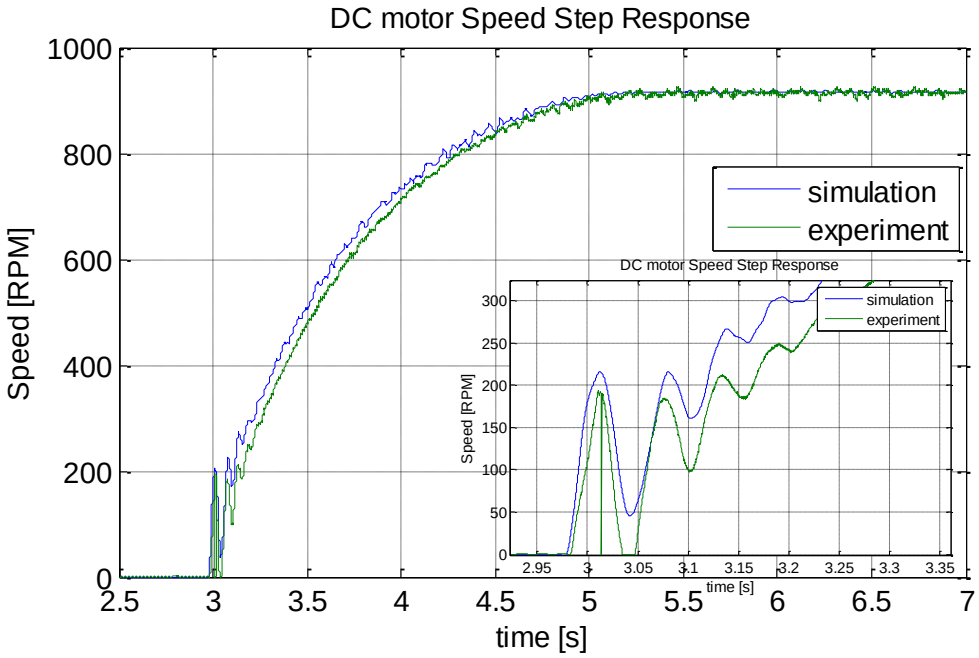


**Figure C:5: Transient Response Drive train dynamics for Hybrid Wind Turbine Test Rig**

It can be seen that the mathematical model can represent the experimental oscillations reasonably well, given the simplifications and assumptions stated above. The oscillation occurs mainly at the beginning, where the transient torque is the largest. The oscillation phases out as the speed response moves towards the steady state value.

[11] An ideal step voltage input with the DC power supply could not be realised.

## *C.4 Isothermal Expansion for Scroll Air Expander*

Experiments and steady state exergy analysis showed that the drop in temperature during the expansion process of the scroll air expander has little effect on the torque speed characteristic for low input pressures (i.e. 1 to 5 *bar*). In that way, isothermal expansion can be assumed and the mathematical model for the scroll expander can be simplified. The isothermal power output of the expander is calculated and compared to the polytropic expansion process with known temperature from measurement results. If ideal gas is assumed the output power for both, isothermal and polytropic expansion is calculated as follows:

$$P_{iso} = p_{in}\dot{V}\log\left(\frac{p_{out}}{p_{in}}\right) \qquad \textbf{Eq. C:12}$$

$$P_{poly} = \frac{p_{in}\dot{V}\left(\left(\frac{p_{out}}{p_{in}}\right)^{\frac{n-1}{n}} - 1\right)}{n-1}n \qquad \textbf{Eq. C:13}$$

with:

| | | | |
|---|---|---|---|
| $P_{iso}$ | = | Power under isothermal expansion | $[W]$ |
| $P_{poly}$ | = | Power under polytropic expansion | $[W]$ |
| $p_{in}$ | = | Upstream pressure | $[Pa]$ |
| $p_{out}$ | = | Downstream pressure | $[Pa]$ |
| $\dot{V}$ | = | Volumetric air flow under pressure $p_{in}$ | $[m^3/s]$ |
| $n$ | = | Polytropic index | $[-]$ |

Since the real polytropic index of the scroll air expander for Eq. C:13 is unknown, measurements of the downstream temperatures were conducted and exergy analysis is applied.

$$P_{poly} = \dot{B}_{in} - \dot{B}_{out} \qquad \textbf{Eq. C:14}$$

$$\dot{B}_{in} = \dot{m}\left(c_p(T_{in} - T_{amb}) - T_{amb}\left(c_p \ln\left(\frac{T_{in}}{T_{amb}}\right) - Rln\left(\frac{p_{in}}{p_{amb}}\right)\right)\right) \qquad \textbf{Eq. C:15}$$

$$\dot{B}_{out} = \dot{m}\left(c_p(T_{out} - T_{amb}) - T_{amb}\left(c_p \ln\left(\frac{T_{out}}{T_{amb}}\right) - Rln\left(\frac{p_{out}}{p_{amb}}\right)\right)\right) \qquad \textbf{Eq. C:16}$$

with:

| | | | |
|---|---|---|---|
| $\dot{B}_{in}$ | = | Flow exergy before expansion | $[W]$ |
| $\dot{B}_{out}$ | = | Flow exergy after expansion | $[W]$ |
| $p_{in}$ | = | Upstream pressure | $[Pa]$ |
| $p_{out}$ | = | Downstream pressure | $[Pa]$ |
| $p_{amb}$ | = | Ambient pressure | $[Pa]$ |
| $T_{in}$ | = | Inlet air temperature | $[K]$ |
| $T_{out}$ | = | Outlet air temperature | $[K]$ |
| $T_{amb}$ | = | Ambient air temperature | $[K]$ |
| $\dot{m}$ | = | Air mass flow rate | $[kg/s]$ |
| $R$ | = | Gas constant | $[\frac{J}{KgK}]$ |
| $c_p$ | = | Ratio of specific heat | $[\frac{J}{KgK}]$ |

The results are listed in Table C:1 under varying inlet pressure.

**Table C:1: Comparison between polytropic and isothermal expansion**

| $T_{in}$ | $\dot{m}$ | $p_{in(abs)}$ | $T_{out}$ | $P_{poly}$ | $P_{iso}$ | $P_{poly}/P_{iso}$ |
|---|---|---|---|---|---|---|
| 290K | 0.01kg/s | 3*bar* | 269K | 918W | 930W | 0.013 |
| 290K | 0.01kg/s | 4*bar* | 258K | 1149W | 1174W | 0.022 |
| 290K | 0.01kg/s | 5*bar* | 249K | 1328W | 1363W | 0.0256 |

## *C.5 Wind Turbine Emulator Control*

The control strategy for the emulator is introduced in Figure C:6.

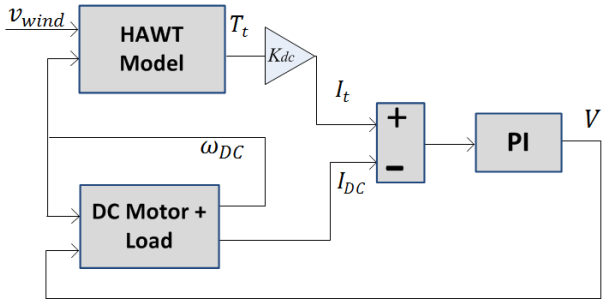


**Figure C:6: Emulator Controller for Steady State Analysis**

It can be seen that the DC motor model with mechanical load is modelled. In parallel, the HAWT model outputs the turbine torque $T_t$ that it would have produced under given wind speed input and the rotational speed given by the DC motors. In fact, the rotational speed of the DC motors and the HAWT is synchronised. The torque that is generated by the wind turbine is used to calculate the electric current with the torque coefficient $K_{dc}$ of the DC motor. This equivalent current $I_t$ and the current drawn by the DC motor $I_{DC}$ are compared, whereby a PI controller is in place so that $I_{DC}$ tracks $I_t$ (see Figure C:6). However, the model that is shown in Figure C:6 accounts for steady state analysis. Although the torque can be matched using that system, the inertias of the HAWT and the DC motors are inherently different, leading to different transient responses. A method of overcoming this issue is presented in [134].

# *Appendix D System Parameters*

**Table D:1: System Model Parameters**

| *Parameter* | *Value* | *Description* |
|---|---|---|
| **General** | | |
| $c_0$ | 0.0404 | $= \sqrt{\frac{k}{R\left(\left(\frac{k+1}{2}\right)^{(k+1)/(k-1)}\right)}}$ |
| $c_d$ | 0.8 | Discharge constant |
| $c_k$ | 3.864 | $= \sqrt{\frac{2}{k-1}\left(\frac{k+1}{2}\right)^{(k+1)/(k-1)}}$ |
| $c_r$ | 0.5283 | $= \left(\frac{2}{k+1}\right)^{(k)/(k-1)}$ |
| $k$ | 1.4 | Ratio of specific heats |
| $R$ | 287 *J/(kgK)* | Gas constant |
| **PMSG** | | |
| $R_s$ | 6 *ohm* | Stator resistance |
| $L$ | 17.5 *mH* | Inductance |
| $p_n$ | 8 | Pole pairs |
| $\psi$ | 0.44 *Vs* | Magnetic flux |
| $\tau_{fr,gen,static}$ | 0.51 *Nm* | Static friction torque |
| $\tau_{fr,gen,vis}$ | 0.01 *Nms* | Viscous friction |
| $J_{gen}$ | 0.015 *kgm²* | Mechanical inertia |
| **Scroll Air Expander** | | |
| $r$ | 5.5e-3 *m* | Radius orbit |
| $\rho_0$ | 9.5e-3 *m* | Initial radius of curvature |
| $k$ | 0.003183 | Opening value for curvature |
| $z$ | 3.33e-2 | Height scroll walls |
| $\tau_{fr,air,static}$ | 0.307 *Nm* | Static friction torque |

| | | |
|---|---|---|
| $\tau_{fr,air,viscous}$ | 0.0044 *Nms* | Viscous friction |
| $A_{in}$ | 4.9e-4 $m^2$ | Cross-sectional are inlet |
| $A_{out}$ | 8.52e-5 $m^2$ | Cross-sectional area outlet |
| **Scroll Compressor** | | |
| $r$ | 5.5e-3 *m* | Radius orbit |
| $\rho_0$ | 9.5e-3 *m* | Initial radius of curvature |
| $k$ | 0.003183 | Opening value for curvature |
| $z$ | 3.33e-2 | Height scroll walls |
| $\tau_{fr,air,static}$ | 0.307 *Nm* | Static friction torque |
| $\tau_{fr,air,viscous}$ | 0.0044 *Nms* | Viscous friction |
| $A_{dis}$ | 8.52e-5 $m^2$ | Cross-sectional area outlet |
| **PSD** | | |
| $J_R$ | 0.046 $kgm^2$ | Mechanical inertia ring gear |
| $J_c$ | 4.15 $kgm^2$ | Mechanical inertia carrier |
| $i$ | 5 | Gear ratio from sun to ring gear |
| $R_0$ | 1.5 | Gear ratio from ring gear to generator |
| $R_1$ | 1.0 | Gear ratio from turbine shaft to carrier shaft (was initially 1.205, but changed later during the project) |
| $\tau_{fr,gear,c,static}$ | 0.174 *Nm* | Static friction torque carrier shaft input |
| $\tau_{fr,gear,c,viscous}$ | 0.0075 *Nms* | Viscous friction carrier shaft input |
| $\tau_{fr,gear,s,static}$ | 0.13 *Nm* | Static friction torque sun gear input |
| $\tau_{fr,gear,s,viscous}$ | 0.0015 *Nms* | Viscous friction sun gear input |
| **DC motor** | | |
| $k_c$ | 0.252 *Nm/A* | Torque constant |
| $L_a$ | 0.78 *mH* | Armature inductance |
| $J_{dc}$ | 0.0014 $kgm^2$ | Mechanical inertia |
| $R_a$ | 0.25 *ohm* | Armature resistance |

| | | |
|---|---|---|
| $\tau_{fr,dc,static}$ | 0.3 *Nm* | Static friction torque |
| $\tau_{fr,dc,viscous}$ | 7.125e-4 *Nms* | Viscous friction |

# *Appendix E Test Rig Design*

## *E.1 List of Gearbox Parts*

**Table E:1: List of Gearbox Components**

| ITEM NO. | PART NUMBER | Add. Description | QTY. |
|---|---|---|---|
| 1 | ISO - Internal spur gear 1.5M 120T 20PA 15FW S100S25OD 1.0AF | Ring gear | 1 |
| 2 | Carrier1 | Planet Carrier Top | 1 |
| 3 | ISO - Spur gear 1. 5M 48T 20PA 15FW S40C60H30L42.0N | Planet Gear | 3 |
| 4 | HR32004XJ | Tapered Roller Bearing d=20,D=42 | 6 |
| 5 | Spacer Planets | Holding the tapered bearings for the planet gears | 3 |
| 6 | ISO 4017 - M8 x 20-N | Bolts | 3 |
| 7 | Carrier2 | Planet carrier bottom | 1 |
| 8 | Scroll Shaft | | 1 |
| 9 | 7903C Angular Ball Bearings | Tapered Roller Bearing d=17, D=30, B=7 | 2 |
| 10 | Lid Bottom | | 1 |
| 11 | Flange Scroll Side | | 1 |
| 12 | HR33008J | d=40,D=68,B=22 | 1 |
| 13 | Hub Bottom | | 1 |
| 14 | Adapter Turbine | Planet carrier shaft | 1 |
| 15 | Lid Top | | 1 |
| 16 | ISO 4017 - M5 x 10-N | Bolts | 5 |
| 17 | Ring Carrier | | 1 |
| 18 | ISO 4018 - M5 x 10-NN | Bolts | 10 |

| | | | |
|---|---|---|---|
| 19 | ISO 4018 - M5 x 30-NN | Bolts | 14 |
| 20 | Circlip DIN 471 - 15 x 1 | | 1 |
| 21 | O-ring 65x3.55-B-ISO 3601-1 | Sealing | 1 |
| 22 | ISO - Spur gear 1.5M 24T 20PA 15FW S20C75H30L15.0S1 | Sun gear | 1 |
| 23 | AN02 M15 NSK | Lock Nut M15 | 1 |
| 24 | 12X30X7 HMS5 RG | Radial shaft Seal | 1 |
| 25 | O-ring 42.5x3.55-A-ISO 3601-1 | Sealing | 1 |
| 26 | 7904A5 Angular Ball Bearing | d=20, D=37, B=9 | 2 |
| 27 | AN04 M20 NSK | Lock Nut M20 | 1 |
| 28 | 15X40X7 HMS5 V | Radial shaft Seal | 1 |
| 29 | AW02 M15 NSK | MB 2 A Washer Lock Nut M15 | 1 |
| 30 | AW04 M20 NSK | MB 4 Washer Lock Nut M20 | 1 |
| 31 | ISO 8676 - M8x1.0 x 16-N | Bolts | 2 |
| 32 | Key ISO 2491 5x3-25-A | | 1 |

## *E.2 Gearbox Drawings*

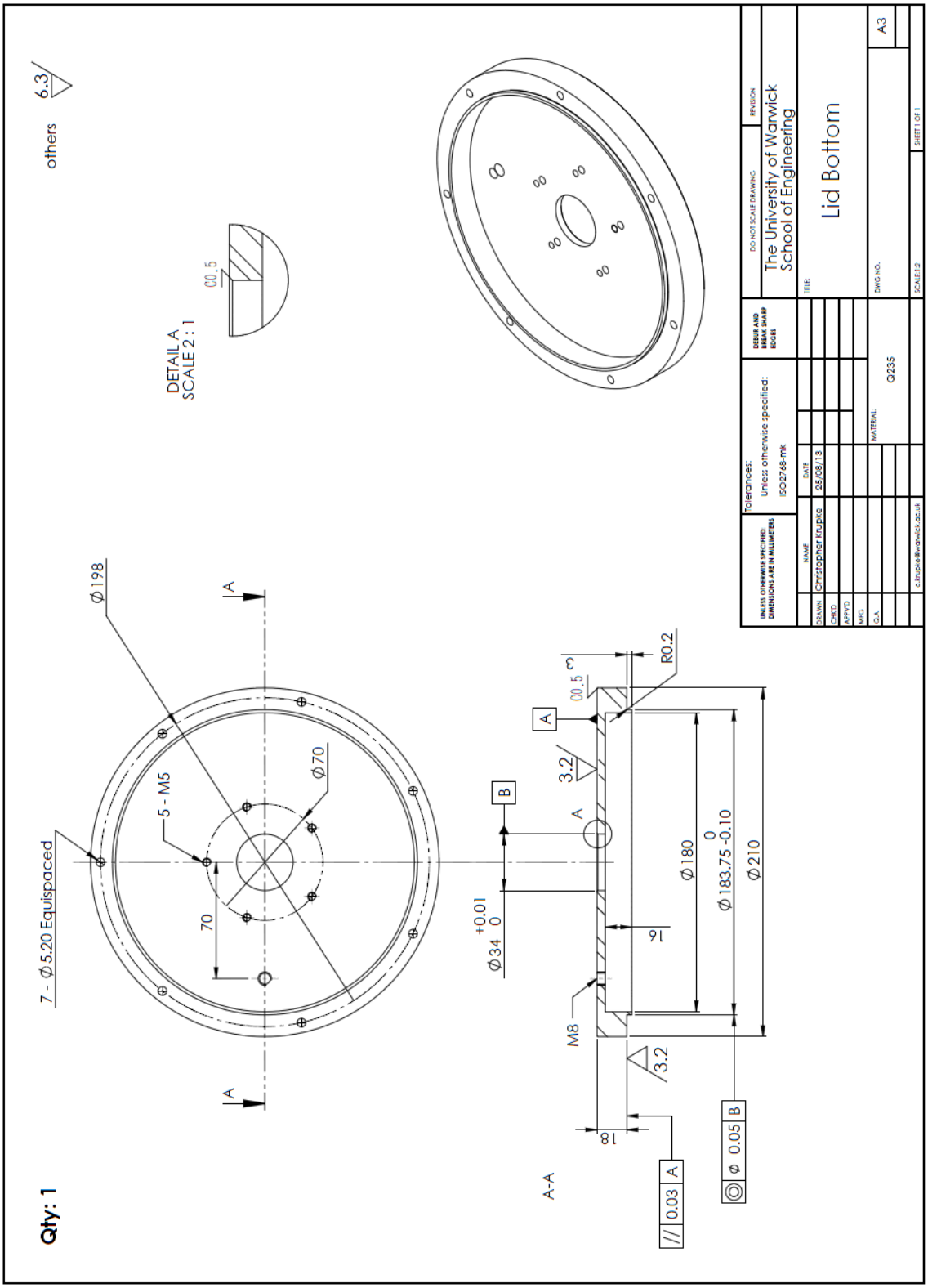

**Qty: 1**

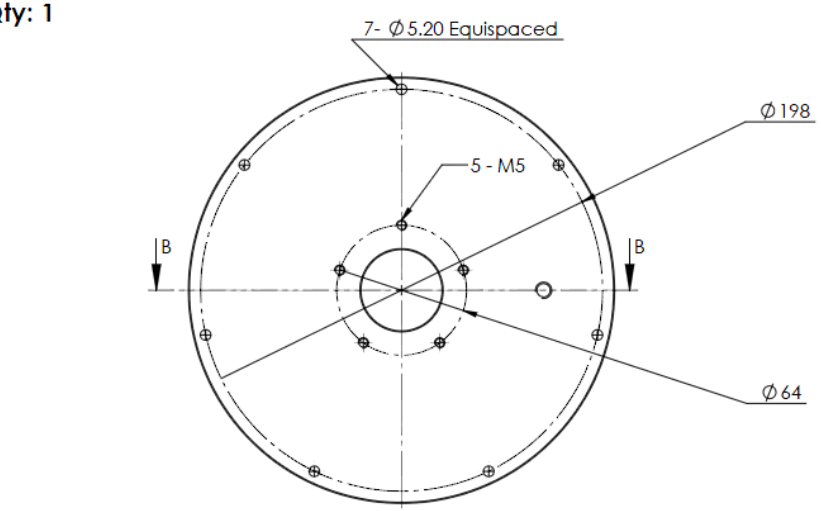


others 6.3

DETAIL A
SCALE 2 : 1

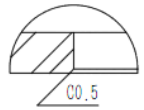


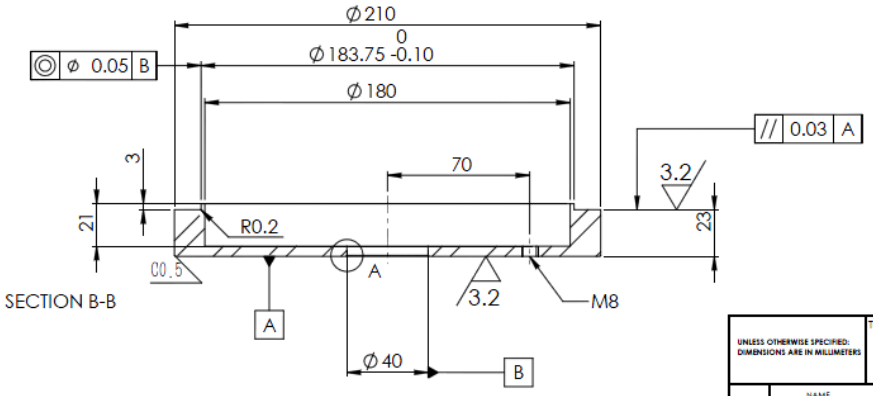


SECTION B-B

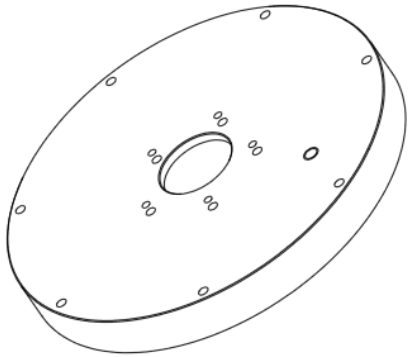

| | | | | | |
|---|---|---|---|---|---|
| UNLESS OTHERWISE SPECIFIED: DIMENSIONS ARE IN MILLIMETERS | Tolerances: Unless otherwise specified: ISO2768-mk | DEBUR AND BREAK SHARP EDGES | DO NOT SCALE DRAWING | REVISION | |
| | | | The University of Warwick<br>School of Engineering | | |
| NAME | DATE | | TITLE: | | |
| DRAWN Christopher Krupke | 25/08/13 | | Lid Top | | |
| CHK'D | | | | | |
| APPV'D | | | | | |
| MFG | | | | | |
| Q.A | | MATERIAL: Q235 | DWG NO. | | A3 |
| c.krupke@warwick.ac.uk | | | SCALE:1:2 | SHEET 1 OF 1 | |

| | |
|---|---|
| Module | 1.5 |
| Circular Pitch | 180 |
| Number of Teeth | 120 |
| Pressure Angle | 20° |
| Face Width | 15 |

All 6.3

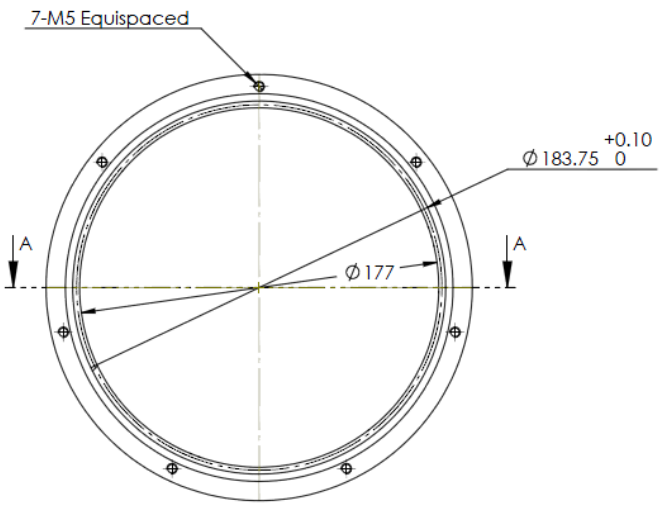


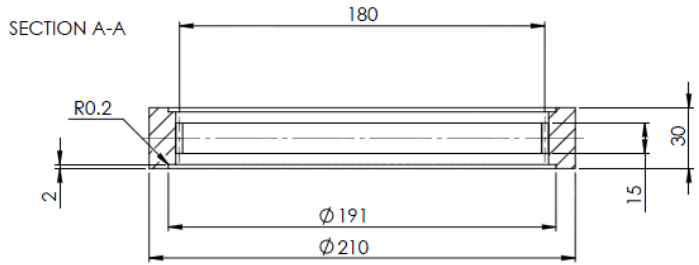


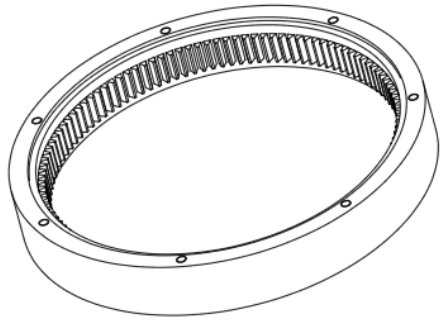

Teeth finishing: Grinding preferred

| | | | | | |
|---|---|---|---|---|---|
| UNLESS OTHERWISE SPECIFIED: DIMENSIONS ARE IN MILLIMETERS | Tolerances: Unless otherwise specified: ISO2768-mk | DEBUR AND BREAK SHARP EDGES | DO NOT SCALE DRAWING | REVISION | |
| | | | The University of Warwick<br>School of Engineering | | |
| NAME | DATE | | TITLE: RingGear | | |
| DRAWN Christopher Krupke | 11/07/13 | | | | |
| CHK'D | | | | | |
| APPV'D | | | | | |
| MFG | | | | | |
| Q.A | | MATERIAL: 20MnCr5 | DWG NO. | | A3 |
| contact c.krupke@warwick.ac.uk | | | SCALE:1:2 | SHEET 1 OF 1 | |

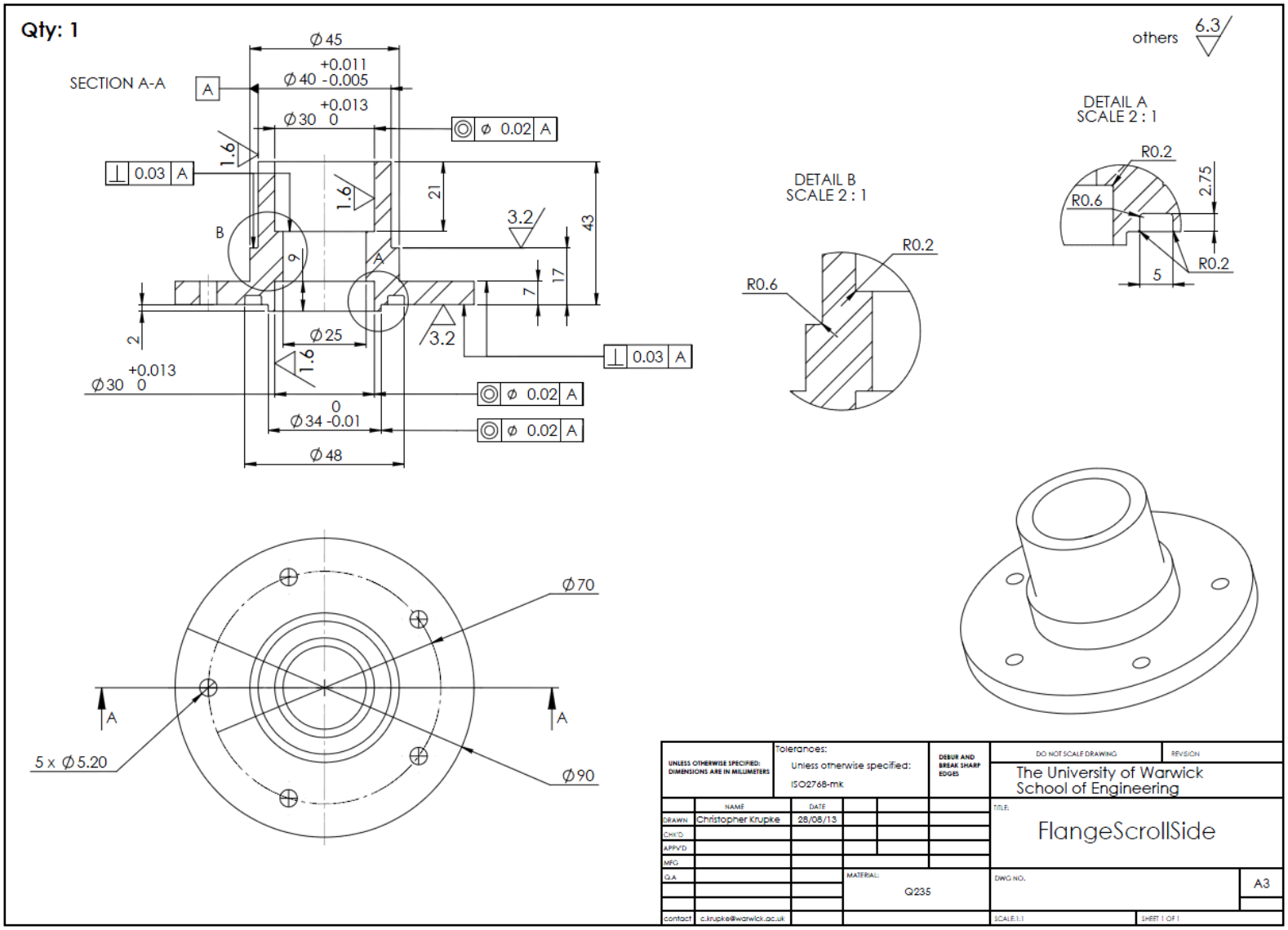
Qty: 1
others 6.3
SECTION A-A
Ø45
+0.011
Ø40 -0.005
+0.013
Ø30 0
Ø 0.02 A
0.03 A
1.6
21
3.2
43
17
7
9
2
Ø25
Ø30 +0.013 0
0
Ø34 -0.01
Ø48
DETAIL B
SCALE 2 : 1
R0.2
R0.6
DETAIL A
SCALE 2 : 1
2.75
5
Ø70
Ø90
5 x Ø5.20
UNLESS OTHERWISE SPECIFIED: DIMENSIONS ARE IN MILLIMETERS
Tolerances:
Unless otherwise specified:
ISO2768-mk
DEBUR AND BREAK SHARP EDGES
DO NOT SCALE DRAWING
REVISION
The University of Warwick
School of Engineering
NAME
DATE
DRAWN Christopher Krupke 28/08/13
CHK'D
APPV'D
MFG
Q.A
MATERIAL:
Q235
TITLE:
FlangeScrollSide
DWG NO.
A3
contact c.krupke@warwick.ac.uk
SCALE:1:1
SHEET 1 OF 1

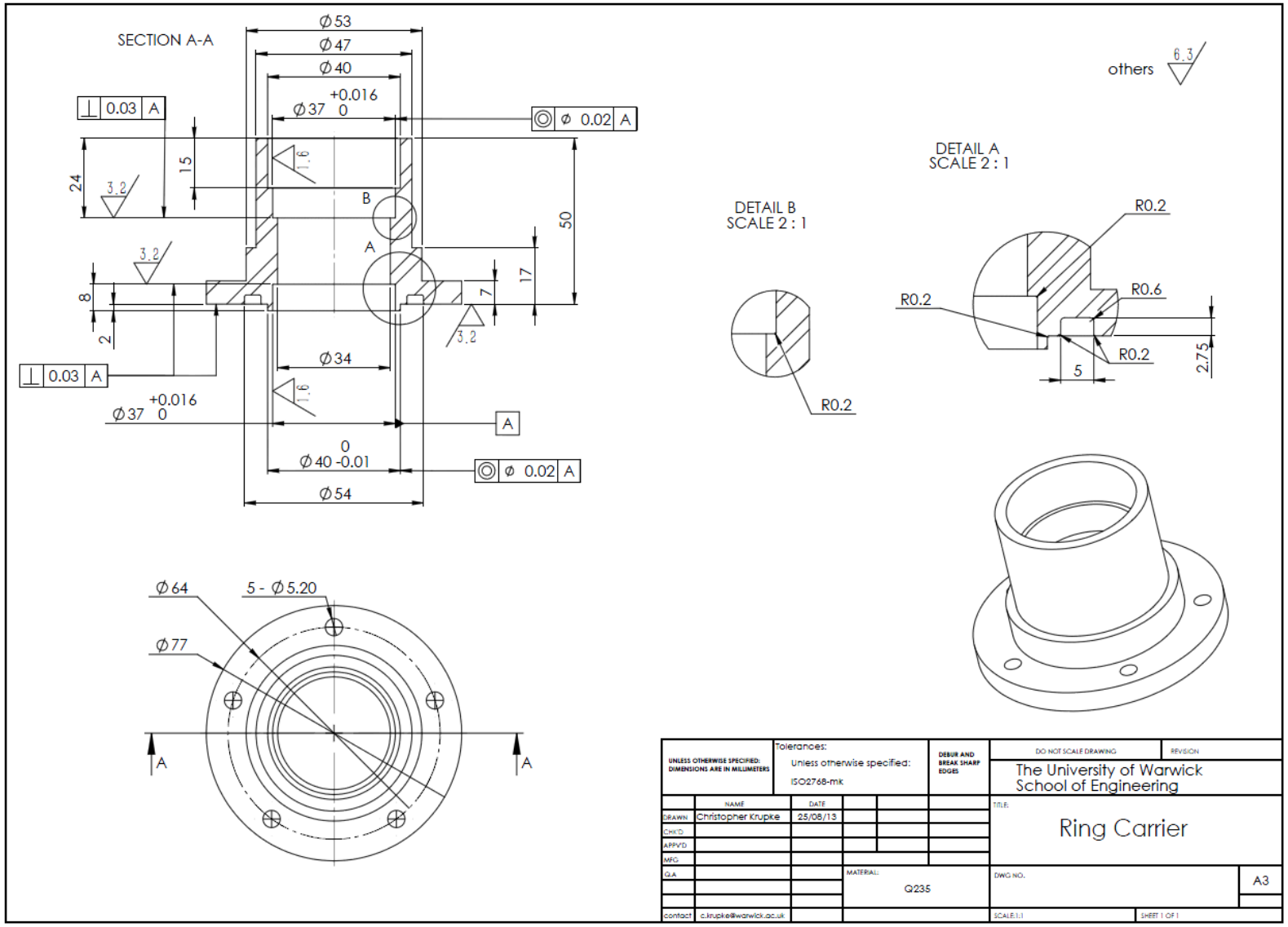
SECTION A-A
Ø53
Ø47
Ø40
+0.016
Ø37 0
0.03 A
Ø 0.02 A
15
24
50
17
8
2
7
Ø34
0
Ø40 -0.01
Ø54
others
6.3
DETAIL A
SCALE 2 : 1
R0.2
R0.6
5
2.75
DETAIL B
SCALE 2 : 1
Ø64
5 - Ø5.20
Ø77
The University of Warwick
School of Engineering
Ring Carrier
Christopher Krupke
25/08/13
Q235
A3
c.krupke@warwick.ac.uk

**Qty: 1**

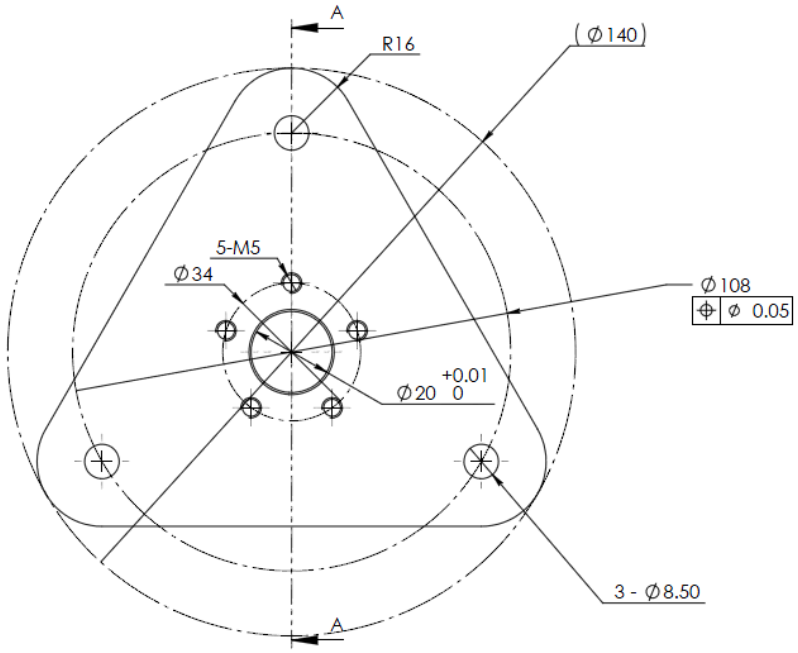


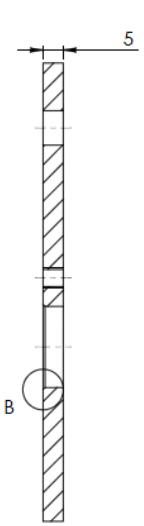


A-A

All 6.3

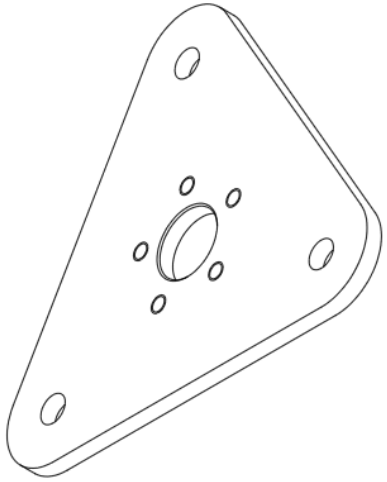

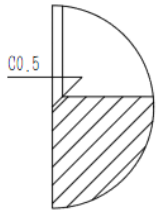


DETAIL B
SCALE 5 : 1

| | | | | | |
|---|---|---|---|---|---|
| UNLESS OTHERWISE SPECIFIED: DIMENSIONS ARE IN MILLIMETERS | Tolerances: Unless otherwise specified: ISO2768-mk | DEBUR AND BREAK SHARP EDGES | DO NOT SCALE DRAWING | REVISION | |
| | | | The University of Warwick<br>School of Engineering | | |
| | NAME | DATE | TITLE: | | |
| DRAWN | Christopher Krupke | 25/08/13 | Carrier1 | | |
| CHK'D | | | | | |
| APPV'D | | | | | |
| MFG | | | | | |
| Q.A | | | MATERIAL: | DWG NO. | A3 |
| | | | Q235 | | |
| contact | c.krupke@warwick.ac.uk | | SCALE:1:1 | SHEET 1 OF 1 | |

**Qty: 1**

All 6.3

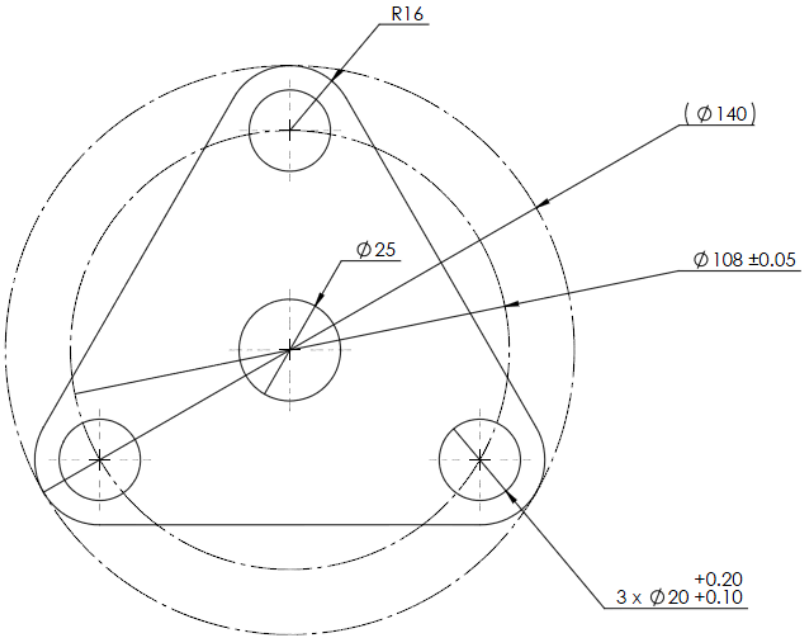


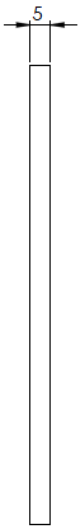


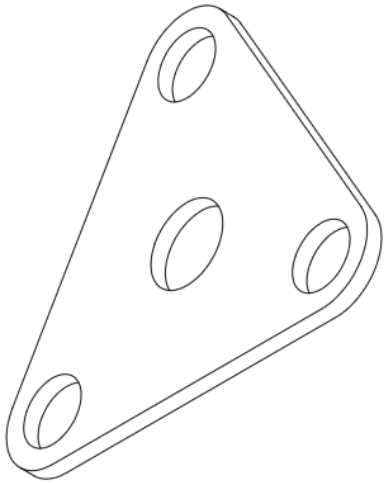

| | | | | | |
|---|---|---|---|---|---|
| UNLESS OTHERWISE SPECIFIED: DIMENSIONS ARE IN MILLIMETERS | Tolerances: Unless otherwise specified: ISO2768-mk | | | DEBUR AND BREAK SHARP EDGES | DO NOT SCALE DRAWING / REVISION |
| | NAME | DATE | | | The University of Warwick<br>School of Engineering |
| DRAWN | Christopher Krupke | 25/08/13 | | | TITLE: Carrier2 |
| CHK'D | | | | | |
| APPV'D | | | | | |
| MFG | | | | | |
| Q.A | | | MATERIAL: Q235 | | DWG NO. / A3 |
| contact | c.krupke@warwick.ac.uk | | | | SCALE:1:1 / SHEET 1 OF 1 |

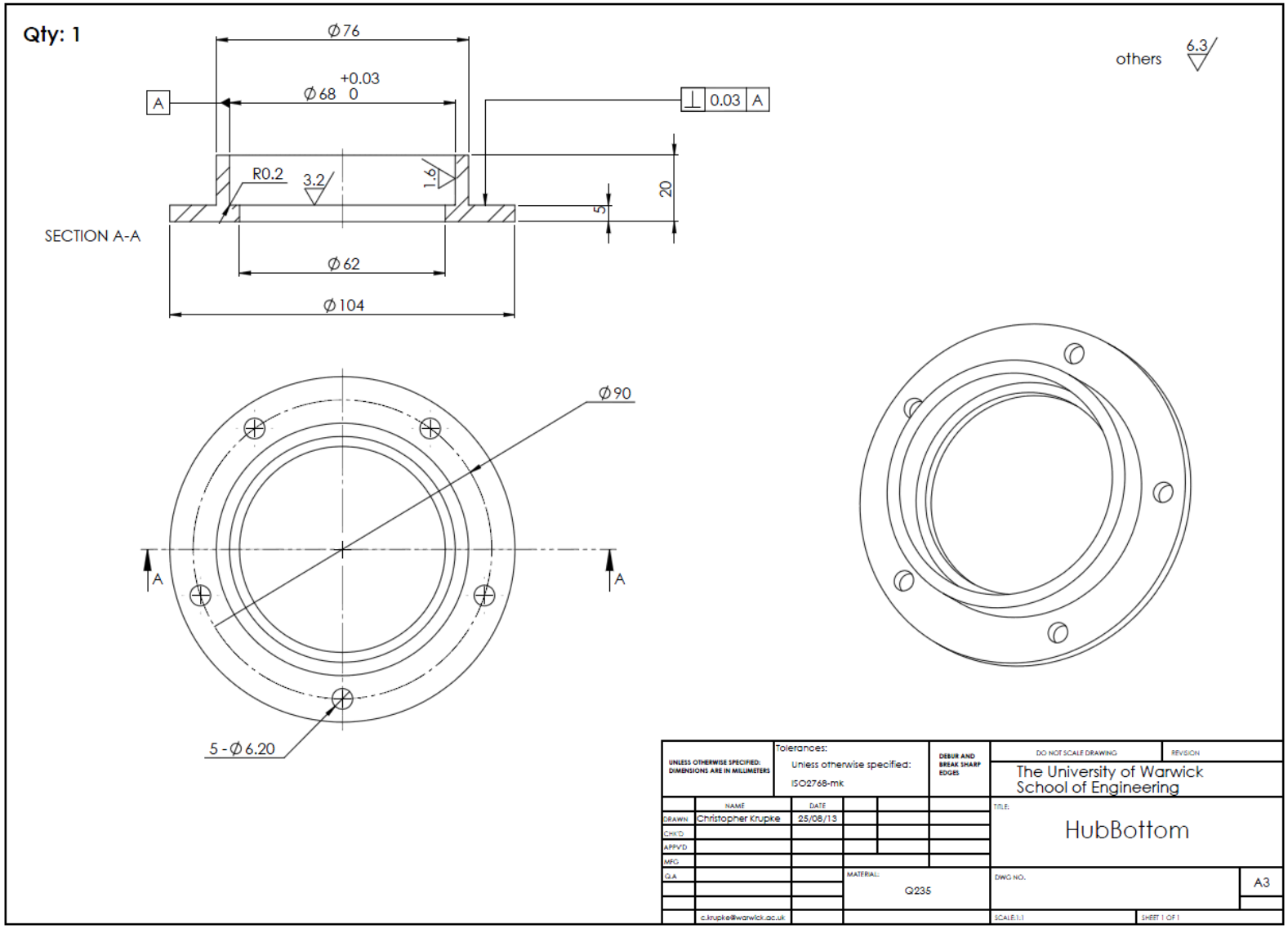
Qty: 1
Ø76
+0.03
Ø68 0
A
0.03 A
others
6.3
R0.2
3.2
1.6
5
20
SECTION A-A
Ø62
Ø104
Ø90
A
A
5 - Ø6.20
UNLESS OTHERWISE SPECIFIED: DIMENSIONS ARE IN MILLIMETERS
Tolerances:
Unless otherwise specified:
ISO2768-mk
DEBUR AND BREAK SHARP EDGES
DO NOT SCALE DRAWING
REVISION
The University of Warwick
School of Engineering
NAME
DATE
DRAWN
Christopher Krupke
25/08/13
CHK'D
APPV'D
MFG
Q.A
TITLE:
HubBottom
MATERIAL:
Q235
DWG NO.
A3
c.krupke@warwick.ac.uk
SCALE:1:1
SHEET 1 OF 1

| | |
|---|---|
| Module | 1.5 |
| Circular Pitch | 36 |
| Number of Teeth | 24 |
| Pressure Angle | 20° |
| Face Width | 15 |

others 6.3

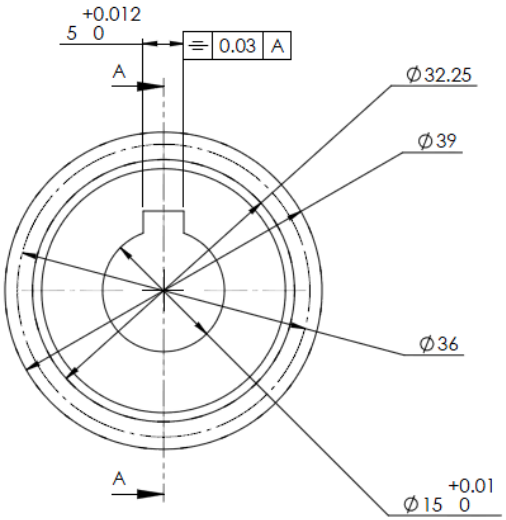


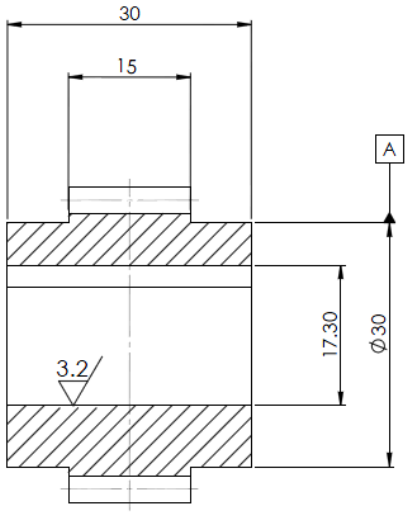


SECTION A-A

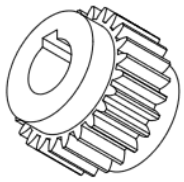

Teeth finishing: Grinding preferred

| | | | | | |
|---|---|---|---|---|---|
| UNLESS OTHERWISE SPECIFIED: DIMENSIONS ARE IN MILLIMETERS | Tolerances: Unless otherwise specified: ISO2768-mk | DEBUR AND BREAK SHARP EDGES | DO NOT SCALE DRAWING | REVISION | |
| | | | The University of Warwick<br>School of Engineering | | |
| | NAME | DATE | TITLE: | | |
| DRAWN | Christopher Krupke | 25/08/13 | SunGear | | |
| CHK'D | | | | | |
| APPV'D | | | | | |
| MFG | | | | | |
| Q.A | | | MATERIAL: | DWG NO. | A3 |
| | | | 20MnCr5 | | |
| contact | c.krupke@warwick.ac.uk | | SCALE:2:1 | SHEET 1 OF 1 | |

| | |
|---|---|
| Module | 1.5 |
| Circular Pitch | 72 |
| Number of Teeth | 48 |
| Pressure Angle | 20° |
| Face Width | 15 |

others 6.3

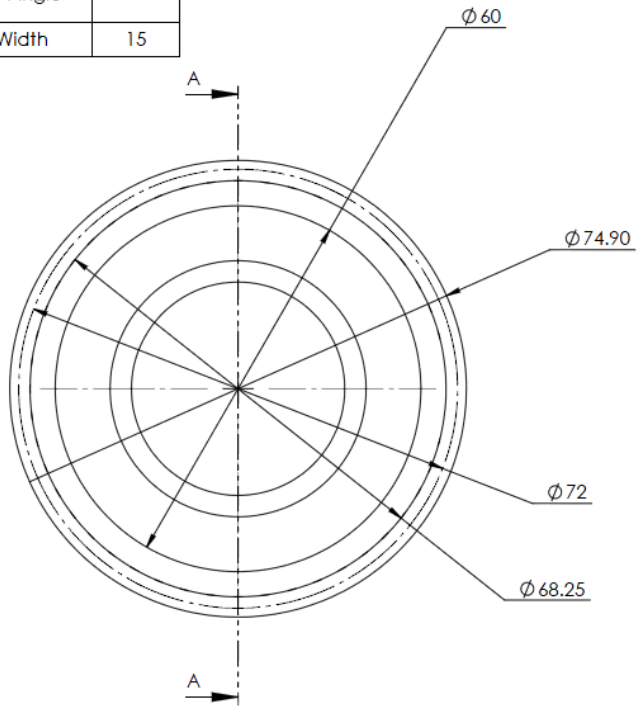


SECTION A-A
SCALE 3 : 2

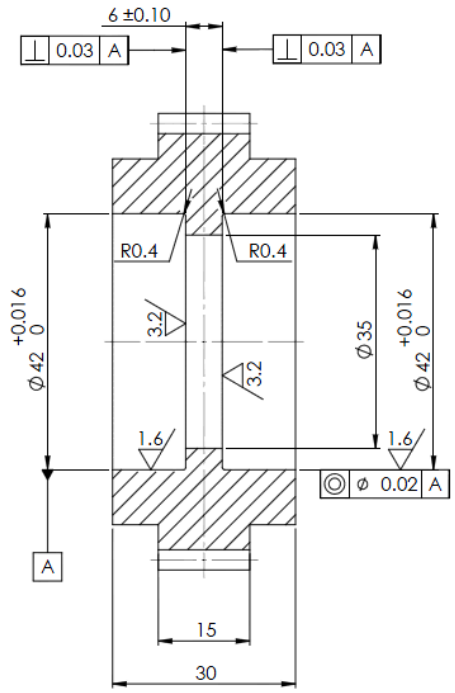


scale: 1:2

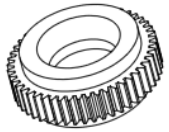

Teeth finishing: Grinding preferred

| | | | | | |
|---|---|---|---|---|---|
| UNLESS OTHERWISE SPECIFIED: DIMENSIONS ARE IN MILLIMETERS | Tolerances: Unless otherwise specified: ISO2768-mk | | DEBUR AND BREAK SHARP EDGES | DO NOT SCALE DRAWING | REVISION |
| | | | | The University of Warwick<br>School of Engineering | |
| | NAME | DATE | | TITLE: | |
| DRAWN | Christopher Krupke | 28/08/13 | | PlanetGear | |
| CHK'D | | | | | |
| APPV'D | | | | | |
| MFG | | | | | |
| Q.A | | | | | |
| | | MATERIAL: | | DWG NO. | A3 |
| | | 20MnCr5 | | | |
| contact | c.krupke@warwick.ac.uk | | | SCALE: 3:2 | SHEET 1 OF 1 |

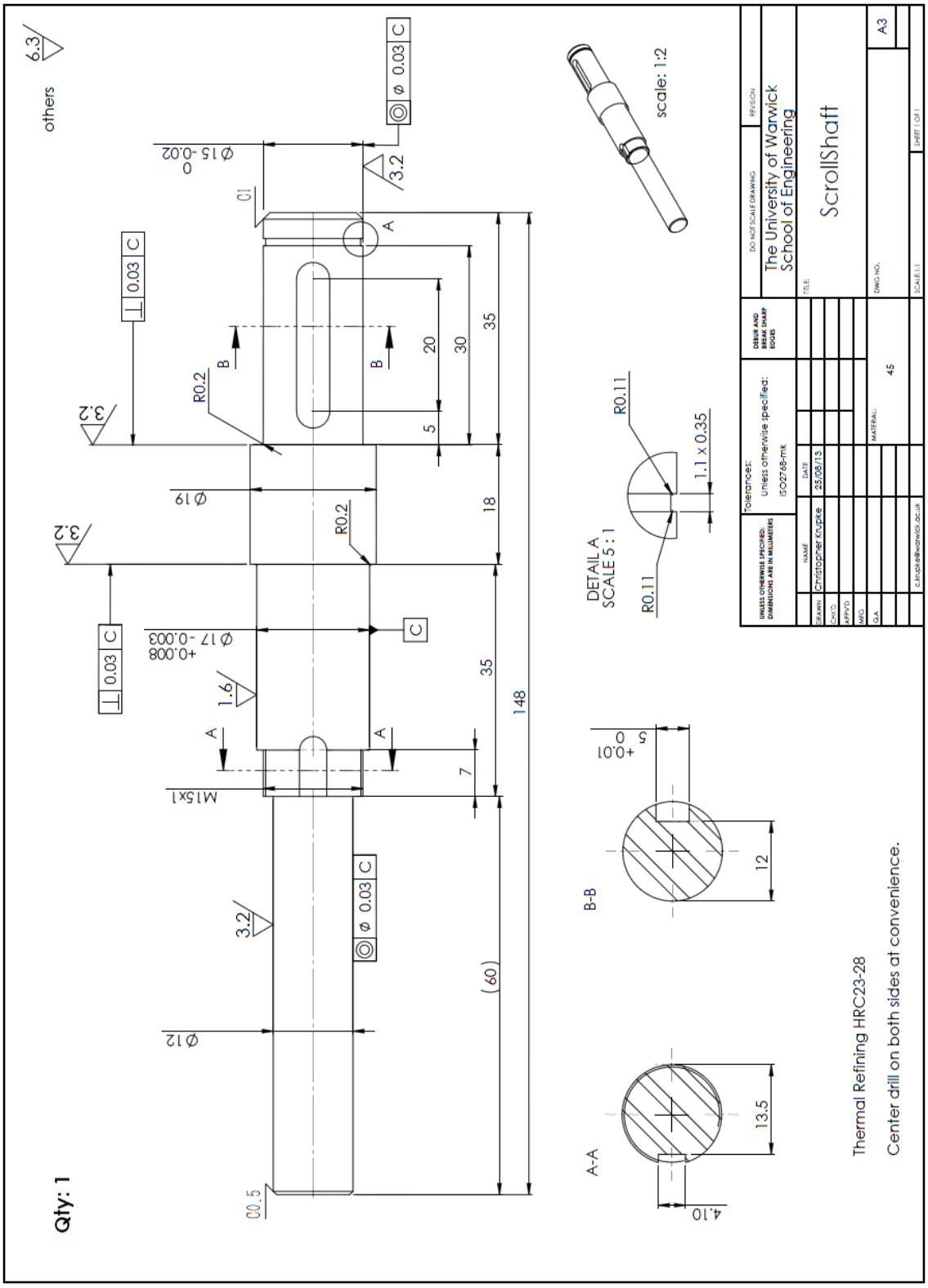
others
6.3
Qty: 1
scale: 1:2
DETAIL A
SCALE 5 : 1
R0.11
1.1 x 0.35
A-A
B-B
Thermal Refining HRC23-28
Center drill on both sides at convenience.
The University of Warwick
School of Engineering
ScrollShaft
Christopher Knipke
25/06/13
45
A3

**Qty: 1**

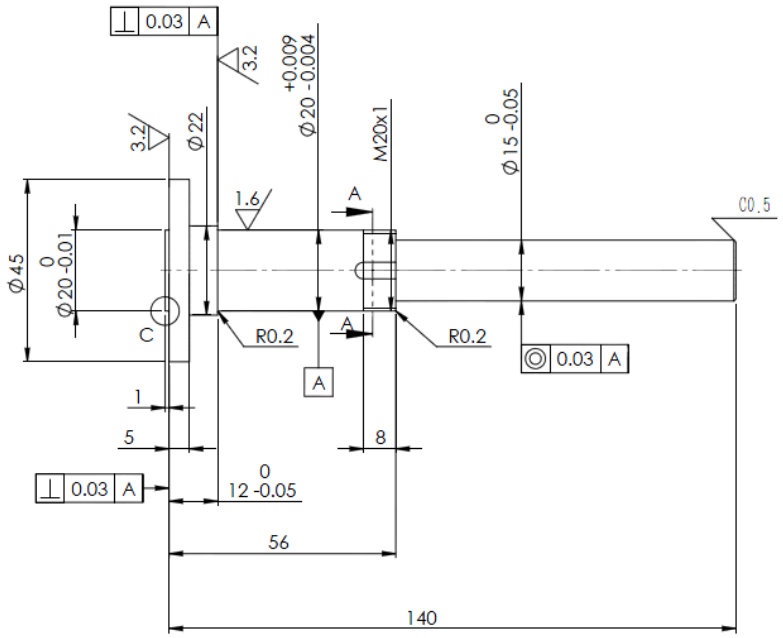


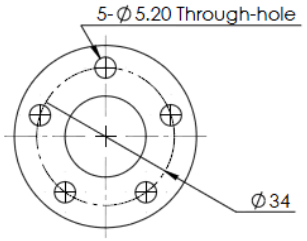


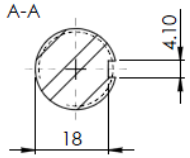


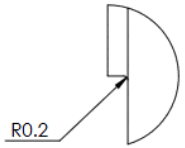


DETAIL C
SCALE 5 : 1

others 6.3

Thermal refining HRC23-28

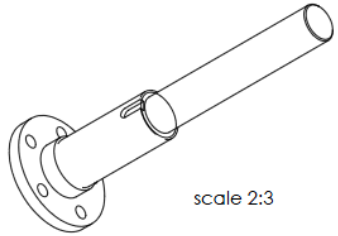

scale 2:3

Center drill on both sides at convenience.

| | | | | | |
|---|---|---|---|---|---|
| UNLESS OTHERWISE SPECIFIED: DIMENSIONS ARE IN MILLIMETERS | Tolerances: Unless otherwise specified: ISO2768-mk | | DEBUR AND BREAK SHARP EDGES | DO NOT SCALE DRAWING | REVISION |
| | | | | The University of Warwick<br>School of Engineering | |
| | NAME | DATE | | TITLE: | |
| DRAWN | Christopher Krupke | 25/08/13 | | AdapterTurbine | |
| CHK'D | | | | | |
| APPV'D | | | | | |
| MFG | | | | | |
| Q.A | | | MATERIAL: 45 | DWG NO. | A3 |
| | c.krupke@warwick.ac.uk | | | SCALE:1:1 | SHEET 1 OF 1 |

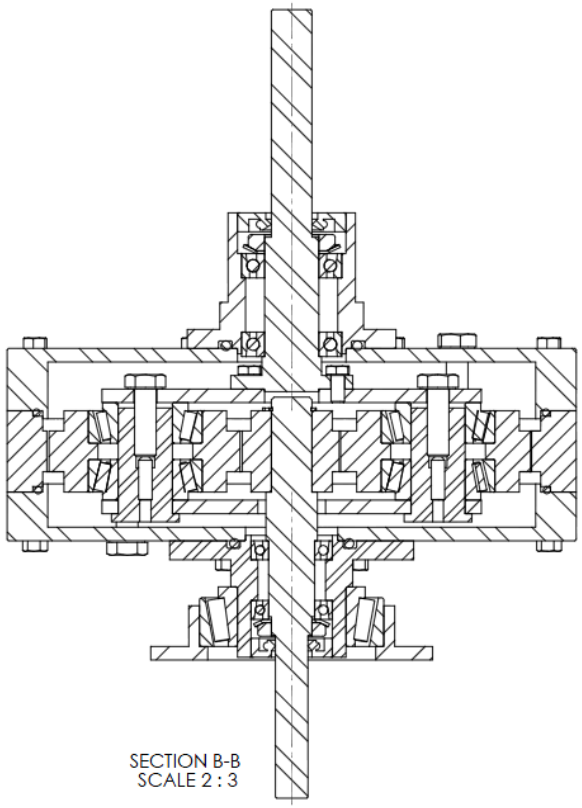

SECTION B-B
SCALE 2 : 3

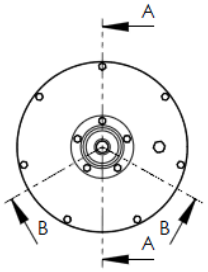


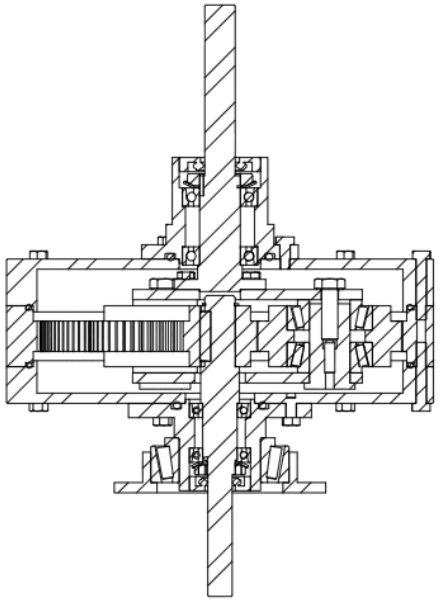

SECTION A-A
SCALE 1 : 2

| | | | | | |
|---|---|---|---|---|---|
| UNLESS OTHERWISE SPECIFIED: DIMENSIONS ARE IN MILLIMETERS | Tolerances: Unless otherwise specified: ISO2768-mk | | DEBUR AND BREAK SHARP EDGES | DO NOT SCALE DRAWING | REVISION |
| | | | | The University of Warwick<br>School of Engineering | |
| | NAME | DATE | | TITLE: | |
| DRAWN | Christopher Krupke | 25/08/13 | | Gear Assembled Cut | |
| CHK'D | | | | | |
| APPV'D | | | | | |
| MFG | | | | | |
| Q.A | | | MATERIAL: | DWG NO. | A3 |
| | | | | | |
| Kontakt: | c.krupke@warwick.ac.uk | | | SCALE:1:5 | SHEET 1 OF 1 |

## *E.3 Hardware and Instrumentation Components*

**Table E:2: Hardware and Instrumentation Components**

| Entity | Description | Quantity |
|---|---|---|
| Torque/Speed Sensor | TorqSense RWT411-EC-CK | 2 |
| Encoder DC motor | British Encoder PPR 1500 | 1 |
| Analogue Amplifier | TRM Electronics 20A 100V Analogue amplifier | 2 |
| Volumetric Flow Sensor | Festo MS6-SFE-F5-P2U-M12 | 1 |
| Pressure sensor | Festo SDE1-D10-G2-W18-L-PU-M8 | 2 |
| Thermocouple | K6 Type Thermocouple | 1 |
| Voltage transducer | LEM - LV 25-P - VOLTAGE TRANSDUCER, PCB - LV 25-P | 2 |
| Current transducer | LEM - LTS 6-NP - CURRENT TRANSDUCER, 6A, PCB - LTS 6-NP | 2 |
| Solenoid pressure regulator | Festo MPPE 3-1/4-10-010-B | 1 |
| Compressed air filter, manual regulator and lubricator unit | MSB6-1/2-FRC5:J1M1-Z | 1 |
| Resistor | 1.) Pentagon PHD 750 60R | 6 |
| | 2.) Pentagon PHD 750 22R | 3 |
| Power supply unit for DC motors | Digimess Concept series DC Power Supply SM3040 | 1 |
| Power supply unit for sensors | 1.) TTi EL302RT Triple Power Supply | 2 |
| | 2.) TRACOPOWER - TML 15515C - PSU, ENCAPSULATED, 15W, 5V, +/-15V - TML 15515C | 1 |
| Inverter | ABB ACS355 3kW | 1 |
| Air Receiver | SEALEY power products SA200T (200ltr) | 1 |
| Real-Time Controller | OPAL RT OP5600 | 1 |
| Personal Computer | Intel(R) Core(TM) i7-3770 CPU @3.40GHz 8Gb RAM | 1 |